京都大学大学院工学研究科
社会基盤工学専攻博士論文
令和 6 年 12 月

Doctoral Thesis
Department of Civil and Earth Resources Engineering
Graduate School of Engineering
Kyoto University
December 2024

Source Mechanism and Modeling of Seismic Events Causing Fault–Slip Rockbursts in Deep Mining

Geophysics Earth Resources Engineering

李亚涛 (LI YATAO)

Ph.D. Dissertation

Source Mechanism and Modeling of Seismic Events Causing Fault–Slip Rockbursts in Deep Mining

2024

李亚涛 (LI YATAO)

Abstract

Fault–slip rockburst has become a critical concern as mining operations reach greater depths, posing substantial risks to the stability and safety of underground environments. This research investigates the mechanisms of fault–slip rockbursts induced by mining activities, aiming to provide both theoretical advancements and practical strategies to mitigate seismic hazards in deep mining operations. Through the development of advanced numerical models and validation with field data, this study offers a comprehensive analysis of fault reactivation and its dynamic consequences, with an emphasis on understanding seismic wave propagation and its impact on mining infrastructure.

The initial phase of the study focuses on a 2-D plane-strain numerical model designed to assess how mining-induced stress perturbations influence fault stability. The model analyzes key parameters such as fault dip angle, mining proximity to faults, and the ratio of shear to normal stress. Results demonstrate that while an increase in shear stress alone does not destabilize the fault, a reduction in normal stress significantly contributes to fault reactivation, particularly in footwall mining scenarios. This model was applied to the Yuejin coal mine, where a mining-induced earthquake occurred in 2010, successfully predicting coseismic slip patterns and confirming the model's reliability in assessing static stress effects.

Building on the 2-D analysis, the study then advances to a 3-D numerical model that incorporates more complex fault geometries and stress distributions. The 3-D model includes the intermediate principal stress (σ_y), which is critical for capturing the full range of stress interactions affecting fault stability but often neglected in simpler models. The results reveal how panel length, panel orientation, and far-field stress direction influence fault–slip behavior, showing that longer mining panels and specific orientations significantly increase the likelihood of coseismic slip. Validation with field data from the Yuejin coal mine further supports these findings, demonstrating the robustness of the 3-D model in real-world mining scenarios.

In addition to the static analysis, dynamic rupture simulations were performed to

study the propagation of seismic waves generated by fault slip. The simulations provide insights into the distribution of peak particle velocity (*PPV*) and peak particle acceleration (*PPA*), which are critical for assessing the impact of seismic waves on mining support systems. The areas experiencing the highest *PPV* and *PPA* values were found to coincide with the most severe damage observed during the "8.11" coal burst accident. These findings highlight the importance of accounting for dynamic processes when assessing seismic risks in mining environments, as static models alone cannot fully explain the observed damage patterns.

This research advances the understanding of mining-induced seismicity by establishing a comprehensive modeling framework that integrates both static and dynamic fault–slip mechanisms. The combination of 2-D and 3-D numerical models, along with dynamic simulations, provides a robust, predictive approach for assessing fault–slip rockburst behavior and its impacts on mining infrastructure. These models offer practical guidance for designing safer mining layouts by identifying areas most vulnerable to seismic damage and optimizing support systems to mitigate risks. The results highlight the essential role of dynamic rupture processes and seismic wave effects in seismic hazard assessments for deep mining.

Acknowledgments

The PhD journey has been both challenging and rewarding, and I could not have completed this thesis without the unwavering support and guidance from my supervisor, friends, family, and colleagues. I would like to express my deepest gratitude to everyone who contributed to this work.

First and foremost, I would like to offer my profound thanks to my supervisor, Professor Eiichi Fukuyama, for his exceptional guidance, patience, and wisdom throughout my PhD studies. His extensive knowledge, insightful suggestions, and continuous support greatly enriched my research and helped me navigate the most complex challenges. Professor Fukuyama's meticulous attention to detail, coupled with his unwavering encouragement, pushed me to achieve more than I ever thought possible. I feel deeply honored to have studied under his supervision, and his influence will continue to inspire my future academic endeavors.

I would also like to express my sincere gratitude to Assistant Professor Nana Yoshimitsu, who provided invaluable advice and shared her vast expertise during various stages of my PhD. Her encouragement gave me the confidence to pursue my research with determination and enthusiasm.

My heartfelt thanks extend to Associate Professor Junichi Takekawa, Associate Professor Yoshitaka Nara, Professor Weiren Lin, and Professor Sumihiko Murata for their continuous support and thoughtful discussions, which were a source of strength throughout this challenging process.

I am also deeply grateful to all my Lab members, whose contributions, both academically and personally, made this journey much easier and more enjoyable. Their camaraderie and support have been invaluable to me during my research.

Finally, I would like to thank my family and friends for their endless support, patience, and encouragement throughout my PhD journey. Without their belief in me, this accomplishment would not have been possible.

Contents

List of Figures and Tables

the maximum value of k (k_{max}). The dashed line with open circles represents the distributions of k at L = 200 m (Fig. 5a), as a function of φ.

xyz-coordinate system is situated at the bottom left corner of the figure. L_s and L_d represent local coordinates along the fault strike and dip directions, respectively. These coordinates are set to 0 at the cross-section where the mining level intersects the fault at $y = 0$. W_m is the length of the panel. D_m represents the mining distance, with the positive direction indicating the hanging wall side and the negative direction indicating the footwall side. Vertical far-field stress is denoted as σ_z, and horizontal far-field stresses in the x- and y-directions are denoted as σ_x and σ_y, respectively; (b) Schematic diagram of the panel rotation angle, where the 'rotation center' denotes the commencement of rotation. Rotation starts from a position parallel to the local coordinate L_s at 0°, with the angle increasing in a counterclockwise direction; (c) Diagram illustrating the principal stress rotation angle. The orientation at 0° is aligned with the positive direction of the x-axis, encompassing a clockwise rotation around the z-axis, resulting in an incremental increase in angle.

of the 3-D model simulating mining-induced faulting and earthquake. *L1-L6* represents different geological layers in the 3-D structural model, with *L*1 being the surface layer and *L6* the deepest layer. (b) Local coordinate system on the working face. P_L is the panel length, P_W is the panel width, D_m is the mining distance, and L_s is the distance along the fault strike direction. (c) Local coordinate system on the fault plane. L_s represents the length along the fault strike direction, starting from the origin at the intersection of the fault plane and the working face, located on the left side at (x, y, z) = (1400, 200, 200), and extends along the intersection of the fault and coal seam centerline in the positive y-direction. L_d represents the length along the fault dip direction, starting from the same origin and extending upwards, with positive values in the upward direction along the fault plane.

Fig. 4-4 Plane of weakness with outward normal vector oriented at angle α to the direction of σ_1.

Fig. 4-5 Conceptual diagram of the slip-weakening friction model: μ_s and μ_d represent yield and residual friction coefficients, D_c indicates critical slip distance.

Fig. 4-6 Initial stress distribution for dynamic rupture calculation in Model_Cao, with D_m = 60 m, and μ_s = 0.375. (a) σ_n distribution, (b) Shear stress, τ_1, distribution along dip direction (L_d), (c) Shear stress, τ_2, distribution along strike direction (L_s). (d) Static slip with μ_s = 0.375. The orange circular region in the figure represents the designated nucleation zone, calculated based on Eq. 4-6.

Fig. 4-7 Mesh size and time step setting. (a) Number of grids inside the cohesive zone under different layers and critical slip distance D_c. The heterogeneous layers are denoted as L1 to L5. (b) Time step setting according to the Courant-Friedrichs-Lewy (*CFL*) condition. *CFL* values are less than 0.71. As the results for L5 and L6 are identical, only the results up to L5 are displayed.

Chapter 1 Introduction

1.1 Background and research motivation

With the global demand for energy and mineral resources rising, the depths of coal and metal mining operations continue to increase. Mining operations are progressing from shallow to deeper layers, triggering various new geological challenges, particularly mining-induced seismicity (Ranjith et al., 2017). Currently, coal mining operations in China are advancing at a rate of 8–25 m annually. By the end of 2022, more than 50 coal mines in China had reached depths exceeding 1,000 m, with the deepest mine reaching 1,510 m (Kang et al., 2023). Deep mining in proximity to faults can trigger sudden failure of coal and adjacent rocks, resulting in roadway roof collapse due to the violent release of strain energy (Cheng et al., 2019; Wang et al., 2021a; Li et al., 2007; Foulger et al., 2018; Zhou et al., 2022). Mining-induced seismic events not only threaten the safe operation of mines but can also cause significant casualties, equipment damage, and operational disruptions (Mark 2016; Wei et al. 2018).

Faults, as naturally occurring geological discontinuities, are sensitive to various factors, including the background stress field, geological structure, fault friction, and disturbances to local stress fields caused by mining activities. Mining operations lead to stress redistribution, causing stress concentration at fault zones, potentially triggering fault slip and inducing seismic events (Song and Liang, 2021; Wei et al., 2020). These stress perturbations pose serious risks to fault stability and mine safety. Therefore, understanding the mechanisms of mining-induced seismicity, particularly the quantitative analysis of mining effects on fault stability, stress distribution, static slip, and rupture processes, is fundamental to ensuring safe mine operations and developing effective disaster prevention strategies.

The increasing depth of mining operations has significantly elevated the frequency and intensity of induced seismic events, becoming a major safety challenge for deep mines in resource-rich countries such as China, South Africa, and Canada (Corner 1985; Foulger et al., 2018; Mngadi et al., 2019). In recent years, severe seismic events and rockbursts in deep coal mines, such as those in Yuejin and Yanzhou coal mines in China, have led to substantial economic losses and human casualties (Cai et al., 2021; Li et al., 2014). These incidents highlight gaps in the theoretical understanding of seismic mechanisms and the lack of effective mitigation strategies in practical mining operations. Consequently, the study of mining-induced seismicity holds crucial theoretical and practical importance.

1.2 Prior studies and existing challenges

1.2.1 Rockburst: An induced-earthquake event

(1) Definition of rockburst

Since Cook (1965) first introduced the concept of rockburst, numerous definitions have emerged, but no globally accepted standard has been established. Generally, rockburst definitions can be categorized based on phenomena, energy, seismicity, and hazards. Early definitions, such as those proposed by Russenes (1974), were based on phenomenology, combining the characteristics of surrounding rock failure and geotechnical analysis. One point of contention in these definitions is whether static brittle failures (e.g., caving, spalling, or slabbing) should be considered rockbursts. As a result, subsequent definitions focused more on violent rock failure and the ejection of rock fragments. Linkov (1994) emphasized that the essence of a rockburst lies in the surrounding rock acquiring kinetic energy.

From an energy perspective, more recent definitions emphasize the rapid release of energy during rockburst events, with accumulated strain energy widely considered the primary energy source. In this context, rockbursts are akin to seismic events and have been defined as seismic activities (Kaiser et al., 1996; Li et al., 2007) or even as small-scale artificial earthquakes (Cai, 2016). This conceptual framework prompted the extensive application of microseismic monitoring technologies in rockburst research. Numerous studies employed advanced seismic monitoring systems to conduct case analyses in hard rock mines (Li et al., 2016; Masethe et al., 2023; McKinnon, 2006; Ortlepp, 2000), coal mines (Cai et al., 2019; Lu et al., 2015), and hydropower projects (Liu et al., 2019a), aiming to elucidate the source mechanisms of fault–slip rockbursts. Additionally, rockbursts are of significant concern in engineering practices due to their potential for causing substantial economic losses and endangering worker safety, highlighting their importance for both evaluation and design in engineering projects.

Several factors influence the occurrence of rockbursts, including geological conditions, excavation methods, and external disturbances (Tan, 1992; Ortlepp and Stacey, 1994). To analyze rockbursts as seismic activities, key information such as timing, location, and magnitude must be identified.

The timing of rockbursts is crucial yet complex, and reliable methods for predicting their occurrence remain challenging to achieve. (Askaripour et al., 2022; Basnet et al., 2023). In the construction of the Jinping II Hydropower Station, most rockbursts occurred within 0.5 to 8 hours after excavation, while some took place between 6 and 30 days after excavation (Wang et al., 2012). Intermittent rockbursts were also observed, particularly near the working face (Lu et al., 2024; Yang et al., 2019; Zhang et al., 2024). Generally, the frequency of rockbursts decreases over time following excavation. This delayed response is often related to stress redistribution, viscoplastic behavior of the rock, and the gradual activation of complex geological structures, such as faults, making the prediction of rockburst timing extremely challenging and a topic for further research (He et al., 2023).

Location is another key factor, with rockbursts typically occurring near the working face due to excavation-induced disturbances, especially at areas of high stress concentration such as tunnel arches or sidewalls. In some cases, rockbursts can occur hundreds of meters away from the working face or even in completed tunnels, mainly due to delayed dynamic disturbances. Geological conditions also play a significant role in determining rockburst locations (Zhang et al., 2020). Rockbursts are less common in sedimentary rock compared to igneous or metamorphic rock (Afraei et al., 2019a; 2019b), indicating that rockburst occurrence is the result of an interplay between construction processes and geological conditions.

A rockburst has a single magnitude that represents its size, but the resulting shaking varies across locations depending on factors like distance, rock type, and mining conditions (Jarufe Troncoso et al., 2022; Ma et al., 2018; Si et al., 2020; Zhao et al., 2018).

Moment Magnitude (M_w) quantifies this event by analyzing the physical properties of the rockburst based on recorded waveforms. While magnitude provides a single value for the event's size, intensity varies geographically, indicating the shaking level at each site. This intensity depends primarily on the distance from the fault rupture. Instrumental data from monitoring stations can provide calculated estimates for shaking intensity at specific locations. Chen et al. (2015) proposed a classification method based on microseismic monitoring, incorporating radiated energy and the severity of surrounding rock damage for quantitative evaluation.

(2) Classification of rockburst

Accurate and unified classification of rockbursts is crucial for selecting appropriate protective or control measures (Kaiser and Cai, 2012). Rockburst classification is typically based on three main criteria: timing, failure mechanism, and triggering mechanism. From a timing perspective, rockbursts can be classified as immediate or delayed. In terms of failure mechanisms, rockbursts are commonly divided into fault–slip bursts, strainbursts, and pillar bursts (Fig. 1-1). Ortlepp and Stacey (1994) and Ortlepp (1997) categorized rockbursts into five types: strainburst, buckling, face crush/pillar burst, shear rupture, and fault–slip burst. Broadly, buckling-type rockbursts can be considered strainbursts, while shear rupture types align with fault–slip bursts. Kaiser and Cai (2012) focused on three primary categories: strainburst, pillar burst, and fault–slip burst. Rockbursts generally arise from either localized mining-induced energy release causing source damage (e.g., strainburst without significant remote dynamic stress) or from dynamically-induced events, where remote seismic activity transfers energy or significantly increases dynamic stress, contributing to damage (e.g., strainburst triggered by a remote seismic event). Rockburst phenomena are closely related to fault slip. This classification, as used by Chen et al. (2015), Fan et al. (2016), and Jian et al. (2018), combines pillar bursts with strainbursts and simplifies the original five rockburst sources. Regarding triggering mechanisms, rockbursts are classified into strainbursts and impact-induced rockbursts. Strainbursts occur spontaneously, while impact-induced rockbursts are triggered by external disturbances and can occur in low-stress conditions or existing underground structures. For instance, energy from seismic waves caused by fault slip may not constitute the primary energy release of a rockburst, but it can elevate the system's stored energy to the threshold necessary to trigger a rockburst.

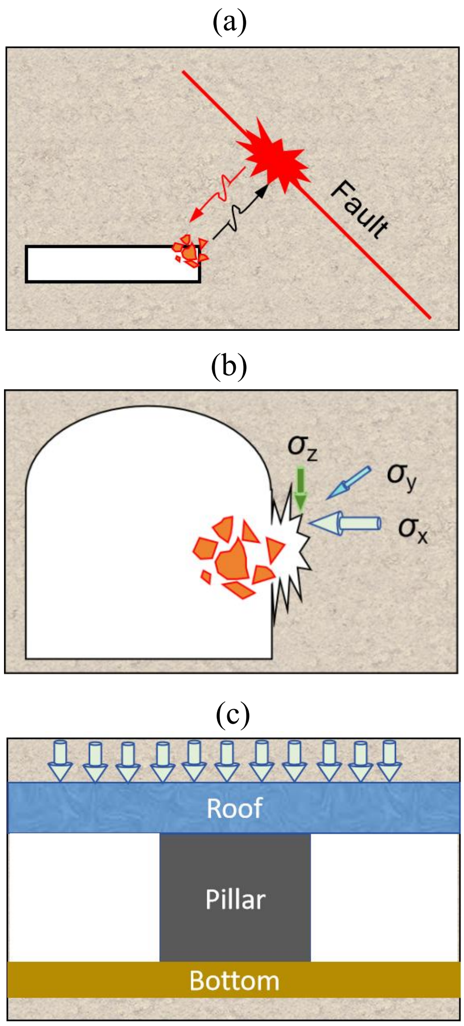

Fig. 1-1 Schematic illustration of rockburst in deep mining. (a) fault–slip rockburst; (b) Strain rockburst; (c) Pillar rockburst. Modified after Cai et al. (2021), Chen et al. (2024), and Ortlepp and Stacey (1994).

Fault–slip rockbursts occur when localized stress concentrations or fault slips cause sudden fracturing of mine rock, releasing large amounts of stored strain energy and generating intense seismic vibrations (Cao et al., 2023; Gao et al., 2021; Lu et al., 2019). This phenomenon is particularly common in deep coal mining operations, especially when the working face is near fault zones, where the frequency of rockbursts increases significantly (Konicek et al., 2019; Wang et al., 2017). fault–slip rockbursts not only cause severe damage to mining faces and equipment but can also lead to mine collapses and equipment failure (Balsamo et al., 2010). The interaction between fault slip and rockburst is highly complex, with seismic waves generated during fault slip potentially triggering additional rockbursts. Therefore, understanding the mechanisms of fault–slip rockbursts is critical for effective risk management.

1.2.2 Literature review on fault–slip rockburst

With the expansion of deep mining operations, mining-induced seismicity and fault–slip rockbursts have become major concerns for mine safety. Significant research has been dedicated to uncovering the mechanisms behind these phenomena, aiming to enhance safety measures and reduce seismic risks. Insights into fault–slip behavior and rockburst mechanisms have been gained through field observations, theoretical analysis, numerical modeling, and experimental studies. These investigations focus on two main aspects: how mining activities induce fault slip, and how such slip impacts the mining activities.

(1) Field observations

Numerous studies have investigated how deep mining operations and tunnelling, lead to fault instability and induce seismic events through stress redistribution. For example, Verdon et al. (2018) conducted an in-depth investigation of the Thoresby Colliery in Nottinghamshire, UK, where each longwall panel measured approximately 300 m wide, 1000 to 3000 m long, and 2.5 m high (Younger, 2016). They localized seismic events, compared their locations with the propagation of the mining face over time, and analyzed seismicity rates relative to the volume of coal extracted. By using spectral analysis and event frequency-magnitude distributions, they assessed the structural scale of the sources generating these events. The study revealed that the majority of seismic events were closely related to the movement of the longwall face, particularly within 300 m ahead of it, demonstrating that the longwall mining operations directly induced seismicity in the region. Zhang et al. (2022) studied a fault–slip rockburst with a local magnitude of 2.3 that occurred in a deeply buried tunnel in China. This fault–slip rockburst delayed construction by nearly two months and caused extensive tunnel damage. Through detailed observation of tunnel damage and continuous microseismic monitoring at the site, they identified that the rockburst originated from the hanging wall of a filled structural plane, with surrounding rock masses dynamically fracturing along this plane. The event was marked by intermittent microseismic activity, which severely disrupted normal construction schedules. The primary frequency of the microseismic events associated with the rockburst was 13 Hz, allowing for the recording of the complete development and occurrence process of the fault–slip rockburst. Further analysis of stress evolution during the rockburst process revealed that tensile fractures were predominant during the preparatory stage, while shear fractures and structural plane displacements occurred immediately before the rockburst. Due to the presence of a nearby fault, a substantial number of cracks developed rapidly and coalesced, leading to extensive tunnel damage. Zhang et al. (2023b) conducted a study on a fault–slip rockburst event that occurred during Tunnel Boring Machine (TBM) excavation in a deeply buried tunnel in China, utilizing microseismic monitoring and geological surveys to investigate the event. They analyzed the spatiotemporal evolution of microseismic activity and stress drop. During the development stage of the fault–slip rockburst, most microseismic events were identified as tensile failures, accompanied by a few mixed-mode and shear events. At the onset of the fault–slip rockburst, microseismic activity was dominated by shear events with some mixed-mode failures, attributed to dynamic fault rupture. The accumulated energy near the fault was released intermittently, resulting in rockbursts and mud inflow into the tunnel.

(2) Theoretical analysis

Kidybinski (1981) highlighted that the inherent capacity of natural coal to accumulate and swiftly release elastic strain energy is a critical factor for rockbursts in deep coal mines. This insight underpins the bursting liability theory, which centers on the rock mass's potential to store energy and generate impact damage. According to this theory, rockburst occurrence is primarily governed by the rock's intrinsic characteristics. Bursting liability is seen as an inherent property of the rock medium; when it surpasses a certain threshold, a rockburst is triggered. Ortlepp (1992) observed significant rockbursts in a deep South African gold mine when high-stress remnants were mined. Large seismic events recorded by the WSSN station, about 60 km away, aligned with several shear ruptures encountered in the mine. Detailed examination of two ruptures confirmed them as rockburst sources. Scanning electron microscopy revealed distinct features in the fresh "rock flour" providing strong evidence of intense "impact rebound" during fault slip events. Based on elastic theory, Wang et al. (2021a) developed a mechanical model that incorporates mining-induced stresses to calculate the distribution of shear and normal stresses on the fault plane. The model analyzes normal and reverse faults under conditions where the lateral pressure coefficient is greater than or less than 1.0, respectively. Using the elastic energy of the fault, the model attempts to assess the likelihood of fault slip. Additionally, considering the engineering context and this mechanical model, they further suggest that interactions between the fault and overlying strata may induce coal bursts as the mining face approaches the fault. He et al. (2016) examined rockburst mechanisms in discontinuous rock masses by modeling energy changes induced by tunneling under linear elasticity. They found that elastic strain energy increases within an annular zone extending three tunnel diameters from the center, irrespective of tunnel size, in situ stress, or stress ratio. Identifying a Rockburst-Prone Zone within one diameter from the tunnel center, they noted that tunneling amplifies shear stress along preexisting discontinuities, causing block displacement before intact rock failure. Using the discrete element method (Cundall and Strack, 1979), they quantified kinetic, strain, and dissipated energy, finding that kinetic energy from strain relaxation grows with higher initial stress and lower frictional resistance of discontinuities. Ma et al. (2018) identified rockburst precursors by observing alignment between acoustic emissions and damage indicators, classifying them into three seismogenic models based on spatiotemporal patterns. Using seismology principles—stress buildup, shadow, and transfer—they proposed three rockburst criteria: spatiotemporal stress evolution, microseismic event magnitude and clustering, and sudden apparent volume changes. Their analysis of microseismic and landsonar data highlights rock heterogeneity and fracture intersections as primary triggers for rockburst initiation. Bai et al. (2022) indicated that deep mining activities induce unloading and reactivation of discontinuous structures (such as faults and folds), leading to the release of elastic strain energy, which can further trigger fault–slip rockburst.

(3) Numerical modeling

Due to the typically concealed nature of fault hypocenters and the difficulty in acquiring the data such as fault zone profiles, mechanical properties of fault gouge, and frictional parameters, accurately predicting and forecasting fault–slip-induced rockbursts presents substantial challenges (Ortlepp, 1992; Stewart et al., 2001). Numerical modeling has become an essential tool to overcome these limitations, enabling the simulation of conditions and mechanisms leading to fault–slip rockbursts. However, due to the complexity and high computational cost of dynamic analysis, in these cases, the risk of fault–slip rockbursts is typically evaluated by correlating relevant indicators such as stress concentration, seismic moment, and dissipated energy with conditions in underground excavations (e. g., Cai et al., 2019; Xiao et al., 2022).

The geometry structure of the mine, including the presence of previously mined-out seams, played a critical role in limiting the size of seismic sources. Additionally, Wei et al. (2020), through 2-D numerical simulations, analyzed the concentration of shear stress around faults caused by longwall mining. The results indicated that fault slip predominantly occurred near coal seams, particularly in regions where normal stress experienced a significant reduction. They further observed that seismicity was notably reduced when the mining face was within 20 m of a fault, providing essential insights into how mining activities influence static fault slip. The idea that longwall mining-induced shear stress concentration can activate faults has been widely supported by other studies (Cheng et al., 2019; Li et al., 2024a; Ma and Zhang, 2023; Song and Liang, 2021; Sun et al., 2023). Furthermore, Shan et al. (2023) used the finite difference method to simulate pressure unloading and fault slip caused by excavation, analyzing how mining operations parallel to faults affect the stability of overlying rock masses. Their research confirmed that mining-induced stress changes are the primary cause of fault instability and provided detailed quantitative analysis of stress concentration and unloading mechanisms.

Bigarre et al. (1992) used discrete element method (DEM), the Three-Dimensional Distinct Element Code (3DEC) (Itasca, 2021b), to quantify the seismic moment associated with fault–slip-induced coal bursts, evaluating the risk based on fault–slip and geological structures. Similarly, Islam and Shinjo (2009) employed the Boundary Element Method (BEM) to simulate dynamic fault failure, using stress concentration zones to assess the potential for dynamic rupture. Naji et al. (2018) performed quasi-static analysis using the finite difference method (FDM), FLAC3D (Itasca, 2021a) to investigate shear zone-type rockbursts in the Neelum-Jehlum Hydropower Project, where they examined stress concentration due to shear zone slip and its influence on rockburst initiation.

When numerical modeling results are validated against field monitoring data, they can help identify key triggers for fault–slip and subsequent rockbursts. For instance, Sjöberg et al. (2012) employed 3DEC to simulate fault–slip potential in the Luossavaara-Kiirunavaara Aktiebolag mine, comparing numerically calculated seismic moments with field-monitored seismic data to assess how different mining sequences affect the potential for fault reactivation.

While static analysis of seismic magnitude provides insight into the potential magnitude of seismic events, it lacks the ability to capture dynamic processes, such as seismic wave propagation, which are critical for assessing the risk of rockbursts. To overcome this limitation, dynamic analyses are required. Manouchehrian and Cai (2017) conducted point-source dynamic simulations using the finite element method (FEM), Abaqus2D (Dassault, 2021) to assess how discontinuities influence rockburst occurrence around tunnels, finding that rockbursts were more severe near geological structures. Sainoki and Mitri have conducted several studies using FLAC3D, performing both static and dynamic analyses to evaluate parameters like fault–slip velocity, rupture propagation, and peak particle velocity (Sainoki and Mitri, 2014a; 2014b; 2014c; 2015a; 2015b).

Cao et al. (2023) further explored these dynamics by utilizing a source time function in FLAC3D, demonstrating that increased vibration velocity and displacement due to dynamic fault–slip loading, combined with a sharp rise in abutment stress and strain energy density, are critical precursors for coal bursts (Liu et al., 2019b). As the distance between the longwall face and the fault decreases, the coal seam experiences elevated stress, leading to strain energy accumulation. Once dynamic fault–slip loading is transferred to the coal seam, the superposition of static stress and strong seismic wave vibration significantly increases the likelihood of coal bursts. Similarly, Gao et al. (2021) simulated dynamic fault rupture by instantaneously reducing the shear strength of the fault—adjusting parameters such as cohesion, tensile strength, and friction angle—to explore how fault–slip behavior contributes to rockburst hazards. These studies also emphasized the importance of fault geometry (e.g., fault length, dip angle, and proximity to underground workings) in influencing rockburst outcomes, and evaluated the effectiveness of support systems such as rock bolts. Furthermore, they analyzed the impact of weak zones (such as regions with low Young's modulus) on the dynamics of fault–slip rockbursts.

(4) Experimental studies

He et al. (2012) examined how bedding plane orientation affects rockburst behavior in sandstone under triaxial unloading. In their tests, they set unloading planes either parallel or perpendicular to bedding planes, capturing fracture processes with high-speed cameras and observing microstructural details via SEM. Fractal analysis assessed fragment velocity, mass, and fragmentation extent. Results showed that unloading perpendicular to bedding planes led to strength-controlled failure, higher fragment velocities, and deep fractures, while parallel unloading produced stability-controlled failure, lower velocities, and flatter fractures. Meng et al. (2017) focused on the key factors influencing fault–slip rockbursts in deep hard rock tunnels, such as rock type, normal stress, and surface roughness. They conducted constant normal load shear tests on rough, interlocking asperity surfaces to study the shear behavior and acoustic emission characteristics associated with fault–slip rockbursts. Using these shear tests, they simulated and measured the rockburst process under high-stress conditions, testing samples of granite, marble, and cement mortar while recording real-time energy changes with acoustic emission (AE) monitoring.By varying parameters including normal stress, surface roughness, infill materials, and shear history, they evaluated each factor's influence on fault–slip rockburst initiation. Their findings revealed that granite samples experienced substantial stress drops and brittle failure after peak stress, releasing high energy levels and showing a high tendency for rockburst. In contrast, marble and cement mortar samples exhibited stable shear failure with lower rockburst risk. The study further demonstrated that post-peak stress drop correlates positively with normal stress, indicating that higher normal stress increases both rockburst likelihood and intensity. Additionally, rougher surfaces facilitated pronounced brittle failure and greater stress drops, leading to higher energy release.

In the experiments, for rock failure under triaxial conditions, advancements in triaxial testing equipment have enabled numerous laboratory studies to investigate how various rock types respond to different stress conditions (Mogi 1971; Feng et al. 2020; Ødegaard and Nilsen 2021). It is widely recognized that intermediate stress has a significant impact on rock behavior, as shown through true triaxial experiments (Hu et al. 2023; Haimson and Chang 2000, 2002; Chang and Haimson 2012). In deep mining near faults, triaxial tectonic stress plays a pivotal role (Diederichs 2003; Gao et al. 2018, 2020), emphasizing the importance of further studying how intermediate far-field stress influences fault slip. Under true triaxial compression conditions, intermediate stress has a significant effect on rock failure behavior (Mogi, 1967, 1971, 2007; Chang and Haimson, 2000, 2012; Haimson and Chang, 2000, 2002). Wiebols and Cook (1968) proposed an energy criterion for rocks, theoretically examining the impact of intermediate stress on rock strength, while Zheng and Deng (2015) applied a failure probability model to study this effect. Wang et al. (2021b) conducted a micromechanical analysis using a DEM particle-based model. Hu et al. (2023) further investigated the influence of intermediate stress on rockbursts using a DEM-based structural analysis model, combining experimental and numerical simulations. Based on this, they applied the Mogi strength criterion to develop strength criteria for assessing rockburst potential and intensity in practical engineering applications.

When assessing the hazards of fault dynamic rupture in deep mining, seismic wave propagation must be carefully considered (Hildyard, 2002; Buijze et al., 2019; Cheng et al., 2019; Cai, 2024). Seismic waves generated by fault rupture have a significant impact on underground stability (Sainoki et al., 2020). Studies have shown that peak particle velocity (*PPV*) and peak particle acceleration (*PPA*) play a critical role in affecting mining environments (Jiang et al., 2020; Gao et al., 2021). The complexity of underground environments, characterized by faults, ore bodies, and mined-out spaces, leads to complex wave fields, including reflected, refracted, and diffracted waves. Even minor disturbances from transmitted seismic waves can trigger pillar rock bursts in rock masses already close to failure (Gibowicz, 2009; Wang et al., 2023). Therefore, accurately assessing seismic parameters such as PPV and peak particle acceleration (PPA) due to fault–slip bursts is essential for designing effective dynamic support systems in mining (Stacey, 2012).

1.2.3 Remained problems in fault–slip rockbursts

Despite significant progress in understanding mining-induced seismicity and fault–slip rockbursts, considerable challenges remain in accurately predicting these events and comprehensively understanding their underlying mechanisms. These challenges are concentrated in several key areas:

(1) Interaction between shear and normal stresses

Recent studies predominantly focus on the influence of shear stress concentration on fault stability, with relatively less attention given to changes in normal stress (Wei et al., 2020; Song and Liang, 2021; Shan et al., 2023; Wu et al., 2021; Jiao et al., 2021; Lyu et al., 2021; Zhang et al., 2023a; Zhu et al., 2021). However, normal stress plays a critical role in fault–slip mechanisms, as its increase or decrease directly affects frictional resistance along fault planes, altering slip potential. The difficulty of defining precise fault geometries, particularly in deep mines, often limits our understanding of normal stress distribution, thus hindering comprehensive risk assessments for fault–slip-induced rockbursts.

Most existing models treated shear and normal stress separately rather than examining their combined effects (e.g., Cao et al., 2023; Jiao et al., 2021; Wang et al., 2021a). Mining-induced stress perturbations generate complex changes in both shear and normal stress around faults, with distributions that vary across different directions and depths, potentially leading to multi-directional fault instability. The fault stress ratio in the Mohr-Coulomb criterion (i.e., the ratio of shear to normal stress) is a crucial indicator of fault stability; however, its application often lacks robust data support. The absence of synchronized field measurements makes it difficult to accurately evaluate the role of combined shear and normal stress effects in fault–slip behavior.

(2) Influence of intermediate principal stress (σ_y) and working face layout on fault slip

2-D in-plane static numerical studies highlight coseismic slip characteristics along fault dip directions. During mining-induced reverse fault reactivation, coseismic slip may also occur along strike directions. When mining activities are conducted near faults, localized stress disturbances can significantly increase the likelihood of mining-induced seismic events. However, the 2-D Mohr-Coulomb failure criterion assumes rock failure is governed solely by minimum and maximum principal stresses, leaving the potential influence of intermediate principal stress uncertain—especially when mining-induced stress disturbances occur along fault surfaces. Furthermore, the role of intermediate principal stress (σ_y), as well as the layout and length of the working face (W_m), in coseismic slip remains unclear when mining operations approach faults.

(3) Evaluation of dynamic response of supporting system against seismic waves

Simplified fault models commonly used in current research, such as uniform slip models and source functions, provide insight into seismic wave impacts on mining faces due to fault rupture (e.g., Cai et et., 2021; Cao et al., 2023; Gao et al., 2021; Sainoki and Mitri 2014). However, these approaches often overlook the complex dynamic behavior of faults in deep mining environments. In deep mining, fault slip is influenced by both tectonic stress and mining-induced stress perturbations, resulting in multifaceted rupture processes. Simplified models tend to neglect the non-uniformity and dynamic propagation of fault rupture, failing to capture stress perturbations that vary with depth, fault geometry, and material properties. The propagation of seismic waves, energy accumulation, and release during dynamic rupture affect fault slip behavior. Accurately simulating the full complexity of non-uniform slip and dynamic responses in deep mining remains a challenge.

Seismic wave propagation induced by fault slip significantly impacts the stability of mining environments. Current studies lack precise modeling of seismic wave effects, which is essential for designing effective dynamic support systems. The absence of detailed fault rupture models limits the ability to capture wave propagation characteristics accurately, affecting predictions of mining infrastructure's dynamic response. Particularly in mining, key seismic parameters such as *PPV*, and *PPA*, which influence support system design, are challenging to evaluate without high-resolution modeling that incorporates field data. A refined modeling approach, combining field observations and higher resolution, is necessary to accurately predict the impact of seismic waves on infrastructure in complex geological settings.

(4) Dynamic and static modeling approaches

Dynamic and static modeling each offer distinct advantages in fault–slip rockburst studies. Static models are relatively simple and well-suited to simulate stress concentration and long-term fault–slip trends but lack the capacity to capture transient stress wave propagation. In contrast, dynamic models better capture transient fault–slip processes, making them more suitable for studying stress wave propagation and non-uniform fault slip. In deep mining, various stress perturbations create compound effects in fault zones, requiring models that simulate both long-term stress accumulation and instantaneous stress release and slip behavior. Integrating dynamic and static analyses is expected to be a significant future direction in fault–slip rockburst research.

1.3 Research objectives

The primary objective of this research is to develop a further understanding of the mechanics and modeling of fault–slip rockbursts in deep mining. Specifically, this study aims to improve the precision of fault–slip event predictions by incorporating key factors such as mining-induced stress distribution, fault orientation, and dynamic rupture characteristics. These enhancements provide deeper insights into fault slip under mining conditions, offering practical guidance to mitigate seismic risks in mining operations.

1.3.1 Mining-induced fault rupture and coseismic slip based on 2-D numerical investigation

Chapter 2 systematically examined mining-induced fault instability using the fault stress ratio as a key analytical tool. The investigation focused on two critical aspects of fault reactivation: fault failure and coseismic slip. It was found that the magnitude of mining-induced seismic events is more closely linked to the extent of coseismic slip than to stress alone, underscoring the need for detailed analysis of both fault failure and slip processes. Two models were employed to address these factors. The first model examined stress disturbances and the fault stress ratio under the assumption of infinite fault frictional strength. The second model incorporated a friction coefficient to enable a quantitative study of coseismic slip distribution, considering variables such as mining distance and the background stress ratio. These models provided valuable insights into the mechanisms driving mining-induced fault instability. Furthermore, chapter 2 identified a gap in existing research by questioning the effectiveness of traditional terminal mining line designs in deep mining operations near faults under high tectonic stress conditions. By exploring the mining-induced fault stress ratio and coseismic slip, the study offered a clearer understanding of the underlying mechanisms of fault instability. The fault reactivation model developed in this study was specifically tailored to conditions at the Yuejin coal mine in China, focusing on the effects of fault failure and coseismic slip as the mining face approaches the fault.

1.3.2 Impact of stress field rotation, working face, and fault orientation

Chapter 3 utilizes 3-D numerical simulations to investigate the effects of stress field rotation and the orientation of the working face and fault on fault slip mechanisms, focusing on their influence on fault reactivation and induced seismicity. The primary goal is to evaluate how these factors affect fault reactivation and coseismic slip by employing robust static numerical models that explicitly incorporate fault friction. This analysis provides deeper insights into the relationship between mining operations and fault stability, with particular emphasis on the role of intermediate stress and mining geometry. The study systematically examines the influence of σ_y and W_m on faulting behavior, considering both panel layout and an interface friction model. This 3-D analysis expands upon the 2-D model proposed by Li et al. (2024a), addressing the added complexities introduced by intermediate principal stress and varying panel dimensions.

1.3.3 Dynamic fault rupture and the seismic wave impact on the working face

Chapter 4 integrates static stress analysis with dynamic fault rupture simulations to quantitatively assess the effects of fault slip and seismic wave propagation on the dynamic response of mining faces and infrastructure. This research aims to provide a theoretical foundation and practical solutions for mitigating the risks of fault–slip rockburst in deep mining environments. A comprehensive model is constructed, incorporating both tectonic stresses and mining-induced disturbances, to better understand how dynamic ruptures near faults impact mining stability. Building on the underground structural models of the Yuejin coal mine (Cai et al., 2023; Cao et al., 2023), the model is developed to estimate mining-induced seismic motions affecting mining faces. This model accounts for both tectonic and mining-induced stresses to capture the complexity of fault–slip behavior. Dynamic rupture analysis is introduced to estimate key parameters such as rupture velocity, moment rate function, and rupture duration. This approach offers deeper insights into fault reactivation and its impacts on coal seam stability, surrounding rock masses, and mining infrastructure. Additionally, critical seismic parameters such as peak particle velocity (PPV), peak particle acceleration (PPA), and dominant seismic wave frequencies are assessed to evaluate the effects of dynamic rupture on mining operations. By integrating these dynamic factors with field observations, the modeling approach enhances predictive capabilities and provides valuable insights for safer mining practices.

1.4 Structure of the thesis

This thesis is organized into six chapters, each addressing key challenges in mining-induced fault reactivation and seismic risks (Fig. 1-2). It combines static and dynamic modeling techniques to offer a comprehensive analysis, with innovative contributions in the modeling and understanding of fault–slip mechanisms and their practical implications for mining safety.

Chapter 1: Introduction

This chapter outlines the motivation for investigating mining-induced seismicity in deep mining environments, where the risk of fault reactivation and rockbursts increases significantly. The key challenge addressed is the need to accurately assess seismic risks due to complex interactions between mining activities and fault systems. A review of existing studies highlights the gaps in integrating static stress analysis with dynamic rupture simulations, setting the stage for the research objectives of developing a combined modeling approach. The main innovation lies in proposing a framework that unites static and dynamic analysis to fully capture fault behavior and its impact on mine safety.

Chapter 2: Mining-induced fault rupture and coseismic slip based on 2-D numerical investigation

This chapter tackles the challenge of understanding how mining activities near faults affect fault stability, particularly under static stress conditions. A 2-D plane-strain numerical model is developed to systematically investigate stress distributions and fault reactivation. This model focuses on key parameters such as mining distance, fault dip angle, and the fault stress ratio.

Chapter 3: Comprehensive 3–D modeling of mining-induced fault slip: impact of panel length, panel orientation and far-field stress orientation

This chapter addresses the need for a 3-D analysis to better understand how factors such as panel length, panel orientation, and far-field stress orientation affect fault stability. A 3-D finite element model is developed, with a focus on incorporating σ_y to evaluate the full stress tensor effects on fault reactivation. This model allows for the investigation of how mining geometry and the orientation of stress fields influence fault slip.

Chapter 4: 3-D numerical modeling of deep mining-induced fault rupture and seismic wave radiation to the working face of Yuejin coal mine

This chapter provides quantitative simulations of dynamic rupture in deep mining context and addresses the challenge of simulating seismic wave propagation following mining-induced fault rupture. Parameters such as PPV and PPA are calculated to assess the impact of seismic waves on mining infrastructure.

Chapter 5: Discussion

This chapter brings together the findings from Chapters 2 through 4, offering a thorough discussion of the broader implications for mining safety. It highlights the advancements made in modeling fault reactivation and simulating dynamic ruptures, emphasizing how these contributions enhance both the theoretical understanding of fault mechanics and their practical applications in mining operations. Additionally, this chapter addresses the limitations of the current models and explores opportunities for future research, including the integration of real-time monitoring data with numerical simulations to dynamically assess and mitigate seismic risks in mining environments.

Chapter 6: Conclusions

The final chapter provides a summary of the key contributions made by this research, highlighting theoretical advancements in understanding the mechanics of fault–slip rockbursts. It also addresses the practical implications for improving safety in deep mining operations. Future research should focus on combining numerical modeling with physical experiments and real-world monitoring data.

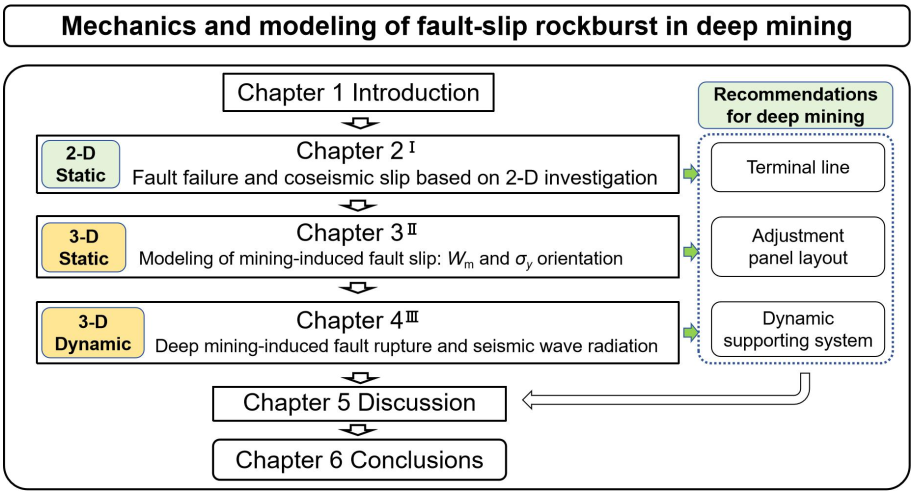

Fig. 1-2 Structure of this thesis. Roman numbers shown in this figure indicate the published papers, and papers under review on these topics mentioned in each chapter (I: Li et al., 2024a; II: Li et al., 2024b submitted; III: Li et al., 2024c submitted).

Chapter 2 Mining-induced fault rupture and coseismic slip based on 2-D numerical investigation

Declaration:

The research presented in this chapter has been published in the following article:

Li Y, Fukuyama E, Yoshimitsu N (2024a) Mining-induced fault failure and coseismic slip based on numerical investigation. Bulletin of Engineering Geology and the Environment 83(10):386. https://doi.org/10.1007/s10064-024-03888-3

The content of this chapter has been appropriately adapted to align with the overall theme of this dissertation.

Assessing the risk of mining-induced earthquakes is crucial for mining safety and disaster mitigation. In this study, I investigated fault failure and coseismic slip as mining activities approach the fault, using a 2-D plane strain model. I focused on the stress ratio of shear stress to normal stress on the fault (k) and coseismic slip on the fault in relation to variables such as the working face location, fault dip angle, fault friction coefficient (μ_s), and depth-dependent background stress field. I examined two models, one with infinite μ_s (i.e. no fault failure) to analyze total stress disturbance on the fault, and another with finite μ_s ranging between 0.5 and 0.8 to estimate coseismic slip. My study yields the following key findings. Fault reactivation induced by mining activities is primarily caused by an increase in k rather than by an increase in shear stress. Hanging wall mining induces instability beneath the mining level, whereas footwall mining provokes instability above it. By utilizing the concept of the fault stress ratio (k), this study elucidates the mechanisms responsible for the pronounced instability induced by footwall mining. Fault stability is highly sensitive to the fault dip angle and mining distance, which are crucial factors in assessing the potential for induced earthquakes. Higher μ_s values lead to small regions of coseismic slip under the same stress environment. Based on these findings, I interpreted a possible cause of the induced earthquake at the Yuejin coal mine on August 11th, 2010, and introduced a quantitative approach for establishing the terminal mining line.

2.1 Introduction

Since the advent of deep mining operations worldwide, mining-induced earthquakes have emerged as a significant concern due to their potential to cause severe damage to mining infrastructure and surrounding areas (Mark 2016; Wei et al. 2018; Kang et al. 2023). Verdon et al. (2018) conducted a comprehensive investigation on an earthquake associated with longwall mining operations at Thoresby Colliery, Nottinghamshire, one of the deep coal mines in the United Kingdom. They presented compelling evidence that the mining operations directly induced seismic events in the region. The reactivation of faults due to mining operations can occasionally lead to catastrophic rock (coal) and gas outbursts (Cao et al. 2001; Karacan et al. 2008; Balsamo et al. 2010). For example, a coal burst accident in the Yima Qianqiu coal mine in China in November 2011 was attributed to fault reactivation (Cai et al. 2021). At the No. 25110 working face of the Yuejin coal mine in China, a total of 20 coal burst accidents were caused by fault reactivation as mining activities gradually approached the F16 fault (Li et al. 2014).

Given the increasing demand for coal resources and the ongoing trend of mining at greater depths, the risk associated with mining-induced earthquakes could potentially escalate in the forthcoming years (Ranjith et al. 2017). Currently, coal mining operations in China extend to increasingly greater depths at 8-25 m annually. By the end of 2022, more than 50 coal mines in China had reached mining depths of over 1000 m, with the deepest mine reaching a depth of 1510 m (Kang et al. 2023). Deep mining operations in proximity to faults can prompt sudden failure of coal and adjacent rocks, culminating in roadway roof collapse due to violent strain energy release (Chen et al. 2018; Wang et al. 2021; Li et al. 2007; Foulger et al. 2018; Zhou et al. 2022).

Theoretically, stress disturbance due to faulting is rigorously expressed by the slip distribution on the fault as representation theorem (e.g., Aki and Richards 2002; Kostrov and Das 1988). To properly incorporate the effect of the stress field on the fault, friction theory (e.g., Jaeger et al. 2007; Scholz 2019) has been employed. Therefore, coseismic fault slip is one of the essential aspects when considering the impact of stress disturbance on fault stability. Given that the faulting caused by deep mining may lead to rock (coal) bursts, considerable research has been conducted to understand the mechanisms underlying mining-induced fault slip (e.g., Wei et al. 2020). Song and Liang (2021) employed numerical simulation methods to investigate the impact of hanging wall mining. They studied the mechanism behind groundwater outbursts resulting from fault activity, with a particular focus on the perspective of induced stress concentration. Wu et al. (2021) analyzed the behavior of a working face as it advanced towards the hanging wall of a normal fault, focusing on investigating the influence of different coal pillar widths from the abutment pressure and found that high dip faults were more likely to induce earthquakes. Shan et al. (2023) investigated the characteristics of excavation-induced pressure unloading and fault slip in the overlying rock mass during mining parallel to the fault using the finite difference method. These studies focused on fault reactivation induced by mining in view of the stress distribution. They carefully considered increased abutment pressure, stress concentration, and pressure unloading, attributing the stress change due to mining as a primary cause of fault instability.

Past studies on fault instability caused by mining activities primarily focused on shear stress concentration and did not discuss the changes in normal stress (Wei et al. 2020; Song and Liang 2021; Shan et al. 2023; Wu et al. 2021; Jiao et al. 2021; Lyu et al. 2021; Zhang et al. 2023; Zhu et al. 2021). In contrast, I introduce an approach based on the Mohr-Coulomb criterion as my rock failure criterion, emphasizing the critical role of normal stress in fault instability. I consider the fault stress ratio, which is defined as the ratio of shear stress to normal stress on the fault. It provides a more accurate measure of fault stability. This stress ratio is crucial, as mining activities induce perturbations both in shear and normal stress on the fault. Therefore, it is essential to take into account both shear and normal stress in assessing mining-induced earthquakes. In my research, I systematically investigated mining-induced fault instability by employing the fault stress ratio.

In my approach, I consider two aspects of fault reactivation: fault failure and coseismic slip. The magnitude of induced earthquake events is primarily influenced by the extent of coseismic slip rather than just stress, highlighting the necessity of in-depth investigations into both fault failure and coseismic slip processes. To achieve this, I utilize two models. The first model investigates mining-induced stress disturbances and the fault stress ratio using a model with infinite fault frictional strength. The second model introduces a friction coefficient on the fault, allowing me to quantitatively study coseismic slip distribution concerning various factors such as mining distance and background stress ratio. These two models provide a better understanding of the mechanisms behind mining-induced fault instability.

Moreover, my study addresses a gap in existing research by questioning the applicability of traditional terminal mining line designs in deep mining operations under high tectonic stress environments near faults. By investigating the mining-induced fault stress ratio and coseismic slip along the fault, my analysis offers insights into the underlying mechanisms of mining-induced fault instability. In this study, I constructed a fault reactivation model tailored to the conditions at the Yuejin coal mine in China, specifically investigating the impacts of fault failure and coseismic slip as the mining face approaches the fault.

2.2 Numerical modeling procedures

2.2.1 Model overview and input parameters

I utilized a 2-D plane-strain model employing a thin rectangular volume, as depicted in Fig. 2-1. The computational volume measured 2400 m in length along the mining direction (x-direction), 1200 m in the vertical direction (z-direction) and had a width of 10 m (y-direction). Since the origin was situated at the left bottom corner of the modeling region and the positive direction was defined as upward. The depth, denoted as h, was expressed as h = 1600 - z. In this model, the depth ranged from 400 m to 1600 m.

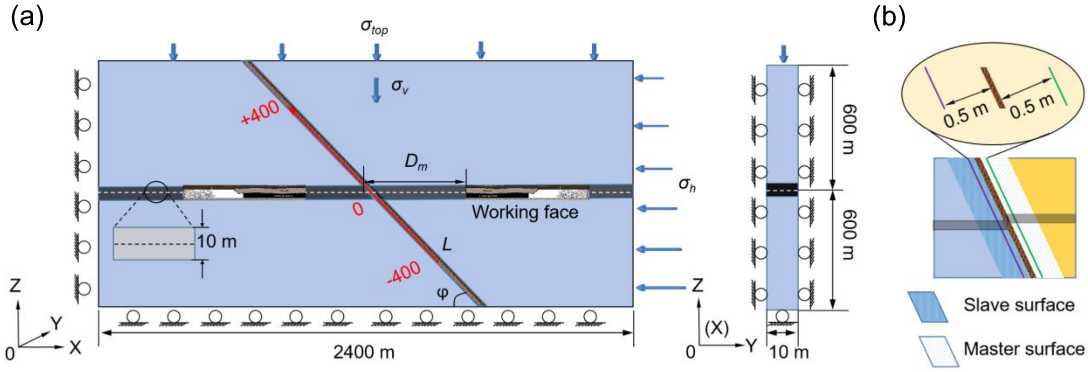

Fig. 2-1 A schematic illustration of the 2-D plane strain model, including the coal mining working face and the fault ahead of the working face. (a) The *xyz*-coordinate system is set as shown in the bottom left of the figure. The origin is located at the bottom left corner of the modeling region. σ_{top} is the σ_{zz} stress at the top of the model that simulates overburden weight. σ_v is vertical principal stress. σ_h is horizontal principal stress in the x-direction. On the left and bottom sides of the model, the displacement boundary condition is applied as described in the text. φ stands for fault dip angle. The local coordinate (red line) L is set along the fault, being the origin is at the center of the coal seam, and the positive direction of L is taken upward. D_{m} is the mining distance measured from the origin of the local coordinate L to the working face, taken positive at the hanging wall side. The thickness of the coal seam is 10 m. (b) Master and slave surfaces are applied to the model. The green line, located 0.5 m from the fault, represents the measurement line, along which τ, σ_n, and coseismic slip are measured on the hanging wall side. Similarly, the purple line, positioned 0.5 m away from the fault, represents the measurement line on the footwall side. (Reproduced from Li et al., 2024a)

The key governing equation used in static equilibrium analysis was written as follows;

$$\nabla \cdot \boldsymbol{\sigma} + \boldsymbol{F} = 0 \tag{2-1}$$

where $\boldsymbol{\sigma}$ is the total stress tensor, and $\boldsymbol{F}$ represents the body forces, including gravity. I introduced the following displacement boundary conditions,

$$u_x = 0 \quad \text{at } x = 0 \text{ m},$$
$$u_y = 0 \quad \text{at } y = 0 \text{ m and } y = 10 \text{ m, and} \tag{2-2}$$
$$u_z = 0 \quad \text{at } h = 1600 \text{ m}$$

where u_i is i-component displacement, and i takes either x, y, or z.

Next, I set the following stress boundary conditions,

$$\sigma_v = \rho g h, \qquad \sigma_h = r_b \sigma_v \tag{2-3}$$

where σ_v and σ_h are vertical and horizontal far field principal stress, ρ is the density, and g is the gravitational acceleration. Compression stress was assigned positive in this study. r_b was the background stress ratio defined as

$$r_b = \frac{\sigma_h}{\sigma_v} \tag{2-4}$$

In this study, k is referred to as the fault stress ratio, consistent with the definition of slip tendency introduced by Morris et al. (1996). The fault stress ratio quantifies the potential for fault reactivation under a specific stress field and is defined as the ratio of shear stress (τ) to normal stress (σ_n) acting on the fault:

$$k = \frac{\tau}{\sigma_n} \tag{2-5}$$

where τ is shear stress, and σ_n is normal stress on the fault. This parameter provides a critical measure for assessing fault stability, with higher values indicating a greater likelihood of fault slip. For further details, refer to Morris et al. (1996).

I used the Mohr-Coulomb criterion to evaluate the fault failure, as shown in Eq. 2-6,

$$\tau_f = C + \mu_s \sigma_n \tag{2-6}$$

where τ_f is the fault frictional strength, σ_n is the normal stress applied on the fault, μ_s is the friction coefficient, and C, the cohesion is assumed to be zero. By comparing k with μ_s (or τ *with* τ_f), I could evaluate the stability of the reverse fault due to mining-induced stress disturbance and coseismic slip.

I investigated the effect of parameters such as r_b, fault dip angle φ, and mining distance D_m on k. It should be noted that D_m represented the distance between the fault and the mining face, and was considered positive when the mining face was located on the hanging wall side. In this study, I considered two background stress ratios, r_b = 2 and 3, six φ at every 10° from 20° to 70°, and D_m ranging between 0 m and 200 m, with a constant panel width of 200 m. I assumed that coal seam and rock layers have the same density and elastic properties in the computation area, as shown in Table 2-1. In order to calculate the distribution of total stress change on the fault under the mining activities, I assumed that the fault frictional strength was infinite (i.e., μ_s is infinite, and no slip is allowed to occur) and measured the stress disturbance on the fault. Subsequently, I computed k by introducing the Mohr-Coulomb criterion with various μ_s.

As shown in Fig. 2-1, I introduced a local coordinate denoted as L along the fault. The origin of L was set at the intersection of the fault and the center of the coal seam layer, taking upward as positive and downward as negative. Using L facilitated the understanding of the spatial relationship between k, D_m, and φ.

Table 2-1 Parameters of the numerical model

Parameters	Values	Parameters	Values
Young's modulus, E (GPa)	15	Cohesion stress, C (MPa)	0
Poisson's ratio, v	0.25	Depth, h (m)	400 – 1600
Shear modulus, G (GPa)	6.5	Mining distance, D_m (m)	-200 – +200
Density, ρ (kg/m^3)	2400	Mining level, (m)	1000
Fault dip angle, φ (°)	20 – 70 (30)*	Panel width, (m)	200
Background stress ratio, r_b	2 or 3 (1.5)*	Mining thickness, (m)	10 (11.5)*
friction coefficient, μ_s	0.5 – 0.8	Dip angle of the coal seam, (°)	0 (12)*

* The parameters in brackets represent the actual parameters of the Yuejin coal mine from Cai et al. (2021). This table refers to Li et al. (2024a).

2.2.2 The characteristic feature of k as a function of r_b and φ

Before conducting the simulation, a theoretical analysis was performed to investigate the characteristic feature of k as a function of r_b and φ within a reverse fault environment by adjusting the background stress to the local coordinate system. These theoretical solutions enabled me to gain basic insights into how much r_b and φ affected k distribution on the fault. In Fig. 2-2a, it was observed that as r_b increases, k also increases. Fig. 2-2b shows the critical angle represented by the marked stars. When r_b was held constant, and φ was smaller than the critical angle, increasing φ led to an increase in k. Conversely, when φ was larger than the critical angle, increasing φ resulted in a decrease in k. Furthermore, the analysis conducted in Fig. 2-2 revealed that under the same background stress, a smaller φ resulted in a larger magnitude of k, potentially increasing the risk of mining-induced earthquakes.

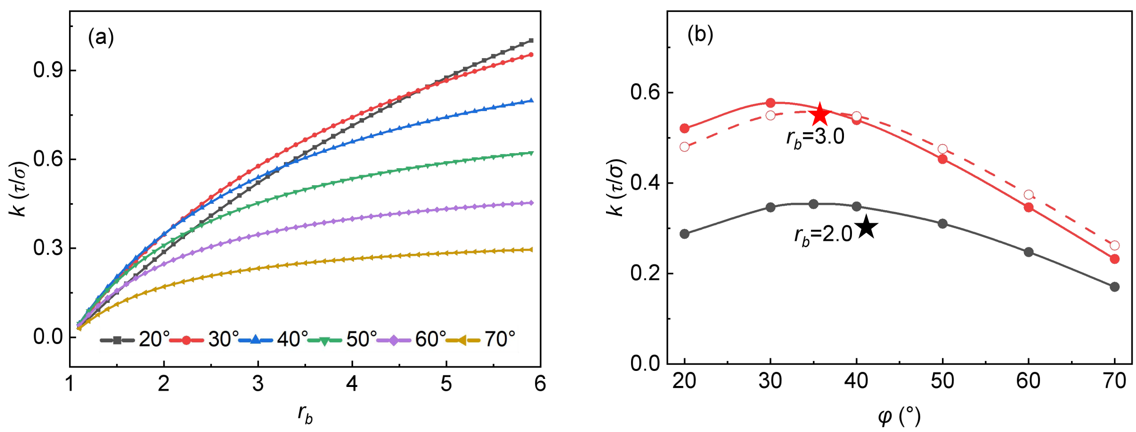

Fig. 2-2 Distribution of k as a function of r_b and φ. (a) Distributions of k, as a function of r_b when φ is 20°, 30°, 40°, 50°, 60°, and 70°. (b) Distributions of k as a function of φ for the cases where r_b = 2 and 3. Red and black stars represent the maximum value of k (k_{max}). The dashed line with open circles represents the distributions of k at L = 200 m (Fig. 2-5a), as a function of φ. (Reproduced from Li et al., 2024a)

2.2.3 Numerical simulation and mesh generation

I used the finite element method software Code_Aster (Ver. 14.6) to simulate the coal mining-induced faulting process (see http://www.code-aster.org for details). The mining-induced stress disturbance and coseismic slip on the fault were calculated using a 2-D plane strain model, as shown in Fig. 2-1. Salome-Meca Ver. 2015.1 was utilized as the pre-and post-processor for Code_Aster, to construct a mesh model consisting of 216,486 tetrahedron elements with nodes set on the vertex. The dimensions of the elements were kept smaller than 10 m. On the contacting interfaces between the upper and the lower fault surfaces, the dimension of the elements was set to less than 1 m using the sub-mesh method, as shown in Fig. 2-1b.

2.3 Analysis of mining-induced fault failure and coseismic slip

2.3.1 Investigation of stress perturbations and k-disturbance along fault

(1) Characterization of mining-induced stress distribution along fault

In my analysis, I measured the stress disturbance resulting from mining activities by assuming that the fault shear strength was infinite. Subsequently, I evaluated the influence of mining-induced stress distribution along the fault as a function of D_m.

Fig. 2-3 illustrates the stress distribution along the fault in the specific case of D_m = 20 m, r_b = 3, and φ = 20º. In Fig. 2-3b, the shear stress τ at point A (L = 80 m, L stands for the coordinate along the fault dip) on the fault was 9.1 MPa. As I moved along point B (L = -18 m), the stress gradually decreased to a minimum value of 1.7 MPa. Then, it increased to the maximum value of 16.2 MPa at point D (L = -168 m). At depths deeper than point D (L = -168 m), τ decreased again and reached a constant value of 8.7 MPa around L = -350 m. The normal stress (σ_n) shown in Fig. 2-3c exhibits an opposite behavior. It began to vary from 25.9 MPa at point A (L = 80 m), increased to its highest value of 36 MPa at point B (L = -18 m), then decreased to 8.3 MPa at point C (L = -118 m), and increased again to L = -220 m achieving the constant value of 26.4 MPa.

Examining the stress ratio k, as shown in Fig. 2-3a, it was found to vary from 0.35 at point A (L = 80 m) to a minimum value of 0.05 at point B (L = -18 m). Subsequently, k increased to a maximum of 1.69 at point C (L = -118 m), then decreased again until reaching a constant value of 0.32 at L = -350 m along the fault. In the area above point A (L = 80 m) on the fault, k was a constant value of 0.35. Since τ and σ_n were constant in this region, the mining effect was considered negligible.

Based on the above results, I could observe that τ and σ_n decreased along the fault above L = -60 m. Since the mining-induced τ decreased faster than σ_n, this resulted in a decrease in k and an increase in fault stability. On the other hand, for the case below L =

-60 m, an increase in k could make the fault unstable and generate a coseismic slip. Therefore, the term fault stress ratio k could be used to quantify fault stability. It is insightful to perform a fault instability analysis prior to the fault with finite strength.

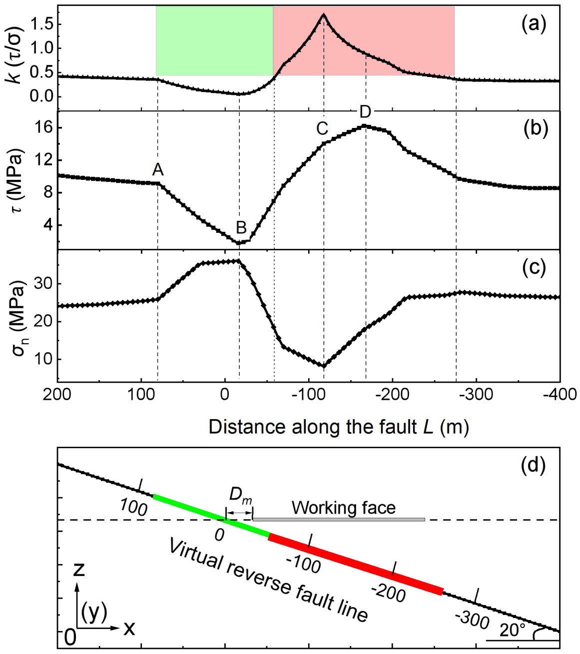

Fig. 2-3 Mining-induced stress distribution along the fault when D_m = 20 m, r_b = 3, and φ = 20°. (a) distribution of k, (b) distribution of τ, and (c) distribution of σ_n along the fault. (d) The geometry between the fault (black, green, and red lines) and the working face (gray solid horizontal line). Green and red areas/lines in (a) and (b) stand for where k decreases and increases due to mining activity, respectively. (Reproduced from Li et al., 2024a)

(2) The relationship between D_m and k

To assess the risk of mining-induced fault reactivation, I analyzed the dependence of k on D_m. Fig. 2-4 depicts the variation of k as the mining activity approached the fault when r_b = 3 and φ = 20°. It could be observed that the maximum value of k (k_{max}) increased when the working face gradually approached the fault. For example, when D_m = 100 m, the maximal value k_{max} became 1.1 at L = -220 m, then gradually increased to 1.7 at L = -100 m when D_m = 0 m. Simultaneously, the minimum value of k (k_{min}) decreased gradually as mining activity approached the fault.

In Fig. 2-4, $k_{\min}$ was proportional to D_m, which indicates that the mining activity contributed to stabilizing the fault. In contrast, the increase in $k_{\max}$ as D_m decreases indicated that mining activity had the potential to make the fault unstable in this specific area. The value of D_m, determined based on the findings of this study, was crucial in evaluating fault instabilities and mitigating the risk of induced earthquakes.

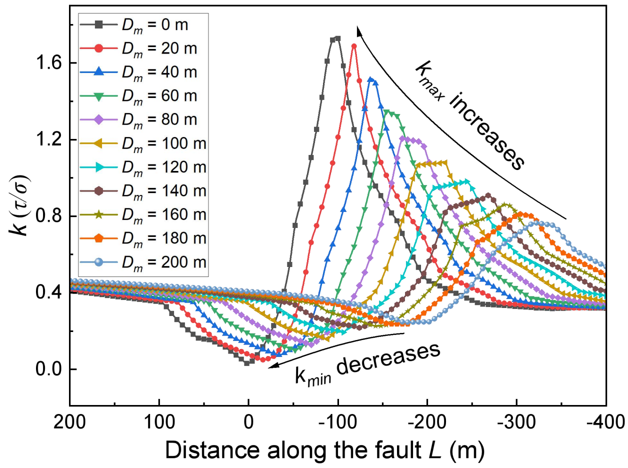

Fig. 2-4 The distribution of k along the fault as a function of distance along the fault. Different color corresponds to different D_m when $r_b = 3$ and $\varphi = 20^{\circ}$. (Reproduced from Li et al., 2024a)

(3) The influence of φ on the distribution of k

I investigated the effect of φ on the distribution of k by altering φ at every 10° interval from 20° to 70° and show the results in Fig. 2-5. The investigation was performed under $r_b = 3$ and $D_m = 0$ m. The results showed that the value of k remains constant from $L = 100$ m to $L = 200$ m along the fault. This implied that the mining activities do not have a significant impact on the value of k. Therefore, I evaluated the k values at $L = 200$ m as the mining-unaffected ones and plotted the result in Fig. 2-2b. Notice that the curve with open circles in Fig. 2-2b indicated the dependence of k as a function of fault dip angle φ. It slightly increased at $20° \leq \varphi \leq 30°$ and decreased at $40° \leq \varphi \leq 70°$. From the plots shown in Fig. 2-2b, it was concluded that the numerical results were validated by the theoretical ones explained in section 2.2.

In Fig. 2-5, I observed that φ significantly affects the distribution of k along the fault. Specifically, from the results shown in Fig. 2-5a, for different values of fault dip angle φ, the corresponding range of k values could be determined. For example, when φ = 70°, k ranged from 0.18 to 0.40; in the case of φ = 40°, k ranged from 0.26 to 1.03; and for φ = 20°, k ranged from 0.03 to 1.73. Thus, I found that a smaller value in φ induces a larger value in k. Fig. 2-5a showed that k along the fault was sensitive to φ. Therefore, the coal mining activities in the vicinity of a fault with a small φ could cause drastic k changes and have a larger potential to induce earthquakes. Fig. 2-5c shows the variation of k_{max} as a function of φ. k decreased gradually from 1.73 to 0.4 as φ increased from 20° to 70°. The above results suggested that φ significantly influenced the range of k and its distribution along the fault.

In Fig. 2-5a, the mining site could be divided into three distinct zones. In Zone 1, the initial area demonstrated stability without significant changes. Zone 2, on the other hand, experienced an increase in fault stability due to mining-induced k decrease. Conversely, mining operations in Zone 3 resulted in a decrease in fault stability.

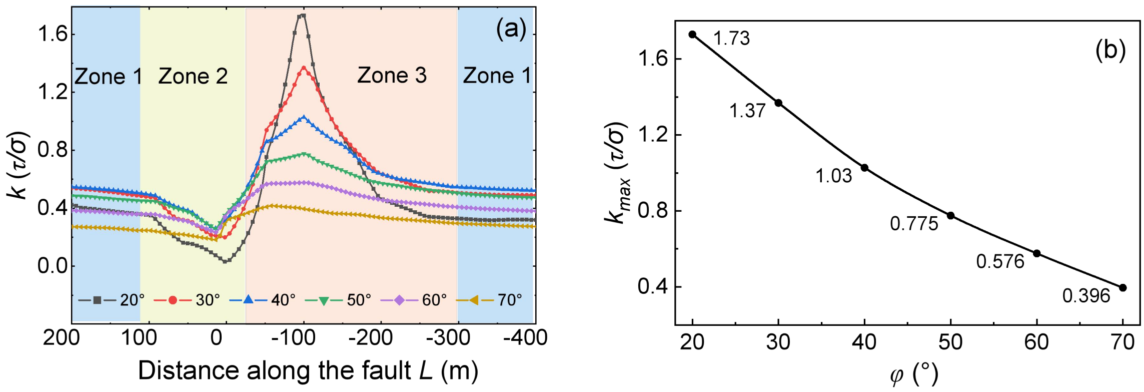

Fig. 2-5 Distribution of k along the fault with different φ when D_m = 0 m and r_b = 3. (a) Distribution of k for φ from 20° to 70° at 10° intervals. Zone 1 represents the initial area where no mining-induced stress disturbances occur. Zone 2 corresponds to an area where mining activities lead to an increase in fault stability. In contrast, Zone 3 denotes an area where mining operations result in a decrease in fault stability; (b) Variation of k_{max} as a function of φ at L = -100 m. (Reproduced from Li et al., 2024a)

2.3.2 Coseismic fault slip under contact friction

(1) σ_n, τ, k, and coseismic slip distribution

After analyzing the stress distribution using the infinite μ_s fault model, further investigation was conducted using the finite μ_s model by introducing contact interfaces on the fault. Specifically, I evaluated the stress drop under the conditions of $r_b = 2$ and φ = 30°. The stress drop was measured as the difference in τ between the hanging wall and the footwall sides. In this study, I introduced a new term called 'k-drop' (Δk), which is defined as the difference between k on the hanging wall side ($k_h = \tau^h / \sigma_n^h$) and that on the footwall side ($k_f = \tau^f / \sigma_n^f$).

$$\Delta k = k_h - k_f \tag{2-7}$$

where τ^h, σ_n^h, τ^f and σ_n^f represent the shear and normal stress on the hanging wall and footwall sides of the fault, respectively. These stresses were evaluated at the locations 0.5 m off the fault, as indicated in Fig. 2-1b, as purple and green thin lines, respectively. In the third panel of Fig. 2-6a, k also generated some difference as the stress drop induced k as observed in Figs. 2-6b and 2-6c. It should be emphasized that this definition for k is only valid for reverse fault environments.

Fig. 2-6 shows the distributions of σ_n, τ, k, and coseismic slip along the fault, assuming that $\mu_s = 0.55$ and D_m = 90 m. In Figs. 2-6b and 2-6c, I could observe that τ decreased and generated a stress drop where k was larger than 0.55 due to mining activity. This indicates that the regions with larger values of k were more prone to experiencing stress drop due to coseismic slip on the fault. In contrast, σ_n remained relatively unchanged above and below the fault. The coseismic slip occurred in the region where k exceeded the threshold condition of $\mu_s = 0.55$. The slip zone was confined to the region below the mining level, specifically, ranging from L = -110 m to -340 m along the fault. The largest slip (0.14 m) was observed at L = -200 m on the fault. Note that the slip was asymmetric concerning L = -200 m along the fault. Therefore, an asymmetrical slip could be attributed to the asymmetric distribution for L = -200 m of the Δk along the fault. The asymmetric slip distribution disappeared if φ was close to 90°. Figs. 2-6b and 2-6c reveal that Δk and stress drop exhibit different shapes, attributed to the influence of σ_n (as shown in the top panel of Fig. 2-6a) with varying values across different positions within the slip zone.

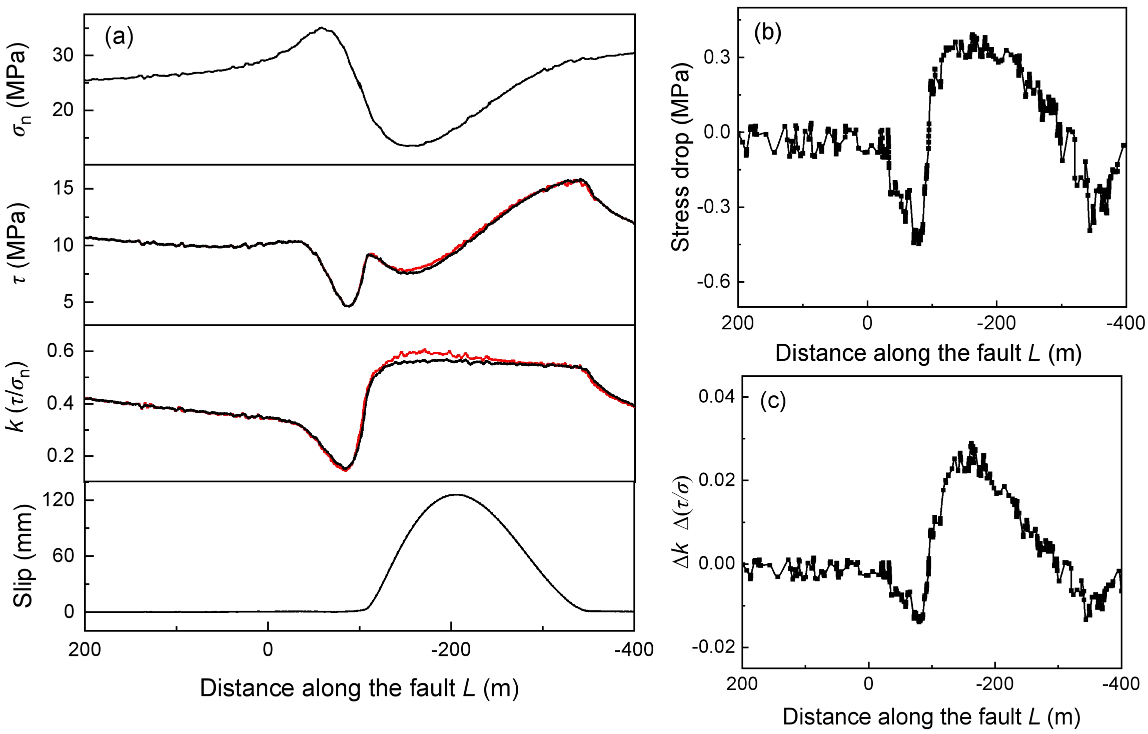

Fig. 2-6 Distributions of σ_n, τ, k, and coseismic slip along the fault under the condition of D_m = 90 m, μ_s = 0.55, and φ = 30°. (a) Distributions of σ_n, τ, and k on the hanging wall and footwall, respectively. The red curves represent τ and k at the hanging wall side, and the black curves represent τ and k at the footwall side. The bottom trace is the distribution of coseismic slip on the fault. (b) Stress drop distribution in τ of Fig. 2-6a. **c** Δk distribution in k of Fig. 2-6a. (Reproduced from Li et al., 2024a)

(2) k distribution for various μ_s

To investigate the influence of μ_s on the distribution of Δk along the fault, I varied the value of μ_s from 0.5 to 0.8. As shown in Fig. 2-7, the length of Δk region decreased from 296 m (from L = -89 m to L = -385 m) for μ_s = 0.5 to 98 m (from L = -152 m to L = -250 m) for μ_s = 0.8. In contrast, as μ_s decreased from 0.8 to 0.5, it was observed that the coseismic slip zone increased from 90 m to 280 m, respectively. My analysis revealed that higher values of fault frictional strength (μ_s) result in larger Δk occurrences due to nearby mining activities. In contrast, lower values of μ_s were associated with expanded coseismic slip zones. The data presented in Table 2-2 provided a summary of coseismic slip instances characterized by distinct μ_s.

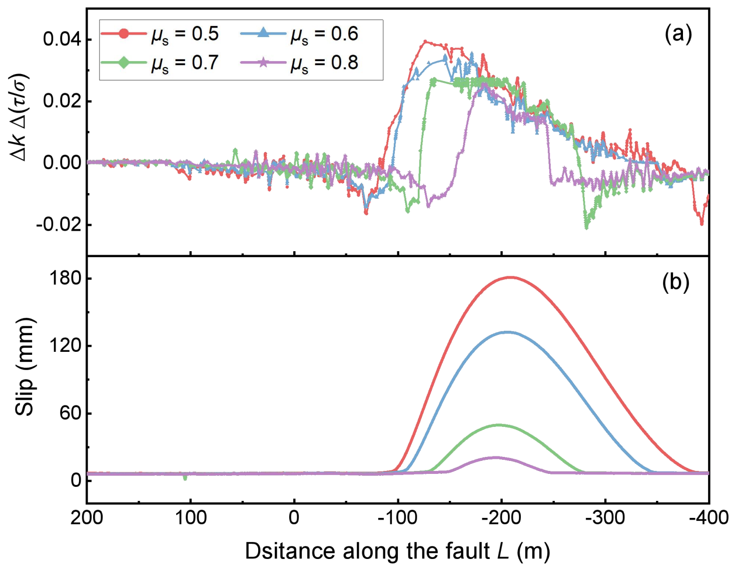

Fig. 2-7 Distribution of (a) Δk and (b) coseismic slip along the fault for different μ_s from 0.5 to 0.8 under the condition of $r_b = 2$, $D_m = 90$ m, and $\varphi = 30^{\circ}$. (Reproduced from Li et al., 2024a)

Table 2-2 Fault coseismic slip for different μ_s

μ_s ($D_m = 90$ m)	Maximum slip (mm)	Slip zone length (m)
0.5	180	280
0.6	130	230
0.7	50	148
0.8	20	90

Note：This table refers to Li et al. (2024a).

(3) Influence of D_m on coseismic slip in hanging wall and footwall mining

Fig. 2-8a illustrates the coseismic slip distribution above the mining level on the fault, considering the variation of D_m from -10 m to -170 m at 40 m intervals with $r_b = 2$ and $\mu_s = 0.7$. The fault began to slip at slightly larger than D_m = -200 m. With the working face approaching the fault from D_m = -170 m to D_m = -10 m, the length of the coseismic slip zone and the maximum slip increased (Table 2-3).

Fig. 2-8b illustrates the coseismic slip distribution that appeared beneath the mining level on the fault, considering the variation of D_m from 10 m to 170 m at 40 m intervals with $r_\mathrm{b} = 2$ and $\mu_\mathrm{s} = 0.7$. The fault began to slip at slightly larger than D_m = 170 m, and with the working face approaching the fault from D_m = -170 m to D_m = -10 m, the length of the coseismic slip zone and the maximum slip increased (Table 2-3).

Table 2-3 Fault coseismic slip for different D_m ($\mu_s = 0.7$)

D_m		Maximum slip (mm)	Slip zone length (m)
Hanging wall mining	10	265	232
	50	123	191
	90	50	138
	130	12	37
	170	7	3
Footwall mining	-10	447	273
	-50	215	240
	-90	130	215
	-130	80	190
	-170	44	159
	-200	14	58
Yuejin coal mine	-10	275	213
	-50	108	178
	-90	46	130
	-130	15	63
	-170	6	3

Note：This table refers to Li et al. (2024a).

Fig. 2-8d presents simulation results based on the actual conditions at the Yuejin coal mine (as depicted in Fig. 2-8c). These results indicate that the location of the coseismic slip was situated below the mining level, and the magnitude of this slip, prompted by mining activities, closely parallels the fault slip observed during hanging wall mining (see Fig. 2-8b and Table 2-3).

I found that under the same $|D_m|$ conditions, footwall mining resulted in a larger coseismic slip size and dislocation length compared to hanging wall mining, although their relative shape of slip distribution was similar. In other words, footwall mining induced more significant fault instability than hanging wall mining.

Since I assumed depth-dependent background stress, the stress drop differed between the slip zones caused by footwall mining and those caused by hanging wall mining. In contrast, the stress change resulting from mining-induced stress was consistent. Consequently, footwall mining would cause a larger fault slip than hanging wall mining.

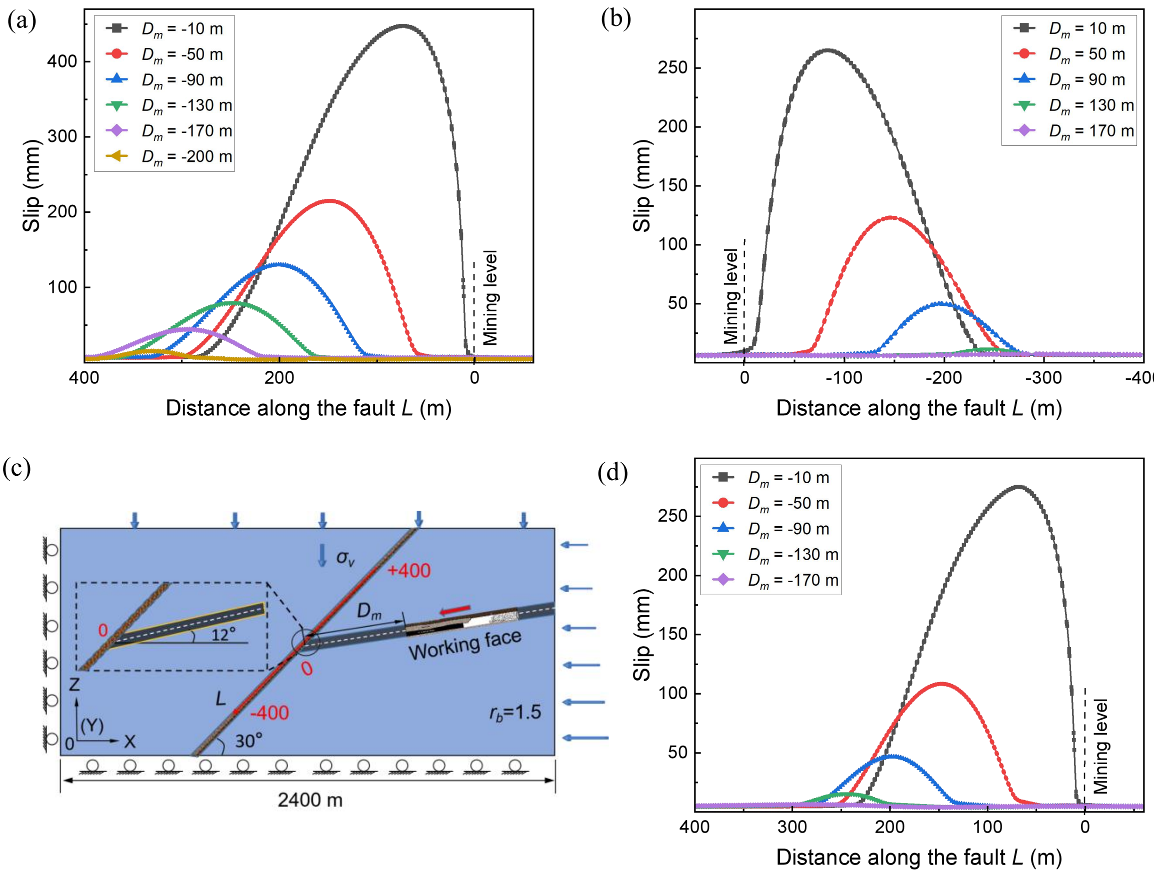

Fig. 2-8 Slip distributions for different D_m ranging from 10 m to 170 m at 40 m intervals under footwall and hanging wall mining conditions, (a) for footwall mining with r_b = 2, μ_s = 0.7, and φ = 30°, and (b) for hanging wall mining with r_b = 2, μ_s = 0.7, and φ = 30°. (c) A schematic illustration of the 2-D plane strain model based on the

conditions at Yuejin coal mine. The scale and coordinate system of the model, including both global and local systems, align with those presented in Fig. 2-1a. The background stress ratio (r_b) is 1.5. The coal seam, intersected by the fault, lies 1000 m deep, dips at an angle of 12°, and has an average thickness of 11.5 m. (d) Slip distributions with footwall mining at Yuejin coal mine with the conditions r_b = 1.5, μ_s = 0.7, φ = 30°, and a coal seam dip angle of 12° based on the model shown in (c) . (Reproduced from Li et al., 2024a)

(4) Estimation of seismic magnitudes and nucleation size

I estimated the seismic moment, M_0, of the mining-induced earthquake in the case of D_m = 90 m, 50 m, and 10 m. M_0 was defined as follows (Aki 1967; Kanamori and Anderson 1975; Aki and Richards, 2009),

$$M_0 = GL_sL_wD \tag{2-8}$$

where G is the shear modulus of the rocks on the fault, which is 6.5 GPa in this study (Table 2-1), L_s and L_w are the coseismic slip length and the width along the fault, respectively. D is the average coseismic slip on the fault. Here, I assumed that L_s and L_w followed the empirical relation of $L_s = 2L_w$ for moderate-sized earthquakes (Geller 1976). Therefore, given the conditions that D_m = 90 m, 50 m, and 10 m, L_w was calculated to be 74 m, 87 m, and 115 m, respectively. These calculations also applied to the footwall mining and Yuejin mining conditions, as shown in Table 2-4. They were consistent with the empirical relationship among M_w, L_s, L_w, and D (Wells and Coppersmith 1994; Wells 2013).

Using M_0 in the unit of Nm, I calculated the moment magnitude M_w from the following equation (Hanks and Kanamori 1979);

$$M_w = \frac{\log M_0 - 9.1}{1.5} \tag{2-9}$$

The reason why I used moment magnitude (M_w) is that it is based on the physical values. Thus, it is easy and suitable to apply to the present numerical simulation results. When comparing the magnitudes predicted by numerical simulations with those observed in the field, I need to pay attention to the magnitude scale.

The values for M_w were compiled and presented in Table 2-4. It was crucial to carefully consider the terminal mining lines for deep mining nearby faults, particularly in high tectonic stress environments, to mitigate disastrous fault ruptures. My simulation results indicated that hanging wall mining generates fault coseismic slip below the mining level when D_m was less than 170 m. As shown in Fig. 2-9, the length of the coseismic slip zone increased as D_m decreased.

Table 2-4 Fault parameters and moment magnitudes for the cases computed

D_m (m)		D (mm)	Average L_s (m)	L_w (m)	M_w
Hanging wall mining	10	125	232	116	2.8
	50	55	191	95.5	2.5
	90	24	138	69	2.0
Footwall mining	-10	200	273	136.5	3.1
	-50	102	240	120	2.8
	-90	60	215	107.5	2.6
Yuejin coal mine	-10	130	213	106.5	2.8
	-50	50	178	89	2.4
	-90	20	130	65	2.0

Note：This table refers to Li et al. (2024a).

The nucleation length is the critical length of the initial crack where the unstable rupture starts to propagate outward if the initial crack size exceeds the critical size (Uenishi and Rice 2003). The coseismic slip length can be compared with the nucleation length. It is important to highlight that when the slip zone size caused by mining activity exceeds the nucleation zone size, there is a potential to generate a large earthquake by expanding the rupture outside the slip zone. According to Uenishi and Rice (2003), the nucleation length L_n could be expressed under the linear slip weakening law (Andrews, 1976) as follows:

$$L_n = 1.158\frac{ED_c}{2(1-\nu^2)(\tau_f-\tau_d)} \tag{2-10}$$

where D_c is the slip-weakening distance, E is Young's modulus, ν is Poisson's ratio. $\tau_f - \tau_d$ is the breakdown strength drop. τ_f is the fault shear strength, τ_d is the dynamic shear strength.

If D_c was small and/or the strength dropped, i.e., τ_f -τ_d was large, L_n became short. In the present study, D_c was assumed to be 0.03 m, based on typical seismic observations (Abercrombie and Rice 2005), τ_f -τ_d was taken as $0.1\sigma_n$, so the shear stress drop was 2.0 MPa (with an average σ_n of 20 MPa, ranging from 14 MPa to 34 MPa as shown in Fig. 2-6a). These assumptions resulted in L_n being 138 m. Based on the slip data in Table 2-4, I could consider the limitation of D_m as 90 m (Fig. 2-9).

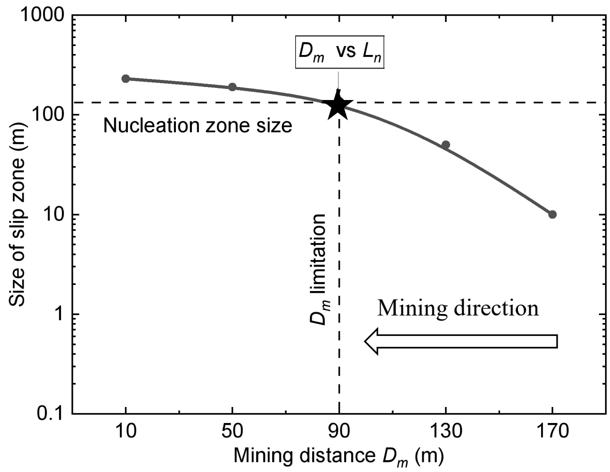

Fig. 2-9 The relation between the coseismic slip zone size and D_m (see Table 2-3). The nucleation zone size of 138 m (broken horizontal line) is assumed under the condition that μ_s - μ_d = 0.1, D_c = 0.03 m, and the average normal stress is 20 MPa. The solid star indicates the location of the limit line of D_m. (Reproduced from Li et al., 2024a)

My simulation results enable the accurate prediction of coseismic slip distribution, which is crucial for identifying the area most susceptible to seismic events. By pinpointing these high-risk zones, mining operations can be planned to avoid or reinforce these areas, thereby minimizing the potential for significant seismic disturbances. Additionally, my method facilitates the redefinition of safe mining stop lines, particularly in deep mining operations where traditional guidelines may be inadequate (National Coal Mine Safety Administration 2000). By considering both shear and normal stress changes that cause fault slip to meet the nucleation length (L_n), which may further induce earthquakes, I estimate seismic magnitudes and nucleation sizes. This approach allows me to establish new stop lines that mitigate the risk of fault reactivation and coseismic slip.

2.4 Discussions

2.4.1 Stress drop

Stress drop, which is the difference in shear stress across a fault before and after an earthquake rupture, is directly associated with the elastic energy released as a consequence of an earthquake rupture (Sato 1972; Kanamori and Anderson 1975; Mayeda and Walter 1996). Fukuyama and Madariaga (1995) derived a relationship between slip and stress drop, which is consistent with the previous works, as a new boundary integral equation of dynamic tensile and shear cracks. They explicitly demonstrated that the final stress drop on the fault was equivalent for both static and dynamic problems.

As shown in Fig. 2-10a, under the condition of r_b = 2 and μ_s = 0.7, the mining-induced stress drop ranged from -6.1 MPa to 6.7 MPa in the case of D_m = 10 m, -1.0 MPa to 1.7 MPa in the case of D_m = 40 m, and -0.4 MPa to 0.8 MPa in the case of D_m = 90 m. The large slip zone caused a larger stress drop zone, and the large slip magnitude generated large values of the stress drop.

To validate the stress drop distribution calculated through Code_Aster, I compared it with that of DC3D (Okada 1992). DC3D provided me with a theoretical representation of fault slip and strain distribution around the fault formulated by Okada (1985) and Okada (1992). I used a subroutine package for DC3D (https://www.bosai.go.jp/e/dc3d.html) to calculate displacement and its space derivatives at any arbitrary point on the inside or surface of the elastic half-space medium due to a uniform slip on a finite rectangular fault.

Since the mining-induced fault slip was not uniform, I assumed a piecewise constant slip distribution divided at an interval of 10 m and computed the stress drop distribution by summing the stress change from these fault elements. In Fig. 2-10b, 2-10c, and 2-10d, the bars shown at the bottom indicated the approximated slip distribution and were used as input to DC3D. The stress drop distribution calculated by DC3D was shown as solid lines with open circles for three cases (D_m = 10 m, 50 m, and 90 m) under the condition of r_b = 2 and μ_s = 0.7. The mining-induced stress drop calculated by DC3D ranged from -7 MPa to 4.6 MPa for D_m = 10 m, -2.1 MPa to 2.1 MPa for D_m = 50 m, and -0.7 MPa to 1.0 MPa for D_m = 90 m. These results were consistent with the results by Code_Aster, shown as solid lines in Fig. 2-10b, 2-10c, and 2-10d.

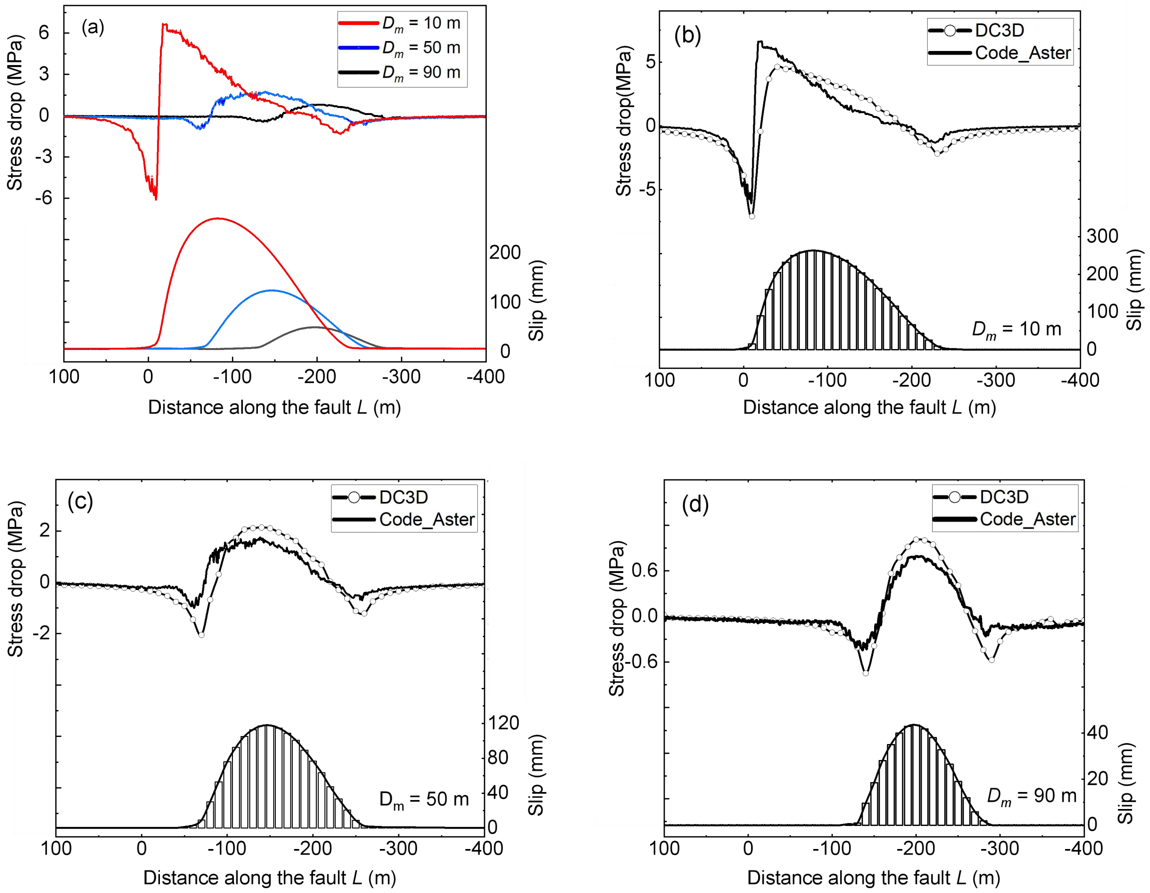

Fig. 2-10 Distribution of stress drop (top) and coseismic slip displacement (bottom) for different D_m under r_b = 2, μ_s = 0.7, and φ = 30°. (a) Stress drops and slip distributions for different D_m obtained from Code_Aster. Comparison of stress drop slip distributions between Code_Aster and DC3D for the case of (b) D_m = 10 m, (c) D_m = 50 m, and (d) D_m = 90 m. The bar graph at the bottom of the figure indicates the piecewise constant slip distribution used in DC3D, and the black curve is the coseismic slip obtained by the Code_Aster. (Reproduced from Li et al., 2024a)

In Fig. 2-10a, I noticed a slight difference in stress distributions between Code_Aster and DC3D. A possible reason for this difference may come from the effect of mesh size in the model used in Code_Aster, especially from the contact interface mesh size on the fault. This was because when I used a coarse mesh model, the discrepancy in stress distribution increased. Actually, I constructed the mesh model that consists of 216,486 tetrahedron elements whose element size at the contact interface was about 0.5 m. This model was close to the limitation in Salome-Meca Ver. 2015.1 with the computer available at this moment. While I could not assert the perfect validity of the present Code_Aster computation, I believed that both results would converge if I decreased the element size of Code_Aster to infinitesimally small.

2.4.2 Application to the mining-induced earthquake in Yuejin coal mine

On August 11th, 2010, an earthquake with a M_L of 2.7 occurred at the No. 25110 working face in the Yuejin coal mine, which was the reactivation of the reverse fault named F16 (Cai et al. 2015, 2021). This event was considered a mining-induced earthquake in my model, occurring at D_{m} equal to -80 m (Li et al. 2018). Considering actual conditions such as coal seam thickness, mining depth, fault dip angle, working face locations, background stress, and fault friction parameters (Table 2-1), I constructed a similar model as that of the Yuejin coal mine (Fig. 2-8c).

My numerical simulation results predicted an earthquake magnitude range of $2.0 \leq M_w \leq 2.8$. This is not surprising, as the mining dimension is roughly equivalent to that of magnitude 2 earthquakes. In my simulation, an earthquake was induced when D_{m} reached 90 m, a value akin to D_{m} from the actual event. However, it should be reminded that my estimate includes a significant amount of uncertainty, especially in fault friction. Despite these uncertainties, my proposed procedure and simulation results can help estimate the coseismic slip distribution due to mining activities and provide crucial information for optimizing mining design and enhancing the safety of mining operations.

In contrast, local magnitude (M_{L}) is primarily used for field observations of small earthquakes. M_{L} is an empirical scale based on the observed maximum amplitudes of recorded seismographs. For small earthquakes (M~3), M_{L} and moment magnitude (M_{w})

are generally consistent. Actually, several empirical relations are proposed. For example, $M_w = 0.81\ M_L + 0.61$ for California (Bakun and Lindh 1977) and $M_w = 0.64\ M_L + 0.84$ for Italy (Bindi et al. 2005). For more details, please refer to Table 6.11 in Havskov and Ottemoller (2010). The magnitude of the Yuejin coal mine event was M_L 2.7. Following the above conversion relations, M_L 2.7 corresponds to M_w 2.8 for California (Bakun and Lindh 1977) or M_w 2.6 for Italy (Bindi et al. 2005).

2.4.3 Fault reactivation: fault failure and coseismic slip

I considered fault reactivation in two aspects: fault failure and coseismic slip. By analyzing the fault stress ratio (k) in a reverse fault environment, I evaluated the sensitivity of various parameters to mining-induced fault instability. A mining-induced earthquake occurred on November 3, 2011, when mining reached near the F16 fault (Cai et al. 2015, 2021). Jiao et al. (2021) developed a refined 3-D numerical model to analyze stress evolution in the surrounding rock near the F16 fault during mining. They used in-situ stress data and geological information around the F16 fault. They observed a decrease in normal stress and an increase in shear stress on the upper fault plane when mining approaches the fault.

In this study, I further estimated the coseismic slip distribution resulting from mining, taking into account the fault friction properties as well as the stress field applied as the working face approached. I observed a significant sensitivity of k along the fault to the dip angle φ, particularly for small φ values, which was also illustrated in Jiao et al. (2021). Coal mining, in such cases, leads to a notable increase in k; thus, it increases the potential for induced earthquakes. By analyzing the fault stress ratio (k) with friction parameters in a reverse fault environment, I assessed the sensitivity of various parameters to mining-induced fault instability. Cai et al. (2021) developed a 3-D numerical model to analyze stress evolution in the surrounding rock near the F16 fault during mining, using in-situ stress data and geological information. They observed a high stress concentration around the coal pillar as mining approached the fault, which is also measured in the current study. However, a simple analysis of the stress state that did not account for the stress ratio and subsequent coseismic slip is not sufficient to capture the fault-induced coal bursts. In this study, I estimated the coseismic slip distribution resulting from mining by considering the fault friction properties and the stress field as the working face approached. Ultimately, earthquakes may be induced when the coseismic slip zone exceeds L_n (Uenishi and Rice 2003).

Zhang et al. (2022) reported the implementation of a pre-mining grouting technique as an idea to enhance the strength of the fault plane, ensuring safety during mining operations in the Yangcun coal mine. As shown in Figs. 2-9 and 2-11 of Zhang et al. (2022), on-site grouting significantly reduced fault slip displacement and ensured safe mining operations across the fault and, suppressed inducing earthquakes. My computation results support their results and observations that the fault coseismic slip was reduced by increasing the fault frictional strength by grouting. In my computation, increasing the friction coefficient from 0.5 to 0.8 results in a substantial reduction in coseismic slip from 280 m to 90 m (Fig. 2-7).

2.4.4 Limitations

The main assumptions of this study were the background stress and friction properties of the fault. Regarding the background stress field, I do not include the heterogeneity of the material, which might alter the stress field. In the practical application of this approach, the material structure should be properly included in the model, which could be feasible in most cases. The background stress ratio r_b also affects the predicted slip distribution on the fault. The parameter r_b does not need to remain constant along the depth; it may vary. My methodology is capable of accommodating this heterogeneity, ensuring accurate modeling and analysis.

Regarding the friction property on the fault, I assumed zero cohesion on the fault. This assumption was sometimes applied to ore mines and gas mines, where the mining-induced fault reactivation process was considered (e.g., Sainoki and Mitri, 2014, 2015; Buijze et al. 2019). Some studies pointed out that cohesion also affects the mining-induced fault stress ratio and coseismic slip (Bizzarri 2010); I should carefully input the cohesion into the simulation. The friction coefficient used in my simulations was based on Byerlee's law (Byerlee 1978) and data from studies on induced earthquakes (Cai et al. 2021). Materials with plate-like structures, such as graphite and talc, exhibited lower friction compared to rocks and minerals with bulk structures. These minerals, often products of hydrothermal alteration, were commonly found in fault gouges and could significantly influence fault strength (Nguyen, 2016; Garofalo, 2023). Therefore, investigation of the friction properties of these minerals was deemed a valuable area for future research. In addition, fault geometry is crucial because this affects the global friction property as well as the stress ratio on the fault (Hok et al. 2011).

The estimation of the nucleation size (L_n) was based on the assumed breakdown shear strength drop ($\tau_f - \tau_d$) and critical slip distance (D_c). L_n was estimated by friction parameters but these parameters are quite difficult to measure in the field but can be obtained by laboratory experiments. I now examine the uncertainty in the friction parameters on L_n. If D_c is increased by 20% from my assumed value, while other conditions remain the same, L_n will increase to 178 m, requiring the terminal mining line to be at least 50 m away from the fault. Similarly, based on Eq. 2-10, I can evaluate the uncertainty in $\tau_f - \tau_d$ on the nucleation length. Hence, it should be emphasized that the parameters, D_c and μ_d need to be carefully estimated for practical applications. Once I obtain these values reliably, I can evaluate the nucleation length following Uenishi and Rice (2003).

2.5 Summary

I conducted a numerical investigation to explore fault failure and coseismic slip phenomena under the conditions of deep coal mining, considering multiple variables including φ (fault dip angle), r_{b} (background stress ratio), D_{m} (mining distance), and μ_{s} (fault frictional strength). My numerical modeling demonstrated that fault reactivations occur not only due to shear stress concentration but also as a result of a decrease in normal stress. Therefore, I proposed that monitoring the k value will serve as the indication for mining-induced fault reactivation. Moreover, the value of k along the fault is found to be highly sensitive to the φ parameter. When φ is small, coal mining will substantially increase the k value on the fault, elevating the potential for induced earthquakes.

Hanging wall mining induces fault instability beneath the mining level, whereas footwall mining generates slip above the mining level. And footwall mining yields greater instability under similar conditions. Both μ_s and D_m are critical in determining coseismic slip and k. To accurately assess the terminal mining line without inducing earthquakes, I conducted quantitative evaluations of in-situ monitoring values for parameters such as stress field, fault geometry, and fault friction. Nevertheless, further investigations are needed to assess the size of the nucleation zone in order to precisely quantify the terminal mining line.

Chapter 3 Comprehensive 3–D modeling of mining-induced fault slip: impact of panel length, panel orientation and far-field stress orientation

I investigated the mining-induced faulting process through 3-D finite element analysis. I examined reverse fault reactivation triggered by mining operations, specifically examining the impacts of panel length (W_m) and intermediate far-field stress (σ_y). I observed that σ_y contributes to fault coseismic slip, with a positive correlation between σ_y magnitude and the fault slip extent. Additionally, a linear increase in the width of the mining-induced coseismic slip zone was observed with an increase in W_m. The maximum slip approached a limit predicted by 2-D plane strain calculations. I further investigated the impact of far-field stress and panel orientation on fault slip, referring to realistic mining conditions. It was observed that intermediate principal stress significantly promotes the slip when the maximum principal stress deviated to the fault normal direction. The average slip and slip area becomes the smallest when the panel was perpendicular to the fault strike. I confirmed that the observation at the F16 fault zone in the Yuejin mine was consistent with my results, highlighting the physical mechanism of mining-induced rock-bursts on preexisting fault. Given the observed slip distribution and the assumed nucleation length, I proposed a modification of the panel layout strategy, in particular, a change in panel layout from nearly parallel to perpendicular to the fault strike. This adjustment reduces the potential for faulting and subsequent induced earthquakes. This modification will contribute to the overall mitigation of seismic hazards associated with mining-induced fault reactivation.

3.1 Introduction

Underground coal mining continues to develop in response to the overwhelming demand in the 21st century (Ranjith et al. 2017). Coal mining depth in China has recently been increased at a rate of 10–25 m/year, with a maximum depth exceeding 1500 m (Kang et al. 2023). By 2023, over 50 coal mines in China will extend below 1000 m. Deep mining faces many risks owing to the in situ stress generated by the overburden pressure and tectonic movements. Coal mining at such great depths can induce substantial stress perturbations and rotations in the surrounding areas, particularly when mining near faults. Recent studies have found that earthquakes triggered by mining activities usually have smaller magnitudes than natural earthquakes (Buijze et al. 2019). Yet, the frequent occurrence of these earthquakes and their strong association with engineering activities should not be overlooked. Faults near deep mining operations may trigger a violent release of elastic strain energy through fault rupturing. This can result in roadway roof collapse, sudden failure around the working face, and ultimately, endangers the lives of miners (Li et al. 2007; Vardar et al. 2022; Wang et al. 2021; Zhang et al. 2022). For instance, the Yima Qianqiu coal mine in China experienced a coal burst caused by fault reactivation in November 2011, resulting in ten fatalities and the trapping of 75 miners (Cai et al. 2021). Consequently, searching for an accurate assessment of safety risks in deep coal mining is an urgent issue to prevent and mitigate disasters.

Cai et al. (2015) and Jiao et al. (2021b) conducted research focusing on the stress field. They investigated the behavior of faults under compressive shear stress and linked their analysis to the field observations. They highlighted the ease of triggering rock bursts during deep mining near faults through a stability analysis of the F16 fault, focusing on the stress distribution in surrounding rocks and the stress field around the thrust faults (Cai et al. 2015; Jiao et al. 2021b). Kang et al. (2023) addressed complex factors impacting mine integrity, such as high tectonic stress and temperature by proposing innovative solutions aimed at overcoming mining challenges and fulfilling global energy needs. Li et al. (2022, 2023) delved into this work into mining-induced fault failure and coseismic slip, employing a 2-D plane strain model in their numerical investigations. They found fault stability was highly sensitive to fault dip angle and mining distance. To reduce the occurrence of induced earthquakes, they developed a method for determining a terminal mining line, which relied on quantitative analysis of slip-weakening behavior of fault referring to in-situ stress and fault friction coefficient (Uenish and Rice, 2003). Islam and Shinjo (2009) used the boundary element method to investigate mining-induced faulting in the Barapukuria Coal Mine, Bangladesh. Their research highlighted the stress intensity near fault tips and significant deformation along faults caused by mining-induced stress disturbances.

It was widely recognized that intermediate stress exerted a significant influence on rock behavior through true triaxial experiments (Hu et al. 2022, Haimson and Chang 2000, 2002; Chang and Haimson 2012). As true triaxial detection equipment had advanced, numerous experimental laboratory studies explored the behavior of different rock types (Mogi 1971; Haimson et al. 2010; Feng et al. 2020; Ødegaard and Nilsen 2021). Deep mining near faults is impacted by specific triaxial tectonic stress (Diederichs 2003; Gao et al. 2018, 2020), thus further investigation of the relationship between intermediate far-field stress and fault slip is important.

The 2-D quasi-static numerical investigation conducted by Li et al. (2024a) demonstrated the characteristics of coseismic slip along the fault dip direction. Furthermore, Li et al. (2024a) extended this discussion to the fault stability conditions by providing a methodology for a quantitative evaluation of fault instability. Their finding was in concordance with the anticipated outcomes based on the theoretical framework of the 2-D plane strain model (Cervera et al. 2017). During mining-induced fault reactivation, such coseismic slip might occur along the strike direction. When the panel is located near a fault, localized stress disturbances may increase the risk of mining-induced earthquakes. The 2-D Mohr-Coulomb fracture criterion assumes that failure in rocks is governed by the minimum and maximum principal stresses. However, it remains uncertain whether intermediate principal stress affects fault failure, especially when mining-induced stress disturbances appear on the fault surfaces. Furthermore, the influence of intermediate principal stress on the coseismic slip is also unclear when the mining face is located close to the fault. It should be noted that compression stress is taken positively in this study.

To assess the influence of these factors, I conducted a comprehensive three-dimensional (3-D) investigation to further elucidate the impacts of intermediate principal stress (σ_{y}) and panel length (W_{m}, see Fig. 3-1a) on coseismic slip distribution on the fault during the mining activities. I thoroughly examine the impact of W_{m} and σ_{y} on faulting within a mining context, considering panel layout and an interface friction model. In this study, I expand the 2-D model proposed by Li et al. (2024a) to investigate the 3-D effects mentioned above.

The primary aim of this study is to conduct thorough evaluations of the effects of

σ_y and W_m on nearby faulting. Variations in σ_y and W_m are systematically assessed to understand their effects on the occurrence and characteristics of faulting. Robust static numerical models, where the fault friction is explicitly introduced, have been developed. These models are intended to improve predictive capabilities regarding induced earthquakes and contribute to the prediction and mitigation of the mining risk.

3.2 3-D numerical modeling of faulting behavior with finite element method

3.2.1 F16 reverse fault close to Yuejin coal mine

I investigated the fault reactivation at Yuejin coal mine, China, to understand the impact of stress disturbance and fault slip due to nearby mining activities. Referring to the figure in Cai et al. (2015), the reverse fault F16 was characterized by a shallow dip of 30° at 700 m depth and 75° at shallow depth, with an East-West strike direction. This fault was located in complex geological conditions. The target area lay south of the No. 25110 panel, employing longwall top coal caving across 1000 m length, 200 m width, and 1000 m depth (Cai et al. 2015). The investigated area had an average coal thickness of 11.5 m, with a dip angle of 12°. Li et al. (2016) reported 20 coal burst accidents within the No. 25110 panel, which have been attributed to fault reactivation as mining activities progressively approached the F16 reverse fault.

Given the complexity of the geological structure near F16 and the significant limitations in data availability regarding geological conditions and rock properties across various locations, I employed a simplified model (Fig. 3-1a). This model minimizes the need for extensive input data, allowing for a focused investigation of the primary factors affecting the faulting process. Adopting this approach clarifies the essential mechanisms behind mining-induced faulting, ensuring that the research is both efficient and precisely targeted.

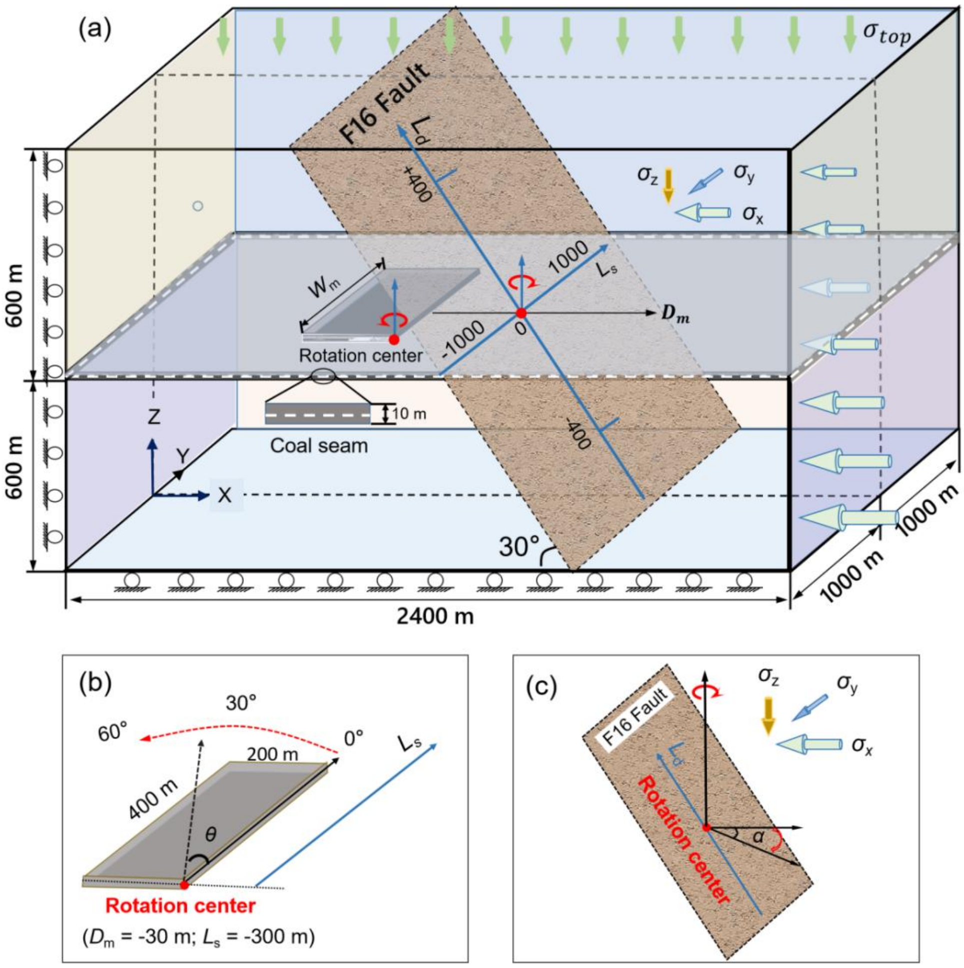

Fig. 3-1 A schematic illustration of the 3-D mining model. (a) Configuration of the deep mining model with a central reverse fault. The direction of the *xyz*-coordinate system is situated at the bottom left corner of the figure. L_s and L_d represent local coordinates along the fault strike and dip directions, respectively. These coordinates are set to 0 at the cross-section where the mining level intersects the fault at $y = 0$. W_m is the length of the panel. D_m represents the mining distance, with the positive direction indicating the hanging wall side and the negative direction indicating the footwall side. Vertical far-field stress is denoted as σ_z, and horizontal far-field stresses in the *x*- and *y*-directions are denoted as σ_x and σ_y, respectively; (b) Schematic diagram of the panel rotation angle, where the 'rotation center' denotes the commencement of rotation. Rotation starts from a position parallel to the local coordinate L_s at 0°, with the angle increasing in a counterclockwise direction; (c) Diagram illustrating the principal stress rotation

angle. The orientation at 0° is aligned with the positive direction of the x-axis, encompassing a clockwise rotation around the z-axis, resulting in an incremental increase in angle.

3.2.2 Setting of numerical modeling

For my analysis, a 3-D model was developed within a cuboid space (Fig. 3-1a). The Cartesian coordinate system (x, y, z) is introduced as shown at the left bottom of Fig. 3-1a. The model dimension is 2400 m × 2000 m × 1200 m along the x, y, and z directions, respectively. The origin was set at the center of the bottom left corner, with the positive direction taken as upward in the z-axis. The depth of the center of the coal seam layer is set at 1000 m. The panel width and height are set at 200 m and 10 m, respectively, while the length of the panel W_m is a parameter to be examined (Fig. 3-1a). The fault is located at the center of the model, where the dip angle φ is 30°. The elastic parameters are set uniformly in the model. Additional details can be found in Table 3-1.

Table 3-1 Mechanical Parameters in the numerical model

Parameters	Values	Parameters	Values
Young's modulus, E (GPa)	15	Background stress ratio, r_x	2
Poisson's ratio, v	0.25	Background stress ratio, r_y	1.5 (1.0, 1.5, 2.0)[a]
Shear modulus, G (GPa)	6.5	Mining level, (m)	1000
Cohesion stress, C (MPa)	0	Panel length, W_m (m)	200 (300, 400, 500)[b]
Density, ρ (kg/m^3)	2400	Panel width, (m)	200
Fault dip angle, φ (°)	30	Mining distance, D_m (m)	-30 m
Depth, h (m)	400–1600	Panel rotation angle, θ (°)	From 0 to 90 every 10
Static friction coefficient, μ_s	0.7	Principle stress rotation angle, α (°)	0, 15, 30
Mining thickness, (m)	10		

Note: a) The values are used to analyze the influence of far-field intermediate principal stress on faulting. b) Values are estimated to examine the impact of panel length, W_m, on faulting.

One challenge in my simulation is computation time, which increases with more elements, thus necessitating a reduction in elements to optimize the analysis. The inherent symmetry of the system, in which the geometry, loads, and constraints exhibit symmetry in the *y*-direction, allows me to explicitly model only the positive half of the system while the other half can be computed as a mirror image of the positive half (Fig. 3-2). Consequently, I could effectively compute the model to interpret the behavior of the system by reducing computational complexity and improving efficiency.

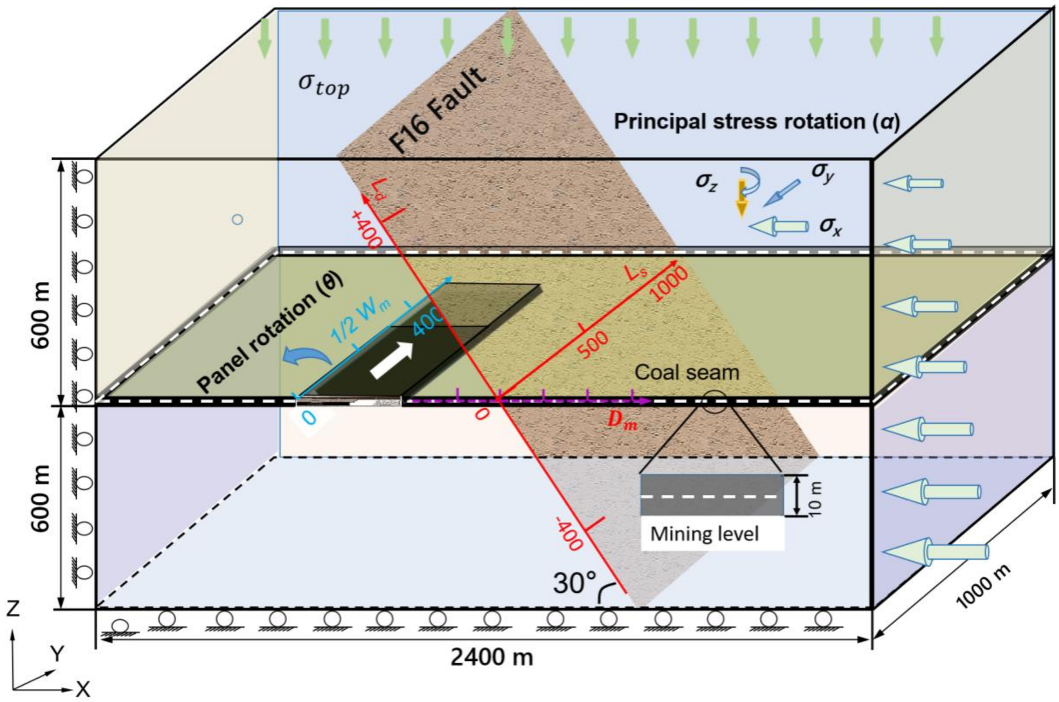

Fig. 3-2 Configuration of the deep mining model with a central reverse fault for the case where the symmetry holds with respect to the *y*-axis. The direction of the *xyz*-coordinate system is situated at the bottom left corner of the figure. The model dimension is 2400 m × 1200 m × 1000 m along the *x*, *y*, and *z* directions.

Further, it is crucial to consider scenarios with asymmetrical conditions, as these can significantly alter the behavior of the system in ways that symmetrical analysis does not account for. In asymmetry cases, where the geometry, loads, or constraints do not exhibit any symmetry in the *y*-direction, full-size modeling is necessary, ranging from y = -1000 m to y = 1000 m. This involves representing the entire system to reflect the uneven distribution of forces and variations in asymmetric geometry.

The mining distance (D_m), the separation distance between the fault and the mining face (Fig. 3-1a), is taken positive when the mining face is on the hanging wall side and negative when it is on the footwall side. In Fig. 3-1a, I used a local coordinate system L_s, which corresponds to the fault strike direction, and L_d, which represents the fault dip direction. The origin of this local coordinate system is set at the intersection point of the center of the fault area and the midpoint of the coal seam layer. Positive L_d values are for the upward direction, while negative values signify the downward direction. By employing this local coordinate system on the fault, I investigated the spatial relationship between fault stress ratio (k), D_m, and φ.

3.2.3 Governing equations, assumptions, and input parameters

The static equilibrium analysis in this study is based on the key governing equations, which can be expressed as:

$$\sigma_{ij,j} + f_i = \mathbf{0} \tag{3-1}$$

where $\sigma_{ij,j}$ represents the spatial derivative of stress tensor and f_i is the body force field per unit volume.

In Fig. 3-1a, as part of my investigation into stress distribution, I strategically altered the boundary conditions by specifically modifying the background stress conditions. This modification was applied exclusively to the y-axial faces, which correspond to the intermediate far-field principal stress direction. It is important to explain that σ_x, σ_y, and σ_z represent the principal stresses applied at far-field and oriented in the x, y, and z directions, respectively. My model encompasses a volume five times greater than that of the study area (the mining-fault-affected zone). This substantial increase in volume allows for enhanced resolution within the study area as well as in the expanded boundary zones, offering a more detailed analysis of the effects within and surrounding the mining-fault-affected zone. The x-axis is aligned with the direction of the maximum principal stress, the y-axis is oriented along the panel length, representing the intermediate far-field principal stress direction, and the z-axis, corresponding to the mining depth h (as detailed in Table 3-1), indicates the minimum principal stress direction. To clarify the boundary conditions within the framework of my model, I introduce $\sigma_z(h)$, which is self-gravity and represents the stress condition along the z-axis. This critical parameter serves as a reference for comparing the stress conditions along the x- and y-axes. More specifically, the following stress boundary conditions are introduced:

$$\begin{cases} \sigma_x(2400, y, h) = r_b^x \sigma_z(h) \\ \sigma_y(x, 2000, h) = r_b^y \sigma_z(h) \\ \quad \sigma_z(h) = \rho\, g\, h \end{cases} \tag{3-2}$$

where r_b^i is the i-component background stress ratio, and i takes either x or y. ρ is density and g is gravitational acceleration.

The displacement **U** is zero at the origin point ($x = 0, y = 0, z = 0$): i.e., $\mathbf{U}(0,0,0) = 0$. This condition signifies that the degrees of freedom are constrained at the origin, providing a fixed reference point for my analysis.

(1) Shear stress on a rotated plane: application of stress tensor and rotation matrix

In the 3-D context, I generalize the shear (τ) and normal stress (σ_n) expressions for any plane orientation using basis vectors. This includes subdividing shear stress on the fault plane into components along the strike and dip. These shear stress components are illustrated in Figs. 3-1b and 3-1c. Using a rotation matrix ($\boldsymbol{R}$), σ_n and τ are calculated by rotating the fault plane within a fixed coordinate system. I compute the stresses on a rotated plane following the method outlined by Jager et al. (2007, Chapter 2.6). I define the stress state in a global xyz-coordinate system (Fig. 3-1a) by the stress tensor $\boldsymbol{\sigma}$ (Eq. 3-3). The stress tensor ($\boldsymbol{\sigma}$) is a 3×3 matrix as follows.

$$\boldsymbol{\sigma} = \begin{bmatrix} \sigma_{xx} & \sigma_{xy} & \sigma_{xz} \\ \sigma_{yx} & \sigma_{yy} & \sigma_{yz} \\ \sigma_{zx} & \sigma_{zy} & \sigma_{zz} \end{bmatrix} \tag{3-3}$$

Then, I transform this stress tensor into a local coordinate system corresponding to the rotated plane using a rotation matrix $\boldsymbol{R}$ (Eq. 3-4). The rotation matrix ($\boldsymbol{R}$**)** describes the transformation from the global to the local coordinate system (Fig.3-1a). For a given plane orientation with a dip angle, φ, and the principal rotation angle, α, the rotation matrix can be expressed as follows:

$$\boldsymbol{R} = \begin{bmatrix} \sin\varphi\cos\alpha & -\sin\alpha & \cos\varphi\cos\alpha \\ \sin\alpha\sin\varphi & \cos\alpha & \sin\alpha\cos\varphi \\ -\cos\varphi & 0 & \sin\varphi \end{bmatrix} \tag{3-4}$$

where, each column of $\boldsymbol{R}$ represents the unit vectors of the local coordinate system in the global coordinates (Jaeger et al. 2007, Chapter 2.6).

Transform the stress tensor from the global coordinate system to the local coordinate system using the formula below.

$$\boldsymbol{\sigma}^{'} = \boldsymbol{R}\boldsymbol{\sigma}\boldsymbol{R}^{T} \tag{3-5}$$

Here, $\boldsymbol{\sigma}'$ is the stress tensor represented in the local coordinate system, and $\boldsymbol{R}^{\mathrm{T}}$ is the transpose of $\boldsymbol{R}$. In this equation, $\boldsymbol{\sigma}'$ embodies the stresses originating from geological structures as well as disturbances induced by mining activities.

In $\boldsymbol{\sigma}'$, the shear stress components are located off the diagonal, e.g., σ_{xz}' or σ_{xy}' in my study, I use the τ_1 and τ_2. Specifically, the values of σ_n, τ_1 and τ_2 are calculated as follows:

$$\begin{cases} \sigma_n = \sigma_{xx}^{'} \\ \tau_1 = \sigma_{xz}^{'} \\ \tau_2 = \sigma_{xy}^{'} \end{cases} \tag{3-6}$$

where τ_1 is shear stress component along the fault dip direction, τ_2 is shear stress component along the fault strike direction, and σ_n is normal stress on the fault. In the analysis, positive normal stress values indicate compression.

(2) Mohr-Coulomb fracture criterion in 3-D mining condition

To further investigate the influence of σ_y on the fault failure and coseismic slip behavior, I introduce the fault stress ratio k as

$$k = \frac{\sqrt{\tau_1^2 + \tau_2^2}}{\sigma_n} \tag{3-7}$$

In this definition, $\sqrt{\tau_1^2 + \tau_2^2}$ represents the maximum shear stress on the fault, where τ_1 and τ_2 correspond to the shear stresses along the dip and strike of the fault plane, respectively. Following the Wallace-Bott hypothesis, the slip direction is assumed to be the same as the maximum stress direction (Wallace 1951; Bott 1959). σ_n is normal stress on the fault. k represents the ratio that controls the criterion for slip by comparing the friction coefficient.

For an inclined fault, it is imperative to decompose the stress onto the fault plane. Based on Eq. 3-6, the maximum shear stress and normal stresses can be expressed as follows:

$$\begin{cases} \tau^2 = {\sigma'_{xy}}^2 + {\sigma'_{xz}}^2 \\ \sigma_n = \sigma'_{xx} \end{cases} \tag{3-8}$$

Substituting the expressions for shear and normal stresses into the following Mohr-Coulomb fracture criterion:

$$\tau \geq \mu_s \sigma_n + C \tag{3-9}$$

where μ_s is friction coefficient and C is cohesion. I then obtain the following relation assuming $C = 0$.

$$\sqrt{{\sigma'_{xy}}^2 + {\sigma'_{xz}}^2} \geq \mu_s \sigma'_{xx} \tag{3-10}$$

This equation can judge whether fault slips or not. If this inequality is satisfied, the stress state on the fault plane initiates fault slip. Following the Wallace-Bott hypothesis, the shear slip direction is the same as the maximum stress direction (Wallace 1951; Bott 1959).

I employed the Mohr-Coulomb fracture criterion that slip occurs if $k > \mu$, unless there is no occurrence of slip. Here, shear and normal stress consist of the stress disturbance due to mining and the background stress as follows.

$$\begin{cases} \tau_1 = \tau_1^0 + \tau_1^m \\ \tau_2 = \tau_2^0 + \tau_2^m \\ \sigma_n = \sigma_n^0 + \tau_n^m \end{cases} \tag{3-11}$$

where superscripts 0 and m indicate the values under background conditions and those induced by mining, respectively. Similar to the fault stress ratio k, I can introduce the background stress ratio k_0 and the mining-induced stress ratio k_m as follows.

$$\begin{cases} k_0 = \dfrac{\sqrt{\tau_1^0 + \tau_2^0}}{\sigma_n^0} \\ k_m = \dfrac{\sqrt{\tau_1^m + \tau_2^m}}{\sigma_n^m} \end{cases} \tag{3-12}$$

To investigate the effect of the principal stress and panel orientations on the fault slip distribution under asymmetric conditions, I introduced two angular parameters, α and θ. α represents the clockwise rotation angle between the direction of maximum principal stress and the fault normal on the horizontal plane. θ indicates the counterclockwise rotation angle of the panel, measured from the fault strike, with the rotation center located at the corner of the panel (Figs. 3-1a and 3-1b). Angle α quantifies the principal stress direction on both the panel and the fault, crucial for evaluating structural stability and integrity. Conversely, angle θ illustrates the influence of the panel rotation on fault slip, keeping the directions of background principal stress and fault strike the same. This approach enables a precise examination of the mechanical interactions and their implications for fault slip.

Detailed discussion on the influence of fault dip angle and rotation of far-field stress (Fig. 3-1c) on the background stress ratio (k_0) is provided in Fig. 3-3. The background fault stress state (σ_n^0/s_z, τ_1^0/s_z, τ_2^0/s_z) on the k_0 value is shown in Fig. 3-3a. While maintaining a constant fault dip angle (φ) of 30° and r_b^y of either 1.0, 1.5, or 2.0, I demonstrate the changes in σ_n^0/s_z, τ_1^0/s_z, τ_2^0/s_z and k_0 on the fault plane under various orientations of far-field principal stress. This stress field is achieved by the rotation around the z-axis, initiating from the positive direction of the y-axis at 0°, with clockwise rotation is positive. Fig. 3-3a shows that with α below 10°, k_0 maintains a constant value of 0.34. As α increases, k_0 behaves differently depending on the value of r_b^y. In conditions where α is 15°, 30°, or 45°, an increased r_b^y clearly promotes contributions to both σ_n^0/σ_z and τ_2^0/σ_z (Figs. 3-3b, c and d). Specifically, as r_b^y escalates, there is a corresponding increase in σ_n^0/σ_z, which further intensifies with φ. Smaller r_b^y results in greater τ_2^0/σ_z, a trend that magnifies with an increasing φ.

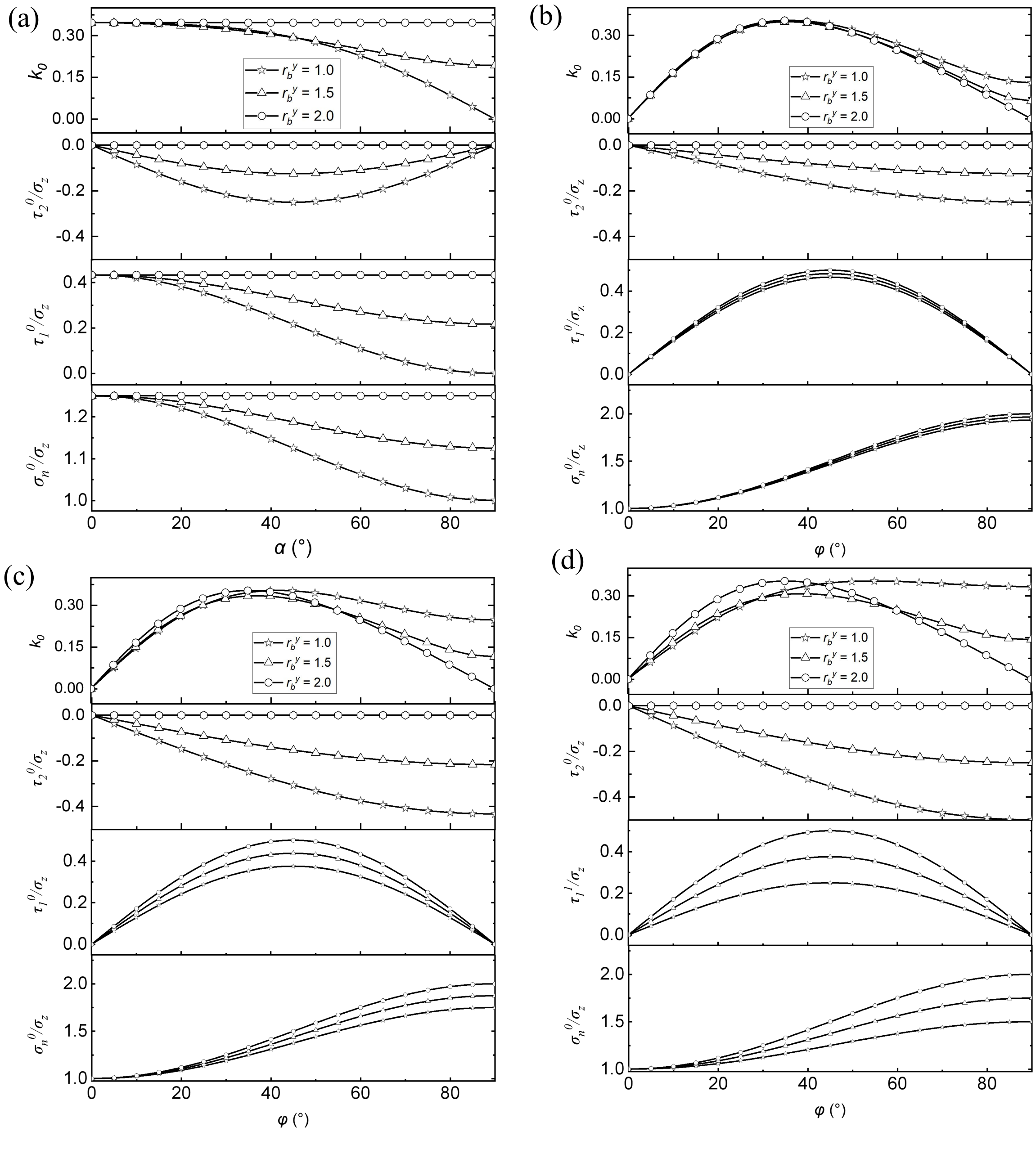

Fig. 3-3 The influence of fault dip angle (φ) and rotation of far-field stress (α) (Fig. 3-1c) on the background stress ratio (k_0). In the diagram presented, I plotted the stress values normalized by σ_z. (a) k_0, s_n^0/s_z, t_1^0/s_z, and t_2^0/s_z as a function of α with a fixed φ value of 30° for the cases of r_b^y = 1.0, 1.5, and 2.0; (b) k_0, s_n^0/s_z, t_1^0/s_z, and t_2^0/s_z as a function of φ for a fixed α value of 15°for the cases of r_b^y = 1.0, 1.5, and 2.0; (c) k_0, s_n^0/s_z, t_1^0/s_z, and t_2^0/s_z as a function of φ for a fixed α value of 30°for the cases of r_b^y = 1.0, 1.5, and 2.0; (d) k_0, s_n^0/s_z, t_1^0/s_z, and t_2^0/s_z as a function of φ for a

fixed α value of 45° for the cases of r_B^y = 1.0, 1.5, and 2.0.

3.2.4 Mesh generation and FEM solvers

I employed Code_Aster Ver. 14.6 (http://www.code-aster.org), a finite element method (FEM) software for simulating fault reactivation induced by mining in a 3-D model. I focused on the stress disturbance and fault coseismic slip due to coal mining proximity.

To enhance computational efficiency, I leveraged the symmetric properties of the model by using half of the model for calculations. This approach, illustrated in Fig. 3-1a, allowed me to extrapolate the half-model results to a full-model representation, as shown in Fig. 3-2. In my model, I utilized 486,836 tetrahedral elements for the half-model configuration. I expanded to 949,330 elements for the full-model analysis to compute the effects of principal stress and panel rotation. For meshing, I utilized the sub-mesh method via Salome-Meca 2015.1. This method involves creating finer meshes (sub-meshes) within a larger mesh structure, enhancing detail accuracy without extensive computation. Specifically, the slave surface, positioned closer to the mining face, was meshed with elements smaller than 1 m to capture detailed deformation. On the other hand, the master surface, situated further from the mining operations, utilized a slightly larger element size of less than 2 m. As the distance from the fault plane increased, the mesh size expanded to 50 m, balancing detail with computational efficiency.

3.3 Results of 3-D numerical modeling: the effects of W_m and σ_y

This section presents the results derived from the model shown in Fig. 3-1a. My primary object is to examine the impact of W_m and σ_y on fault failure and coseismic slip behavior. By conducting a parameter search study, I aim to offer insights into the intricate interplay between mining activities and fault reactivation for various W_m and σ_y.

3.3.1 Effect of σ_y on mining-induced fault slip

(1) Effects of σ_y on shear stress and coseismic slip

Mining-induced stress on the fault plane and its interactions with σ_y are crucial to the development of faulting. When shear stress surpasses the fault frictional strength within a given friction state, slip occurs following the Mohr-Coulomb fracture criterion (Fig. 3-1d). To investigate the influence of σ_y on faulting, I considered three cases of σ_y to analyze its effects on slip during mining; Case 1 for $r_b^y = 2.0$, Case 2 for $r_b^y = 1.5$ and Case 3 for $r_b^y = 1.0$. These cases correspond to the stress environment of $\sigma_x = \sigma_y > \sigma_z$, $\sigma_x > \sigma_y > \sigma_z$, and $\sigma_x > \sigma_y = \sigma_z$, respectively.

Figs. 3-4 and 3-5 illustrate the distributions of normal stress (σ_n), shear stress (τ), their ratio (k), and coseismic slip along the fault plane, for the case of $r_b^y = 1.5$, $D_m = -30$ m, and $W_m = 400$ m. Figs. 3-4b and 3-4d show a non-linear relationship between the total shear stress distribution and the total slip on the fault, highlighting the complexity of stress interactions and fault shear slip behavior. The maximum slip on the fault was 251 mm, occurring at $L_s = 0$ m and $L_d = 110$ m, as shown in Fig. 3-4d. Figs. 3-4a and 3-4b intuitively illustrate the distribution of stress disturbances along the fault plane induced by mining activities. The computation result (Figs. 3-4c and 3-4d) may suggest a relationship between the mining-induced k and the observed slip along the fault plane. However, this comes from the saturation of k due to the fracture criterion ($\mu_s = 0.7$) that I assumed.

The distributions of slip shown in Figs. 3-4d, 3-6a, and 3-6b provide detailed dependence on r_b^y for three cases. Specifically, Fig. 3-6c illustrates the cumulative slip along the fault dip direction originating from point $L_s = 0$ m for all three cases. The maximum slip was 257 mm in Case 1, 251 mm in Case 2, and 245 mm in Case 3. Fig. 3-6d presents the cumulative slip along the strike direction, originating from point $L_d = 110$ m for each case. I found that σ_y had a central symmetrical influence on the fault slip along the strike direction. Notably, a higher σ_y led to a larger slip zone, but σ_y did not significantly affect the total slip distribution.

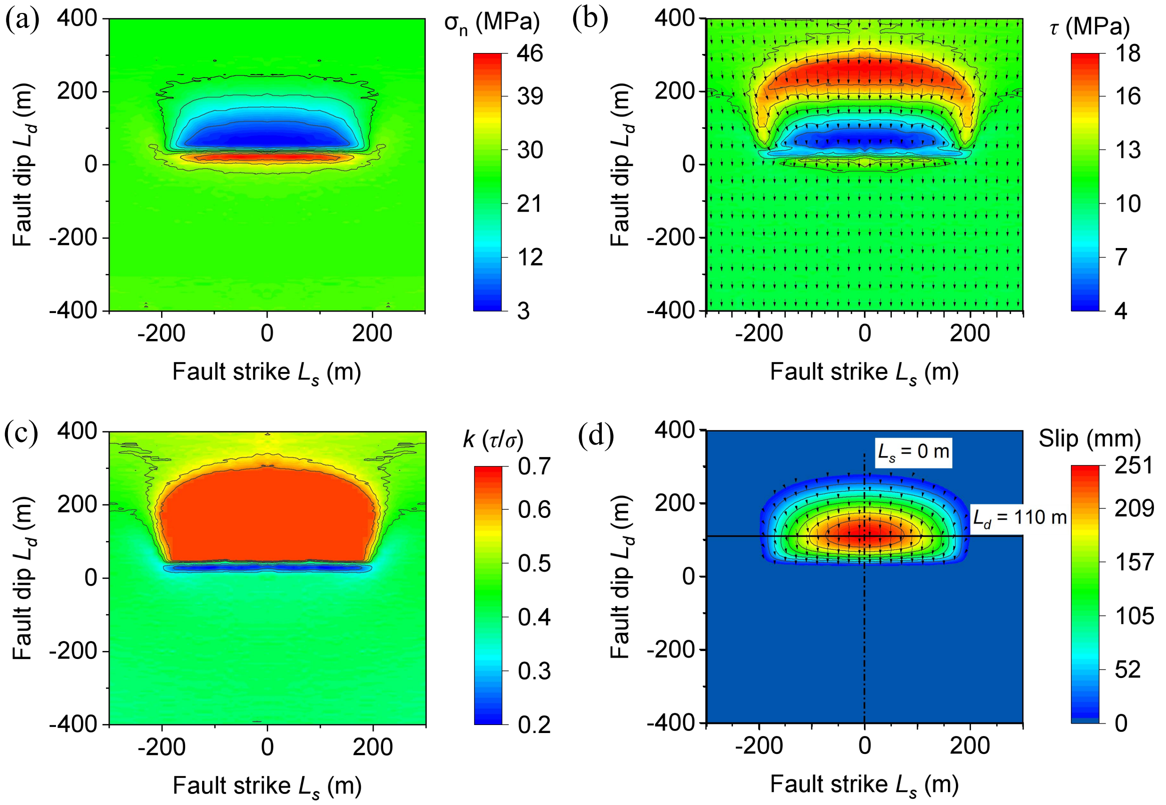

Fig. 3-4 Mining-induced slip and stress distribution on the fault plane, considering the parameters $r_b^y = 1.5$, $D_m = -30$ m, and $W_m = 400$ m. (a) The spatial distribution of σ_n; (b) The spatial distribution of τ. The black arrow indicates the size and direction of t on the fault; (c) The spatial distribution of k; (d) The spatial distribution of slip. The black arrow indicates the size and direction of the total slip on the fault.

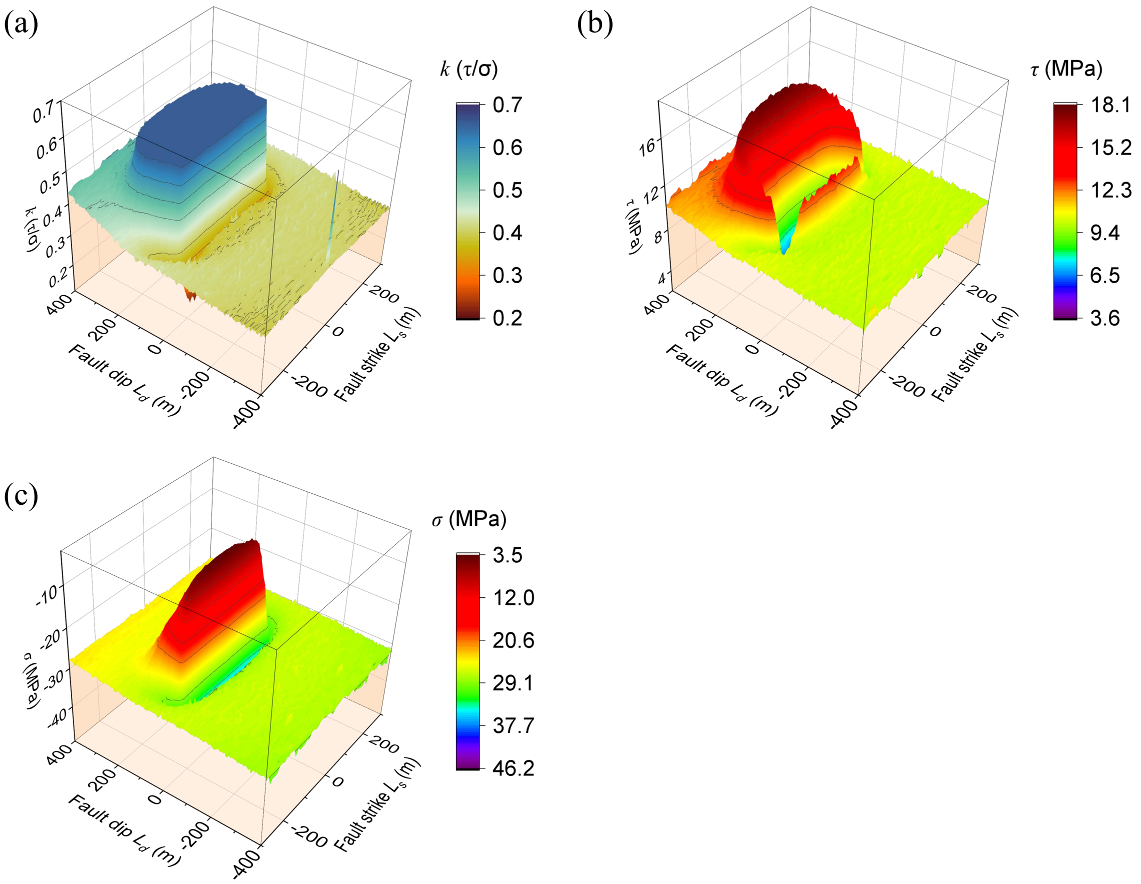

Fig. 3-5 Mining-induced stress and k distribution on the fault plane, considering the parameters $r_b^y = 1.5$, $D_m = -30$ m, and $W_m = 400$ m. (a) The spatial distribution of k; (b) The spatial distribution of τ; (c) The spatial distribution of σ.

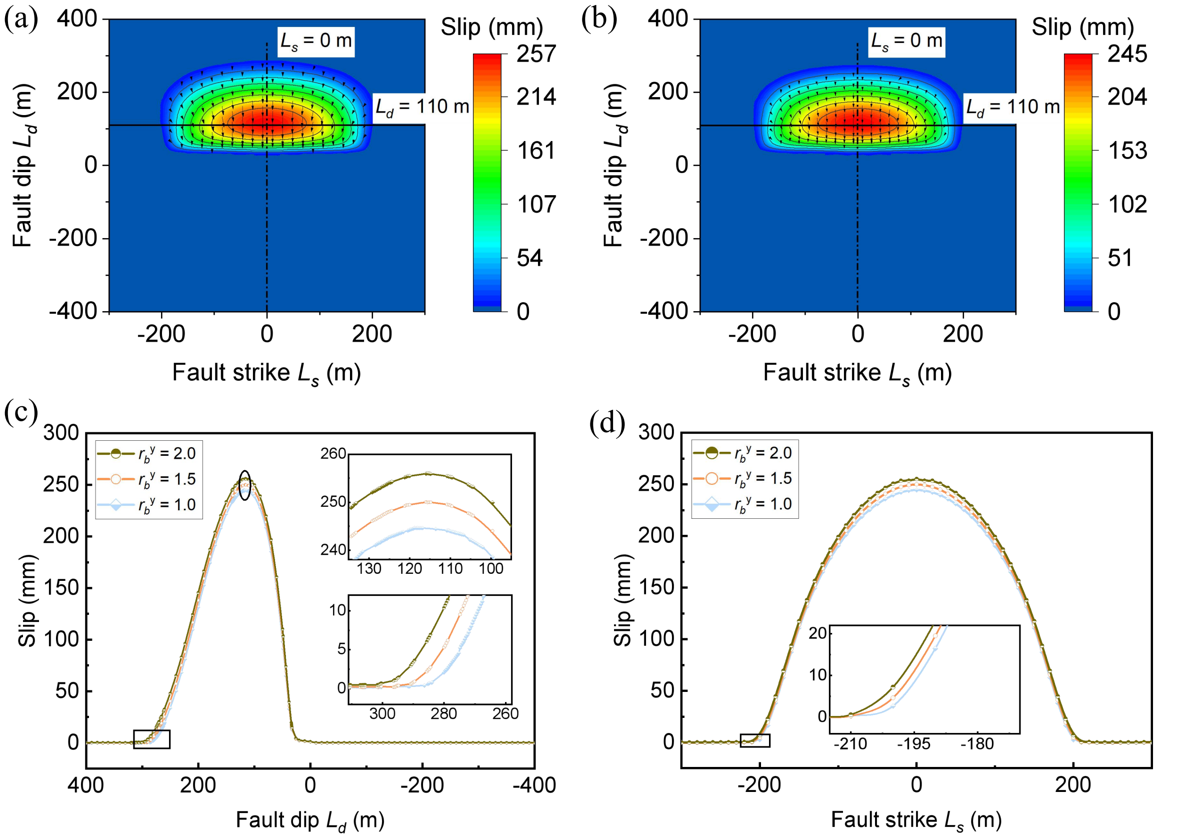

Fig. 3-6 Slip Variation under different σ_y with D_m of -30 m on the footwall side, $\mu_s = 0.7$, and $W_m = 400$ m. (a) Slip distribution on the fault plane with $\sigma_x = \sigma_y > \sigma_z$ ($r_b^y = 2.0$); (b) Slip distribution on the fault plane with $\sigma_x > \sigma_y = \sigma_z$ ($r_b^y = 1.0$); (c) Slip sectional curves along the fault dip direction for the three cases at $L_s = 0$ m; (d) Slip sectional curves along the fault strike direction for the three cases at $L_d = 110$ m.

(2) Effects of σ_y on stress and slip components in strike direction

Figs. 3-7a, 3-7b, and Fig. 3-8 show a distinct correlation between the slip component and τ_2 along the fault strike direction. Fig. 3-7a unveils a central symmetrical pattern in the slip component around the point at $L_s = 0$ and $L_d = 150$ m, highlighting significant symmetry along the line. The shear stress component showed a similar pattern as displayed in Fig. 3-7b. Below the mining level ($L_d < 0$ m), both the slip and τ_2 become zero. This indicates that the shear stress along the fault strike direction was solely generated by mining activities, which agrees with the initial boundary conditions of the model.

To further investigate the distribution of the slip components, I examined the slip distribution along three cross-sections. Two of them were selected along the dip direction at L_s = -150 m and L_s = 150 m, as illustrated in Figs. 3-7c and 3-7d, respectively. Other plots were along the strike direction (L_d = 150 m along the dip), as shown in Figs. 3-7e and 3-7f. The shape of the slip distribution along the fault dip direction was found to be different from that of the total slip pattern in Figs. 3-6c and 3-6d.

The slip curves in my analysis showed two distinct trends. The blue curve in Fig. 3-7c, corresponding to L_s = -150 m, displayed negative slip values. In contrast, the red curve, associated with L_s = 150 m along the fault strike, exhibited positive slip values. These two slip curves aligned with the corresponding trends of τ_2 in Fig. 3-7d. The largest slip of 26.6 mm occurred along the red curve and was consistent with the blue curve. The fault slip distribution along the fault strike shows an asymmetric pattern centered at the origin (0,0) (Fig. 3-7e). The distribution of τ_2 closely matches the slip patterns along the fault strike, showing a linear relationship between τ_2 trends and slip variations along the fault strike (Fig. 3-7f).

Table 3-2 Maximum slip along fault strike under three σ_y states

Model	r_b^x	r_b^y	Total slip (mm)	Fault slip area (×10^4 m^2)	Maximum slip along strike (mm)	
					L_d = 150 m	L_d = -150 m
Case 1	2.0	2.0	257	9. 50	28.66	-28.66
Case 2	2.0	1.5	251	8.78	26.65	-26.65
Case 3	2.0	1.0	245	8.03	24.78	-24.78

Fig. 3-9 shows the slip distribution along the fault strike direction for the three cases. At L_s = 150 m along the fault strike, the maximum slips were 28.6 mm for Case 1 (r_b^y = 2.0), 26.6 mm for Case 2 (r_b^y = 1.5), and 24.7 mm for Case 3 (r_b^y = 1.0). Similarly, at L_s = -150 m along the fault strike, the maximum slips were -28.6 mm (Case 1), -26.6 mm (Case 2), and -24.7 mm (Case 3). Fig. 3-9b shows the detailed slip distribution along the fault dip direction, ranging from L_d = -20 m to 70 m. Fig. 3-9c depicts the slip distribution along the strike direction at L_d = 110 m along the fault dip. The maximum slip values for the three σ_y cases were summarized in Table 3-2.

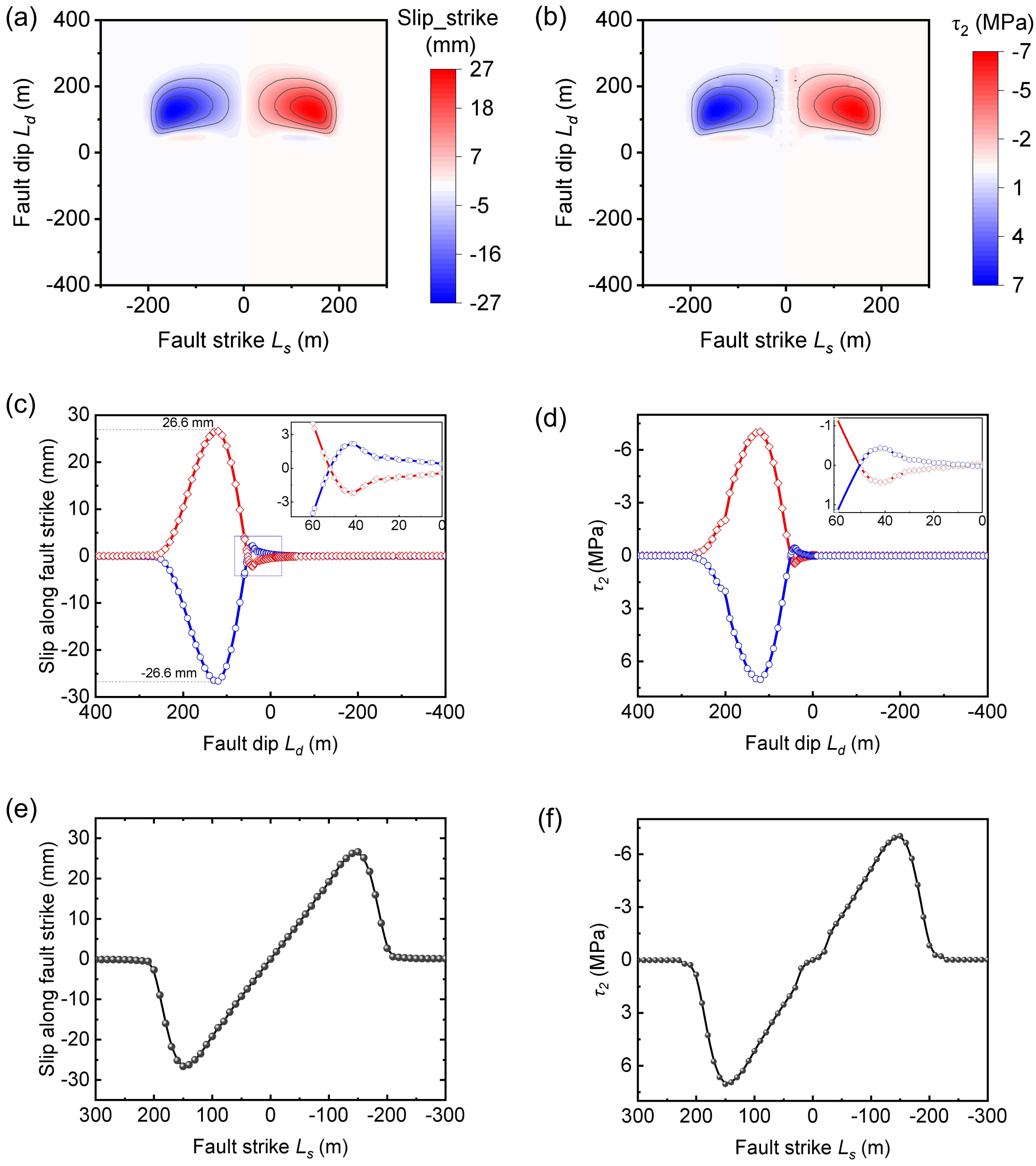

Fig. 3-7 Shear stress and slip components along the strike direction. (a) Slip component and (b) shear stress component. (c) Slip component and (d) stress components along dip for L_s = 150 m (red curve) and L_s = -150 m (blue curve); (e) Slip component and (f) shear stress components along strike for L_d = 150 m.

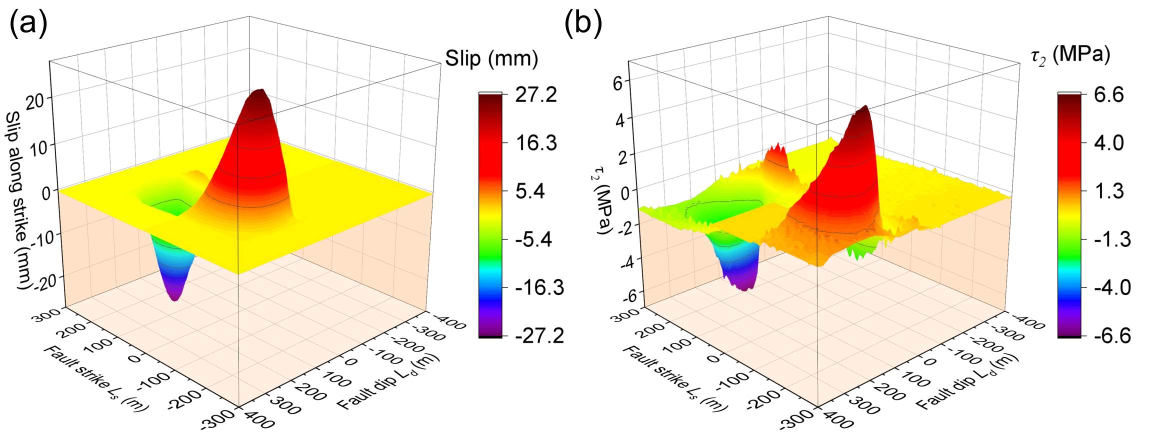

Fig. 3-8 Shear stress and slip components along the fault strike direction in 3-D plots: (a) Slip components along the fault strike direction on the fault plane; (b) Shear components along the fault strike direction on the fault plane.

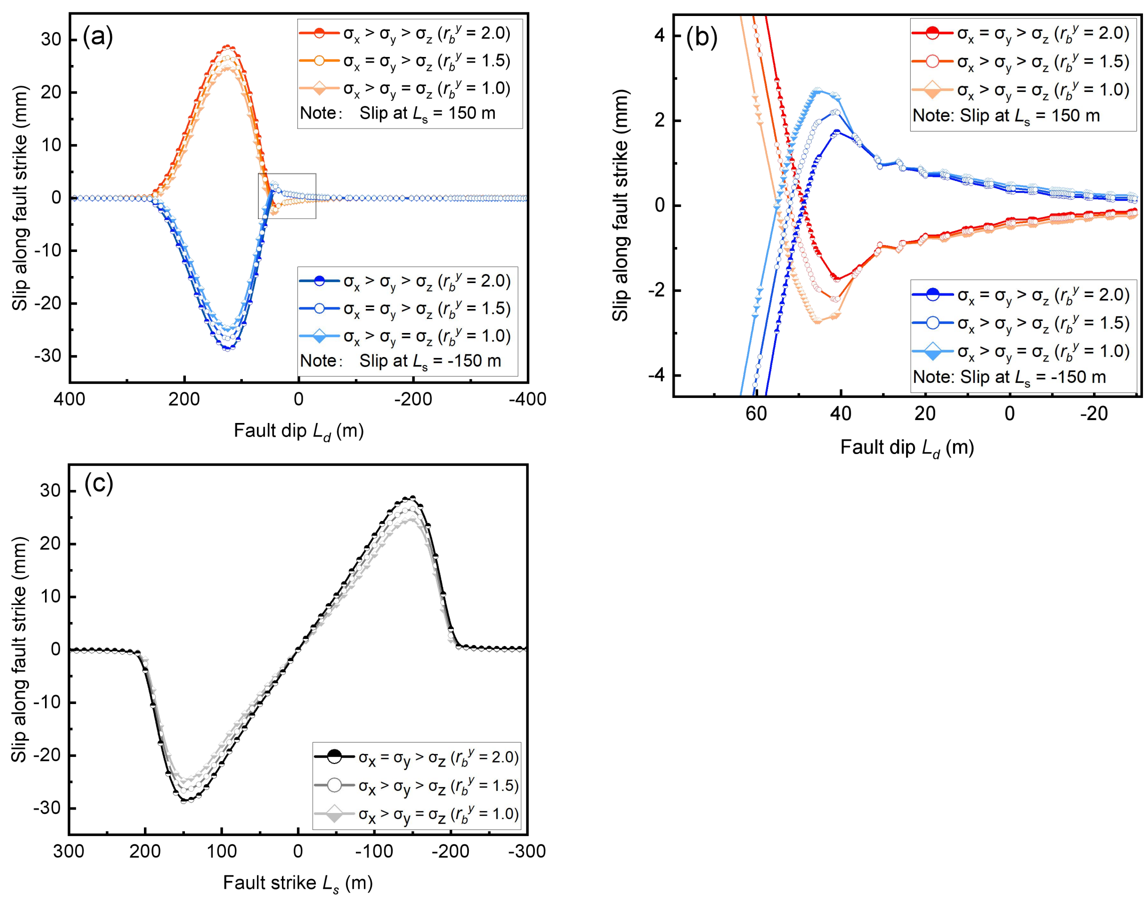

Fig. 3-9 The relationship between the coseismic slip components and the length of the fault strike direction with different intermediate far-field stress under the

conditions of D_m = 30 m and μ_s = 0.7. (a) Slip components along the fault dip direction at L_s = 150 m and L_s = -150 m along the fault strike for three different intermediate far-field stress cases; (b) Partial magnified view of the coseismic slip along strike component within the designated rectangular region in panel (a); (c) Slip components along the fault strike direction at L_d = 150 m along the fault dip for three different intermediate far-field stress cases.

(3) Mining-induced fault slip under various far-field stress orientations

I considered the cases where the principal stress direction was not parallel or perpendicular to the fault strike direction. I investigated the impact of far-field principal stress orientation on fault slip distribution, referring to the realistic mining conditions. I examined the effects of different far-field principal stress orientation α, as shown in Fig. 3-1c. I considered the cases where α is either 0°, 15°, or 30°. To achieve this condition, I rotated the fault and mining area counterclockwise the same amount around the z-axis, keeping the principal stress the same as before. I no longer utilized the symmetry of the model in this analysis. I investigated the distribution of mining-induced coseismic slip under W_m = 200 m and D_m = -30 m.

Fig. 3-10 showed the maximum slip and slip area for α = 0°, 15°, and 30° and for r_b^y = 1.0, 1.5 and 2.0 cases. When α was 0°, the length of the maximum slip zone along the fault strike and dip directions expanded as r_b^y increased. This expansion in slip length was relatively modest, varying between 2-4 m with a slip increment of 2.3-3.2 mm. This was consistent with the result shown in Fig. 3-6 and indicated that intermediate far-field stress facilitated fault slip. At a rotation angle of α = 15°, clear increases were seen in slip length along the strike, measuring 225.4 m, 234.9 m, and 242 m for r_b^y values of 1.0 (Case 3), 1.5 (Case 2), and 2.0 (Case 1), respectively. Similarly, at α = 30°, the slip lengths were 210.8 m, 227.0 m, and 242.9 m for the same r_b^y values, illustrating the significant contribution of intermediate far-field principal stress to the length of the coseismic slip. The data in Fig. 3-10 also confirmed that as the intermediate far-field principal stress increased. There was a corresponding increase in slip length along the fault strike. At α = 15°, slip values were 125.6 mm, 131.8 mm, and 136.9 mm for r_b^y values of 1.0, 1.5, and 2.0, respectively. At α = 30°, these slips were 115.2 mm, 126.6 mm, and 136.8 mm, reinforced the notion that intermediate far-field principal stress significantly contributed to coseismic slip.

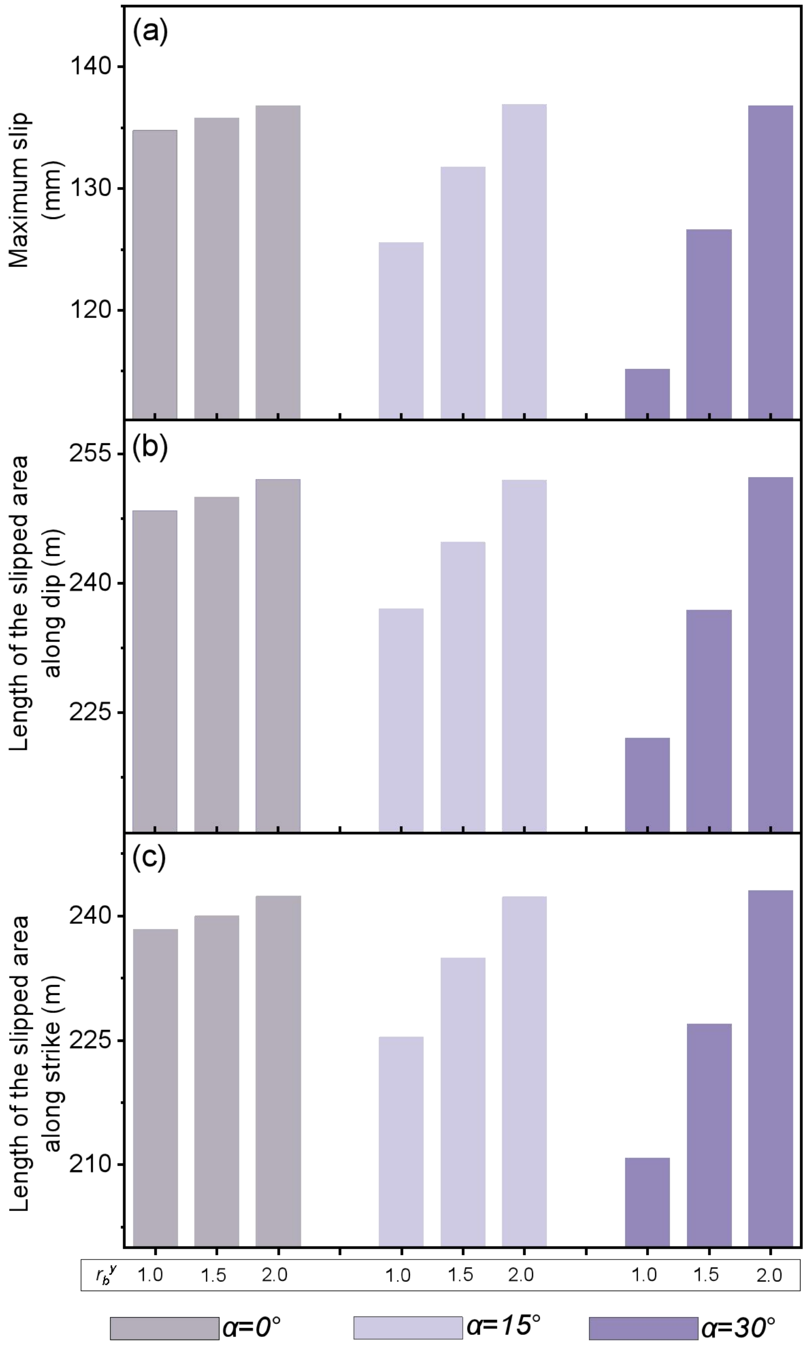

Fig. 3-10 Coseismic slip with far-field stress rotating counterclockwise around the z-axis by 0°, 15°, and 30°, with intermediate far-field stress r_b^y values of 1.0, 1.5, and 2.0, W_m = 200 m, and D_m = -30 m. (a) Maximum slip; (b) Length of the slipped area

along dip, and (c) Length of the slipped area along strike.

In 3–D simulations, fault slip includes a component along the strike direction, which was not included in 2–D simulations (Li et al. 2024a). I analyzed the distribution of coseismic slip along the strike direction under three different intermediate far-field principal stress conditions. Fig. 3-11a demonstrated that at α of 0°, the maximum and minimum slip curves along the strike were symmetrically distributed. The maximum slip increases from 27.3 mm to 31.5 mm as intermediate far-field principal stress increases from $r_b^y = 1.0$ to $r_b^y = 2.0$, indicating a promoting but relatively small effect on the slip distribution. Figs. 3-11b and 3-11c show that stress rotation significantly modified the symmetry of the slip components along the strike direction. Notably, the intermediate principal stress and the strike-slip component exhibit a positive correlation. Here, the positive direction for strike-slip movement was defined as a right-lateral strike-slip fault movement. It was observed that intermediate principal stress significantly promoted the positive (right-lateral) strike slip motion, while low intermediate principal stress resulted in a large negative (left-lateral) slip in the strike component.

Fig. 3-3a illustrated that the impact of intermediate principal stress increases with α when $\varphi = 30°$. Concurrently, Figs. 3-3b, c, and d presented the distribution of background stress (σ_n^0, τ_1^0 and τ_2^0) and k_0 as functions of φ at α values of 15°, 30°, and 45°. Qualitative behaviors observed in Fig. 3-3 support the results presented in Figs. 3-9, 3-10, and 3-11, highlighting that σ_n^0, τ_1^0 and τ_2^0 remain constant when transitioning from $r_b^y = 1.0$ to 2.0 at $\alpha = 0°$ (see Fig. 3-3a).

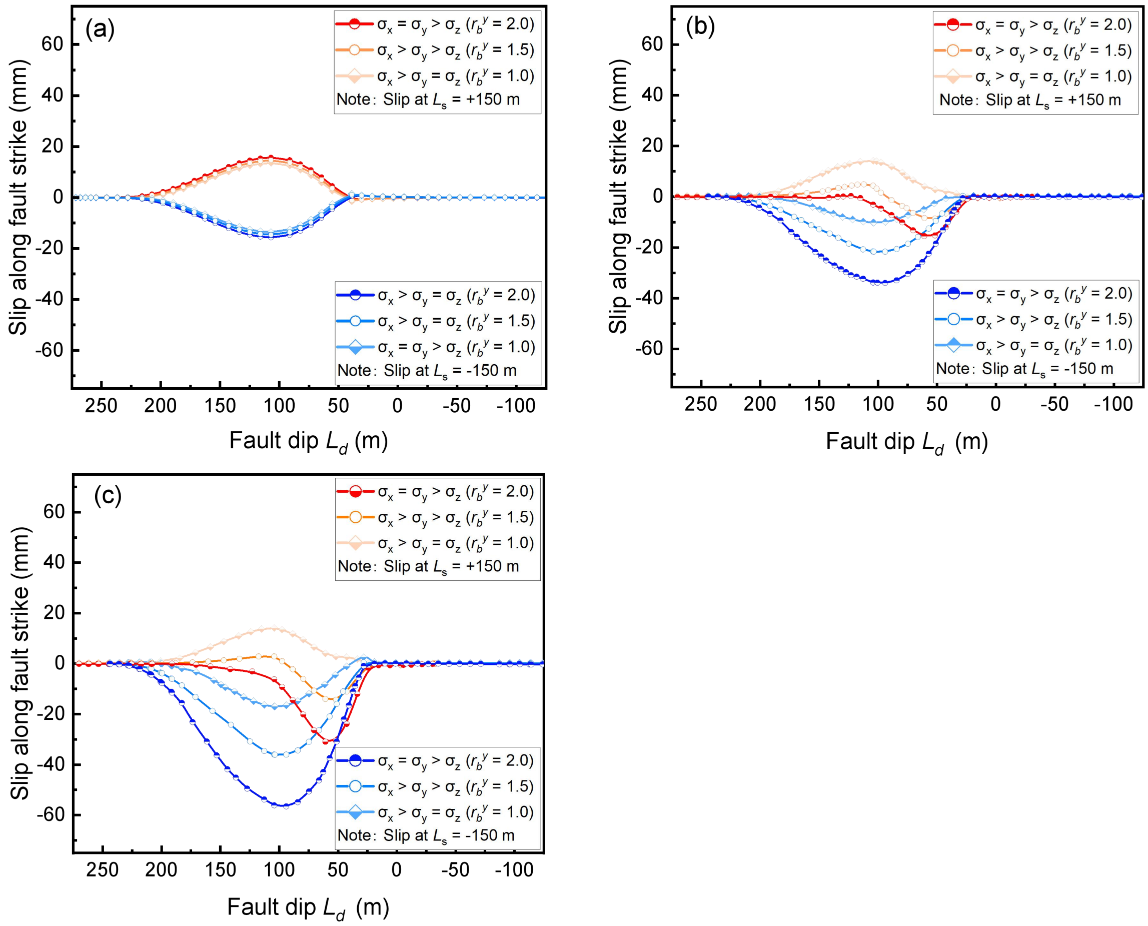

Fig. 3-11 Coseismic slip along the fault strike component with far-field stress rotating counterclockwise around the *z*-axis by (a) 0°; (b) 15°; and (c) 30°, with intermediate far-field stress r_b^y values of 1.0, 1.5, and 2.0, W_m = 200 m, and D_m = -30 m.

3.3.2 Effect of panel length W_m on mining-induced fault slip

I investigated the influence of W_m on fault reactivation using a 3-D model with W_m of 200 to 500 m. The optimization of W_m plays a crucial role in maximizing mining strategies and ensuring the overall stability of mining operations.

(1) Slip length and slip displacement under different W_m

Fig. 3-12 shows the spatial distributions of fault slip for W_m between 200 and 500 m in every 100 m in the case of D_m = -30 m and μ_s = 0.7. From Figs. 3-12a-d, I see a correlation between the width of the slip zone along the fault strike direction and W_m.

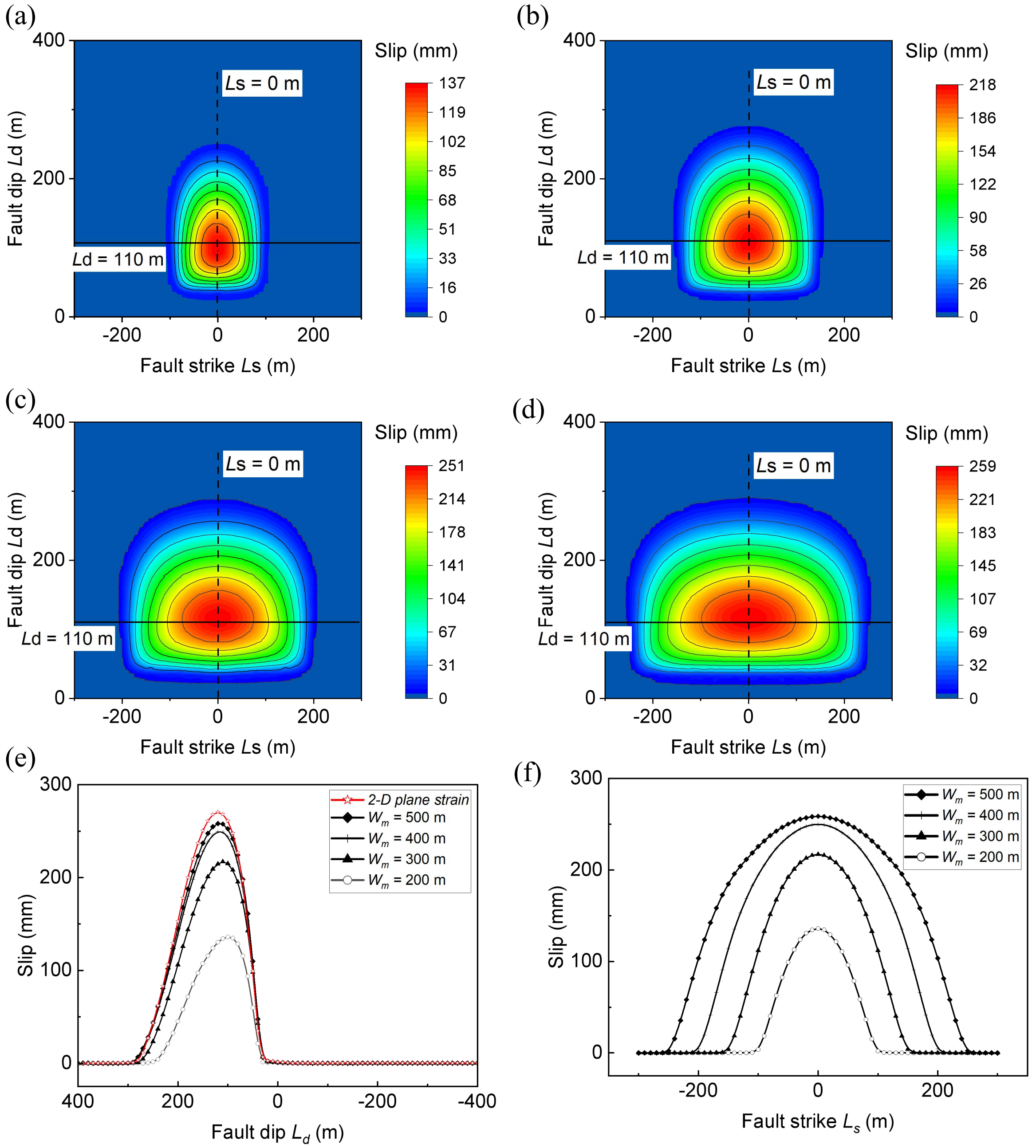

Fig. 3-12 The distribution of fault slip investigated under the influence of varying panel lengths, ranging from W_m = 200 m to W_m = 500 m at intervals of 100 m with D_m = -30 m and μ_s = 0.7. (a) Fault slip distribution for a panel length of W_m = 200 m; (b) for W_m = 300 m; (c) for W_m = 400 m; and (d) for W_m = 500 m; (e) Fault slip curves at L_s = 0 m along the fault dip direction; (f) Fault slip curves at L_d = 110 m along the fault strike direction.

I examined the fault slip distribution along the fault dip at $L_s = 0$ m for various W_m in Fig. 3-12e. I observed a relationship between W_m and maximum fault slip. Large W_m led to an enlarged slip area with a large maximum slip. This was also confirmed by the fault slip curves along the fault strike direction shown in Fig. 3-12f.

(2) Relation between W_m and fault reactivation area

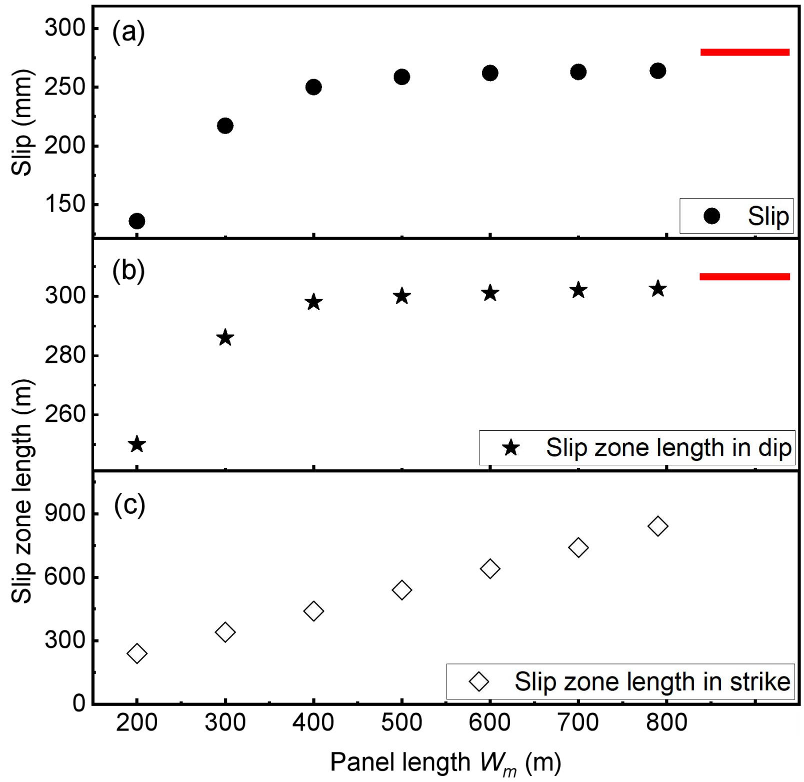

Fig. 3-13 Correlations of W_m with (a) maximum slip; (b) Slip zone length in dip-direction and (c) strike-direction. The red bars represent the 2-D plane strain result from Li et al. (2024a).

I analyzed the relationship between W_m and fault reactivation area, aiming to elucidate the influence of W_m on the extent of fault reactivation. I found that an increase in W_m (Fig. 3-13) led to a proportional elongation of the fault along the slip direction, and the elongation of the fault in the dip direction exhibited a decreasing trend as W_m increased. The red curve in Fig. 3-12e is the slip distribution for the 2-D modeling (Li et al. 2024a). This 2-D result is considered as the maximum slip when W_m is infinite. This allowed me to confidently conclude that the maximum slip zone width along the fault strike under these conditions was 270 m.

(3) Mining-induced fault slip under various panel orientations

In this section, I investigated how the orientation of mining panels relative to the fault strike influences coseismic slip along the fault plane. Specifically, I focused on the effects of the mining face direction with respect to the fault strike when the maximum principal stress direction is perpendicular to the fault (i.e., $\alpha = 0°$).

The panel with W_m = 400 m located at D_m = -30 m is considered here. I considered the effect of panel direction on fault slip, with the counterclockwise panel direction angle (θ) from 0° to 90° at a step of 15°. The rotation center is located at D_m = -30 m and L_s = -200 m. When a working face is parallel to the fault strike, θ = 0°. In this case, the working face extends along y = -200 ~ 200 m. When working face is perpendicular to the fault, θ = 90°, and working face spans y = -300 ~ -100 m. This range was chosen to cover a broad spectrum of possible orientations of the mining panel relative to the fault. The intermediate far-field stress value (r_b^y) was set at 1.5, keeping other parameters fixed at W_m = 400 m, D_m = -30 m, and α = 0°.

Fig. 3-14 provided a representation of the variations in fault slip patterns and intensity under different panel rotation angles. It illustrates how the panel orientation affects the fault slip. As the panel rotates, I can observe the changes in the zone and magnitude of coseismic slip along the fault plane. Initially, at θ = 0°, the maximum slip was 251.2 mm, then it decreased to approximately 97.5 mm at θ = 45°. Upon further increase of θ toward 90°, maximum slip moderately increases again to 145.7 mm. The fault slip area was observed to be 96,000 m^2 at 0°, gradually decreasing to 56,000 m^2 with the angle reaching 90°. Furthermore, the average slip was 150.6 mm at θ = 0°, progressively decreasing to around 40.8 mm as θ approaching to 90°. These results suggested that panel rotation influences the pattern and slip area of fault slip. For instance, in the orange shaded area (θ＜30°), there was a noticeable concentration of slip along specific sections of the fault, which areas considered to increase seismic risk (Fig. 3-14).

The smallest average slip and slip area occurred when the panel was perpendicular to the fault strike, which suggests operational safety and decreases the probability of mining-induced seismic events. Utilizing the effect of panel rotation on fault coseismic slip obtained in this study allows for mining plans with low fault slip levels.

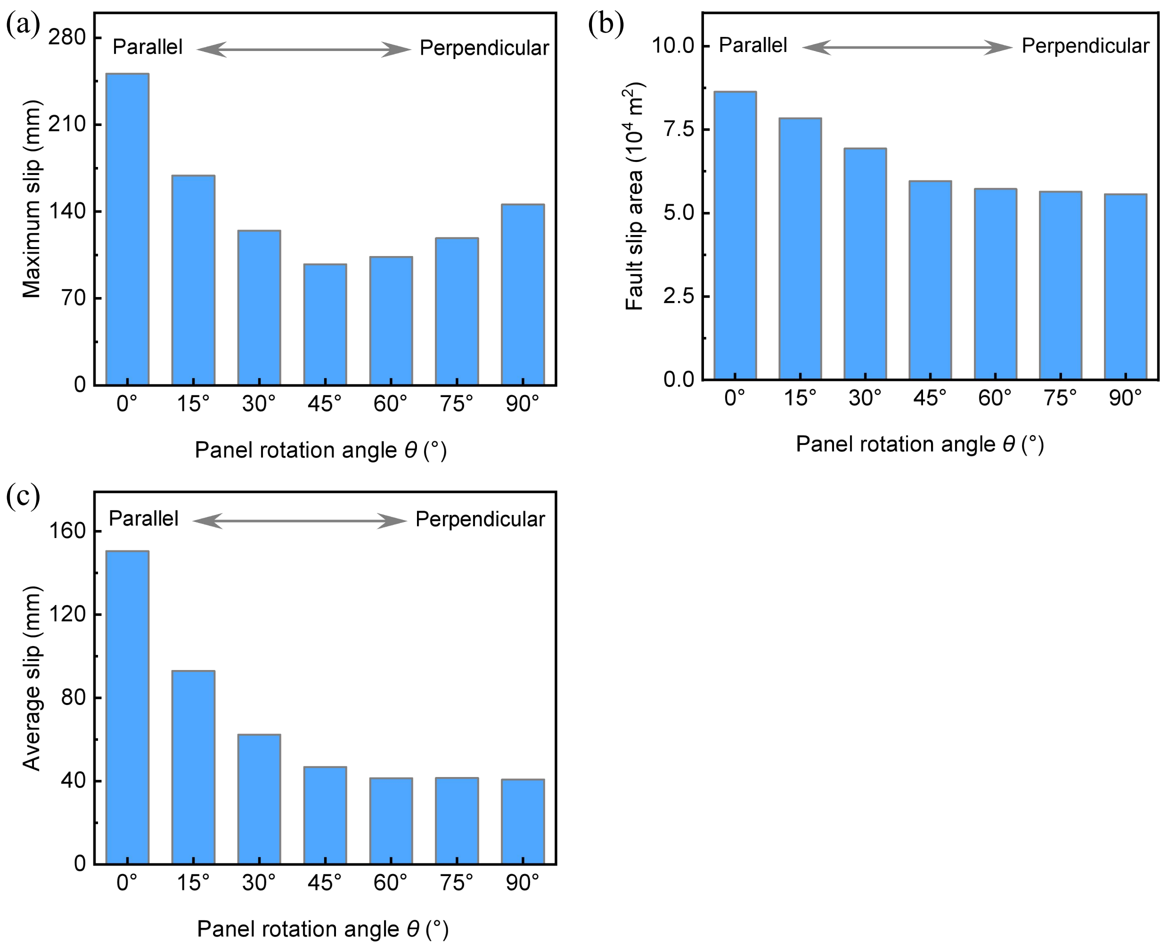

Fig. 3-14 Fault coseismic slip, as the panel rotates counterclockwise along the fault strike from 0° to 90°, with increments of 15°, under conditions of r_b^y =1.5, W_m = 400 m, and D_m = -30 m. (a) Maximum slip; (b) Fault slip area; (c) Average slip.

3.4 Application to the induced earthquake at Yuejin coal mine

The 25110 working face, located in Yuejin Coal Mine, China, was selected for investigation due to its susceptibility to fault slip induced rock bursts, which pose significant safety risks in underground coal mining operations. According to Li et al. (2014), the coal seam at the 25110 working face varies in thickness from 8.4 to 13.2 m, with a depth of 950 to 1000 m. The mining area is characterized by complex geological features, with the F16 reverse fault significantly influencing the stress distribution within the mining region (Liu et al. 2019). Seismic systems installed for monitoring seismic activity have effectively captured the spatial locations of rock burst events. The inclination of the F16 reverse fault at the mining site ranges from 28° to 35° (Cao et al. 2023).

As the mining activities approached the fault area, roof strata fractured simultaneously, leading to an increase in static stresses within the surrounding rocks. The burst was induced by the interaction between the fault slip and surrounding rocks. Although the static stress within the surrounding rocks had not independently reached a critical level, the combined effect with the F16 fault slip triggered the rock burst. A relatively large induced earthquake (M_L = 2.7) occurred close to the 25110 working face on August 11, 2010 (Fig. 3-15, Li et al. 2014). This event, triggered by the sudden reactivation of the F16 reverse fault, caused widespread seismic activity and damaged 363 m of the gateway (Figs. 9 and 10 in Li et al. (2014)), leading to disruptions in the mining environment (Li et al. 2018; Jiao et al. 2021a).

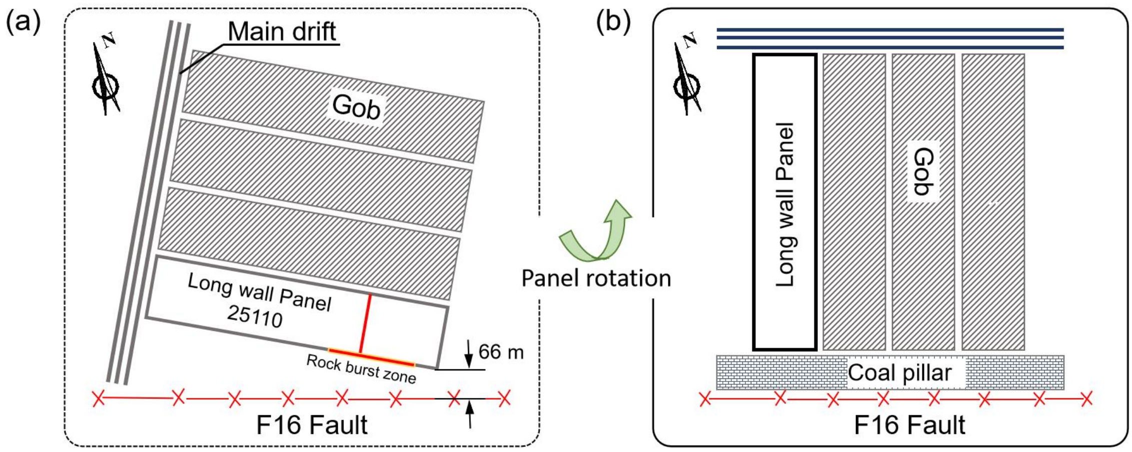

Fig. 3-15 Schematic diagram of direction adjustment layout of the panels. (a) Layout of mining panels and rock burst events at Yuejin Coal Mine; (b) Reconfiguring panel layout: from nearly parallel to perpendicular to the fault strike. The orange and red lines in Longwall panel 25110 in (a) show the rock burst event and the corresponding mining line at the time of the incident, respectively. This figure is drawn based on Li et al. (2014) and Cai et al. (2021).

I conducted a quantitative investigation into the fault coseismic slip, with a focus on the simplified F16 fault. I investigated the distribution of fault slip caused by various conditions, including changes in panel length, panel orientation, far-field stress direction, and the magnitude of intermediate principal stress. My numerical simulation, derived from a simplified model that incorporates both regional panel characteristics and fault properties, provided insights into the magnitude range of mining-induced earthquakes.

In this study, I quantitatively examined that with increasing panel length, fault slip progressively expands along the fault dip direction, eventually approaching the numerical solution for a 2-D plane strain model (Li et al. 2024a). The slip distribution along the fault strike exhibits a positive linear correlation with panel length (Fig. 3-13). This observation aligned with the induced earthquake event depicted in Fig. 3-15. Mining operations were conducted for θ = 15° and α = 8° and the seismic event occurred after the panel length reached approximately W_m = 120 m (Cai et al. 2015, Li et al. 2018). Integrating this with the results from Fig. 3-13 concerning panel length and Fig. 3-14 concerning panel rotation, I estimated the magnitude at W_m = 120 m had M_L ranging between 2.8 and 2.9. This magnitude closely corresponds to the seismic event observed in August 2011 at the same location.

3.5 Discussion

3.5.1 Estimation of seismic moments

Fig. 3-13 presented the slip distribution beneath the mining level on the fault, with W_m varying from 200 to 800 m at 100 m intervals, for the case of r_b = 2 and μ_s = 0.7. As W_m increased, both the length of the slip zone and maximum slip increased.

I estimated the seismic moment, denoted as M_0, of mining-induced earthquakes with W_m. M_0 is defined as follows (Aki 1967; Kanamori and Anderson 1975):

$$M_0 = GAD \tag{3-13}$$

where G is the shear modulus of the rocks (6.5 GPa in this study, Table 3-1), A is the slip area, and D is the average slip on the fault. The moment magnitude M_w is defined by the following equation (Hanks and Kanamori 1979) for M_0 in units of Nm:

$$M_w = \frac{2}{3}(\log M_0 - 9.1) \quad (3\text{-}14)$$

For the four cases of W_m, M_w was approximately 3 (Table 3-3). The observed local magnitude (M_L 2.7) of the Yuejin coal mine event was more or less the same order as my estimates. This may implicitly suggest that my assumptions made for the modeling were not so different from the actual conditions, although I need to pay attention to the uncertainties in the scales between M_L and M_W, as well as the differences in elastic constants and background stress. These magnitude estimations could be useful in mining operations and the surrounding geological conditions to ensure appropriate safety measures (Song et al. 2022).

Table 3-3 Moment magnitude of four different W_m cases

W_m (m)	Maximum slip (mm)	Average slip (mm)	Fault slip area ($\times 10^4$ m^2)	M_0 ($\times 10^{13}$ N·m)	M_w
200	137	75.1	3.94	1.92	2.79
300	218	121.2	6.21	4.89	3.06
400	251	139.6	8.78	7.97	3.20
500	259	142.9	11.01	10.22	3.27

Foulger et al. (2018) compiled a database for induced earthquakes that occurred worldwide by various origins. I could see in that database that a typical magnitude for coal mining induced earthquake was M3, which is almost the same order as the present study.

3.5.2 Estimation of terminal mining line

It could be useful if my method accurately estimated the terminal mining lines since it is essential to mitigate the risk caused by fault ruptures. For this purpose, I consider a nucleation model based on a linear slip-weakening friction law (Uenishi and Rice 2003). In this nucleation model, nucleation size can be determined. At the beginning, the slip stably grows within the nucleation zone. If the slip zone exceeds the nucleation size, the slip becomes unstable and propagates outside the nucleation zone. Therefore, this nucleation size can be used as the terminal mining line. The slip zone induced by mining activities surpassed the theoretical nucleation radius (r_n) (Galis et al. 2015). The concept of a critical nucleation radius, essential for initiating spontaneous dynamic rupture in a linearly elastic and homogeneous 3-D medium, was first introduced by Day (1982). The formula was as follows:

$$r_n = \frac{7\pi}{24}\frac{G(S+1)D_c}{\tau_0 - \tau_f} \tag{3-19}$$

where D_c represents the slip weakening distance and S denotes the relative fault strength defined as the ratio of the strength excess $(\tau_s - \tau_0)$ to the stress drop $(\tau_0 - \tau_f)$ as defined as follows.

$$S = \frac{\tau_s - \tau_0}{\tau_0 - \tau_f} \tag{3-20}$$

Thus, S could be used to evaluate how close a system is to failure or slip.

Eq. 3-19 offers a comprehensive understanding of the initiation of unstable rupture in 3-D. If D_c is smaller or stress drop is larger, r_n becomes shorter. Based on the shear stress shown in Fig. 3-3b, I estimated the initial shear stress (τ_0) to be 11.8 MPa and the average static fault strength (τ_s) to be approximately 13 MPa. I assumed an average normal stress (σ_n) of 20 MPa from Fig. 3-3a. Considering typical observed values in seismic studies (Abercrombie and Rice 2005), I assumed D_c = 0.03 m and $\mu_s - \mu_d$ = 0.1, leading to r_n = 223.3 m by Eq. 3-19. It was essential to emphasize that precise estimation of D_c and μ_d was critical for practical applications.

Based on the circular nucleation model by Day (1982), Uenishi (2009) expanded this methodology by incorporating an elliptical fault model to address the nucleation zone in 3-D. Uenishi (2009) provided a more detailed formulation of the major (a_c) and miner (b_c) radii of the elliptical nucleation zone in 3-D mode II environments as follows.

$$\begin{cases} a_c = 0.624\dfrac{E(\sqrt{\nu(2-\nu)}) + (1-\nu)K(\sqrt{\nu(2-\nu)})}{(1-\nu)(2-\nu)}\dfrac{G}{W} \\ b_c = (1-\nu)a_c \end{cases} \tag{3-21}$$

where

$$K(k) = \int_0^1 \frac{1}{\sqrt{(1-t^2)(1-k^2t^2)}} dt \tag{3-22}$$

$$E(k) = \int_0^1 \sqrt{\frac{1-k^2t^2}{1-t^2}} dt \tag{3-23}$$

$$W = \frac{D_c}{\tau_s - \tau_f} \tag{3-24}$$

$K(k)$ and $E(k)$ are the complete elliptic integral of the first and second kinds, respectively. a_c and b_c represent the critical lengths of the semi-major and semi-minor axes of the rupture ellipse. W is a constant weakening rate ($W > 0$) as shown in Fig. 2 of Uenishi and Rice (2003) and n is the Poisson ratio.

Uenishi (2009) derived the critical lengths across a wide range of aspect ratios m and v. For the sliding mode, the condition $m \approx 1/(1- v)$ with $v = 0.25$ gives that the critical lengths of the rupture region are $2a_c = 2.589\ G/W$ and $2b_c = 1.951\ G/W$ (Uenishi, 2009). From Eq. 3-10, I calculated the critical distances for the major axis as $a_c = 252.4$ m, and the minor axis as $b_c = 190.2$ m. These values are not different from the value of 223.3 m obtained from Eq. 3-8. The slip area is approximately 37,704.2 m², corresponding to about 96% of the 339,416.1 m^2 in Table 3-3. Through my calculations, the magnitude (M_w) of induced earthquakes at this nucleation zone is estimated to be around 2.8, which is similar to the size of the induced earthquakes occurring at the Yuejin coal mine.

Shan et al. (2023) highlighted the risks of mining activities increased by parallel mining to a fault strike that causes more pronounced rock movement and infrastructure damage based on field monitoring and simple numerical modeling. My study provides further insight into the dynamics of fault slip. As illustrated in Fig. 3-14, I investigated the effect of panel rotation along the fault strike from 0° to 90°, with 15° increments, under conditions of $r_b^y = 1.5$, $W_m = 400$ m, and $D_m = -30$ m. I then obtained that the slip area and average slip could be minimized when the panel orientation was perpendicular to the fault strike. This result, focusing on the changes in fault slip due to panel rotation, further corroborates the observations by Shan et al. (2023) regarding the significant activation of mining-induced faults and suggests that fault perpendicular mining activities may mitigate the extent of fault slip. This will offer a potential strategy to reduce the risks associated with fault reactivation under mining conditions. The increase in shear stress on the fault plane, a critical precursor to coseismic slip, was another concerning factor associated with parallel mining activities (He et al. 2023; Zhang et al. 2023; Ma et al. 2020).

3.5.3 Comparison of fault slip based on 2-D plane strain results

Li et al. (2024a) investigated mining-induced fault coseismic slip using a 2-D plane strain model, concentrating on the impact of mining activities on the stress ratio at faults in reverse fault environments. Their research was pivotal in understanding fault stability, identifying the fault dip angle, and mining distance as critical factors in earthquake induction. They demonstrated a pattern of coseismic slip primarily along the fault dip. They also introduced a method for determining a terminal mining line, crucial for earthquake damage mitigation, by integrating in-situ stress and fault friction coefficient, which underscores the influence of these factors on the evaluation of fault stability.

In the present 3-D analysis, I obtained consistent results along the fault dip direction between those with large W_m under 3-D conditions (Fig. 3-12) and those in 2-D modeling (Li et al. 2024a), affirming the 2-D plane strain hypothesis. The present study expanded to assess the effect of intermediate far-field stress (σ_y) on fault slip behavior under controlled triaxial stress conditions and examined the dependence of W_m on coseismic slip distribution. Further, by addressing issues such as variations in panel length, panel rotation, and both the magnitude and rotation of far-field stresses, I obtained detailed fault slip distribution under various mining environments. This advancement serves to refine predictive models for induced earthquakes and develop strategies for their prevention and damage mitigation.

The present study corroborates the crucial findings from 2-D calculations (Li et al. 2024a) and extends the spatial fault slip distribution into 3-D perspectives. This advancement enriches the discourse on mining-induced fault slip by offering a more comprehensive view. Specifically, I bridge the gap between theoretical models and field observations by comparing my results directly with observational data (Cai et al. 2015; Du et al. 2022).

3.5.4 Limitations and future research

My research has successfully elucidated the impact of panel length, far-field stress, and fault orientations. Nevertheless, I acknowledge the necessity for more encompassing models capable of accurately representing the intricacies of geological formations and fault dynamics (Mo et al. 2020). Further research should incorporate heterogeneous models that reflect the complexity of geological formations more accurately (Xue et al. 2023; Yao et al. 2023; Sainoki et al. 2023).

Future study needs to discuss the influence of fault roughness on the fault friction parameters and rupture preparation process (Barton and Choubey 1977; Fukuyama et al. 2018; Yamashita et al. 2018; Sainoki and Mitri 2014). While such aspects are acknowledged, the distribution of coseismic slip on faults with varying roughness due to mining remains unexplored in depth. Fault roughness may be a critical factor that influences the mechanical behavior of faults, particularly their slip and stability (Zhou et al. 2021; Morad et al. 2022). Investigating how different roughness levels affect fault coseismic slip and stress distribution in mining contexts is an essential area for future research.

3.6 Summary

I conducted a comprehensive investigation of the fault slip in relation to the panel location relative to the fault as well as the parameters W_m and σ_y using a 3–D finite element static modeling. My analyses yielded the following conclusions:

1) Intermediate far-field stress, σ_y, increases coseismic slip on faults adjacent to mining activities, with a direct correlation between the magnitude of σ_y and the extent of the slip. The effect of σ_y on fault slip distribution becomes more pronounced as the orientation between the intermediate principal stress and the fault shifts from parallel to an increased angle.

2) A linear relationship was observed between the width of the mining-induced coseismic slip zone and W_m. As W_m increased, the maximum slip observed in the study approached a limiting value derived from the 2-D plane strain model. This suggests the

applicability of 2-D models for preliminary estimations of slip magnitudes for large W_m cases. It also emphasizes the necessity of 3-D modeling to fully comprehend the complexities of mining-induced fault coseismic slip.

3) My numerical simulations have been validated by observation from the F16 fault in the Yuejin mine, emphasizing the pivotal role that mining-induced fault coseismic slip plays in the dynamics of rockburst mechanisms.

4) Given my findings and the measured L_n, I recommended shifting the panel layout orientation from parallel to perpendicular to the fault strike. This adjustment aims to mitigate induced earthquake responses, reduce the likelihood of fault activation, and bolster the safety and stability of the mining environment.

Chapter 4 3-D numerical modeling of deep mining-induced fault rupture and seismic wave radiation to the working face of Yuejin coal mine

Near fault mining activities often induce complex stress disturbances that can lead to fault–slip rockbursts and seismic wave radiation. This sometimes causes significant hazards for underground operations. Accurate evaluation of possible dynamic fault ruptures under such stress conditions is essential for mining safety. In this study, focusing on the F16 reverse fault in the Yima coal field, I model the static fault slip distribution and dynamic rupture propagation under realistic tectonic stress conditions and layered geological structures using the finite element method. The key parameters I investigated include fault slip distribution, rupture velocity, moment magnitude, and moment rate function. The moment magnitudes were estimated between 2.4 and 2.6, consistent with the local magnitude of 2.7 observed during the "8.11" coal burst accident. The estimated rupture velocities were from 0.9 km/s to 1.7 km/s with the rupture duration between 73 and 76 ms. I also evaluated the maximum peak particle velocity (*PPV*) and maximum peak particle acceleration (PPA) on the roof of mining face. The maximum PPV and *PPA* were 0.39 m/s and 26.6 m/s^2, respectively with dominant frequencies of 6 to 9 Hz and 14 to 20 Hz. These computation results will serve for designing robust, asymmetric support systems capable of withstanding dynamic loads and preventing from resonance induced by seismic waves. This study provides a quantitative framework for assessing mining-induced seismic events and offers practical guidance for enhancing safety protocols in deep mining operations.

4.1 Introduction

The migration of coal mining to deep coal measures has significantly increased the occurrence of mining-induced seismic events. These events are characterized by the sudden and violent release of stored strain energy, which poses substantial risks to both the safety and operational efficiency of mining activities (He et al., 2018; Wang et al., 2023). Such seismic events often lead to hazardous working conditions, damage to underground infrastructure, and disruptions in production. Over 170 coal mines in China have experienced rockbursts as mining extends into deeper layers (Wang et al., 2016). Notable incidents, such as the 2005 Sunjiawan Coal Mine explosion and the 2012 rock burst in Xi'an Coal Mine, emphasize the urgent need to mitigate these risks (Cao et al., 2023a). Similar events have been reported globally, such as at the Rudna Mine in Poland and the Austar Coal Mine in Australia (Hatherly, 2013; Lizurek et al., 2015; Vardar et al., 2018; Kozlowska et al., 2021), underscoring the global importance of managing these hazards effectively.

These rockbursts are often classified into three types: strainburst, pillar burst, and fault–slip rockburst (Hedley, 1992; Askaripour et al., 2022). Among them, fault–slip rockbursts are particularly important as they occur close to the mining activity due to the stress disturbance caused by the mining that modifies the stress field on the fault. And they emit strong seismic waves and generate damages (Li et al., 2019). For instance, in the Longfeng coal mine, 72% of rockbursts were fault-related, with 62% occurring near roadways adjacent to fault zones (Kong et al., 2019, 2023; He et al., 2023). The 2010 "8.11" coal burst in the Yima coal field is another example that highlights the severe damage due to fault–slip rockbursts (Li et al., 2014; Yang et al., 2021; Cao et al., 2023b; Cai et al., 2021). Wang et al. (2020a) emphasized the rapid release of the accumulated strain energy during these violent events. Thus, understanding the mechanisms of fault–slip rockbursts is essential for developing effective mitigation strategies.

Comprehensive monitoring and geological assessments, particularly advances in microseismic technology, are essential for mitigating the risks associated with fault–slip rockbursts and have been instrumental in enhancing the detection of these events (Czarny et al., 2019; He et al., 2017; Lu et al., 2019; Cai et al., 2018, 2019, 2020). In parallel, numerical simulations have provided insights into fault behavior during longwall mining operations (Jiang et al., 2020; Wei et al., 2020). However, many previous studies have focused on static deformations without adequately considering the dynamic effects of fault reactivation and the seismic wave emissions associated with such events (Cai et al., 2021; Wang et al., 2021).

When assessing the hazards of fault–slip rockbursts in engineering fields such as deep mining, it is essential to consider seismic wave propagation (Buijze et al., 2019; Cheng et al., 2019; Cai, 2024; Sainoki et al., 2020; Hildyard, 2002). Even minor disturbances from these waves can trigger pillar rock bursts in rock masses already close to failure (Gibowicz, 2009; Wang et al., 2023). In mining environments, analyzing the impact of peak particle velocity (*PPV*) helps develop damage assessment methods, including those based on plastic strain energy evaluations (Jiang et al., 2020; Gao et al., 2021). Consequently, accurately evaluating seismic parameters such as *PPV* and peak particle acceleration (*PPA*) in fault–slip rockbursts is crucial for designing effective dynamic support systems (Stacey, 2012).

One of the key challenges in the dynamic modeling of fault–slip rockbursts is to accurately estimate the non-uniform stress distribution along faults, especially when the fault is located near the mining operations. Such stress disturbance plays a critical role in evaluating how mining-induced stresses affect fault slip and its impact on mining faces. To address this, I constructed a comprehensive stress field model that includes both tectonic stresses and mining-induced disturbances. This approach allows me to better understand how dynamic ruptures near faults influence mining stability. Based on the underground structural models of the Yuejin coal mine by Cai et al. (2023) and Cao et al. (2023b), I construct a fault rupture model for the estimation of mining-induced seismic motions that affect mining faces. This model incorporates both tectonic and mining-induced stresses to capture the complexity of fault–slip behavior. Based on my previous static fault modeling results (Li et al., 2024a; 2024b), I introduce dynamic rupture analysis to estimate key parameters such as rupture velocity, moment rate function, and rupture duration. This dynamic approach provides deeper insights into fault reactivation and its impacts on coal seam stability, surrounding rock mass, and mining infrastructure. Additionally, I assess critical seismic parameters such as *PPV*, *PPA*, and dominant seismic wave frequencies, enabling me to evaluate the effects of dynamic rupture on mining faces. By integrating these dynamic characteristics with field observations, my modeling approach enhances predictive capabilities and contributes valuable insights into safer mining practices.

4.2 Numerical model and assumptions

4.2.1 Structural model for mining-induced fault rupture and seismic wave radiation

(1) Geological setting of the F16 reverse fault and Yima coal field

The Yima coal mining area in Henan Province, China, covers 110 km^2 and includes five major coal mines: Yangcun, Gengcun, Qianqiu, Yuejin, and Changcun (Wang et al., 2020b). The primary seam, No. 2 coal seam, lies at depths between 29 and 941 m. The unstable F16 thrust fault at the southern boundary poses significant coal burst risk, especially for the nearby Qianqiu and Yuejin mines (Wang et al., 2020b). The F16 fault, an east-west trending compression-shear reverse fault, spans 45 km through several coal mines, including Changcun, Yuejin, Qianqiu, Gengcun, and Yangcun, in the Yima coalfield (Fig. 4-1a). Its dip angle ranges from 75° at shallow depth to between 15° and 35° at deep depth under a high horizontal tectonic stress environment (Cao et al., 2023b; Cai et al., 2021; Jiao et al., 2021). Due to ongoing mining activities, the stress field around the fault is disturbed, which may lead to frequent reactivation of the fault (Fig. 4-1). This will significantly impact mining safety and operations. The Yuejin coal mine primarily targets the No. 2-1 coal seam located at depths between 800 and 1200 m with a thickness of 7.4 to 13.8 m and an inclination angle of 12° (Fig. 4-1b). It provides an ideal case study for investigating mining-induced fault ruptures due to its proximity to the F16 reverse fault. Such configuration of fault and mining face allows me a detailed examination of the interactions between mining activities and fault reactivation. These could be critical to understand the seismic risks in deep mining environments.

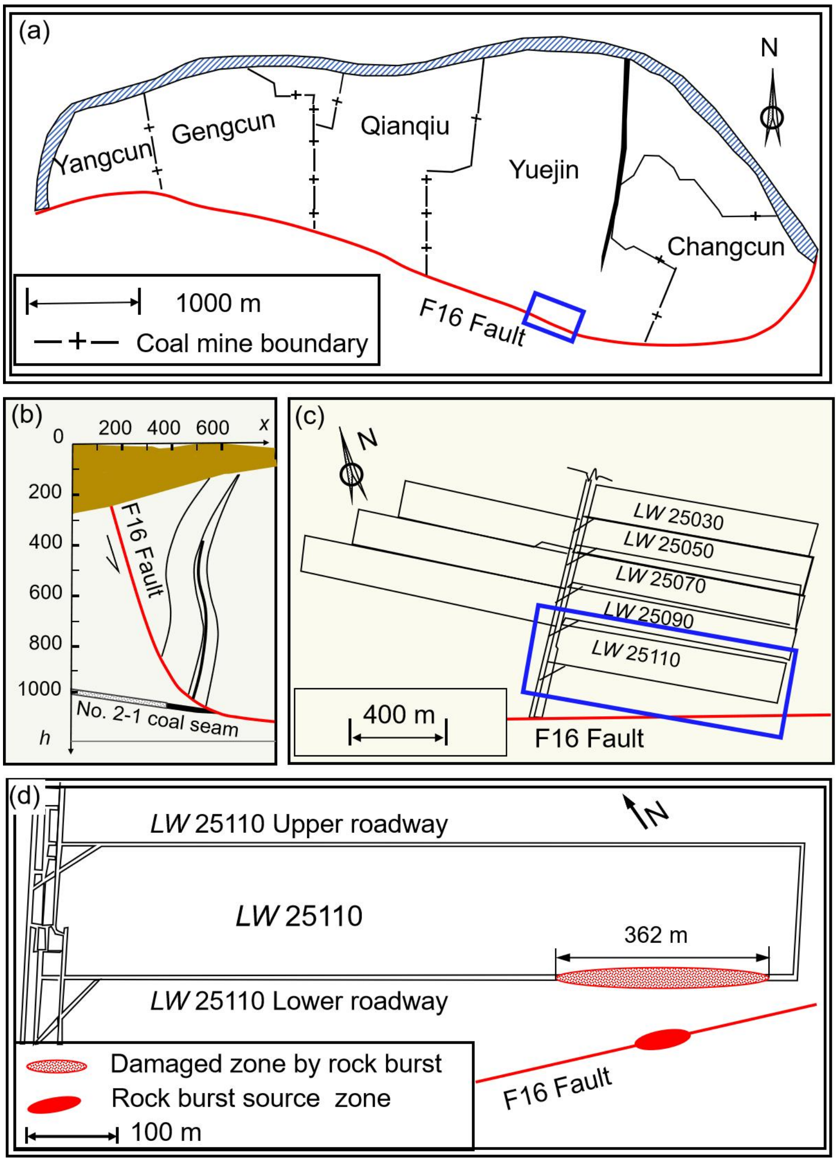

Fig. 4-1 Configuration of the 25110 working face with F16 fault, Yuejin coal mine, China (modified from the figures in Cao et al., 2023; Wang et al., 2019; Cai et al., 2021). (a) Map of the Yima coal field. (b) Geological cross-section of the Yuejin coal mine. (c) Map view of the Yuejin coal mine layout. (d) Map depicting rock burst and fault locations near the LW 25110 area. The blue rectangle in (a) is magnified and shown in (b). Similarly, the blue rectangle in (b) is further magnified and displayed in (c).

(2) Selection and justification of parameters

I focus on the Yima coal field as the target area and reference previous studies that used data from this location. By comparing these data, as shown in Table 4-1 (Du et al. 2022; Wang et al. 2020; Cao et al. 2023; Jiao et al. 2021; Cai et al. 2021), I have found variations in layer properties within the same coal field. These differences arise from variations in the shallow rock layer's properties across different locations and the assumptions made in each study, which contribute to data discrepancies. This further emphasizes the need to consider the heterogeneous stratum effect.

Here, I use the data summarized in Table 4-1, averaging the values for density, Young's modulus, and Poisson's ratio. I then calculate S-wave and P-wave velocities.

Table. 4-1 Summary of parameters in numerical modeling for rockburst in previous studies

Model size (m*m*m)	**Layers**	**Thickness (m)**	***P* (kg/m³)**	***G* (GPa)**	***v***	***E* (GPa)**	**V_s (km/s)**	**V_p (km/s)**	**Reference**
700*1250*250	sandy conglomerate	105.0	2680	8.4	0.16	19.4	1.765	2.779	Du et al. (2022)
	mudstone	25.0	2430	3.4	0.19	8.1	1.185	1.914	
	coal seam	8.5	1350	0.8	0.24	2.0	0.775	1.322	
	sandy mudstone	7.5	2510	5.1	0.21	12.4	1.431	2.364	
	sandstone	104	2720	8.6	0.16	20.1	1.782	2.804	
192*48*192	conglomerate rock	114.96	--	3.7	0.19	8.9	1.182	1.910	Wang et al. (2020)
	mudstone	33.6	--	2.8	0.17	6.6	1.081	1.714	
	coal seam	9.6	--	2.5	0.17	5.9	1.363	2.162	
	siltstone	7.77	--	3.3	0.18	7.8	1.145	1.833	
450*400*140	sandstone 1	74	2650	9.7	0.22	23.7	1.913	3.200	Cao et al. (2023)
	mudstone 1	18	2530	3.9	0.24	9.7	1.242	2.123	
	coal seam	8	1450	1.2	0.23	2.9	0.910	1.531	
	mudstone 2	12	2550	4.2	0.24	10.4	1.283	2.196	
	sandstone 2	40	2650	9.7	0.22	23.7	1.913	3.200	
1150*1198*979	overlying strata	--	2700	7.2	0.23	17.6	1.628	2.749	Jiao et al. (2021)
	hard strata	--	2707	10.5	0.22	25.6	1.970	3.288	
	main roof	--	2807	11.5	0.21	27.9	2.028	3.347	
	immediate roof	--	2173	2.1	0.24	5.1	0.977	1.670	
	coal seam	--	1440	1.4	0.16	3.3	0.994	1.562	
	direct bottom	--	2673	9.1	0.25	22.7	1.841	3.189	
	basic bottom	--	2461	9.1	0.35	24.6	1.925	4.007	
1365*1050*350	conglomerate	Caprock	2600	3.4	0.15	7.8	1.144	1.780	Cai et al. (2021)
	sandy mudstone	4	2600	3.2	0.15	7.4	1.109	1.728	
	coal seam	2	1300	0.8	0.27	2.0	0.784	1.405	
	mudstone	18	2200	1.6	0.18	3.8	0.853	1.371	
	coal seam	11	1300	0.8	0.27	2.0	0.784	1.405	
	mudstone	4	2200	1.6	0.18	3.8	0.853	1.371	
	sandstone	Basement	2700	3.6	0.15	8.3	1.155	1.795	

Note: *G*: Shear modulus; *v*: Poisson's ratio; *E*: Young's modulus; *ρ*: Density. The light green areas represent original data from the cited paper, while the remaining sections show results derived from the corresponding physical formulas. In Wang et al. (2020), the density data for the light blue areas were not provided; hence, I supplemented this with density data from Du et al. (2022) to calculate the other physical quantities.

(3) Selection of structural models

As the target simulation site in this study, I investigated previous research in the Yima coal field (Du et al., 2022; Wang et al., 2020b; Cao et al., 2023b; Jiao et al., 2021; Cai et al., 2021) as summarized in Table 4-1. I reviewed previously reported underground structural models and selected the two (Cao et al., 2023b; Cai et al., 2021) that have similar P- and S-wave structures around the coal mine. These two models are referred to as Model_Cao (Fig. 4-2) and Model_Cai (Fig. 4-3). The parameters used for fault static slip and dynamic rupture analysis in Model_Cao and in Model_Cai are provided in Tables 4-2 and 4-3 and Tables 4-2 and 4-4, respectively.

I analyze the stress and slip of the working face and fault plane under the combined effects of far-field stress and mining-induced stress. To achieve this, I extend these models to the surface rather than using a smaller model, allowing for a more accurate capture of dynamic changes in mining-fault interactions, as illustrated in Figs. 4-2 and 4-3. I establish two groups of planar faults within domains of 1400 × 1000 × 1200 m^3 for Model_Cao (Fig. 4-2) and 1800 × 1000 × 1200 m^3 for Model_Cai (Fig. 4-3).

For simplicity, the layers are named *L1* to *L6* from top to bottom (See Figs. 4-2 and 4-3 and Tables 4-3 and 4-4). In these layered models, *L1* is the surface layer, and *L6* is the deepest layer in the model. In Tables 4-3 and 4-4, properties of each layer, such as density, Young's modulus, and Poisson's ratio, were shown. They were referred from Cai et al. (2021) and Cao et al. (2023b). These layered models allow me to simulate more accurately the impact on fault behavior under the heterogeneous structure in the realistic geological environment.

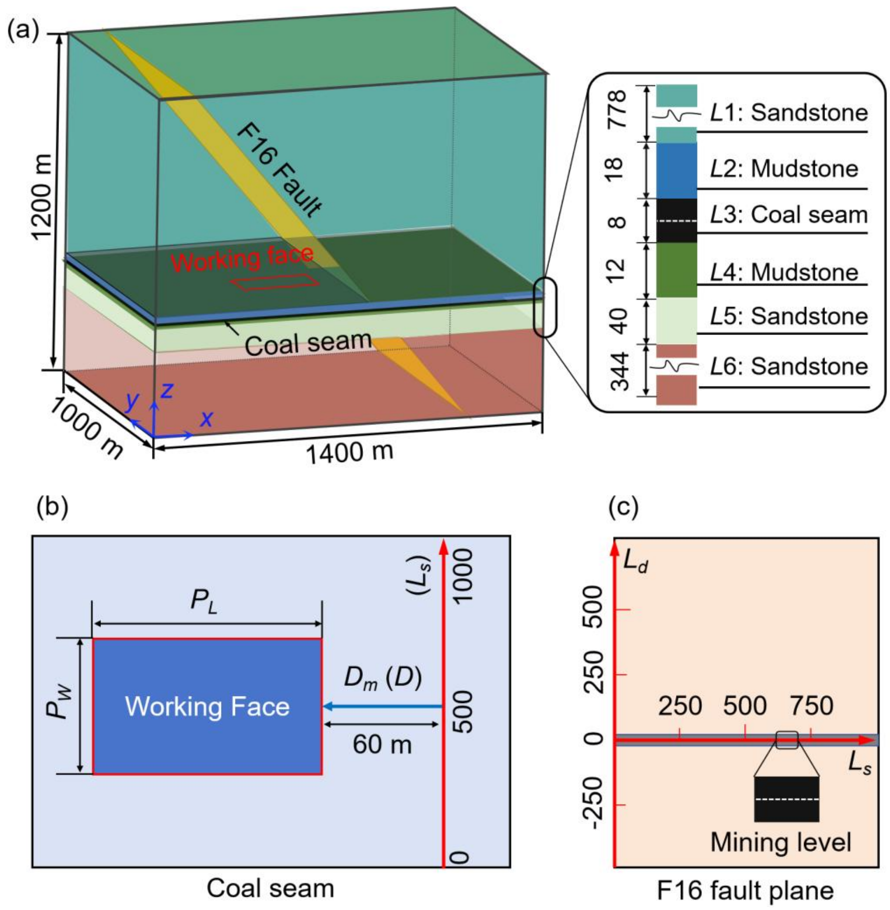

Fig. 4-2 3-D structural model (Model_Cao) based on Cao et al. (2023b). (a) Geometry of the 3-D model simulating mining-induced faulting and earthquake. $L1$-$L6$ represents different geological layers in the 3-D structural model, with $L1$ being the surface layer and $L6$ the deepest layer. (b) Local coordinate system on the working face. P_L is the panel length, P_W is the panel width, D_m is the mining distance, and L_s is the distance along the fault strike direction. (c) Local coordinate system on the fault plane. L_s represents the length along the fault strike direction, starting from the origin at the intersection of the fault plane and the working face, located on the left side at y = 0, and extending horizontally in the positive y-direction. L_d represents the length along the fault dip direction, starting from the same origin and extending upwards, with positive values in the upward direction along the fault plane.

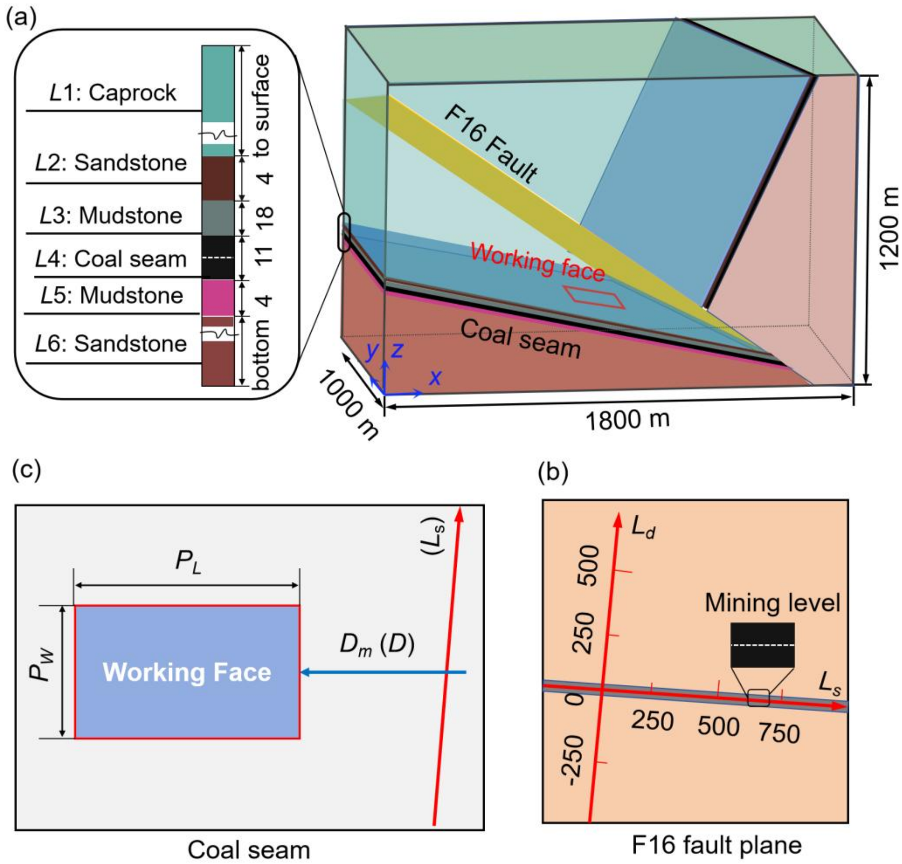

Fig. 4-3 3-D structural model (Model_Cai) based on Cai et al. (2021). (a) Geometry of the 3-D model simulating mining-induced faulting and earthquake. *L1-L6* represents different geological layers in the 3-D structural model, with *L*1 being the surface layer and *L6* the deepest layer. (b) Local coordinate system on the working face. P_L is the panel length, P_W is the panel width, D_m is the mining distance, and L_s is the distance along the fault strike direction. (c) Local coordinate system on the fault plane. L_s represents the length along the fault strike direction, starting from the origin at the intersection of the fault plane and the working face, located on the left side at (x, y, z) = (1400, 200, 200), and extends along the intersection of the fault and coal seam centerline in the positive y-direction. L_d represents the length along the fault dip direction, starting from the same origin and extending upwards, with positive values in the upward direction along the fault plane.

Table 4-2 Parameters used in Model_Cao and Model_Cai for fault static slip and dynamic rupture analysis

Parameters	Model_Cao	Model_Cai
Fault dip angle, φ (°)	50	60
x-component background stress ratio, K_0^x	1.2	1.4
y-component background stress ratio, K_0^y	1.2	1.2
Cohesion stress, C (MPa)	0.3 (0)	0.3 (0)
Dip angle of the coal seam, (°)	0	12
Static friction coefficient, μ	0.268	0.578
Yield friction coefficient, μ_s	0.375	0.628
Residual friction coefficient, μ_d	0.24	0.5
Critical slip distance, D_c (mm)	1	1 (2, 3, 4, 5)
Mining distance, D_m (m)	60 (280~20)	60
Mining level, (m)	800	800-1000
Panel width, P_W (m)	200	200
Panel length, P_L (m)	280	280
Mining thickness, (m)	8	11

Note: The parameters for the mining working face, far-field stress, fault static friction, and dip angle in the table are from Cao et al., (2023b) and Cai et al. (2021). The dynamic friction parameters are assumed data in this study. The values in parentheses are used for parameter study.

Table 4-3 Physical properties of the geological layers of Model_Cao

Layer name	Lithology	Thickness (m)	Young's modulus E (GPa)	Poisson's ratio v	Shear modulus G (GPa)	Density ρ (kg/m^3)	V_s (km/s)	V_p (km/s)
L1	Overlying strata	778	23.7	0.22	9.7	2650	1.913	3.200
L2	Mudstone	18	9.7	0.24	3.9	2530	1.242	2.123
L3	Coal seam	8	2.9	0.23	1.2	1450	0.910	1.531
L4	Mudstone	12	10.4	0.24	4.2	2550	1.283	2.196
L5	Sandstone	40	23.7	0.22	9.7	2650	1.913	3.200
L6	Underlying strata	344	23.7	0.22	9.7	2650	1.913	3.200

Note. The parameters corresponding to actual measurements from the Yuejin coal mine, as reported by Cao et al., (2023b).

Table. 4-4 Physical properties of the geological layers of Model_Cai

Layer Name	Lithology	Thickness (m)	Young's modulus E (GPa)	Poisson's ratio v	Shear modulus G (GPa)	Density ρ (kg/m^3)	V_s (km/s)	V_p (km/s)
L1	Conglomerate	Overburden	7.8	0.15	3.4	2600	1.144	1.780
L2	Sandy mudstone	18	7.4	0.15	3.2	2600	1.109	1.728
L3	Mudstone	18	3.8	0.18	1.6	2200	0.853	1.371
L4	Coal seam	11	2.0	0.27	0.8	1300	0.784	1.405
L5	Mudstone	4	3.8	0.18	1.6	2200	0.853	1.371
L6	Sandstone	Basement	8.3	0.15	3.6	2700	1.155	1.795

Note. The parameters corresponding to actual measurements from the Yuejin coal mine, as reported by Cai et al. (2021).

4.2.2 Stress field and modeling procedure

(1) Background stress field and boundary conditions

The governing equation for static modeling is expressed as the equation of equilibrium below.

$$\sigma_{ij,j} + f_i = 0 \tag{4-1}$$

where $\sigma_{ij,j}$ represents the spatial derivative of the stress tensor and compressional stress is taken as positive. Here, i and j are indices referring to the spatial directions x, y, and z. Comma in $\sigma_{ij,j}$ stands for spatial derivatives. f_i is the i-component body force per unit volume.

To define the initial conditions in the static modeling, I introduce the background stress σ_i, which represents the far-field principal stresses in the x, y, and z directions (i.e., σ_x, σ_y, and σ_z). $\sigma_z\,(x, y, z)$, which is self-gravity and represents the stress condition along the z-axis.

$$\sigma_z(x,y,z) \;=\; g\int_{h_0}^{z} \rho(x,y,h)\,dh \tag{4-2}$$

where the depth h is given by h = 1200-z in meters. g is the gravitational acceleration.

$\sigma_z\,(x, y, z)$ serves as a reference for comparing the stress conditions along the x- and y-axes. More specifically, the following stress boundary conditions are introduced:

$$\begin{cases} \sigma_x(x,y,z) = K_0^x \sigma_z(x,y,z) \\ \sigma_y(x,y,z) = K_0^y \sigma_z(x,y,z) \end{cases} \tag{4-3}$$

where K_0^i is the i-component background stress ratio, and i takes either x or y. $\rho\,(x, y, z)$, as shown in Table 4-3, is the position-dependent density. In addition, I fixed the location of the origin through the computation, i.e., $\mathbf{U}(0,0,0) = 0$, where $\mathbf{U}(x,y,z)$ is the displacement at the point (x, y, z). The origin is set at the left bottom front corner, as shown in Fig. 4-2a. The full stress tensor σ_{ij} characterizes the complete stress state at each point, which arises from the background stress σ_i and the additional stresses induced by the mining.

I utilize depth-dependent initial stresses that satisfy the governing equations in my simulation. Based on these conditions, I specify the Dirichlet boundary conditions for the left (x = 0), bottom (z = 0), and front (y = 0) faces, constraining the degrees of freedom in the x, y, and z directions, respectively. During the dynamic rupture modeling process, all boundaries are treated as absorbing boundaries except for the ground surface and working face. I used the absorbing boundary condition to simulate an infinite domain without reflecting back into the simulation area (Aagaard et al., 2023). On the ground surface and working face, I applied free surface boundary conditions.

(2) Slip criterion for static modeling

I use the Mohr-Coulomb criterion as the friction condition for the static simulations. To express the Mohr-Coulomb criterion for a fault plane under a state of principal stresses, I need to calculate the normal stress and shear stress on the fault plane. Given the principal stresses σ_1, σ_2, and σ_3 ($\sigma_1 > \sigma_2 > \sigma_3$), I can derive the following criterion (Jaeger et al., 2009):

$$\tau = \mu\sigma_n + C$$

$$\text{where} \quad \begin{aligned} \tau &= \frac{\sigma_1 - \sigma_3}{2} sin(2\alpha) \\ \sigma_n &= \frac{\sigma_1 + \sigma_3}{2} + \frac{\sigma_1 - \sigma_3}{2} cos(2\alpha) \end{aligned} \tag{4-4}$$

and τ is the shear stress, σ_n is the normal stress on a fault plane, μ is the static friction coefficient (Table 4-2). C is the cohesion, and α is the angle between the fault normal vector and the direction of the maximum principal stress σ_1 (Fig. 4-4). Here, I assume the Wallace-Bott hypothesis, which states that the slip direction aligns with the direction of maximum stress (Bott, 1959).

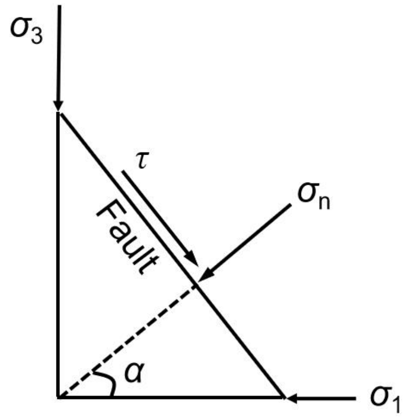

Fig. 4-4 Plane of weakness with outward normal vector oriented at angle α to the direction of σ_1.

(3) Friction law for dynamic rupture modeling

In this study, a spontaneous rupture is modeled using a linear slip-weakening friction law (Ida, 1972). The linear slip-weakening friction model generates shear traction that consists of cohesive stress and an additional component proportional to the fault normal traction (Fig. 4-5). Shear traction decreases from a static value to a dynamic value as slip increases, as represented in Eq. 4-5.

$$\tau = \begin{cases} (\mu_s - (\mu_s - \mu_d)\dfrac{d}{D_c})\sigma_n + C & d \le D_c \; and \; \sigma_n \ge 0 \\ \mu_d \sigma_n + C & d > D_c \; and \; \sigma_n \ge 0 \\ 0 & \sigma_n < 0 \end{cases} \tag{4-5}$$

where μ_s and μ_d denote the yield and residual friction coefficients, respectively, D_c is the critical slip distance, and d is the slip (Table 4-2). D_c, assumed to be between 1 mm and 5 mm, was selected in this study, aligning with those used in previous studies that explored similar fault rupture dynamics in mining environments (Sainoki and Mitri, 2015; Buijze et al., 2019; Wei et al., 2020).

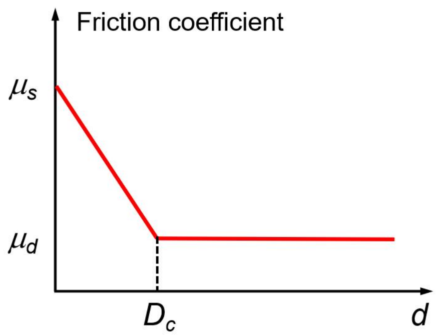

Fig. 4-5 Conceptual diagram of the slip-weakening friction model: μ_s and μ_d represent yield and residual friction coefficients, D_c indicates critical slip distance.

(4) Nucleation procedure in dynamic rupture modeling

To nucleate a dynamic rupture, I take the following procedure. First, I construct the initial stress distribution on the fault based on the background stress with the disturbance from mining activity. Since the nucleation zone is defined as the critical area that change the rupture mode from stable sliding to unstable slip (Andrews, 1976; Uenishi and Rice, 2003; Ampuero and Rubin, 2008). Therefore, I assume here that just before the initiation of dynamic rupture propagation, a tiny preslip occurs quasi-statically to form the nucleation zone. Preslip distribution is computed by static modeling with an appropriate value of μ_s. This μ_s value is determined to fit the preslip area to the nucleation zone size. Then, inside the nucleation zone, initial stress raised a tiny amount to satisfy the slip condition in the slip weakening law to make the rupture initiate. The detailed procedures are explained as follows.

Here I consider the case when D_m is 60 m to reproduce the "8.11" coal burst in the Yuejin coal mine (Cao et al., 2023b). Then, I compute the static slip distribution assuming several tentative μ values. I then measure the slip zone size for each μ value. It should be noted that I consider the μ value which generates the slip zone close to the nucleation zone is considered as μ_s in the dynamic rupture simulations.

I then compare the slip zone size with the nucleation radius (R_{nuc}). R_{nuc} is defined by Eq. 4-6 as follows (see Eqs. 24 and 25 in Galis et al., 2015).

$$R_{nuc} = \frac{\pi}{4}\frac{1}{f_{min}^2}\frac{\tau_s - \tau_d}{(\tau_0 - \tau_d)^2} GD_c$$

where (4-6)

$$f_{min} = \min_x \sqrt{x}\left[1 + \frac{\tau_0^i - \tau_0}{\tau_0 - \tau_d}\left(1 - \sqrt{1 - 1/x^2}\right)\right]$$

and τ_s and τ_d are yield and residual shear strength that correspond to $\mu_s\sigma_n$ and $\mu_d\sigma_n$ in the slip weakening friction law, respectively. τ_0 is the initial shear stress, G is the shear modulus, and D_c is the critical slip distance. τ_0^i is the initial shear stress inside the nucleation zone. Galis et al. (2015) suggested that f_{min} can be evaluated numerically. While Galis et al. (2015) assumed rather uniform stress field, the stress distribution is heterogeneous in the present case. Thus, the term $\frac{\tau_0^i - \tau_0}{\tau_0 - \tau_d}$ is difficult to evaluate. Here, I assume that $\frac{\tau_0^i - \tau_0}{\tau_0 - \tau_d} = 0.1$ considering the average stress field around the nucleation zone. Under this assumption, f_{min} becomes approximately 1.047 at x = 1.01. Based on this result, I select μ_s = 0.375 for Model_Cao and 0.628 for Model_Cai, and estimate $\frac{\tau_s - \tau_d}{(\tau_0 - \tau_d)^2}$ to be approximately 4×10^{-6} and 1.7×10^{-5} respectively. With D_c assumed to be 1 mm and G values taken from Tables 4-3 and 4-4, I calculate the nucleation radius R_{nuc} as 19.8 m for Model_Cao and 40.2 m for Model_Cai.

To fit the nucleation zone to R_{nuc} estimated by Eq. 4-6, I made several trials and found that static slip zone area is very close to that for R_{nuc} when μ_s = 0.375 (Fig. 4-6). I then modify τ within the nucleation zone by increasing 0.5% of the original value, keeping σ_n constant. This stress increase is to initiate dynamic rupture from the nucleation zone. Fig. 4-6 shows the initial stress distribution I use for the further numerical simulations. Once this initial stress state is established, I apply the linear slip weakening law (Eq. 4-5) as a boundary condition on the fault to compute dynamic rupture propagation. At time t = 0, slip initiates inside the nucleation zone and begins to propagate outward.

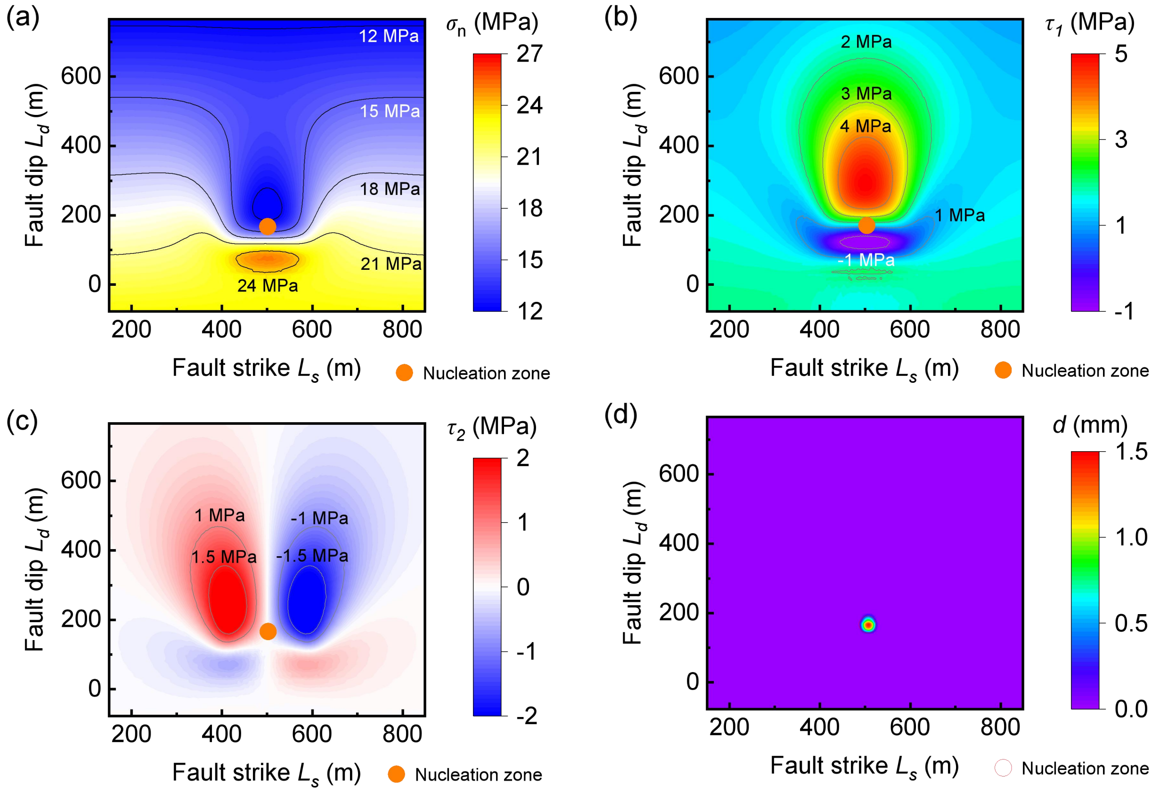

Fig. 4-6 Initial stress distribution for dynamic rupture calculation in Model_Cao, with D_m = 60 m, and μ_s = 0.375. (a) σ_n distribution, (b) Shear stress, τ_1, distribution along dip direction (L_d), (c) Shear stress, τ_2, distribution along strike direction (L_s). (d) Static slip with μ_s = 0.375. The orange circular region in the figure represents the designated nucleation zone, calculated based on Eq. 4-6.

4.2.3 Definitions of parameters estimated from dynamic rupture propagation

I estimate the seismic moment (M_0) of the mining-induced faulting. M_0 is defined as follows (Aki, 1967; Kanamori and Anderson, 1975),

$$M_0 = GA_sD_s \tag{4-7}$$

where G represents the shear modulus (Tables 4-3 and 4-4), A_s is the final slip area, and D_s is the averaged d at the termination of slip. I then calculate the moment magnitude (M_w) using the following formula (Hanks and Kanamori, 1979):

$$M_w = \frac{2}{3}(\log M_0 - 9.1) \tag{4-8}$$

where the unit of M_0 is newton-meters.

I also consider the moment rate function ($\dot{m}$) which can be computed using the following equation.

$$\dot{m}(i\Delta\tau) = \frac{G}{\Delta t}\{(A(i\Delta\tau)D(i\Delta\tau) - A((i-1)\Delta\tau)D((i-1)\Delta\tau)\} \tag{4-9}$$

where $\Delta\tau$ is the time interval of discrete time steps and I applied $\Delta\tau$ =1 ms. $A(t)$ is the slipped area at time t, and $D(t)$is the averaged slip at time t. The moment rate function is the time derivative of seismic moment evolution on the fault. It includes the duration of seismic slip and strength of seismic wave radiation. By using the moment rate function, I can roughly estimate the predominant frequency of seismic waves that emitted from the fault. This function provides key insights on the characteristic feature of near fault motions.

To further investigate the rupture characteristics, I consider rupture velocity ($V_{rupture}$), which represents the propagation speed of the rupture front along the fault. In my simulations, $V_{rupture}$ is measured by tracking the movement of the rupture front over time. The rupture front is defined as the location on the fault where the slip, d, exceeds a threshold of 10^{-3} mm for the first time.

To accurately calculate the $V_{rupture}$, both the initiation point and the termination point of the rupture front must be identified. The initiation point is where d first reaches the 10^{-3} mm threshold, marking the start of the rupture, while the termination point is where the rupture stops progressing and falls below this threshold. By identifying these points, I can track the spatial progression of the rupture along both the strike and dip directions. I record the position of the rupture front throughout the simulation, providing a detailed time history of the rupture movement across the fault. $V_{rupture}$ is then calculated by measuring the distance traveled by the rupture front between the initiation and termination points over successive time steps.

Peak slip rate (V_s^{max}) measures the maximum rate at which slip occurs at various locations along the fault during the rupture, particularly in areas where the fault experiences the most intense slip, such as near the rupture initiation point or other high-stress regions.

The total rupture duration ($T_{rupture}$) is defined as the time from the initiation of the rupture to when the slip distribution stops changing and reaches its final state. Since the slip-weakening law allows for continued slip with minimal values, a threshold is used to determine the termination of the slip. In this study, I define the termination of the rupture as the point when the slip rate falls below a small, pre-defined threshold of 0.0001 m/s. This threshold ensures that I capture the substantial slip during the rupture while excluding negligible post-rupture slip that may continue at very low rates.

4.2.4 Simulation scheme using PyLith

In this study, I utilize a finite element open-source software PyLith 4.00 (Aagaard et al., 2023), which can handle crustal deformations in various scales. PyLith can handle both static and dynamic earthquake faultings. This software has been validated by Aagaard et al. (2013, 2023a). In this study, I utilize PyLith to conduct both static and dynamic simulations to ensure consistency and accuracy in modeling.

To achieve accurate spatial and temporal resolution near the rupture tips, the average diameter of the elements (Δx) is set at 0.5 m. Following the numerical stability conditions (Eq. 4-10) (Palmer and Rice, 1973; Day et al, 2005), Δx is taken as smaller than the one-thirds of the static cohesive zone length (Λ_0) as shown in Fig. 4-7a:

$$\begin{gathered}\Delta x \leq \frac{1}{3}\Lambda_0 \\ \text{where } \Lambda_0 = \frac{9\pi}{32}\frac{G}{1-\nu}\frac{D_c}{\tau_s-\tau_d}\end{gathered} \tag{4-10}$$

The time step (Δt) is set at 0.0001 s, complying with the Courant-Friedrichs-Lewy (CFL) condition, to ensure $CFL < 0.71$, as shown in Eq. 4-11 (Courant et al., 1928). The time step in my current models, as shown in Fig. 4-7b, also satisfies the stability condition.

$$CFL = V_p\frac{\Delta t}{\Delta x} < 0.71 \tag{4-11}$$

For mesh generation, I employ Gmsh (Geuzaine and Remacle, 2009) as the pre-processor to construct a detailed mesh model. These models contain 190,945,851

(Model_Cao) and 194,078,556 (Model_Cai) tetrahedron elements, with 32,851,546 (Model_Cao) and 32,962,729 (Model_Cai) nodes positioned at each vertex. The dimension of the elements along the fault is maintained at 0.5 m. I use the same mesh models for both static and dynamic modeling to maintain consistency between dynamic and static modeling.

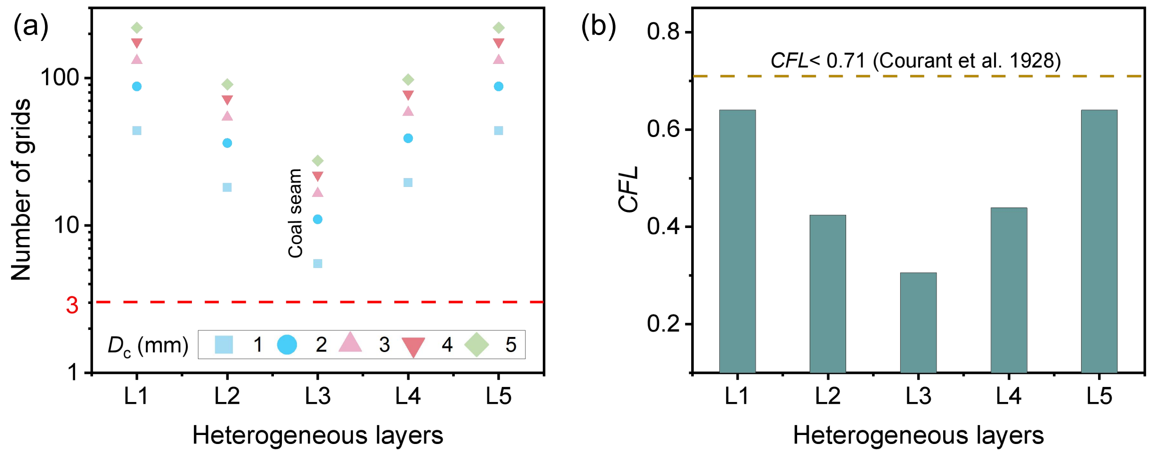

Fig. 4-7 Mesh size and time step setting. (a) Number of grids inside the cohesive zone under different layers and critical slip distance D_c. The heterogeneous layers are denoted as L1 to L5. (b) Time step setting according to the Courant-Friedrichs-Lewy (*CFL*) condition. *CFL* values are less than 0.71. As the results for L5 and L6 are identical, only the results up to L5 are displayed.

4.3 Simulation results

4.3.1 Mining-induced static faulting

(1) Static analysis results

I show the results of static analysis for Model_Cao in Fig. 4-8. The distributions of d, σ_n, and τ on the fault are shown for the case of D_m = 60 m, P_L = 280 m, P_W = 200 m and μ = 0.268. I first compute the stress field before the slip by increasing the friction coefficient to infinity, which is numerically set to 100. In Fig. 4-8a, the σ_n distribution on the fault is shown, which represents the background stress defined by Eqs. 4-2 and 4-3 plus the stress disturbance caused by mining face (P_L = 280 m, P_W = 200 m) located at D_m

= 60 m. I can observe a low σ_n area between L_s = 350 and 650 m and L_d = 100 and 200 m. Such a low σ_n area could be caused by the effect of mining face since the background stress (σ_i) is rather uniform. Although the reduction in σ_n is tiny, it is critical for fault stability since decreased σ_n can lead to increase in the stress ratio τ/σ_n. The increase in τ is observed between L_s = 350 and 650 m and L_d = 0 and 50 m. This is also the stress disturbance by the mining face but this increase stabilizes the faulting since the stress ratio τ/σ_n increases. Fig. 4-8b shows the distribution of τ on the fault plane for the case of infinite μ. The high τ concentration areas ranging from 1.5 MPa to 4.6 MPa is observed at between L_s = 350 and 650 m and between L_d = 100 and 350 m. High τ region has a potential to the faulting.

I then compute the static deformation with μ = 0.268 on the fault. I confirmed that the σ_n distribution is identical to the infinite μ case (Fig. 4-8a). In contrast, the distribution of τ is slightly different from the infinite μ case as shown in Fig. 4-8c. The slip zone corresponds to the high τ area observed in Figs. 4-8d. As well known for the planar fault, only shear stress changes when slip occurred (Fukuyama and Madariaga, 1995; Tada et al., 2000; Romanet et al., 2020). Stress drop is calculated as the difference between shear stress before and after the slip, as shown in Fig. 4-8b and Fig. 4-8c, with the distribution depicted in Fig. 6e. In Fig. 6f, I can see that the stress drop occurs in the fault slip zone, with the highest stress drop at the center of the slip zone (about 1.5 MPa at L_d = 158 m and L_s = 500 m).

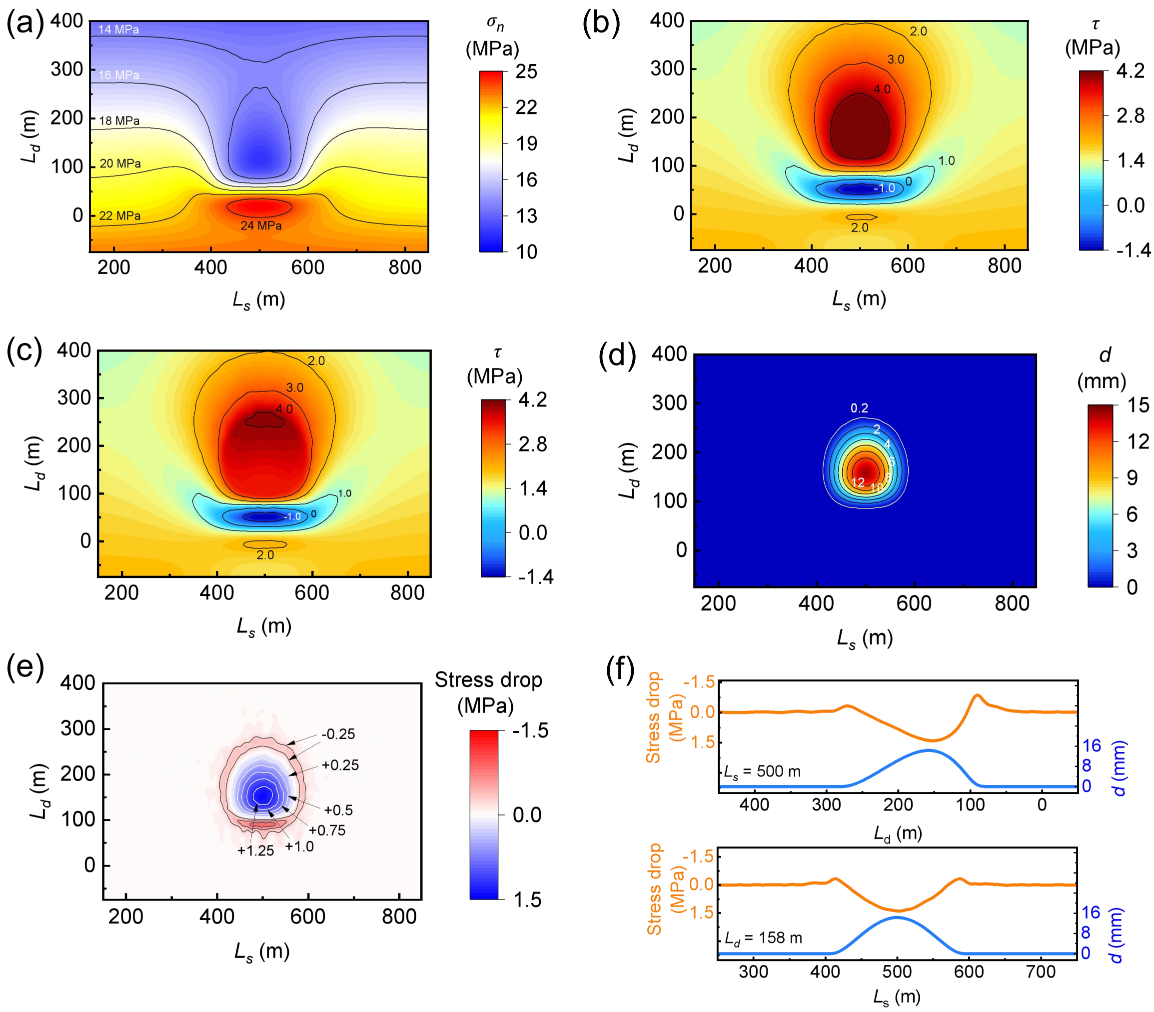

Fig. 4-8 Slip distribution and stress analysis on the fault plane with D_m = 60 m, P_L = 280 m, and μ = 0.268. (a) 2-D spatial variation of σ_n; (b) 2-D spatial variation of τ without slip (μ_s is considered infinite, numerically set as 100); (c) 2-D spatial variation of τ; (d) 2-D spatial variation of fault slip; (e) 2-D spatial variation of stress drop; (f) stress drop across fault strike (L_s) and fault dip (L_d) with specific focus at L_d = 158 m and L_s = 500 m.

(2) Validation analysis of faulting process

I validate the mining-induced faulting process by comparing the shear stress distribution at a specific location with decreasing D_m values, as depicted in Fig. 4-9. The figure illustrates the change in shear stress (τ) as D_m decreases from 280 m to 20 m at the positions L_s = 500 m and L_d = 97 m. My results are compared with those from Cao et al., (2023).

As mining progresses and D_m decreases, the shear stress on the fault plane increases. This trend is evident in Fig. 4-9, where the shear stress rises significantly as the mining face approaches the fault. At the initial distance of 280 m, the shear stress is relatively low, around 0.5 MPa. However, as the distance decreases to 20 m, the shear stress reaches up to 3.0 MPa, indicating a substantial increase in stress concentration near the fault.

The observed increase in shear stress with decreasing D_m underscores the critical role of mining activities in altering fault stability. The validation analysis through the comparison of shear stress changes with decreasing D_m between my study and Cao et al., (2023) provides insights into the mining-induced faulting process. The consistency in observed trends reinforces the robustness of my model. By comparing the results with those of Cao et al. (2023), the reliability of the model is confirmed, further enhancing the understanding of mining-induced fault dynamics.

To confirm the robustness and reliability of my method, I compared the τ at specific locations with various D_m values shown in Cao et al. (2023b) with those obtained in the present study. The close alignment between my results and the those by Cao et al. (2023b) reinforces the robustness and reliability of my analysis.

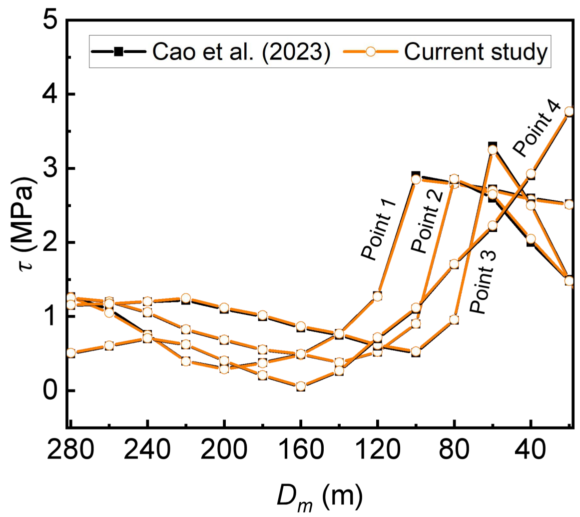

Fig. 4-9 Variation in shear stress with decreasing D_m from 280 m to 20 m at L_s = 500 m.

Fig. 4-10 shows the slip distribution and stress analysis on the fault plane for Model_Cai with D_m = 60 m, P_L = 280 m, and μ = 0.628.

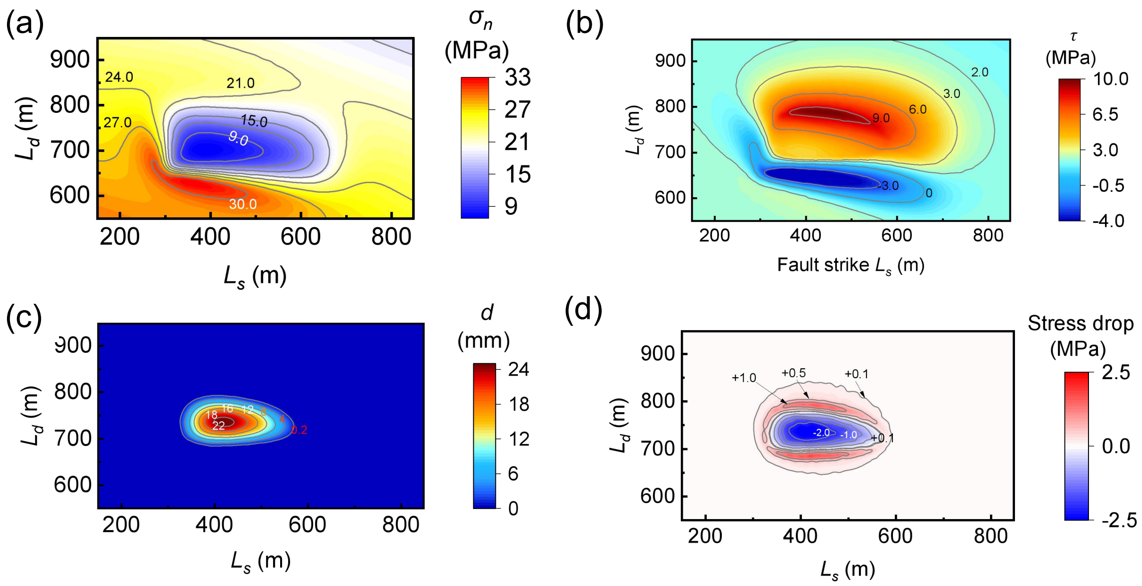

Fig. 4-10 Slip distribution and stress analysis on the fault plane for Model_Cai with D_m = 60 m, P_L = 280 m, and μ = 0.628. (a) 2-D spatial variation of σ_n; (b) spatial variation of τ; (c) 2-D spatial variation of fault slip; (d) 2-D spatial variation of stress drop.

(3) Mechanisms of static faulting: σ_n and τ behavior

I explore the mechanisms of faulting, focusing on the changes in σ_n and τ. Fig. 4-11 provides detailed distributions of σ_n and τ along the fault strike (L_s) at L_d = 158 m and along the fault dip (L_d) L_s = 500 m. In my model, I assumed a planar fault and the background stress increases linearly with depth, so σ_n increases linearly along the dip from shallow to deep areas. The reduction in σ_n observed within the slip regions is due to the mining-induced stress disturbance. In my analysis, the σ_n reduction area due to mining corresponds roughly to the fault slip area. This decrease in σ_n effectively lowers the fault strength, facilitating fault reactivation.

Shear stress τ changes not only by the stress disturbance due to mining but also by the stress drop caused by d. I observe the distribution of mining-induced τ that increases along both the dip and strike directions, especially around the slip region. I cannot attribute the τ accumulation solely to mining activities because the post-slip τ distribution is influenced by the redistribution of stress following the fault slip. This redistribution can cause additional τ accumulation outside the slipped area, which is considered as the stress concentration at the edge of the fault. I can better predict areas prone to fault slip by considering the stress field around the fault. By accounting for the stress drop caused by fault slip, I further validate and extend the conclusions of Li et al. (2024a) from a 2-D plane strain to a 3-D context. My results demonstrate that the reduction in normal stress and the increase in shear stress caused by longwall mining in 3-D space are the fundamental drivers of mining-induced. This understanding is crucial for effective monitoring and mitigation of the risks associated with mining-induced seismic events.

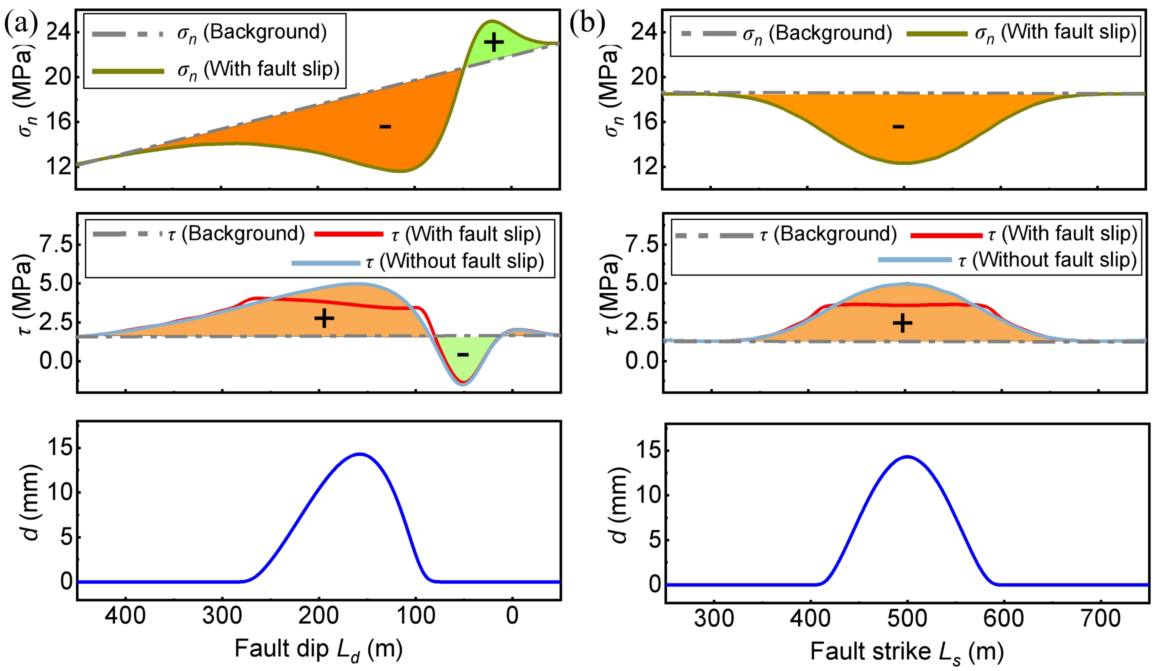

Fig. 4-11 Faulting in deep mining driven by increased shear stress and decreased normal stress. (a) Mining-induced changes in σ_n, τ, and d along L_d specific focus at L_s = 500 m. (b) Mining-induced changes in σ_n, τ, and d along L_s with specific focus at L_d = 158 m. In subfigure σ_n, orange represents mining-induced σ_n release, while green represents σ_n accumulation. In subfigure τ, orange indicates areas of mining-induced τ accumulation, while green indicates τ release. The dashed lines represent the distribution under pure background stress conditions, without the

influence of mining activities.

4.3.2 Mining-induced fault dynamic rupture process

(1) Propagation and arrest of dynamic rupture

I computed the dynamic rupture propagation for Model_Cao after the initiation procedure described in Section 4.2.2. Fig. 4-12 shows snapshots of d and slip rate distribution across the fault under the conditions of D_m = 60 m, P_L = 280 m, μ_s = 0.375, μ_d = 0.24, D_c = 1 mm, and C = 0.3 MPa. The rupture initiated at its nucleation zone and propagated outward. The rupture terminated at approximately 76 ms. 2-D propagation of slip and slip rate are shown in Figs. 4-13, and 4-14. The maximum d of 20 mm occurred at the center of the rupture zone and slipped area is about 3.6×10^4 m^2.

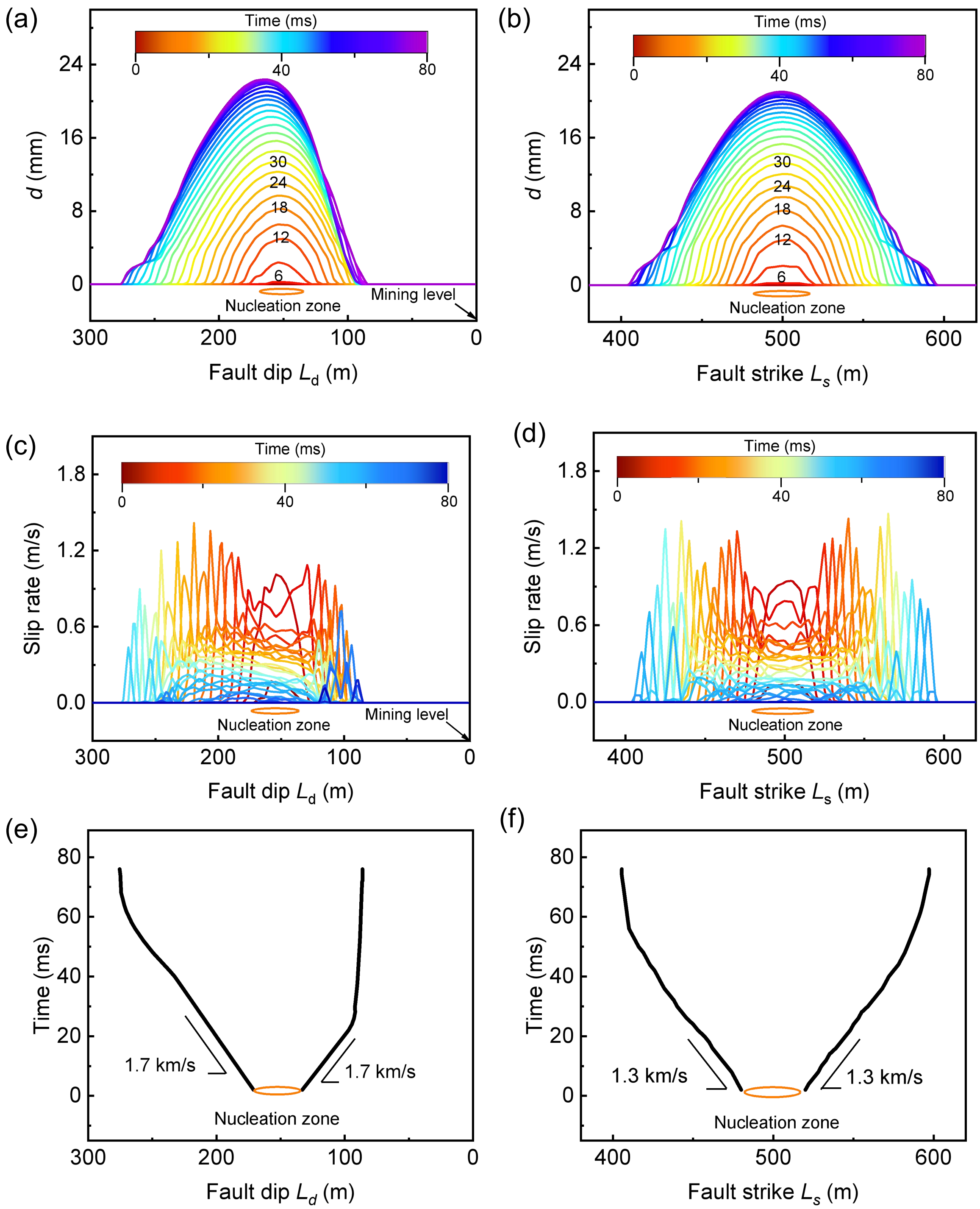

Fig. 4-12 Duration of slip and slip rate during fault rupture in Model_Cao with D_m = 60 m, P_L = 280 m, μ_s = 0.375, and μ_d = 0.24, C = 0.3 MPa. (a) Slip duration along the fault dip at L_s = 600 m; (b) Slip duration along the fault strike at L_d = 158 m; (c) Slip rate duration along the fault dip at L_s = 600 m; (d) Slip rate duration along the

fault strike at L_d = 158 m. (e) Rupture front arrival along the fault dip at L_s = 600 m; (f) Rupture front arrival along the fault strike at L_d = 158 m.

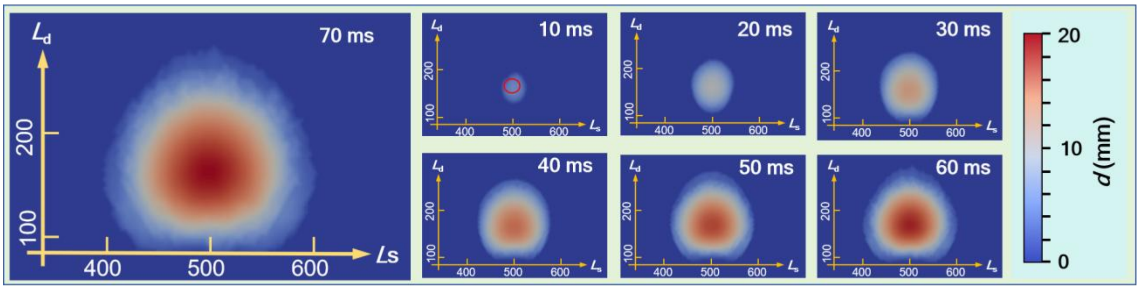

Fig. 4-13 Fault slip distribution at 10 ms intervals in Model_Cao. In the subfigure showing the fault slip distribution at 10 ms, the red circle indicates the nucleation zone.

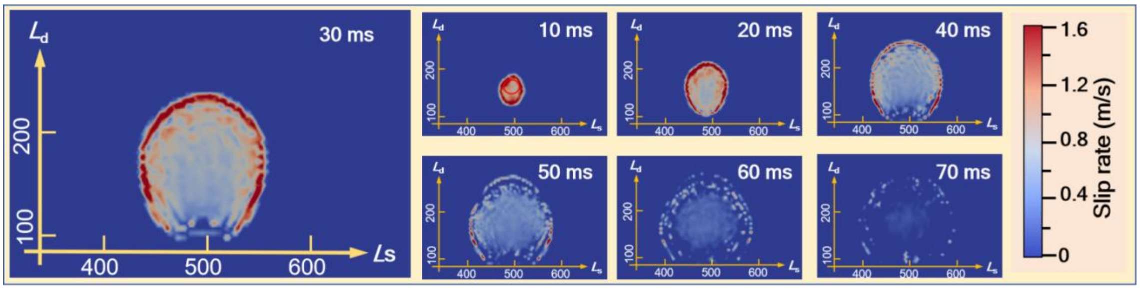

Fig. 4-14 Fault slip rate at 10 ms intervals in Model_Cao. In the subfigure showing the fault slip rate distribution at 10 ms, the red circle indicates the nucleation zone.

Fig. 4-12a illustrates the development of d along the Ld direction (for Ls = 500) as the rupture progresses. The nucleation zone is indicated by the orange elliptical region, which is estimated by the procedure explained in Section 4.2.2 (see also Fig. 4-6). The dynamic rupture initiates by slipping inside the initiation zone simultaneously at time t = 0. The propagation speed toward the shallow section is notably higher than that toward the deeper section. As shown in Fig. 4-12b, the rupture propagates symmetrically along the fault strike at L_s = 500 m. Figs. 4-12c and 4-12d highlight the slip rate distribution along the fault dip and strike. The peak slip rate occurred at the rupture tip, reaching up to 1.6 m/s. The slip rate increased from 0 to 1.0 m/s at the onset of the rupture and continued to rise as the rupture propagated. This slip rate behavior is consistent with past numerical studies based on rate and state friction law (Ampuero and Rubin, 2008) and on field observations (Heaton, 1990). The shallow fault sections experienced faster rupture velocity and higher slip rates compared to the deeper sections could be due to the initial stress condition. Along the fault strike, the slip rate distribution exhibits symmetry because of the symmetrical conditions of stress and friction for Model_Cao. The dynamic rupture results of Model_Cai is shown in Fig. 4-15. As shown in the Fig. 4-12e, $V_{rupture}$ propagating along the fault dip is 1.7 km/s. I further evaluated the $V_{rupture}$ along the fault strike direction. As illustrated in Fig. 4-12f, the propagation along the strike direction exhibits a clear symmetry, with $V_{rupture}$ measured at 1.3 km/s. This symmetry is consistent in both the fault slip and slip rate distributions.

For Model_Cai, Fig. 4-15e shows that the $V_{rupture}$ along the dip direction is about 1.0 km/s. Along the strike direction, the $V_{rupture}$ is observed asymmetry: the left side has a $V_{rupture}$ of 0.9 km/s, while the right side reaches 1.1 km/s. This asymmetry is likely attributed to the non-uniform mining-induced stress disturbances along the strike direction, which are caused by inclined layered structure in the elastic structure model. The snapshots of the slip and slip rate distributions are shown in Figs. 4-16 and 4-17. I summarized the quantitative assessment of dynamic rupture for both Model_Cao and Model_Cai in Table 4-5.

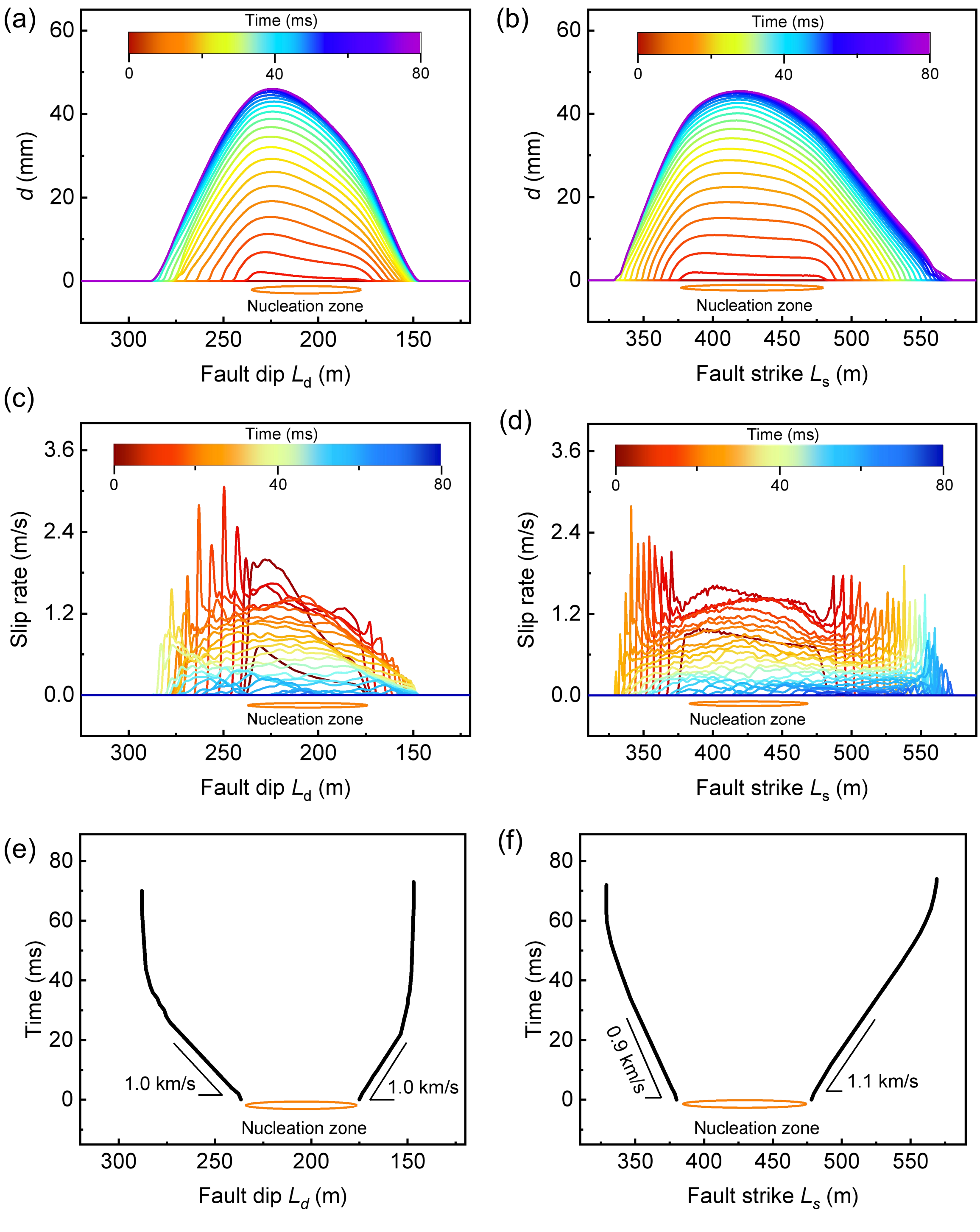

Fig. 4-15 Duration of slip and slip rate during fault rupture in Model_Cai with D_m = 60 m, P_L = 280 m, μ_s = 0.628, and μ_d = 0.5, C = 0.3 MPa. (a) Slip duration along the fault dip at L_s = 420 m; (b) Slip duration along the fault strike at L_d = 220 m; (c) Slip rate duration along the fault dip at L_s = 420 m; (d) Slip rate duration along the fault

strike at L_d = 220 m; (e) Rupture front arrival along the fault dip at L_s = 420 m; (f) Rupture front arrival along the fault strike at L_d = 220 m.

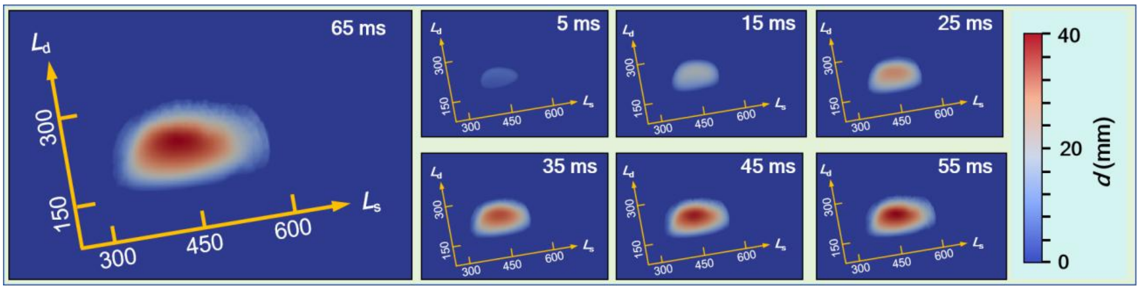

Fig. 4-16 Fault slip distribution at 10 ms intervals in Model_Cai.

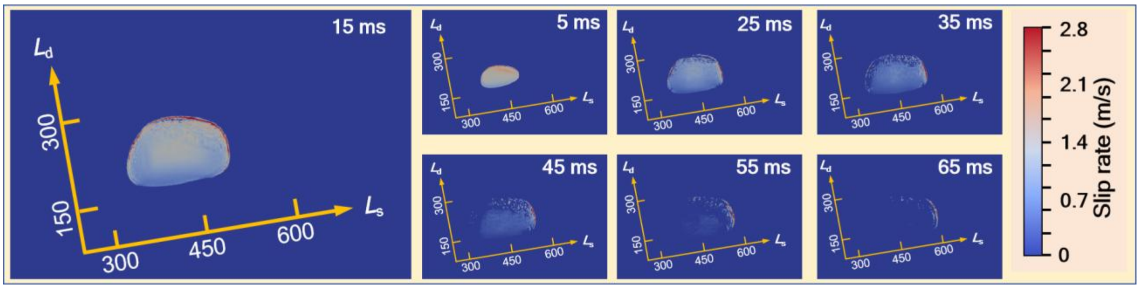

Fig. 4-17 Fault slip rate at 10 ms intervals in Model_Cai.

Table 4-5 Quantitative assessment of dynamic rupture from Model_Cao and Model_Cai

Model	M_0 (Nm)	M_w	$V_{rupture}$ (km/s)		V_s^{max} (m/s)	$T_{rupture}$ (ms)
			Fault dip	Fault strike		
Model_Cao	5.76×10^{12}	2.44	1.7	1.3	1.6	76
Model_Cai	1.13×10^{13}	2.64	1.0	0.9 (left) and 1.1 (right)	3.4	73

Local magnitude (M_L) is often used to measure the magnitude from observed seismograms of small (e.g., M < 3) earthquakes. This empirical scale is derived from the maximum amplitudes recorded on seismographs. Various empirical relationships have been established to express this correlation. For instance, M_w can be estimated as 0.81 M_L + 0.61 in California (Bakun and Lindh, 1977) or 0.64 M_L + 0.84 in Italy (Bindi et al., 2005). For further details, see Table 6.11 in Havskov and Ottemoller (2010). The moment magnitudes (M_w) range approximately from 2.4 to 2.6, which is comparable to the local magnitudes of induced earthquakes in the F16 region (Cao et al., 2023b).

(2) Consistency between the final slip of dynamic rupture and static slip

I compare the final slip distribution of dynamic rupture with that of the static slip results in Figs. 4-18a and 4-18b, which show d along the dip direction at L_s = 500 m and along the strike direction at L_d = 158 m in Model_Cao. Under static conditions (μ = 0.24, detailed in Fig. 4-19), d distribution is shown with a blue curve.

In dynamic conditions (μ_s = 0.375, μ_d = 0.24, D_c = 1 mm), d distribution is represented by an orange curve. The dynamic results show slightly lower d compared to the static ones. Similarly, Figs. 4-18c and 4-18d show the d distributions in Model_Cai along the dip direction at L_s = 420 m and along the strike direction at L_d = 220 m. The static results (μ = 0.50) are shown with a blue curve and the dynamic results (μ_s = 0.628, μ_d = 0.50, D_c = 1 mm) with an orange curve. In this case, the dynamic slip values are again slightly lower than the static slip values.

The discrepancies observed in both Model_Cao and Model_Cai can be attributed to the initiation procedure used in dynamic rupture propagation. In static modeling, the preslip is included in the obtained slip distribution, whereas in dynamic modeling, it is excluded during the initiation process. As shown in Fig. 4-20, the comparison of preslip with the difference between static and dynamic slip indicates indicates that the discrepancy between the two solutions comes from the initiation procedure in the dynamic modeling method.

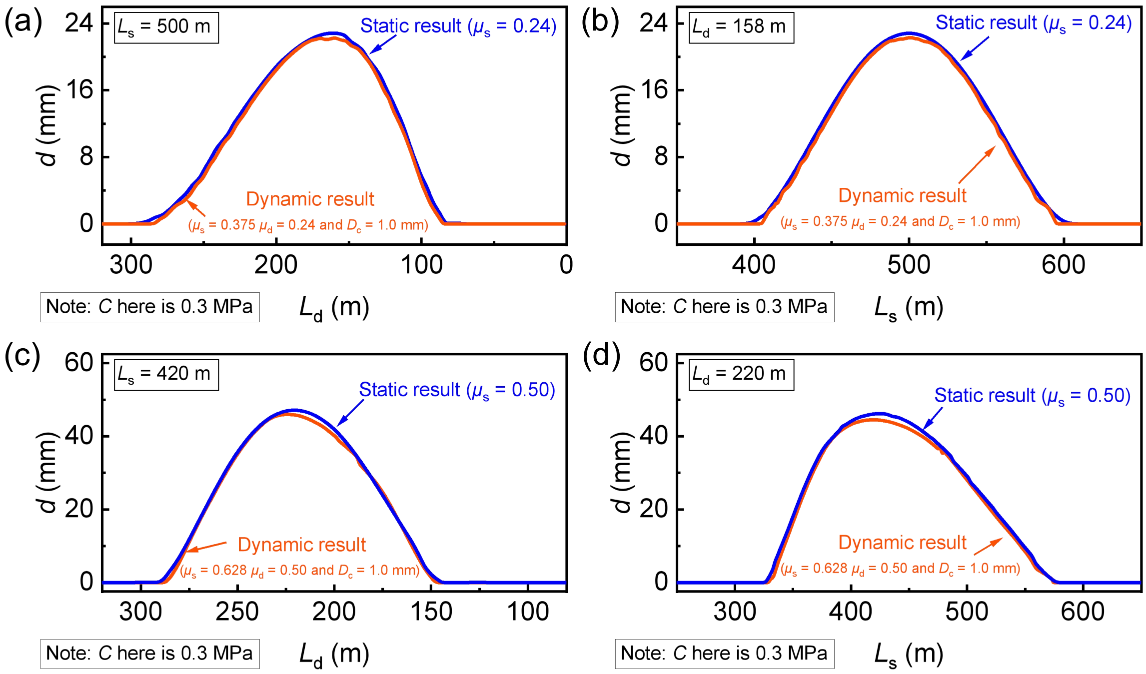

Fig. 4-18 Comparison of static and dynamic rupture stages in Model_Cao and Model_Cai. (a) Slip along the dip direction at L_s = 500 m in Model_Cao. Static condition: μ_s = 0.24; dynamic condition: μ_s = 0.375, μ_d = 0.24, D_c = 1 mm. (b) Slip along the strike direction at L_d = 158 m in Model_Cao. Static condition: μ_s = 0.24; dynamic condition: μ_s = 0.375, μ_d = 0.24, D_c = 1 mm. (c) Slip along the dip direction at L_s = 420 m in Model_Cai. Static condition: μ_s = 0.50; dynamic condition: μ_s = 0.628, μ_d = 0.50, D_c = 1 mm. (d) Slip along the dip direction at L_d = 220 m in Model_Cai. Static condition: μ_s = 0.50; dynamic condition: μ_s = 0.628, μ_d = 0.50, D_c = 1 mm. Blue curve: static result; red curve: dynamic result. Differences are attributed to D_c and the exclusion of nucleation size before rupture in the dynamic model.

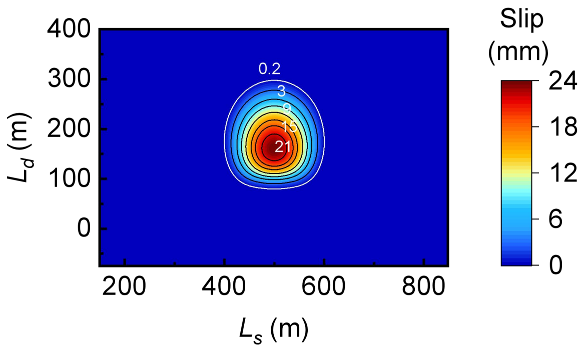

Fig. 4-19 Static modeling results from Cao et al.(2023) for μ_s = 0.24, C = 0.3, and D_m = 60 m.

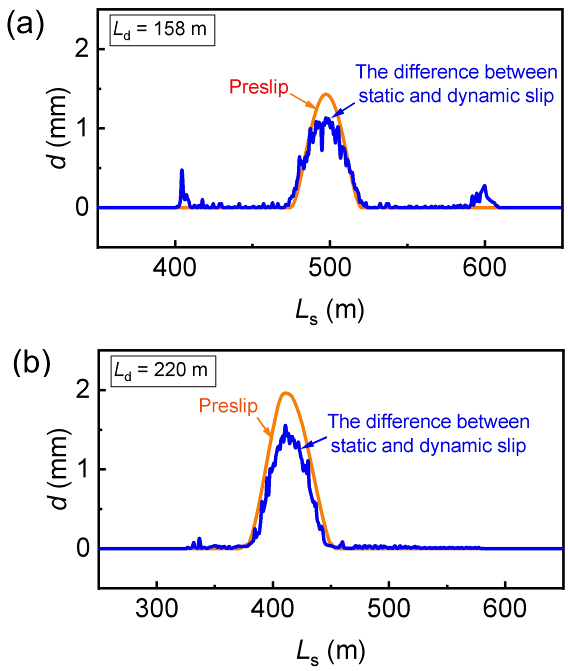

Fig. 4-20 Comparison of preslip with the difference between static and dynamic slip: (a) Model_Cai; (b) Model_Cao.

I performed a quantitative analysis comparing the final dynamic slip and static slip distributions for both models. This analysis confirms that while the overall slip distribution in the dynamic rupture process aligns with the static solution, minor discrepancies remain. Incorporating both static and dynamic modeling approaches enhances the understanding of fault behavior, offering a more comprehensive assessment for seismic risk analysis.

4.3.3 Impact of seismic waves on the working face

Given the proximity of the working face to the seismic source, typically ranging from tens to hundreds of meters, point-source approximation may not work (e.g., Cai et al., 2021; Cao et al., 2023b). Therefore, I use the FEM computation results shown in Section 4.3.2 to evaluate its impact on the working face. I focus on the roof, where the seismic waves arrive first in the current configuration and the most vulnerable part of the mining infrastructure.

(1) Seismic wave analysis

I analyze the impact of seismic waves by examining the peak particle velocity (*PPV*) and peak particle acceleration (PPA) as well as the dominant frequency of velocity (f_v) and that of acceleration (f_a). Using the dynamic rupture modeling results from Section 4.3.2, I measured the seismic waves along the working face at 10 ms intervals as they propagated through heterogeneous rock layers (Figs. 4-21 and 4-22). I focused on amplitude, dominant frequency, and wave duration as the waves traveled through the roof structure. The seismic wave duration at the working face is measured as the time interval from the arrival of the seismic waves at the working face to the timing when the absolute particle velocity attenuates to 10^{-3} m/s. The seismic waves arrive at the working face at approximately 50 ms, and the particle velocity falls to 10^{-3} m/s at around 230 ms in Model_Cao and 280 ms in Model_Cai. Based on these observations, I estimate the seismic wave duration to be 180 ms in Model_Cao and 230 ms in Model_Cai.

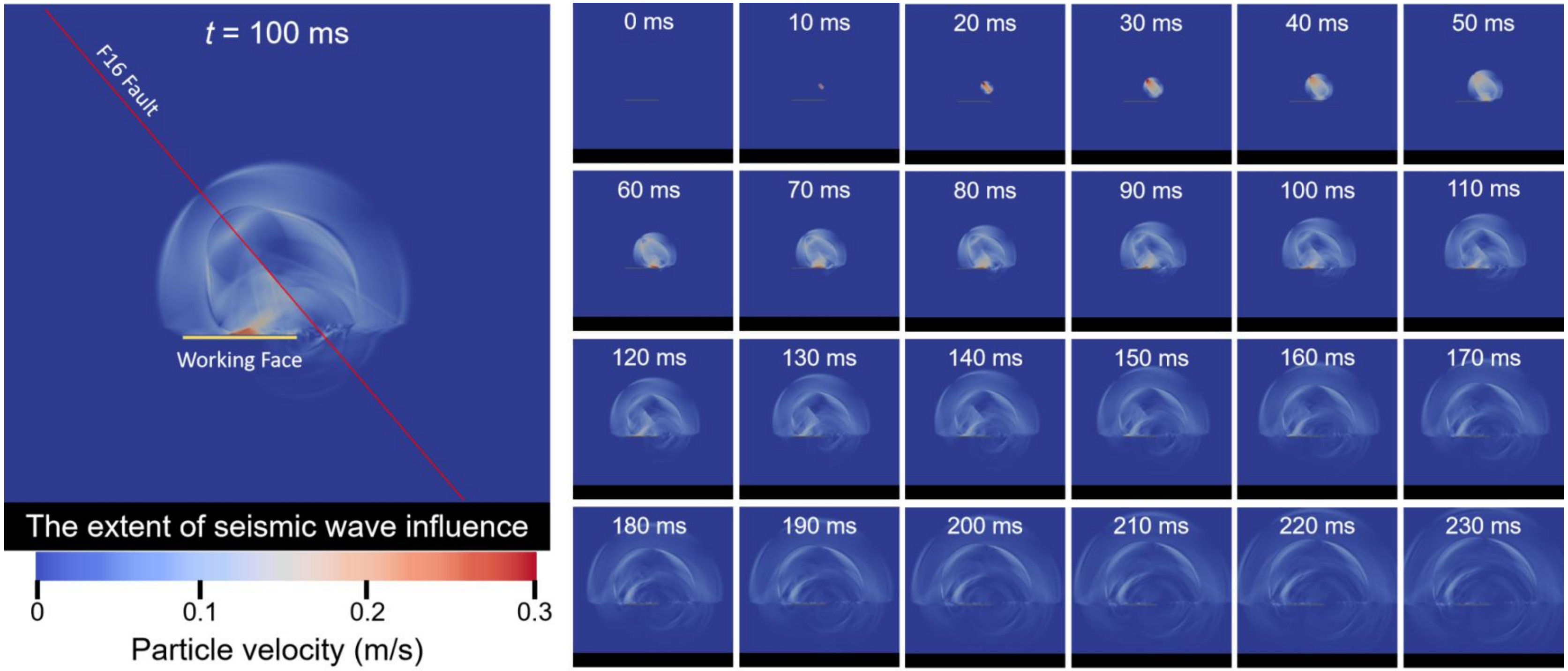

Fig. 4-21 Snapshots of seismic velocity amplitudes on the nearby working face at 10 ms intervals through propagation in heterogeneous rock layers in Model_Cao.

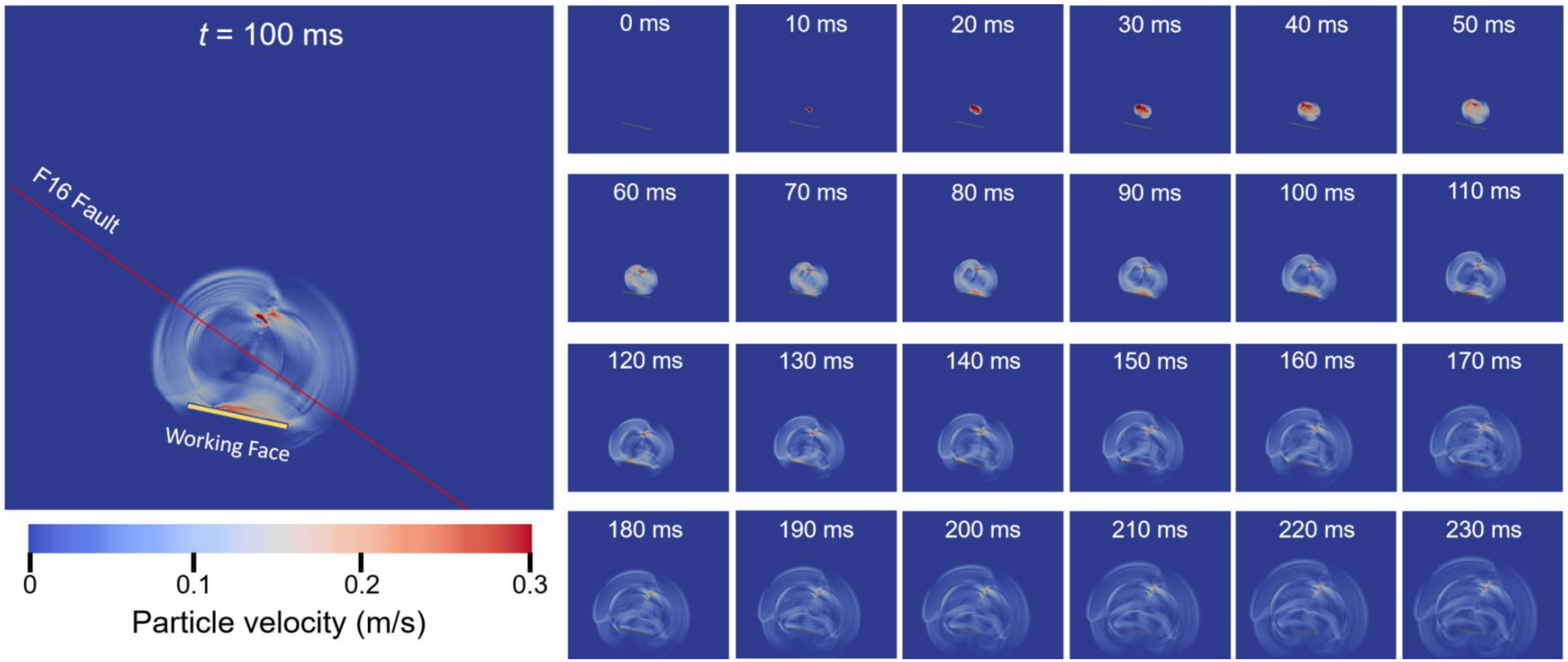

Fig. 4-22 Snapshots of seismic velocity amplitudes on the nearby working face at 10 ms intervals through propagation in heterogeneous rock layers in Model_Cai.

PPV_i and PPA_i are measured separately for each of the three components of the wave field: x, y, and z. For each component, PPV_i and PPA_i are defined as the maximum particle velocity and particle acceleration values over time(Fig. 4-23). PPV and PPA are measured by combining three component waveforms. They are expressed as:

$$\begin{cases} PPV_i(x_0, y_0, z_0) = \max\limits_t [|v_i(x_0, y_0, z_0, t)|] \\ PPA_i(x_0, y_0, z_0) = \max\limits_t [|a_i(x_0, y_0, z_0, t)|] \end{cases} \tag{4-12}$$

$$\begin{cases} PPV(x_0, y_0, z_0) = \max\limits_t \left\{ \sqrt{[v_x(x_0, y_0, z_0, t)]^2 + [v_y(x_0, y_0, z_0, t)]^2 + [v_z(x_0, y_0, z_0, t)]^2} \right\} \\ PPA(x_0, y_0, z_0) = \max\limits_t \left\{ \sqrt{[a_x(x_0, y_0, z_0, t)]^2 + [a_y(x_0, y_0, z_0, t)]^2 + [a_z(x_0, y_0, z_0, t)]^2} \right\} \end{cases} \tag{4-13}$$

where $v_i(x_0, y_0, z_0, t)$ is the particle velocity at the position (x_0, y_0, z_0) and time t in the i-direction, and $a_i(x_0, y_0, z_0, t)$ is the corresponding particle acceleration. Here, i denotes either x, y, or z. $maxPPV$ and $maxPPA$ refer to the maximum values of PPV and PPA on the roof.

In my seismic wavefield analysis, I introduce the local coordinates D and S, as shown in Fig. 4-23. The specific locations where I measured the seismic waves are 1 m above the working face (y = 405 m). To examine the effects of seismic waves, I systematically measure the particle velocities and accelerations along the D axis (at S = 0 m) and along the S axis (at D = 60 m). For both axes, I measured at 10 m intervals to capture the spatial variation of the seismic waves.

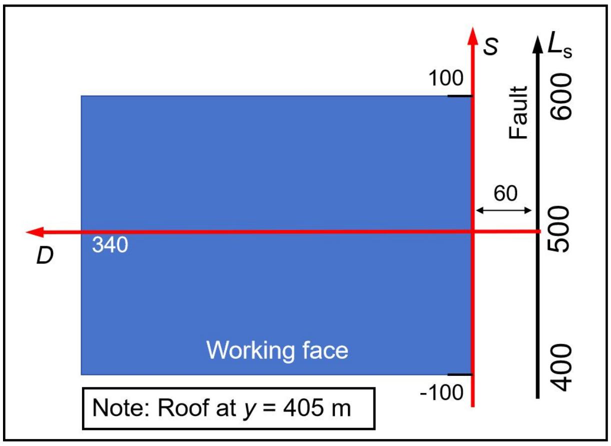

Fig. 4-23 Analysis of the local coordinates D and S on the working face during seismic wave vibrations. The analysis focuses on the position 1 m above the working face, at y = 405 m. Considering the distribution affected by wave fluctuations, I analyze

points at 10 m intervals along D (with S = 0 m) and S (with D = 60 m). Note: For the inclined coal seam model, Model_Cai, I also conducted measurements 1 m along the roof.

In Fig. 4-21, snapshots of particle velocity amplitudes across the *y*-axis are shown. I can see that the direct S waves have the largest *PPV* and *PPA* in the 250 ms time window. After the passage of S waves, the particle amplitudes attenuate rapidly, indicating that the influence of reflected and inhomogeneous waves is minimal. In Figs. 4-24 and 4-25 for Model_Cao and Figs. 4-26 and 4-27 for Model_Cai, it is evident that both velocity and acceleration values are higher at D = 60–140 m compared to those near D = 340 m. The maximum acceleration near the fault reaches 26.6 m/s^2, whereas the minimum value on the left side of the working face is only 2.8 m/s^2. This indicates that the seismic impact is more pronounced closer to the fault, while it diminishes further away. In Fig. 4-28 for Model_Cao, at D = 60 m along the S direction, the y-component displays a clearly symmetric distribution. This outcome is expected, as the rupture pattern along the strike (Fig. 4-12) also exhibits symmetry.

Fig. 4-29 presents the distribution of *PPA* and *PPV* on the roof for both Model_Cao and Model_Cai, showing a clear concentration of higher *PPA* and *PPV* values near the fault side. In Model_Cao, the *PPA* (Fig. 4-29a) and *PPV* (Fig. 4-29b) distributions exhibit a distinct gradient, with values diminishing as the distance from the fault increases. This indicates stronger wave impacts on the working face near the fault. Model_Cai shows a similar attenuation pattern, though with subtle differences in gradient and distribution, as its working face is not parallel to the fault strike (Figs. 4-29c and 4-29d). The *maxPPV* and *maxPPA* values for both Model_Cao and Model_Cai are summarized in Table 4-6.

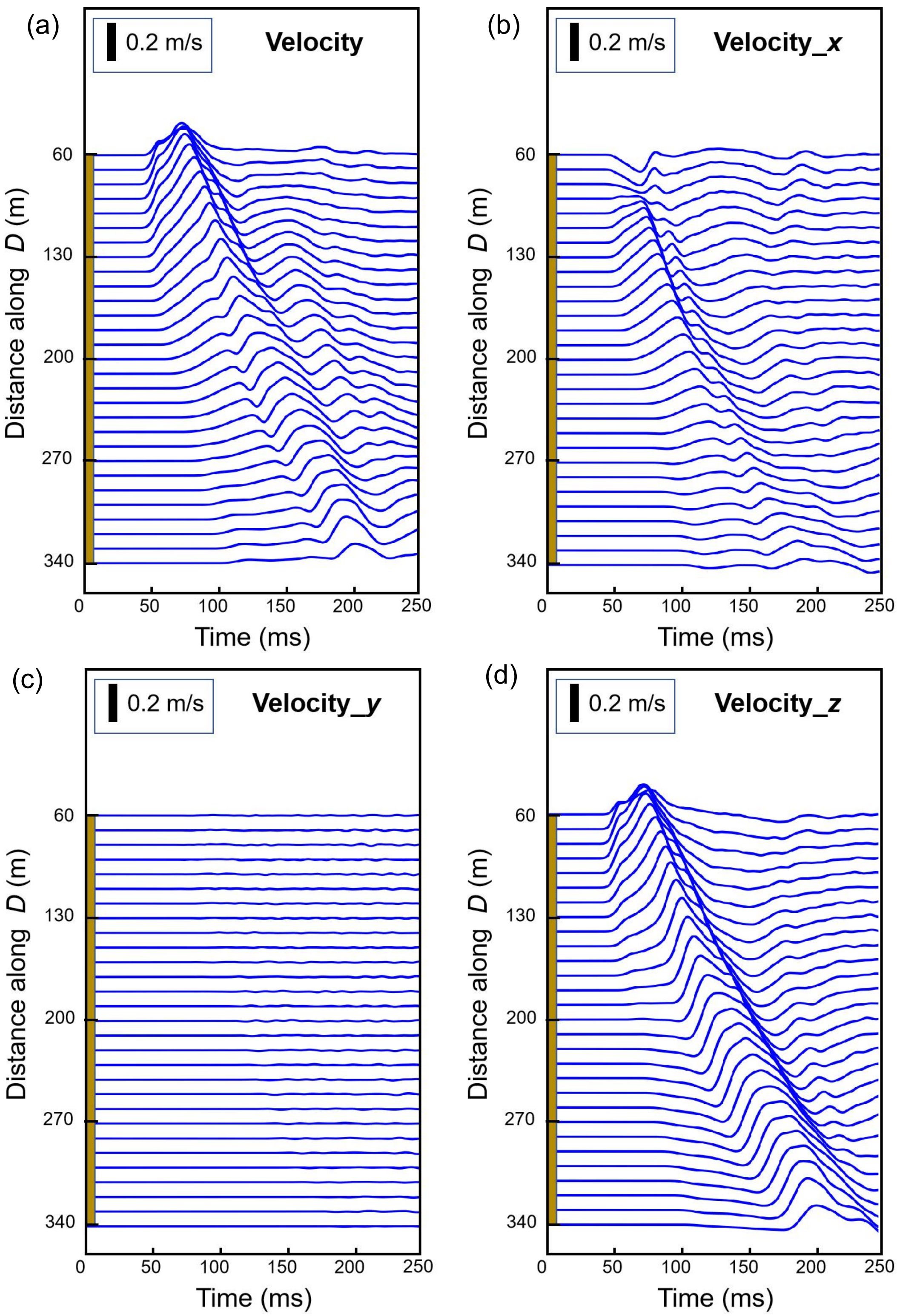

Fig. 4-24 Velocity at 1 m above roof induced by fault rupture in Model_Cao. a–d correspond to velocity and the x, y, and z components, respectively. A total of 29 points were plotted along D at 10 m intervals from the position $S = 0$ m.

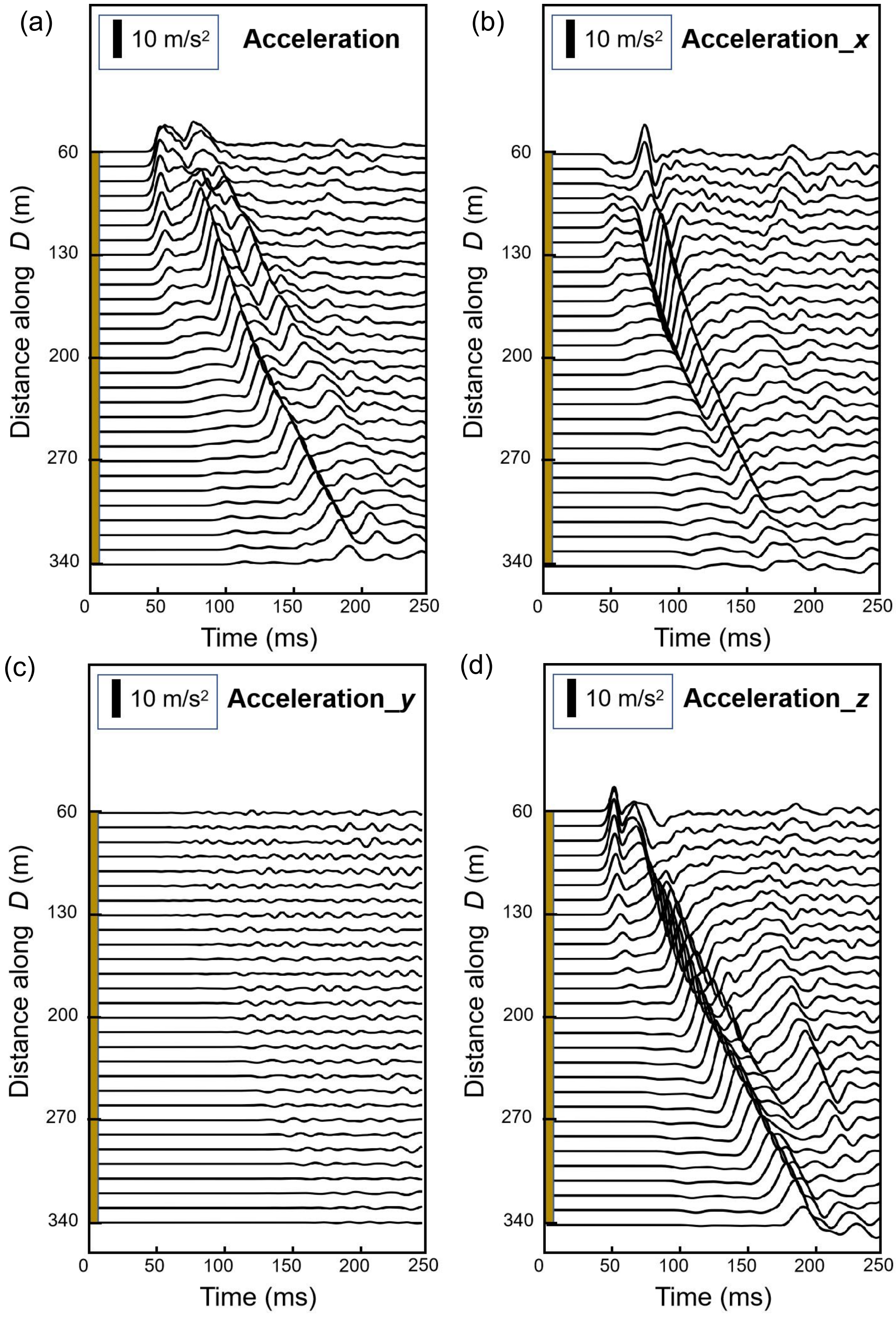

Fig. 4-25 Acceleration at 1 m above roof induced by fault rupture in Model_Cao. a–d correspond to acceleration and the *x*, *y*, and *z* components, respectively. A total of 29 points were plotted along *D* at 10 m intervals from the position *S* = 0 m.

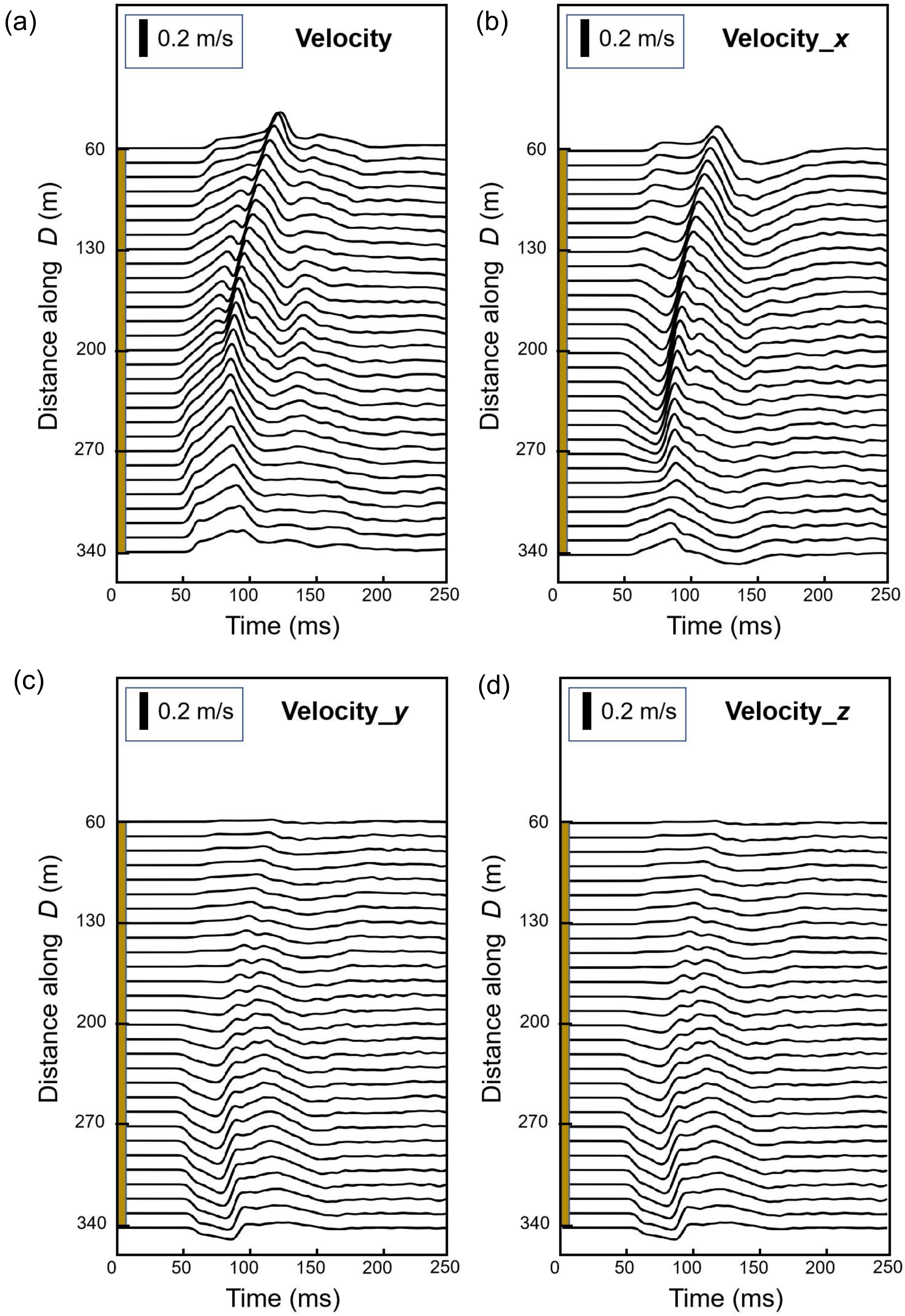

Fig.4-26 Velocity at 1 m above roof induced by fault rupture in Model_Cai. a–d correspond to velocity and the *x*, *y*, and *z* components, respectively. A total of 29 points were plotted along *D* at 10 m intervals from the position *S* = 0 m.

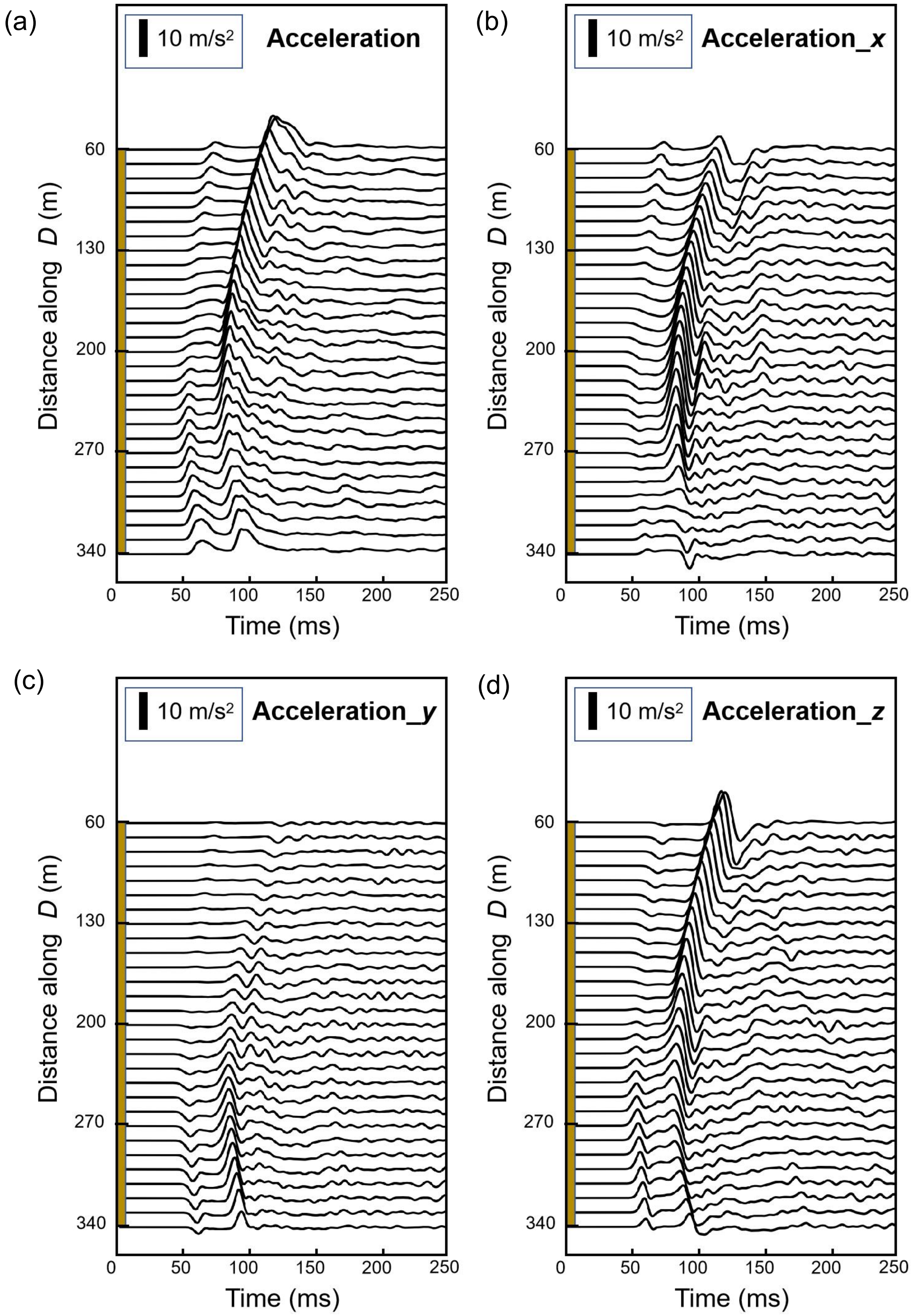

Fig.4-27 Acceleration at 1 m above roof induced by fault rupture in Model_Cai. a–d correspond to acceleration and the x, y, and z components, respectively. A total of 29 points were plotted along D at 10 m intervals from the position S = 0 m.

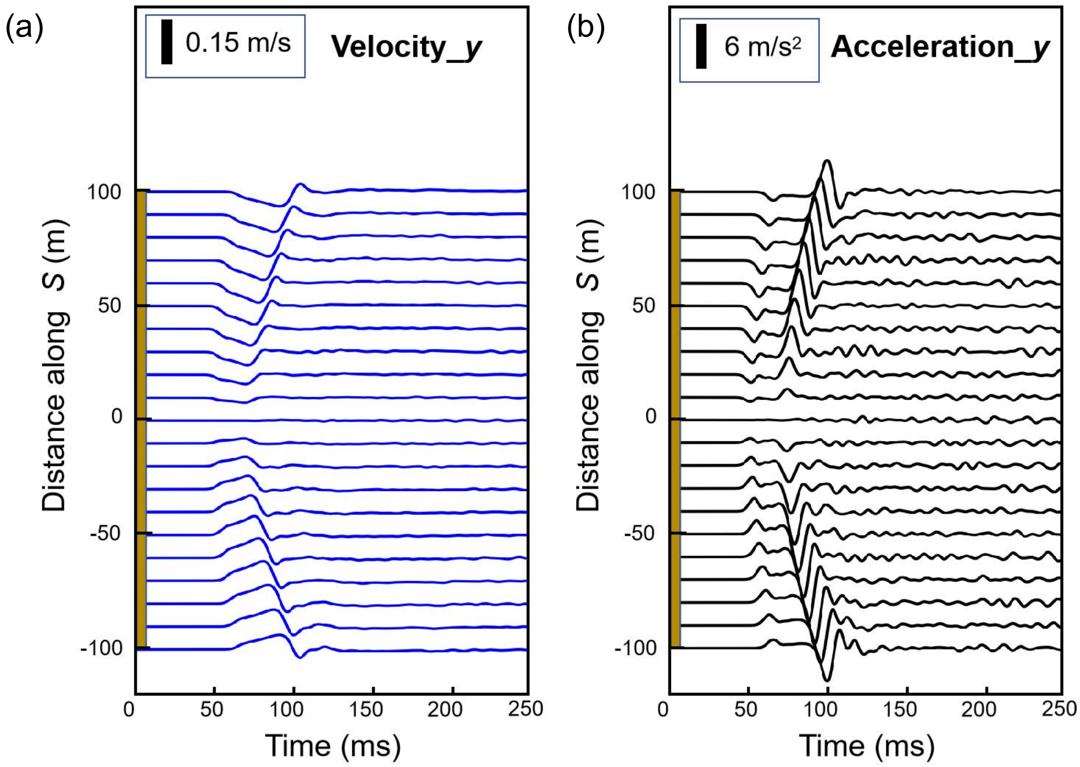

Fig.4-28 Velocity and acceleration in y components induced by fault rupture in Model_Cao. a and b show velocity and acceleration in y components, respectively. A total of 21 points were plotted along *S* at 10 m intervals from position *D* = 60 m.

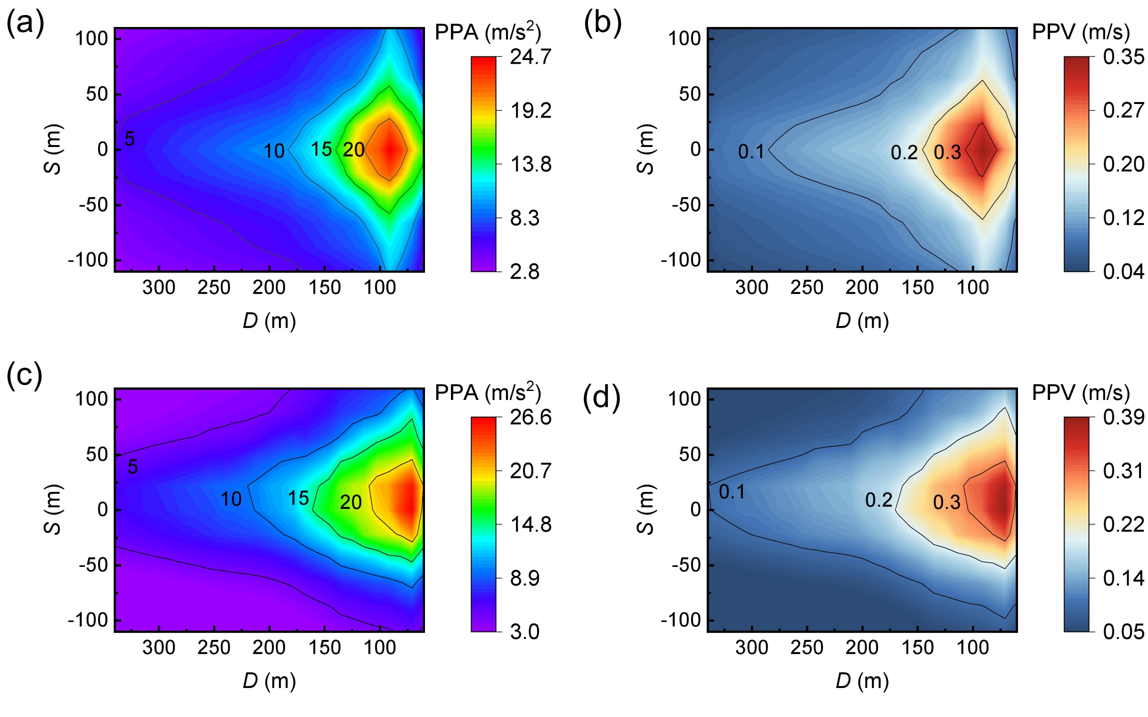

Fig. 4-29 PPA and PPV distribution on the roof: (a–b) PPA and PPV for Model_Cao; (c–d) PPA and PPV for Model_Cai.

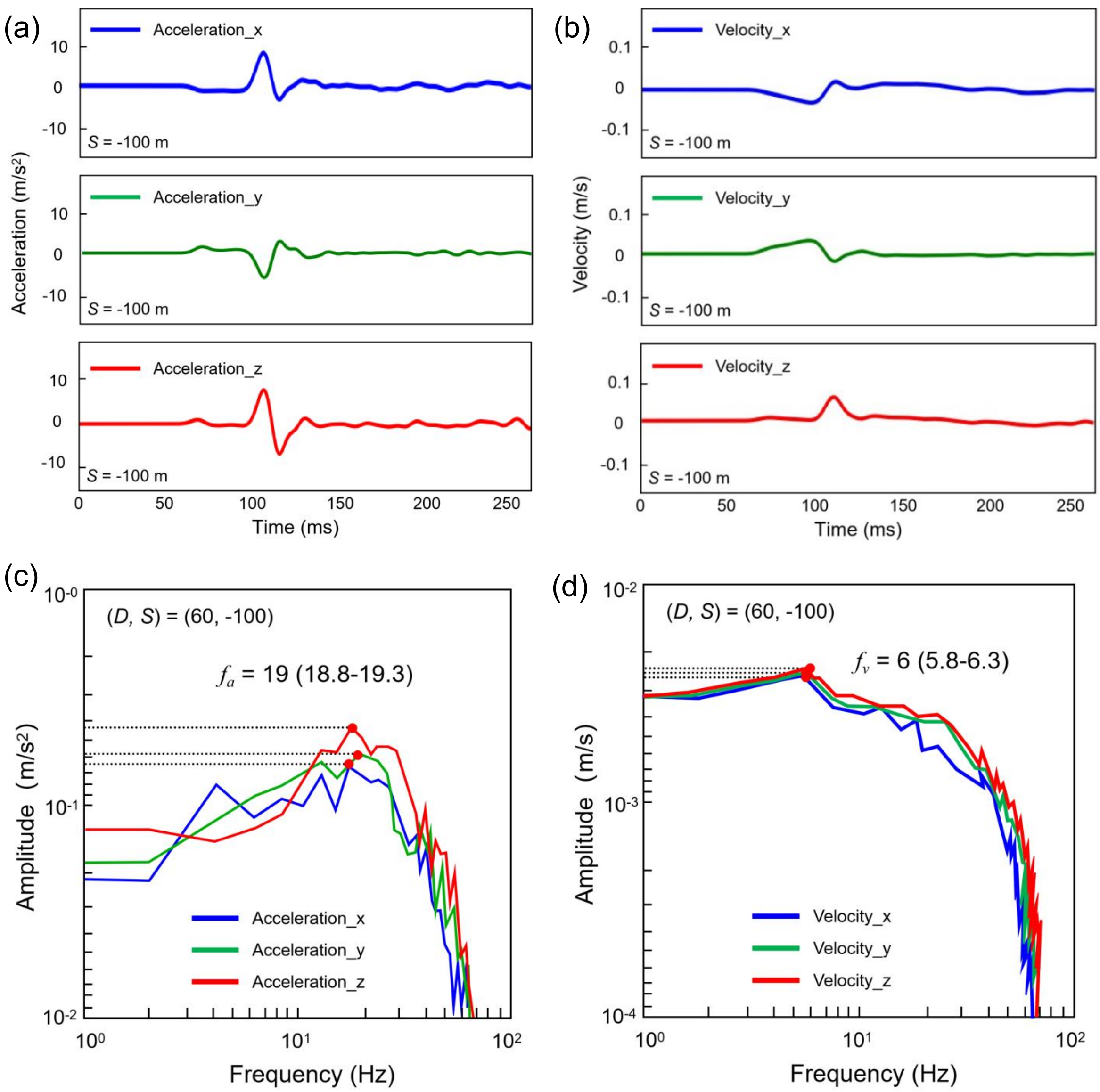

Fig. 4-30 Example of dominant frequency measurement via Fourier transform of time-domain seismic data: (a-b) Seismic data recorded at S = -100 m and D = 60 m in Model_Cao; (c-d) Corresponding Fourier transform of the time-domain data in (a) and (b), with a 30 Hz low-pass filter applied.

The frequency content of the seismic waves impacting the working face plays a significant role since it may cause resonance effects. To accurately identify dominant frequencies, I applied a Fourier transform to the time-domain seismic wave data at 2 m intervals along the roof (Fig. 4-23) and analyzed the Fourier amplitude spectrum. The dominant frequency is determined as the peak in the amplitude spectrum, representing the frequency that contributes most significantly to the wave energy. This approach provides an accurate characterization of the frequency content (Fig. 4-30). In Fig. 4-30, I applied a

30 Hz low-pass filter. Notably, the predominant frequency remains consistent across components, with only minor variations likely due to numerical noise. A summary of the dominant frequencies is provided in Table 4-6.

Mining-induced near-source fault ruptures generate seismic waves with duration of 180 ms in Model_Cao and 230 ms in Model_Cai, potentially causing rapid vibrations that intensify existing fractures or weaknesses in roof structures, leading to small-scale but potentially widespread damage. Additionally, the dominant frequency is closely related to the duration of the moment rate function, influencing the dynamic response of the affected structures.

Table 4-6 Spatial distribution of maximum *PPV*, *PPA*, dominant frequency, and seismic wave duration in Model_Cao and Model_Cai

Term	Model_Cao	Model_Cai
maxPPV (m/s)	0.35 at (*S*, *D*) = (0, 94)	0.39 at (*S*, *D*) = (5, 82)
maxPPVx (m/s)	0.26 at (*S*, *D*) = (0, 102)	0.30 at (*S*, *D*) = (5, 84)
maxPPVy (m/s)	±0.10 at (*S*, *D*) = (±60, 62)	0.13 at (*S*, *D*) = (48, 62) and -0.14 at (*S*, *D*) = (-52, 62)
maxPPVz (m/s)	0.29 at (*S*, *D*) = (0, 92)	0.26 at (*S*, *D*) = (0, 84)
maxPPA (m/s^2)	24.7 at (*S*, *D*) = (0, 94)	26.6 at (*S*, *D*) = (5, 76)
*max*PPAx (m/s^2)	-18.8 at (*S*, *D*) = (0, 100)	-19.5 at (*S*, *D*) = (0, 78)
maxPPAy (m/s^2)	±9.9 at (*S*, *D*) = (±60, 62)	12.2 at (*S*, *D*) = (48, 62) and -13.2 at (*S*, *D*) = (-54, 62)
maxPPAz (m/s^2)	18.4 at (*S*, *D*) = (0, 94)	19.9 at (*S*, *D*) = (0, 68)
Dominant frequency of acceleration, f_a, (Hz)	18~20	14~16
Dominant frequency of velocity, f_v, (Hz)	7~9	6~8
Seismic wave duration (ms)	180	230

(2) Recommendations for seismic impact management on support systems

Given the high *PPV* and *PPA* values and the observed dominant frequencies (7~9 Hz for velocity and 18~20 Hz for acceleration in Model_Cao), it is essential to implement enhanced monitoring and reinforcement strategies for the working face and roadways. The seismic wave durations—180 ms in Model_Cao and 230 ms in Model_Cai—are critical in assessing the dynamic loads from fault–slip rockbursts. Longer exposure to seismic waves increases the risk of resonance, which occurs when the seismic frequencies align with the natural frequencies of the support systems or protective pillars. This can amplify shaking, potentially causing structural damage or failure.

Although the seismic waves in this study last only a few hundred milliseconds, they may still exert enough dynamic disturbance to exacerbate pre-existing fractures or weaknesses in the roof structure, increasing the risk of rockbursts. On the side closer to the fault, I observe a clear concentration of *PPA* and *PPV*, with the *maxPPA* in Model_Cai reaching 26.6 m/s^2 at (S, D) = (5, 76). In contrast, values on the side farther from the fault are below 5 m/s^2. To mitigate these effects, I recommend using an asymmetric support system designed to withstand both peak dynamic loads (as represented by PPV and PPA) and prolonged seismic vibrations on the side closer to the fault, while primarily addressing static loads (background and mining-induced stresses) on the side farther from the fault. On the fault-proximal side, energy-absorbing rockbolts and yielding bolts, which deform plastically under high loads to absorb and dissipate seismic energy, are particularly effective (Kaiser and Cai, 2012; Kang et al., 2020; Rahimi et al., 2020; Wang et al., 2020c).

However, the effectiveness of these systems depends on ensuring their natural frequencies fall outside the dominant seismic frequency range. This requires a detailed frequency analysis during the design process. Engineers should adjust the stiffness, damping characteristics, material properties, or dimensions of the supports to shift their natural frequencies and avoid resonance with the observed seismic frequencies. In a fault–slip rockburst, unstable rock failure releases significant strain energy, requiring a support system that can yield and dissipate dynamic energy. Dynamic rockbolts, reinforced by rebars and strong mesh, are critical for an integrated support system (Cai, 2024). Modifying the geometry or material of energy-absorbing rockbolts can optimize their performance under dynamic loads, reducing the risk of amplification and enhancing structural integrity and safety in mining operations (Sharifzadeh et al., 2020a; 2020b; Wang et al., 2022). Effective energy dissipation is only achieved when all support elements are well-integrated and interact with the rock mass.

In summary, the interplay between the dynamic load, duration and the dominant frequency of seismic waves must be carefully considered when designing support systems. The simultaneous optimization of load-bearing capacity and frequency response is key to preventing resonance and protecting the mining operation from seismic-induced structural failures

4.4 Discussion

4.4.1 Dependence of D_c and C

(1) Effects of different D_c on the rupture process

As D_c increases, fracture energy also rises, reducing rupture velocity and potentially terminating the rupture (Andrews, 1976; Fukuyama and Madariaga, 2000). The moment rate function, a key parameter in earthquake dynamics, represents the rate of seismic energy release during fault slip and provides insights into the rupture process. I investigate how D_c affects fault slip and moment rate during dynamic rupture. Fig. 4-31a presents the moment rate function for different D_c values, showing that as D_c increases, the energy release becomes less intense, with a slower, more gradual release. For D_c = 1 mm, the peak moment rate reaches approximately 3.4×10^{17} Nm/s, while for D_c = 5 mm, it decreases to around 2.3×10^{17} Nm/s. Larger D_c values result in broader curves, indicating a more distributed rupture process and stable fault slip. I further explore the relationship between rupture front propagation speed and D_c. As shown in Figs. 4-31b and 4-31c, I summarize the rupture front arrival along the fault dip for various D_c at L_s = 420 m and along the fault strike for various D_c at L_d = 220 m. Along the fault dip, $V_{rupture}$ is 1.0 km/s when D_c is 1 mm, decreasing to 0.9 km/s as D_c increases to 5 mm (Fig. 4-31b). Similarly, along the fault strike, the left side shows a $V_{rupture}$ of 0.9 km/s at D_c = 1 mm, which decreases to 0.8 km/s at D_c = 5 mm. On the right side, $V_{rupture}$ decreases from 1.1 km/s at D_c = 1 mm to 0.9 km/s at D_c = 5 mm (Fig. 4-31c).

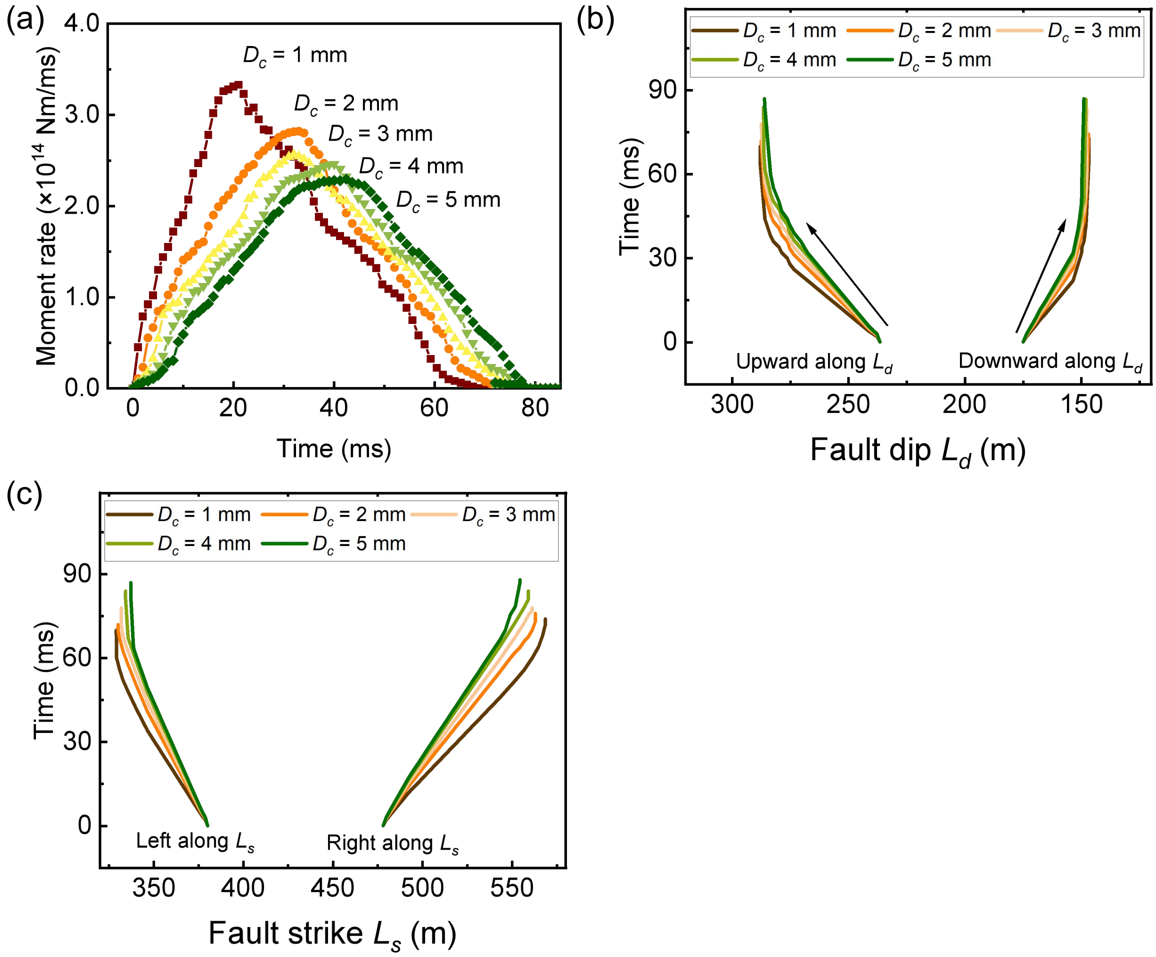

Fig. 4-31 Influence of D_c on dynamic rupture. (a) Moment rate function. (b) Rupture front arrival along L_d for various D_c at L_s = 420 m; (c) Rupture front arrival along L_s for various D_c at L_d = 220 m.

These results indicate that larger D_c values result in more gradual rupture propagation and slower rupture velocities, while smaller D_c values lead to faster rupture velocities. Additionally, larger D_c values reduce the moment rate, resulting in a longer and less intense energy release. By integrating these observations with the theoretical framework (Andrews, 1976; Fukuyama and Madariaga, 2000), I confirm the critical role of D_c in controlling rupture dynamics.

(2) Effects of different C on the rupture process

I analyze the impact of C on the dynamic rupture process. Tenthorey et al. (2003) highlighted that fault cohesion changes over time, and Tenthorey and Cox (2006) developed a model for time-dependent cohesion strengthening in fault zones within continental seismic regions.

My numerical simulations incorporate C into mining-induced dynamic rupture propagation, allowing me to explore how cohesion, based on the linear slip weakening law, evolves during rupture. Fig. 4-32 analyzes the cohesive effects in two models, Model_Cao and Model_Cai. In Fig. 4-32a, the maximum slip in Model_Cao is higher for C = 0 MPa compared to C = 0.3 MPa. At the peak, slip reaches about 30 mm for C = 0 MPa, and 20 mm for C = 0.3 MPa, showing that higher cohesion reduces slip and stabilizes the fault. Similarly, in Model_Cai (Fig. 4-32b), the maximum slip reaches 47 mm for C = 0 MPa, and decreases to 40 mm for C = 0.3 MPa, confirming that C controls fault slip during dynamic rupture.

Figs. 4-32c and 4-32d show the moment rate functions for Model_Cao and Model_Cai, illustrating how cohesion affects energy release during fault slip. Without cohesion (C = 0 MPa), the moment rate is significantly higher, with Model_Cao peaking around 40 ms at approximately 2.6×10^{17} Nm/s, reflecting a rapid rupture process. In contrast, with C = 0.3 MPa, the energy release is more gradual, with a lower peak moment rate of 2.4×10^{17} Nm/s. Similarly, Model_Cai shows a peak moment rate of 3.9×10^{17} Nm/s for C = 0 MPa, which reduces to 3.4×10^{17} Nm/s with higher cohesion. In the absence of cohesion, fault slip is less constrained, leading to more rapid energy release, as indicated by higher moment rate peaks. I further explore the relationship between rupture propagation velocity and C. As shown in Figs. 4-31e and 4-31f, the rupture front arrival along the fault dip is summarized for both models. In Model_Cao, $V_{rupture}$ is 1.7 km/s at C = 0.3 MPa, increasing to 2.1 km/s at C = 0 MPa. Similarly, in Model_Cai, $V_{rupture}$ is 1.0 km/s at C = 0.3 MPa, rising to 1.1 km/s at C = 0 MPa. I also observe that the rupture duration for C = 0 MPa is shorter than that for C = 0.3 MPa. This is because lower cohesion reduces resistance to fault slip, making rupture easier to initiate and allowing for faster rupture propagation.

My results emphasize the role of C in understanding fault behavior during rupture. While numerical models are inherently simplified, they provide valuable insights into how C influences fault stability and rupture dynamics. This study enhances our understanding of fault mechanics, demonstrating that C remains a critical factor to consider, even in simplified models.

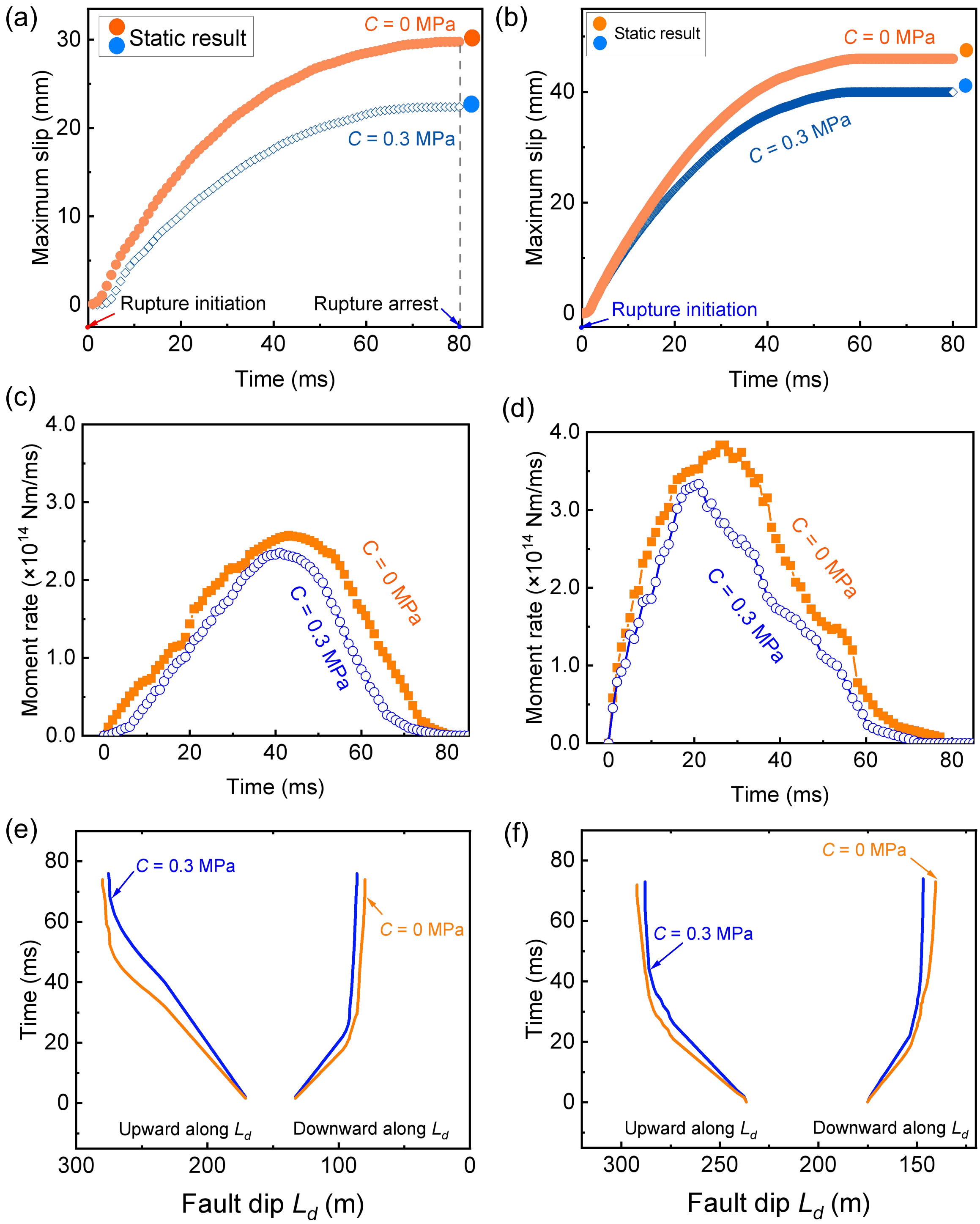

Fig. 4-32 Cohesive effects on dynamic rupture. (a) Maximum slip in Model_Cao (b) Maximum slip in Model_Cai. (c) Moment rate function in Model_Cao. (d) Moment rate function in Model_Cai. (e) Rupture front arrival along the fault dip for in Model_Cao at L_s = 500 m; (f) Rupture front arrival along the fault dip in Model_Cai at L_s = 420 m. Orange and blue dots represent static results for cohesive values of 0 MPa and 0.3 MPa. The measurement point for maximum slip in (a) is located at (L_s, L_d) = (500, 158), and in (b), it is at (420, 220).

4.4.2 Comparisons with observations during the mining operations

To evaluate my simulation results, I compared my simulation results with the observations during mining operations at Yuejin coal mine. According to Cao et al. (2023b), the "8.11" coal burst accident occurred on August 11, 2010, during the early stage of mining on the 25,110 longwall face. Fig. 4-1 illustrates the location and impact of the rock burst accident, with the red hatched region indicating the zone damaged by the burst, This event had a local magnitude of M_L= 2.7 and resulted in severe damage to 362 m of the roadway on the side close to the fault (Fig. 4-1c). At the time, the distance between the longwall face and the fault was about 60 m. *d* was a crucial factor leading to this accident (Cao et al., 2023b; Cai et al., 2021).

Cao et al. (2023b) demonstrated that as mining progresses and the D_m decreases, shear stress on the fault plane significantly increases. They showed an increase in shear stress from 1.2 MPa at D_m = 280 m to 2.8 MPa at 20 m at point 1, highlighting the mining effect on fault stability. I validated their results of shear stress distribution at four points (Fig. 4-9). My results could reproduce those of Cao et al. (2023b) (Fig. 4-9), confirming the robustness of my model.

I analyzed the correlation between my simulation results and the observed damage from the "8.11" coal burst accident. Significant damage was observed in the 362 m section of the roadway, particularly on the side closest to the F16 fault (Fig. 4-33a). I mapped the *PPA* and *PPV* results from Figs. 4-29 onto Fig. 4-33, revealing that the damaged zone aligns with the locations of *maxPPA* and *maxPPV.* Additionally, Fig. 4-29 shows a noticeable decrease in seismic wave intensity on the opposite side of the working face (*D* = 340 m). Considering the seismic wave amplitude, duration, and dominant frequency, it is reasonable to infer that the dynamic rupture of the F16 fault triggered the tunnel support system's failure due to seismic wave propagation.

My dynamic simulation results strongly align with the observed impacts of the fault–slip rockburst, as illustrated in Fig. 4-33. The "O-shaped" supports in the head entry remained unaffected in areas farther from the seismic source, functioning as intended (Fig. 4-33e). However, in the blue circle areas closest to the fault, the supports were severely deformed (Fig. 4-33f), indicating substantial damage caused by the fault–slip rockburst. In the center of the damage zone (Fig. 4-33a), the PPA is approximately 20 m/s^2 in Model_Cai (Fig. 4-33b) and 16 m/s^2 in Model_Cao, while the *PPV* is around 0.32 m/s in Model_Cai (Fig. 4-33c) and 0.25 m/s in Model_Cao. This contrast between damaged and undamaged regions underscores the limitations of static models in accounting for significant damage variations across adjacent areas. It further emphasizes the strong correlation between my dynamic rupture results and the observed damage, demonstrating that my 3-D model effectively captures the dynamic effects driving the rockburst.

The dominant frequency likely overlapped with the natural frequencies of the "O-shaped" supports, intensifying the damage through resonance effects (Sandova and Bobet, 2017; 2020). This possibility is particularly relevant in deep mining environments, where structural elements are subjected to a combination of static loads from the overburden and dynamic loads from seismic events. The ability of my model to accurately predict both the intensity of shaking and its frequency characteristics underscores its robustness and practical relevance to real-world conditions.

Given these results, my study highlights the necessity for robust support systems designed to prevent from predicted *PPV*, *PPA*, f_v, f_a and duration of seismic waves. These systems should be capable of absorbing the energy from significant seismic waves and mitigating resonance effects. By integrating field observations, I demonstrate that my models can reliably predict fault behavior and seismic wave radiations in mining environments.

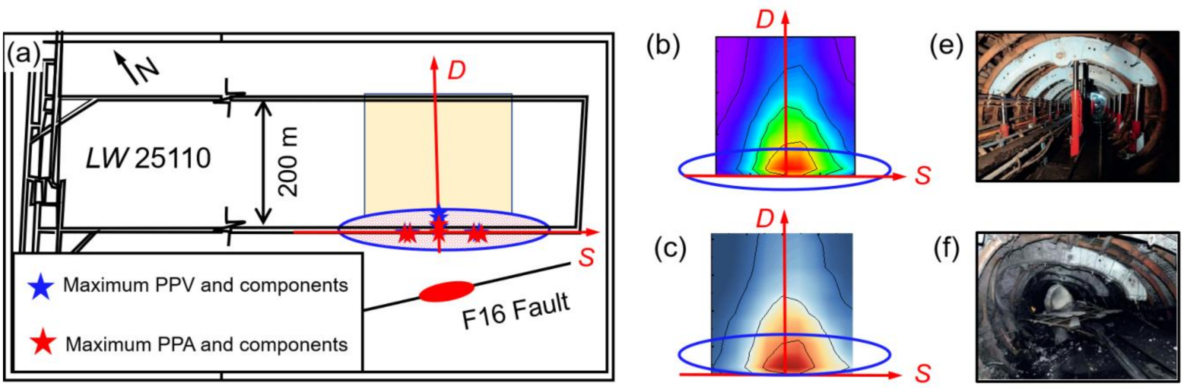

Fig. 4-33 Fault-induced rockburst on the 25110 working face (adapted from Cao et al., 2023; Li et al., 2024a; Wang et al., 2019). (a) Map view of the rockburst and fault location. (b-c) The distribution of PPA and PPV on the roof corresponds to the locations highlighted by the yellow rectangular area in (a). (e) "O-shaped" supports in the head entry unaffected by the rockburst. (f) Deformation of "O-shaped" supports in the head entry impacted by the rockburst. The red and blue stars represent the maximum PPA, PPV, and their respective components.

4.4.3 Limitations

The characterization of the stress on the fault is a most important component in my modeling, yet it remains a significant amount of uncertainty. I assumed a simple background stress field in deep mining environments, but it could be complex due to non-uniform tectonic stress and heterogeneous geological formations. Although my model incorporates field data and insights from previous studies (Cai et al., 2021; Cao et al., 2023b), I need to improve the background stress field by incorporating the in-situ measurements.

A key aspect of my modeling is the introduction of friction law to simulate fault slip and rupture propagation. However, the coefficient of friction μ for the static modeling, yield coefficient of friction μ_s, frictional coefficient of friction μ_d and slip-weaking distance D_c in dynamic modeling were assumed in this study. Although these parameters are crucial in determining the fault behavior, these values cannot be estimated by the in-situ measurements. Thus, I need to use the parameters estimated by the laboratory experiments. These assumptions limit the ability of my model to fully capture the complexity of fault slip behaviors and resultant seismic wave radiations under varying conditions.

I assumed a simplified geological structure for the mining site, particularly uniform material properties within the layers and uniform frictional properties along the fault plane. The model does not fully account for localized variations in rock strength, fault roughness, or the presence of small-scale faults and fractures, which could affect fault slip behavior and seismic wave propagation (Allam et al., 2019). These limitations suggest that further efforts are needed to improve its accuracy in predicting localized phenomena that may occur during mining.

In this study, I assume a planar fault geometry. However, the effects of nonplanar fault geometry have already been significant in rupture propagation, including fault stepover, jog and branching (Harris and Day, 1993; Kame and Yamashita, 1999; Fukuyama and Mikumo, 2006; Xu et al., 2015). However, such nonplanar fault geometry effects on the distribution of slip remain unexplored well. The influence of fault geometry is pivotal in estimating the slip distribution on the faults. Investigating the detailed fault structure in small scale could be worth investigating a priori for the mining operation.

4.5 Summary

Based on the underground structural models of the Yuejin coal mine by Cai et al. (2023) and Cao et al. (2023b), I construct a quantitative model for the estimation of mining-induced fault rupture and its seismic motions on the mining faces. Assuming proper initial stress distribution, I evaluate the non-uniform stress distribution on the fault. Using this stress distribution with appropriate friction coefficients, static slip distribution and dynamic rupture propagation are computed. I then investigate *PPA*, *PPV*, and their corresponding dominant frequencies f_a and f_v as well as the duration of seismic vibration on the mining face are evaluated. These vibration on the mining face could be used to design the support system in the mining faces to improve their stability.

My numerical simulations identify the mechanism of mining-induced fault–slip rockburst as the decrease in σ_n and increase in τ during longwall mining. I assume the nucleation zone model where tiny preslip occurred prior to the dynamic rupture. The preslip size is consistent with the theoretically predicted nucleation zone size (Galis et al., 2015). I then confirm that the static slip distribution is consistent with the final slip distribution computed by dynamic rupture propagation simulation. The rupture velocity reaches 1.7 km/s along fault dip with a peak slip rate of 1.6 m/s for Model_Cao, while for Model_Cai, the rupture velocity is 1.0 km/s and the peak slip rate is 3.4 m/s.

I estimate the moment rate function that shows the rate of seismic radiation energy during the rupture propagation. It also shows a rupture duration of 76 ms in Model_Cao and 73 ms in Model_Cai. I investigate the dependence of both D_c and C on the moment rate and rupture propagation. The results indicate that increasing D_c leads to a more gradual energy release and reduced rupture velocity. Higher C stabilizes fault slip, also resulting in a more gradual energy release and reduced rupture velocity.

Seismic wave analysis shows significant impacts on the working face and roadways, in terms of *PPV*, *PPA*, f_v, f_a and duration. Given the high *PPV* and *PPA* with f_v and f_a as well as the seismic wave duration, robust asymmetric support systems capable of absorbing and dissipating seismic energy are essential. These support designs should further account for the seismic vibration characteristics evaluated in this study to mitigate the risk of structural failure.

Chapter 5 Discussion

5.1 Fault reactivation and slip mechanism

Previous studies have established a valuable framework for understanding fault reactivation mechanisms under varying stress conditions. Notably, the introduction of slip tendency analysis (Morris et al., 1996) has provided an efficient method for evaluating the likelihood of fault slip within a given stress field, emphasizing the critical relationship between shear and normal stresses. This methodology has been widely adopted in seismic risk assessment, particularly for analyzing fault populations across diverse tectonic stress regimes. In the context of deep mining, significant progress has been made in exploring the role of shear stress concentration as a key driver of fault instability (e.g., Song and Liang, 2021; Shan et al., 2023), contributing to our understanding of mining-induced seismic events. Building on this foundation, this dissertation introduces the fault stress ratio, an extension of slip tendency analysis, as a comprehensive parameter to evaluate fault stability. By integrating the effects of both shear and normal stress perturbations, this approach provides a more holistic assessment of fault slip behavior under deep mining conditions. This advancement enables a more detailed understanding of the interplay between stress components, offering improved predictions of fault reactivation and contributing to the development of effective seismic risk mitigation strategies in mining environments.

Fault stability is typically evaluated using the ratio of shear stress (τ) to normal stress (σ_n), as described by Morris et al. (1996). This parameter effectively reflects the propensity of a fault to slip within a given far stress field, with higher values indicating an increased likelihood of fault reactivation. I further organized and integrated the results from Fig. 2-2 in Chapter 2 into a comprehensive diagram, as shown in Fig. 5-1. In fact, the perspective presented in Fig. 5-1 is not novel. Fundamentally, my findings align closely with those of Sibson (1990). This highlights that, despite differences in methodologies and datasets, the core understanding of rupture nucleation mechanisms on unfavorably oriented faults remains consistent with Sibson's seminal framework, providing further support for his theoretical insights.This can be interpreted as the overall stability of a fault prior to mining. If the fault dip angle and background stress conditions (specifically for the reverse faulting regime where r_b>1.0) are known, the overall fault stability can be preliminarily assessed. By analyzing the k-value, which reflects the fault slip tendency, we can determine the fault stability: the larger the k-value (closer to the friction coefficient, μ), the greater the slip tendency of the fault. Building on this, it is logical to further classify the mining-affected area into three zones: (1) fault slip failure zone ($k = \mu$), (2) unstable but unslipped region, and (3) stability-enhanced region, as illustrated in Fig. 2-3.

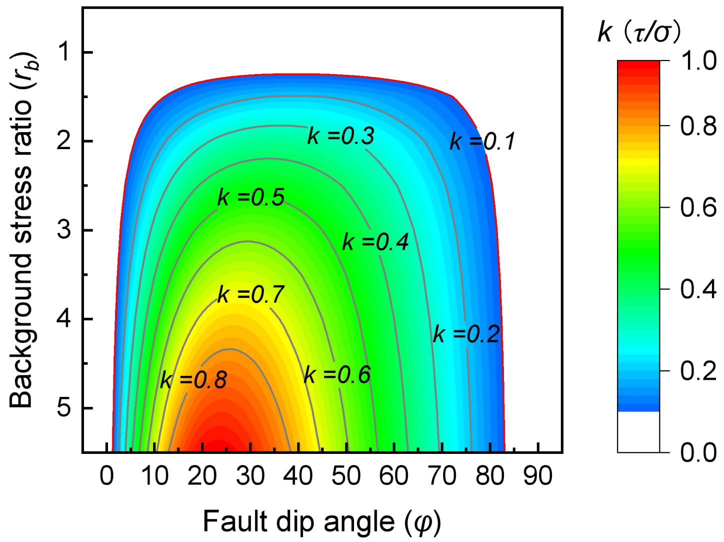

Fig. 5-1 Relationship between fault stress ratio, background stress ratio ($r_b = \sigma_1/\sigma_3$), and fault dip angle (φ), under far-field (background stress) conditions. This figure integrates the results from Fig. 2-2 in Chapter 2, presenting a φ-r_b plane distribution of k, where both the horizontal axis (φ) and the vertical axis (r_b) are treated as variables. Note that this analysis focuses exclusively on the reverse faulting regime, where r_b>1.0.

Fig. 2-5 presents a quantitative analysis of this ratio in a mining environment, revealing that deep mining not only reduces fault stability in certain areas but also enhances stability in others. The Mohr-Coulomb failure criterion (Eq. 2-6) extends the stability analysis by incorporating both the inherent strength of fault materials and frictional resistance. To achieve a more comprehensive evaluation of fault stability, it is essential to consider cohesion (C), a critical material property representing the intrinsic strength of the fault. Based on these considerations, the fault stability metric—fault stress ratio—is revised as follows:

$$K = \frac{\tau - C}{\sigma_n} \tag{5-1}$$

The revised fault stress ratio (K) provides a critical measure for assessing fault stability, with higher values indicating an increased likelihood of fault slip. This modification highlights the direct influence of material strength on reducing the driving shear stress, providing a more accurate representation of fault slip potential. When C is significant, even under high τ, the fault may remain stable. This approach is particularly meaningful for evaluating faults with high intrinsic strength, such as: **Competent rock masses**: Faults with significant cohesion (e.g., intact primary faults) are more resistant to slip despite high shear stress levels. **Strongly bonded faults**: Faults requiring substantial shear stress to overcome cohesion are better captured by this formulation. The comparison with Morris et al. (1996) is summarized in Table 5-1.

Table 5-1 Comparison with Morris et al. (1996)

Aspect	Morris et al. (1996)	Revised fault stress ratio (K)
C inclusion	Assumes $C = 0$, with all shear stress contributing to slip	Accounts for C, emphasizing its stabilizing effect
Applicability	Suitable for cohesionless or fractured faults	Suitable for cohesive or partially intact faults
Definition of τ	Considers all τ as driving force	Only τ exceeding cohesion contributes to slip
Fault slip valuation	May overestimate slip risk for strong faults	Offers a more conservative and accurate evaluation

Note: Studying the evolution of C during fault activation (e.g., gradual degradation from intact rock mass to granular debris) can improve the prediction accuracy of K in dynamic environments.

The role of pore pressure (P_p) is critical in fault slip mechanisms, as it directly alters the effective normal stress (σ_n') acting on the fault plane (Bujize et al., 2019; Ellsworth 2013; Talwani and Acree 1984;). The effective normal stress can be expressed as:

$$\sigma_n^{'} = \sigma_n - P_p \tag{5-2}$$

where σ_n is the total normal stress, P_p is the pore pressure.

Pore pressure reduces the effective normal stress, thereby decreasing the frictional resistance along the fault plane and increasing the likelihood of slip. Consequently, the fault stress ratio (K) can be reformulated to include the effect of pore pressure as follows:

$$K = \frac{\tau}{\sigma_n - P_p} \tag{5-3}$$

This revised expression highlights that an increase in pore pressure (P_p) reduces the effective normal stress, leading to an increase in K. As K approaches the fault's critical threshold, the fault becomes increasingly prone to reactivation and slip.

By including intermediate principal stress in a 3-D modeling framework, I addresses a limitation in traditional 2-D models, which often omit intermediate principal stress (e.g., Haimson and Chang, 2000, 2002). Results demonstrate that intermediate stress can significantly influence coseismic slip, especially when mining-induced stress perturbations interact unfavorably with fault geometries. These findings provide a more nuanced understanding of the factors affecting fault-slip behavior. For example, Chapter 2 shows how footwall mining induces stress disturbances that destabilize regions above the fault. While prior 2-D models have identified shear stress changes as a trigger for fault reactivation (e.g., Song and Liang, 2021), I extend the analysis by incorporating both shear and normal stress effects within a 3-D framework. Similarly, Chapter 3 highlights the critical role of intermediate far-field stress and mining panel geometry in fault reactivation. Findings indicate that increasing intermediate stress or aligning mining panels parallel to fault strike can expand slip areas, providing insights into optimizing mining layouts.

The use of 3-D models offers distinct advantages, particularly in simulating the complex stress distributions in mining environments. Unlike 2-D models, which primarily capture Mode II slip behavior, the 3-D approach reveals the interplay between Mode II (in-plane) and Mode III (anti-plane) slip. These advancements allow for more precise predictions of slip patterns, offering practical guidance for reducing seismic risks in deep mining.

5.2 Comparison of the scenario-based and phenomenological approaches

Research on fault slip mechanisms generally employs either phenomenological approaches or scenario-based approaches. Phenomenological methods rely on empirical observations and statistical models to describe the relationship between fault slip and stress perturbations. For example, the fault mechanics model developed by Wallace and Morris (1986) quantifies the likelihood of fault slip using geometric relationships based on observed data. While these methods are effective for trend analysis, their heavy reliance on observational datasets limits their applicability to specific stress conditions. Additionally, phenomenological approaches often fail to capture the dynamic processes behind fault slip, such as mining-induced stress redistribution and transient rupture evolution. In contrast, scenario-based approaches focus on developing physical models and simulating fault slip under controlled conditions. The scenario-based approach adopted in my thesis offers deeper insights into the underlying mechanisms of fault slip through the following features:

Physics-based modeling: My thesis employs a three-dimensional dynamic fault slip model combined with a linear slip-weakening law to investigate the effects of mining-induced stress perturbations on fault stability. This modeling framework captures the full progression from stress accumulation to fault slip, aligning with the approach of Dunham et al. (2011), which focuses on slip-weakening processes during rupture. Furthermore, the emphasis on cohesion and frictional strength highlights critical physical details often overlooked in phenomenological methods.

Scenario-specific stress state design: To analyze fault stability under mining conditions, my thesis designs various stress scenarios, including changes in mining panel orientation, depth, and fault geometry. For example, mining panels oriented parallel to the fault strike may lead to high shear stress concentration, while adjustments in layout can mitigate stress concentration zones. These scenario-specific simulations provide quantitative insights into stress redistribution, offering practical guidelines for optimizing mining layouts.

Dynamic rupture and seismic wave propagation analysis: My thesis captures the temporal evolution of fault slip through dynamic rupture simulations. Key parameters, such as rupture velocity, slip distribution, and peak particle velocity (*PPV*), are directly computed. The findings reveal the significant influence of fault heterogeneity on slip behavior, consistent with the conclusions of Fang and Dunham (2013), which emphasize the role of fault surface roughness in rupture dynamics.

Model validation and practical applications: The scenario-based simulations demonstrate strong agreement with real-world observations. For instance, the simulated seismic moment magnitude (M_w = 2.4 – 2.6) of the "8.11" Yuejin coal burst closely matches the recorded local magnitude (M_L = 2.7). Furthermore, by analyzing mining-induced seismic wave parameters, my thesis proposes an optimized design for seismic-resistant support systems.

The scenario-based approach offers significant advantages over phenomenological methods by incorporating physical modeling and dynamic simulations. It not only captures the temporal and spatial evolution of fault slip but also provides actionable insights for mitigating seismic risks and optimizing mining operations.

5.3 Advances in dynamic rupture modeling and seismic wave propagation

Dynamic rupture and seismic wave propagation have been topics of active research in mining-induced seismicity. Previous studies have explored factors such as fault friction angle, mining depth, and fault proximity, using static and simplified dynamic models to assess seismic energy release (e.g., Jiang et al., 2020; Li 2024a, 2024b, 2025; Li and Gao, 2025; Sainoki and Mitri, 2014a, 2014b). Building on earlier work (Cai et al.,2021; Cao et al., 2023), this dissertation integrates static stress analyses with dynamic rupture simulations using the finite element method (FEM) (Aagaard et al., 2013). By applying a linear slip-weakening law based on nucleation theory (e.g., Galis et al., 2015), Chapter 4 provides a detailed analysis of dynamic rupture processes.

The nucleation process is a critical component in the study of fault slip and rupture propagation, governing the transition from a quasi-static state to dynamic rupture. In this research, nucleation theory plays a vital role in predicting mining-induced fault slip, particularly in analyzing the effects of localized stress changes on the sliding process. The critical nucleation radius (R_{nuc}) is a key parameter for determining whether the nucleation zone can trigger rupture propagation. Based on the slip-weakening friction law, my thesis calculates the critical nucleation size and evaluates the influence of mining-induced stress and background stress distributions on the spatial extent of R_{nuc}.

To ensure the reliability of nucleation process assumptions, this study validates the results through several approaches. Dynamic rupture analysis reproduces the spatiotemporal evolution of rupture, particularly by examining the slip rate progression during rupture propagation. A comparison between dynamic rupture results and static solutions demonstrates that the final slip distribution from dynamic rupture aligns closely with static equilibrium solutions. Additionally, in the Model_Cao scenario of chapter 4, where the mining face is parallel to the fault strike, the nucleation region exhibits clear symmetry, and the calculated nucleation size is consistent with theoretical predictions.

5.4 Mitigation and control of mining-induced seismicity

Mining-induced seismicity presents unique opportunities for prevention and control compared to natural earthquakes due to its shallow source depth and direct linkage to human activities (Li et al., 2025; Gibowicz, 2009; Xuanmei et al., 2019). Far-field stress refers to the regional stress field caused by large-scale tectonic processes, such as plate movements, and is generally uniform over broad areas (Jaeger 2007; Scholz 2019). In contrast, near-field stress occurs in the vicinity of faults or local structures and is influenced by fault geometry, slip, and stress concentrations. Far-field stress provides the driving force for fault activity, while near-field stress governs the local rupture nucleation and propagation. The two are interconnected, with near-field stress reflecting the localized response to the broader far-field stress regime. In this study, I identified a critical distinction: the stress perturbations caused by mining, referred to here as near-field stresses, are a direct result of anthropogenic activities (Su et al., 2024). This concept of near-field stress may central to understanding and managing mining-induced seismicity.

The influence of far-field stress on fault movement has been extensively examined in studies of rock failure and fault slip, while the localized effects of near-field stress remain insufficiently explored. Stephens et al. (2017) provided valuable insights into this topic through their investigation of the Loch Scridain Sill Complex on the Isle of Mull, Scotland. The research highlighted the combined effects of far-field tectonic stress and near-field volcanic stress on structural evolution. Far-field NW–SE horizontal shortening was identified as the dominant control on the formation and geometry of dykes, whereas near-field radial compressive and tensile stresses, induced by inflation of the central volcanic complex, played a critical role in driving sill emplacement. The interplay between these stresses dictated fracture opening directions and shaped the step-like geometry of sills. Stephens et al. (2017) underscored the role of far-field stress as a regional framework while emphasizing the importance of near-field stress in influencing local magma emplacement and structural deformation.

The findings of Stephens et al. (2017) offered valuable insights for studying induced seismicity, particularly in contexts such as deep coal mining and roadway excavation. Far-field stress has often been regarded as the primary driver of fault slip and seismic activity, a view widely supported in natural earthquake studies (e.g., Xiang and Yang). However, near-field stress, arising from localized stress redistribution and concentration due to excavation or material extraction, played a pivotal role in controlling rock failure and fault slip mechanisms. These observations highlighted the necessity of incorporating near-field stress adjustments into models for analyzing and predicting induced seismicity.

Far-field stress, with its relatively stable distribution and accessibility through in situ monitoring, provides a reliable foundation for understanding induced seismicity. In contrast, near-field stress encompasses additional stress perturbations directly imposed on faults by mining activities. Unlike tectonic earthquakes, where stress sources are deeper and predominantly influenced by far-field tectonic forces, mining-induced seismic events are typically shallower and more localized, reflecting direct human intervention. This distinction necessitates a dual focus on both far-field and near-field stress dynamics to accurately model and mitigate seismic risks in mining environments. My thesis analysis further demonstrated that mining-induced stress disturbances govern not only the initiation of seismic events but also their rapid termination, typically within tens of milliseconds. The termination characteristics, closely aligned with static mechanical solutions, suggested the potential for proactive intervention. By leveraging the predictable nature of these events, the source distribution and potential magnitude of induced seismicity could be estimated in advance. Such predictive capabilities inform critical engineering decisions, including the design of stop lines, optimization of working face layouts, and the selection or enhancement of support systems. These integrative approaches are essential for improving the safety and sustainability of mining operations, particularly in environments prone to mining-induced seismicity.

5.4.1 Key findings supporting seismic risk mitigation

1. Consistency of finalized ruptures with static solutions

Chapter 4 of this dissertation investigates the relationship between dynamic fault rupture processes and static equilibrium solutions, highlighting their practical application in seismic risk mitigation. The research demonstrated that static stress models can accurately predict the spatial distribution of coseismic slip and identify fault segments prone to reactivation. These findings establish a strong connection between theoretical calculations and observed rupture characteristics during mining-induced seismic events.

A key advantage of the static solutions developed in this study is their computational efficiency. Unlike dynamic simulations, which require significant computational resources, static models can quickly delineate potential rupture zones and provide reliable estimates of the earthquake magnitude associated with mining-induced fault slip. This capability is particularly valuable for real-time risk assessments and the design of mitigation strategies in deep mining operations. By leveraging the predictive power of static analyses, this dissertation offers a practical and scalable approach to anticipate seismic hazards, optimize mining layouts, and enhance underground safety.

2. Insights into rupture termination

Chapter 4 of this dissertation provides a comprehensive analysis of the factors influencing rupture cessation in mining-induced seismic events. The termination of rupture is closely linked to the stress distribution before the rupture event. Specifically, the stress ratio in the vicinity of the rupture termination zone was found to be relatively small, a condition caused by mining-induced stress disturbances that redistributed the local stress field and inhibited further fault slip. This phenomenon highlights how mining operations can create zones of reduced shear-to-normal stress ratios, naturally limiting rupture propagation. Dynamic rupture simulations further revealed that rupture termination is influenced by stress redistribution, fault geometry, and material properties such as critical slip distance (D_c) and cohesion (C). The results demonstrate that rupture propagation halts when the energy driving the slip is insufficient to overcome fault resistance, with larger Dc and higher C dissipating stress over wider areas, slowing rupture progression and facilitating termination. Conversely, smaller D_c and lower C result in abrupt rupture cessation and localized energy release. For example, simulations using Model_Cao indicated rupture termination after approximately 76 ms, with diminishing slip amplitudes along fault edges as stress concentrations dissipated.

It is also critical to note that this study employed a uniform friction coefficient in the simulations. While this simplification aids in isolating the influence of stress perturbations on rupture dynamics, it does not capture potential spatial variations in frictional properties. Future studies could explore non-uniform friction to better understand its interaction with mining-induced stress changes and rupture termination mechanisms. These findings provide valuable insights into rupture cessation mechanisms, emphasizing the importance of mining-induced stress alterations, material properties, and fault geometry in controlling fault reactivation and termination. This understanding offers practical guidance for designing safer mining operations by identifying fault segments where ruptures are likely to halt. Optimized mining layouts based on these insights can significantly reduce seismic risks, forming a robust framework for assessing and mitigating seismic hazards in deep mining environments.

Further insights into rupture termination have been provided by studies such as Buijze et al. (2019), which explored the role of pressure changes in the context of hydrocarbon reservoir depletion. Their work demonstrated that variations in reservoir pressure significantly influence rupture propagation and termination. Specifically, pressure depletion reduces the effective normal stress on fault planes, altering the fault's ability to sustain slip and thereby affecting the conditions under which ruptures arrest. These findings highlight the critical interplay between external stress factors and fault stability, offering valuable parallels for understanding rupture termination mechanisms in deep mining environments. Incorporating pressure-related stress changes into rupture arrest criteria could enhance predictive models and improve mitigation strategies for mining-induced seismicity.

Future research should focus on developing a robust criterion for rupture arrest that integrates multiple factors influencing fault stability. This includes the initial stress state, stress drop, fracture energy, and stresses induced by deep mining activities. A comprehensive rupture arrest model would allow for more precise predictions of where and when rupture propagation halts, offering actionable insights for seismic risk management in mining environments. Validating such a criterion against dynamic rupture simulations, as exemplified by studies like Galis et al. (2017), will be crucial for refining its predictive capabilities and ensuring its applicability to real-world scenarios. By bridging theoretical advances with practical validation, this approach has the potential to significantly enhance our ability to mitigate seismic hazards in deep mining operations.

5.4.2 From mechanism study to prevention and control

The integration of near-field stress analysis into mining operations provides a robust framework for mitigating seismic risks associated with mining-induced fault slip. By leveraging a comprehensive understanding of the relationships between mining-induced stress changes, slip distribution, and rupture termination mechanisms, operators can implement strategies to prevent and control seismic events effectively. The following measures outline actionable steps derived from this study:

1. Prevent induced seismic events

Mining-induced seismic events can be mitigated by designing operations that minimize stress accumulation near fault zones. Near-field stress analysis allows for the identification of critical areas prone to stress concentration and potential fault reactivation. By adjusting mining layouts to avoid these zones—such as maintaining a safe distance from major faults or modifying the depth and sequence of excavation—operators can proactively reduce the likelihood of seismic event initiation. Furthermore, incorporating stress field simulations into pre-mining assessments ensures that high-risk fault segments are identified and excluded from critical mining zones.

Controlling seismicity requires the implementation of mining sequences and layouts that promote favorable stress redistribution. For example, staggered mining or alternating the direction of working faces can help dissipate stress more evenly, reducing the risk of uncontrolled fault activation. The results from this research indicate that specific mining geometries, such as panel orientation and length, significantly influence stress redistribution patterns. Tailoring these parameters based on near-field stress analysis can limit stress concentrations and facilitate gradual fault slip, minimizing the intensity of seismic events.

2. Dynamic monitoring and strengthening support systems

Monitoring of stress changes and seismic activity in the vicinity of mining operations enhances the capacity for adaptive management. Technologies such as microseismic monitoring and in-situ stress measurements can provide early warnings of hazardous conditions, allowing operators to adjust mining plans dynamically. By integrating observe data with the predictive models developed in this study, operators can better anticipate fault behavior and implement timely interventions to prevent or mitigate seismic risks. Near-field stress analysis also informs the design and placement of support systems. Areas identified as having high residual stress or slip potential can be reinforced using advanced support technologies such as rock bolts, cable anchors, and shotcrete. This approach ensures that infrastructure is resilient to both static stress accumulation and dynamic impacts from seismic waves.

By transitioning from mechanism studies to actionable prevention and control measures, this research bridges the gap between theoretical insights and practical applications. The integration of stress analysis into mining operations not only enhances safety but also improves operational efficiency by minimizing interruptions caused by seismic events.

5.5 Limitations modeling the nucleation and dynamics of fault slip

Despite the significant theoretical and modeling advances presented in this dissertation, several important areas remain unexplored, warranting further research.

Based on Ohnaka and Shen (1999), the nucleation process involves a transition from a quasi-static phase to dynamic rupture. However, I primarily focus on the propagation of rupture after the nucleation point and does not explicitly model or analyze the nucleation phase. Ohnaka and Shen (1999) detailed the nucleation process as consisting of two distinct phases: a quasi-static phase with slow rupture growth and an accelerating phase leading to dynamic propagation (Fig. 5-2). These phases are influenced by fault surface roughness, with the critical nucleation size (2 R_{nuc}) and slip characteristics varying significantly. My research adopts a model that assumes the rupture begins to propagate dynamically at the critical time (t = 0) with a bidirectional high-velocity rupture. This simplification aids in focusing on rupture dynamics, it omits detailed treatment of the nucleation process. While my work defines the critical size of the nucleation zone (2 R_{nuc}) and integrates this parameter into the dynamic rupture model, the physical mechanisms leading to this critical state remain unaddressed. The absence of a detailed analysis of the nucleation process, including its quasi-static and accelerating phases, limits the ability to explore the scale-dependent factors influencing nucleation in deep mining environments. Incorporating the nucleation model could provide a more comprehensive understanding of how stress accumulation and geometric irregularities of faults contribute to the onset of dynamic rupture (Han et al., 2016; Kato et al., 2012; Ohnaka 1996; Shibazaki and Matsu'ura, 1992, 1998).

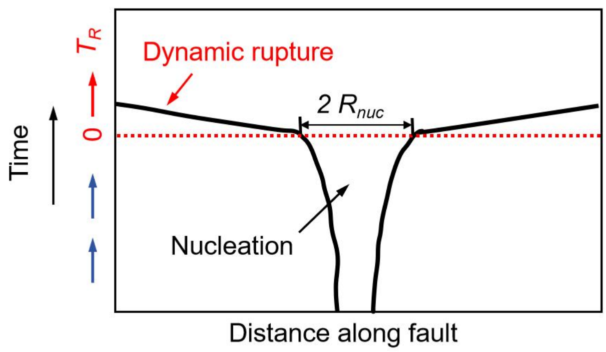

Fig. 5-2 A rupture nucleation model (adapted from Fig. 29 of Ohnaka and Shen, 1999). In this model, it is assumed that rupture initiates and propagates bidirectionally at a rapid rupture velocity starting from the critical time, t =0. The parameter 2 R_{nuc} represents the critical size of the nucleation zone, as defined in Eq. (4-6).

The lack of validation with observational data represents a limitation of my study. Although preliminary validation was conducted using seismic data from the Yuejin coal mine, seismic waveform is required to calibrate the model more accurately. Future research should incorporate seismic wave monitoring and fault slip measurements to enhance the reliability and precision of the model predictions.

Despite its advantages in accuracy and practicality, this approach faces challenges such as high computational costs and reliance on high-quality field data. Future work could focus on improving computational efficiency and incorporating more sophisticated material models (Foulger et al., 2018; Kozłowska et al., 2015) to enhance predictive accuracy. My thesis does not fully account for material heterogeneity or fault topography. The models assume homogeneous rock properties, a simplification that does not reflect the complexity of actual mining environments. Variations in rock strength and fault surface roughness could significantly affect slip behavior (Sainoki and Mitri, 2014; Tal et al., 2018; 2020). Modeling fault–slip in mining contexts has often relied on the classical Mohr-Coulomb criterion to represent shear strength due to its simplicity (Morris et al., 1996). However, this approach may yield inaccurate results when considering natural fault surfaces, which are rarely planar due to factors such as rock mass fabrics, in-situ stresses, and geological structures (Romanet et al., 2024; Wallace and Morris, 1986). Asperities on fault surfaces, governed by net slip, are crucial in regulating friction, slip dynamics, and fault velocity (Dieterich and Kilgore, 1996). Thus, using the Mohr-Coulomb criterion without accounting for fault roughness could oversimplify the modeling of shear strength. To address this, several shear strength models have been proposed, including Barton's empirical model that considers surface roughness based on experimental shear tests and other models that incorporate asperity angle and normal stress ratios (Barton, 1973; Indraratna et al., 2005; Patton, 1966). The complexity of fault behavior is further amplified during dynamic processes like fault–slip bursts, where fault surface properties and slip rates influence how asperities are sheared off, leading to drastic changes in the fault interface (Ryder, 1988). Rate- and state-dependent friction laws have been introduced to simulate such dynamic fault–slip phenomena, commonly observed in both earthquakes and mining-induced seismic events (Dieterich et al., 1979; Ruina, 1983). These friction laws account for slip-rate dependence, allowing for the simulation of slip weakening and strengthening behaviors—key aspects of both natural earthquake mechanisms and mining-induced seismicity (Perrin et al., 1995). Additionally, several studies have explored how fault roughness, from micro-scale to macro-scale, affects frictional parameters such as stress drop and slip weakening distances (Marone and Cox, 1994; Harbord et al., 2017). Experimental and numerical investigations have shown that fault geometry significantly impact fault stability, potentially leading to both aseismic and seismic slip events (Dunham et al., 2011; Fang and Dunham, 2013; Luo and Ampuero, 2018; Shi and Day, 2013; Tal et al., 2018; Xu et al., 2022; Yamashita et al., 2018). These findings highlight the importance of incorporating roughness, dynamic processes, and frictional behavior into models to accurately assess fault–slip risks in deep mining environments. Future work should incorporate greater geological heterogeneity to simulate more realistic mining conditions.

In terms of fault properties, the current elastic model treats the fault as a zero-thickness interface. Evaluating fault friction along a fault zone is complex, as it depends on accurately understanding the factors that govern the local stress conditions (Soliva et al., 2010). In reality, faults contain fault gouge (and/or pressurized fluid) (Haines and Pluijm, 2012; Ishikawa et al., 2014; Liu et al., 2024; Piane et al., 2016; Niwa et al., 2016). Induced seismicity in the presence of pressurized water could exacerbate fault slip, posing serious challenges, particularly in deep mining or subsea environments where water pressure plays a substantial role. Research into fault slip under coupled multiphysical conditions should be pursued to address these concerns.

Chapter 6 Conclusions

6.1 Summary of research outcomes

This thesis systematically investigated the fault–slip mechanisms underlying mining-induced fault reactivation and fault–slip rockbursts in deep mining operations. Through a combination of 2–D and 3–D numerical modeling, I explored stress redistribution, coseismic slip behavior, dynamic rupture processes, and the resulting seismic impacts on mining infrastructure. By simulating stress perturbations, coseismic slip, and seismic wave radiation, this thesis provided key insights into the interaction between mining activities and fault behavior in deep mining operations, highlighting critical factors influencing fault–slip rockbursts and their mitigation strategies.

In Chapter 2, a 2–D plane-strain model was developed to investigate mining-induced fault failure and coseismic slip through finite element analysis. The results showed that mining-induced fault reactivation is driven primarily by changes in the fault stress ratio (shear stress to normal stress). Key factors such as fault dip angle, mining distance, and background stress ratio were found to influence the likelihood of fault instability. Footwall mining was identified as a higher-risk operation, causing more significant fault slip compared to hanging wall mining. To accurately assess the terminal mining line without inducing earthquakes, I conducted quantitative evaluations of in-situ monitoring values for stress field, fault geometry, and fault friction.

In Chapter 3, the effects of panel length, panel orientation, and far-field stress orientation on fault reactivation and seismic slip were examined. Numerical simulations revealed that increasing the width of the mining panel (W_m) expands the coseismic slip zone and intensifies stress disturbances along fault planes. When stress orientation was varied relative to the fault strike, fault slip length increased significantly with greater far-field stress (σ_y). A critical finding was that shifting the panel layout orientation from parallel to perpendicular to the fault strike effectively mitigates induced seismic responses, reduces the likelihood of fault activation, and enhances the safety and stability of the mining environment.

In Chapter 4, the study was expanded to incorporate dynamic fault rupture processes and analyze seismic wave radiation at the working face of the Yuejin coal mine. The models demonstrated that fault–slip rockbursts are triggered by decreases in normal stress (σ_n) and increases in shear stress (τ) during longwall mining. The nucleation zone model with pre-slip accurately captured rupture initiation, consistent with theoretical predictions. The final static slip distributions closely matched those from dynamic rupture simulations, with Model_Cao reaching a rupture velocity of 1.7 km/s and a peak slip rate of 1.6 m/s, while Model_Cai exhibited values of 1.0 km/s and 3.4 m/s, respectively. Seismic energy release rates, derived from moment rate functions, revealed rupture durations of 76 ms (Model_Cao) and 73 ms (Model_Cai).

The analysis further demonstrated that larger critical slip distances (D_c) and higher cohesive strength (C) lead to slower energy release and reduced rupture velocity, which enhances fault slip stability. Seismic wave radiation analysis showed significant dynamic impacts on the working face and roadways, particularly in terms of peak particle velocity (PPV), peak particle acceleration (PPA), dominant frequency (f_v, f_a) and duration. The results underscored the need for robust support systems capable of absorbing seismic energy. These systems should be tailored to the seismic vibration characteristics identified in this study to mitigate structural failure risks in deep mining environments.

6.2 Outlook

Future research should prioritize the integration of numerical modeling, physical experiments, and field monitoring data to improve the accuracy and applicability of fault slip predictions. Specifically, this can be achieved through the development of large-scale laboratory fault models and the deployment of in-situ instrumentation in active mining areas. By combining data from seismic monitoring systems, stress sensors, and displacement measurements, real-time validation of numerical model outputs will become feasible. This comprehensive approach will yield deeper insights into the mechanics of mining-induced fault reactivation and enhance the reliability of predictive tools for fault-slip behavior.

In addition to fault reactivation, further studies are necessary to investigate the impacts of tunneling and deep underground excavation on fault stability and induced seismicity. As mining operations extend to greater depths and increasingly complex underground structures—such as deep tunnels and chambers—are developed, excavation-induced stress perturbations will interact more significantly with existing geological faults. Analyzing these interactions will allow for more accurate prediction of the seismic responses of underground spaces during both construction and operation. This research is critical for ensuring the stability of infrastructure in deep mining environments.

Moreover, future work should explore non-planar faults and the role of fault gouge, pore pressure conditions, and their contribution to mining-induced seismic events. A particular focus on the dynamic rupture process and fault-slip rockburst under these complex conditions is essential for advancing current predictive capabilities. Expanding this understanding will not only aid in controlling seismic hazards but also provide critical insights for other applications, such as dynamic risk assessment in Carbon Capture and Storage (CCS) projects. By bridging mining-induced seismicity research with CCS development, we can address long-term challenges associated with fault stability and induced seismic risks in deep geological reservoirs.

References

Aagaard BT, Knepley MG, Williams CA (2013) A domain decomposition approach to implementing fault slip in finite-element models of quasi-static and dynamic crustal deformation. J Geophys Res Solid Earth 118(6):3059–3079. https://doi.org/10.1002/jgrb.50217

Aagaard BT, Knepley MG, Williams CA (2023) PyLith Manual, Version 4.0.0. Davis, CA: Computational Infrastructure of Geodynamics. https://pylith.readthedocs.io/en/v4.0.0

Abercrombie RE, Rice JR (2005) Can observations of earthquake scaling constrain slip weakening? Geophys J Int 162(2):406–424. https://doi.org/10.1111/j.1365-246X.2005.02579.x

Afraei S, Shahriar K, Madani SH (2019a) Developing intelligent classification models for rock burst prediction after recognizing significant predictor variables; section 1, literature review and data preprocessing procedure. Tunn Undergr Space Technol 83:324–353. https://doi.org/10.1016/j.tust.2018.09.022

Afraei S, Shahriar K, Madani SH (2019b) Developing intelligent classification models for rock burst prediction after recognizing significant predictor variables; section 2, designing classifiers. Tunn Undergr Space Technol 84:522–537. https://doi.org/10.1016/j.tust.2018.11.011

Aki K (1967) Scaling law of seismic spectrum. J Geophys Res 72(4):1217–1231. https://doi.org/10.1029/JZ072i004p01217

Aki K, Richards PG (2009) Quantitative Seismology (2nd Ed.). University Science Books, 700pp.

Allam AA, Kroll KA, Milliner CWD, Richards-Dinger KB, Lawrence Livermore National Lab (LLNL), Livermore, CA (United States) (2019) Effects of fault roughness on coseismic slip and earthquake locations. J Geophys Res Solid Earth 124(11):11,336–11,349. https://doi.org/10.1029/2018JB016216

Ampuero J, Rubin AM (2008) Earthquake nucleation on rate and state faults; aging and slip laws. J Geophys Res 113(B1). https://doi.org/10.1029/2007JB005082

Andrews DJ (1976) Rupture velocity of plane strain shear cracks. J Geophys Res 81(32):5679–5687. https://doi.org/10.1029/JB081i032p05679

Askaripour M, Saeidi A, Rouleau A, Mercier-Langevin P (2022) Rockburst in underground excavations: A review of mechanism, classification, and prediction methods. Underground Space 7(4):577–607. https://doi.org/10.1016/j.undsp.2021.11.008

Bai J, Dou L, Li J, Zhou K, Cao J, Kan J (2022) Mechanism of coal burst triggered by mining-induced fault slip under high-stress conditions: A case study. Front Earth Sci 10. https://doi.org/10.3389/feart.2022.884974

Bakun WH, Lindh AG (1977) Local magnitudes, seismic moments, and coda durations for earthquakes near Oroville, California. Bull Seismol Soc Am 67(3):615–629. https://doi.org/10.1785/BSSA0670030615

Balsamo F, Storti F, Salvini F, Silva A, Lima C (2010) Structural and petrophysical evolution of extensional fault zones in low-porosity, poorly lithified sandstones of the Barreiras Formation, NE Brazil. J Struct Geol 32:1806–1826. https://doi.org/10.1016/j.jsg.2009.10.010

Barton N (1973) Review of a new shear-strength criterion for rock joints. Eng Geol 7(4):287–332. https://doi.org/10.1016/0013-7952(73)90013-6

Basnet MP, Mahtab S, Jin A (2023) A comprehensive review of intelligent machine learning-based predicting methods in long-term and short-term rock burst prediction. Tunn Undergr Space Technol 142:105434. https://doi.org/10.1016/j.tust.2023.105434

Bigarre P, Tinucci J, Ben Slimane K, Piguet J, Besson JC (1992) Three-dimensional modeling of fault–slip rockbursting. Acta Montan Ser A Geodyn 2(88):81–89.

Bindi ML, Biancofiore G, Meacci L, Bellissima G, Nardi S, Pieri M, Vistoli F, Boggi U, Sansevero A, Mosca F (2005) Early morbidity after pancreas transplantation. Transpl Int 18(12):1356–1360. https://doi.org/10.1111/j.1432-2277.2005.00222.x

Bizzarri A (2010) How to promote earthquake ruptures; different nucleation strategies in a dynamic model with slip-weakening friction. Bull Seismol Soc Am 100(3):923–940. https://doi.org/10.1785/0120090179

Bott MHP (1959) The mechanics of oblique slip faulting. Geol Mag 96(2):109–117. https://doi.org/10.1017/S0016756800059987

Buijze L, van den Bogert PAJ, Wassing BBT, Orlic B (2019) Nucleation and arrest of dynamic rupture induced by reservoir depletion. J Geophys Res Solid Earth 124(4):3620–3645. https://doi.org/10.1029/2018JB016941

Byerlee J (1978) Friction of rocks. Pure Appl Geophys 116(4):615–626. https://doi.org/10.1007/bf00876528

Cai M (2016) Prediction and prevention of rockburst in metal mines; a case study of Sanshandao gold mine. J Rock Mech Geotech Eng 8(2):204–211. https://doi.org/10.1016/j.jrmge.2015.11.002

Cai M (2024) Rockburst risk control and mitigation in deep mining. Deep Resour Eng. https://doi.org/10.1016/j.deepre.2024.100019

Cai W, Dou L, Li Z, He J, He H, Ding Y (2015) Mechanical initiation and propagation mechanism of a thrust fault; a case study of the Yima section of the Xiashi-Yima thrust (north side of the eastern Qin Ling orogen, China). Rock Mech Rock Eng 48(5):1927–1945. https://doi.org/10.1007/s00603-014-0666-x

Cai W, Dou LM, Min Z, Cao W, Shi J, Feng LF (2018) A fuzzy comprehensive evaluation methodology for rock burst forecasting using microseismic monitoring. Tunn Undergr Space Technol 80:232–245.https://doi.org/10.1016/j.tust.2018.06.029

Cai W, Dou LM, Si G, Cao A, Guang S, Wang GF, Yan S (2019) A new seismic-based strain energy methodology for coal burst forecasting in underground coal mines. Int J Rock Mech Min 123:104086. https://doi.org/10.1016/j.ijrmms.2019.104086

Cai W, Dou L, Si G, Hu Y (2021) Fault-induced coal burst mechanism under mining-induced static and dynamic stresses. Engineering (Beijing, China) 7(5):687–700. https://doi.org/10.1016/j.eng.2020.03.017

Cai W, Bai X, Si G, Cao W, Guang S, Dou LM (2020) A monitoring investigation into rock burst mechanism based on the coupled theory of static and dynamic stresses. Rock Mech Rock Eng 53(12):5451–5471. https://doi.org/10.1007/s00603-020-02237-6

Cao JR, Dou LM, Konietzky H, Kunyou Z, Min Z (2023a) Failure mechanism and control of the coal bursts triggered by mining-induced seismicity; a case study. Environ Earth Sci 82(7). https://doi.org/10.1007/s12665-023-10856-9

Cao M, Wang T, Li K (2023b) A numerical analysis of coal burst potential after the release of the fault–slip energy. Rock Mech Rock Eng 56(5):3317–3337. https://doi.org/10.1007/s00603-023-03224-3

Cao Y, He D, Glick DC (2001) Coal and gas outbursts in footwalls of reverse faults. Int J Coal Geol 48:47–63. https://doi.org/10.1016/S0166-5162(01)00037-4

Cartwright-Taylor A, Mangriotis M, Main IG, Butler IB, Fusseis F, Ling M, Andò E, Curtis A, Bell AF, Crippen A, Rizzo RE, Marti S, Leung DDV, Magdysyuk OV (2022) Seismic events miss important kinematically governed grain scale mechanisms during shear failure of porous rock. Nat Commun 13(1):6169. https://doi.org/10.1038/s41467-022-33855-z

Cervera M, Barbat GB, Chiumenti M (2017) Finite element modeling of quasi-brittle cracks in 2D and 3D with enhanced strain accuracy. Comput Mech 60(5):767–796. https://doi.org/10.1007/s00466-017-1438-8

Chang C, Haimson B (2000) True triaxial strength and deformability of the German Continental Deep Drilling Program (KTB) deep hole amphibolite. J Geophys Res 105(B8):18999–19013. https://doi.org/10.1029/2000JB900184

Chang C, Haimson B (2012) A failure criterion for rocks based on true triaxial testing. Rock Mech Rock Eng 45(6):1007–1010. https://doi.org/10.1007/s00603-012-0280-8

Chen L, Shen B, Dlamini B (2018) Effect of faulting on coal burst - A numerical modeling study. Int J Min Sci Technol 28(5):739–743. https://doi.org/10.1016/j.ijmst.2018.07.010

Chen S, Tang J, Pan Y (2024) Constitutive model of uniaxial compression for rock (coal) and bursting liability index based on the structure ensemble dynamics theory. Rock Mech Rock Eng. https://doi.org/10.1007/s00603-024-04112-0

Cheng G, Li L, Zhu W, Yang T, Tang C, Zheng Y, Wang Y (2019) Microseismic investigation of mining-induced brittle fault activation in a Chinese coal mine. Int J Rock Mech Min Sci 123:104096. https://doi.org/10.1016/j.ijrmms.2019.104096

Cook NGW (1965) A note on rockbursts considered as a problem of stability. J S Afr Inst Min Metall 65(8):437–446.

Corner B (1985) Seismic research associated with deep level mining; rock burst prediction and vibration damage to buildings in South Africa. Geophysics 50(12):2914–2915. https://doi.org/10.1190/1.1441897

Courant R, Friedrichs K, Lewy H (1928) Über die partiellen Differenzengleichungen der mathematischen Physik. Math Ann 100:32–74.

Cundall PA, Strack ODL (1979) A discrete numerical model for granular assemblies. Géotechnique 29(1):47–65. https://doi.org/10.1680/geot.1979.29.1.47

Czarny R, Pilecki Z, Nakata N, Pilecka E, Krawiec K, Harba P, Barnas M (2019) 3D S-wave velocity imaging of a subsurface disturbed by mining using ambient seismic noise. Eng Geol 251:115–127. https://doi.org/10.1016/j.enggeo.2019.01.017

Dai LP, Pan YS, Li ZH, Wang AW, Xiao YH, Liu FY, Shi TW, Zheng WH (2021) Quantitative mechanism of roadway rockbursts in deep extra-thick coal seams: theory and case histories. Tunn Undergr Space Technol 111:103–116. https://doi.org/10.1016/j.tust.2021.103861

Dassault Systèmes (2021) Abaqus Analysis User's Guide, Version 2021. Providence, RI: Dassault Systèmes.

Day SM (1982) Three-dimensional simulation of spontaneous rupture; the effect of nonuniform prestress. Bull Seismol Soc Am 72(6):1881–1902.

Day SM, Dalguer LA, Lapusta N, Liu Y (2005) Comparison of finite difference and boundary integral solutions to three-dimensional spontaneous rupture. J Geophys Res 110:1–23. https://doi.org/10.1029/2005JB003813

Dieterich JH (1979) Modeling of rock friction: simulation of preseismic slip. J Geophys Res 84(B5):2169–2175. https://doi.org/10.1029/JB084iB05p02169

Dieterich JH, Kilgore B (1996) Implications of fault constitutive properties for earthquake prediction. Proc Natl Acad Sci 93(9):3787–3794. https://doi.org/10.1073/pnas.93.9.3787

Diederichs MS (2003) Manuel Rocha Medal Recipient Rock fracture and collapse under low confinement conditions. Rock Mech Rock Eng 36(5):339–381. https://doi.org/10.1007/s00603-003-0015-y

Du F, Ma J, Guo X, Wang T, Dong X, Li J, He S, Nuerjuma D (2022) Rockburst mechanism and the law of energy accumulation and release in mining roadway: A case study. Int J Coal Sci Technol 9(1):67–17. https://doi.org/10.1007/s40789-022-00521-0

Dunham EM, Belanger D, Cong L, Kozdon JE (2011) Earthquake ruptures with strongly rate-weakening friction and off-fault plasticity, part 2; nonplanar faults. Bull Seismol Soc Am 101(5):2308–2322. https://doi.org/10.1785/0120100076

Ellsworth WL (2013) Injection-induced earthquakes. Science 341(6142):142. https://doi.org/10.1126/science.1225942

Fan X, Scaringi G, Korup O, West AJ, van Westen CJ, Tanyas H, Hovius N, Hales TC, Jibson RW, Allstadt KE, Zhang L, Evans SG, Xu C, Li G, Pei X, Xu Q, Huang R (2019). Earthquake-induced chains of geologic hazards: Patterns, mechanisms, and impacts. Reviews of Geophysics, 57(2), 421–503. https://doi.org/10.1029/2018RG000626

Fan Y, Lu W, Zhou Y, Yan P, Leng Z, Chen M (2016) Influence of tunneling methods on the strainburst characteristics during the excavation of deep rock masses. Eng Geol 201:85–95. https://doi.org/10.1016/j.enggeo.2015.12.015

Fang Z, Dunham EM (2013) Additional shear resistance from fault roughness and stress levels on geometrically complex faults. J Geophys Res Solid Earth 118(7):3642–3654. https://doi.org/10.1002/jgrb.50262

Feng X, Kong R, Yang C, Zhang X, Wang Z, Han Q, Wang G (2020) A three-dimensional failure criterion for hard rocks under true triaxial compression. Rock Mech Rock Eng 53(1):103–111. https://doi.org/10.1007/s00603-019-01903-8

Feng X, Zhao X, Ding Z, Hu Q, Wang D, Cao Z (2024) Numerical study on the influence of fault orientation on risk level of fault slip burst disasters in coal mines; a quantitative evaluation model. Environ Earth Sci 83(3):94. https://doi.org/10.1007/s12665-023-11399-9

Foulger GR, Wilson MP, Gluyas JG, Julian BR, Davies RJ (2018) Global review of human-induced earthquakes. Earth Sci Rev 178:438–514. https://doi.org/10.1016/j.earscirev.2017.07.008

Fukuyama E, Madariaga R (1995) Integral equation method for plane crack with arbitrary shape in 3D elastic medium. Bull Seismol Soc Am 85(2):614–628. https://doi.org/10.1785/bssa0850020614

Fukuyama E, Madariaga R (2000) Dynamic propagation and interaction of a rupture front on a planar fault. Pure Appl Geophys 157(11–12):1959–1979. https://doi.org/10.1007/pl00001070

Fukuyama E, Mikumo T (2006) Dynamic rupture propagation during the 1891 Nobi, central Japan, earthquake: a possible extension to the branched faults. Bull Seismol Soc Am 96(4A):1257–1266. https://doi.org/10.1785/0120050151

Fukuyama E, Tsuchida K, Kawakata H, Yamashita F, Mizoguchi K, Xu S (2018) Spatiotemporal complexity of 2-D rupture nucleation process observed by direct monitoring during large-scale biaxial rock friction experiments. Tectonophysics 733:182–192. https://doi.org/10.1016/j.tecto.2017.12.023

Galis, M., Ampuero, J. P., Mai, P. M., Cappa, F., Lawrence Berkeley National Lab. (LBNL), Berkeley, CA (United States). (2017). Induced seismicity provides insight into why earthquake ruptures stop. Science Advances, 3(12), eaap7528-eaap7528. https://doi.org/10.1126/sciadv.aap7528

Galis M, Pelties C, Kristek J, Moczo P, Ampuero JP, Mai PM (2015) On the initiation of sustained slip-weakening ruptures by localized stresses. Geophys J Int 200(2):890–909. https://doi.org/10.1093/gji/ggu436

Gao F, Kang H, Li J (2021) Numerical simulation of fault–slip rockbursts using the distinct element method. Tunn Undergr Space Technol 110:103805. https://doi.org/10.1016/j.tust.2020.103805

Gao Y, Feng X, Zhang X, Feng G, Jiang Q, Qiu S (2018) Characteristic stress levels and brittle fracturing of hard rocks subjected to true triaxial compression with low minimum principal stress. Rock Mech Rock Eng 51(12):3681–3697. https://doi.org/10.1007/s00603-018-1548-4

Gao Y, Feng X, Zhang X, Zhou Y, Zhang Y (2020) Generalized crack damage stress thresholds of hard rocks under true triaxial compression. Acta Geotech 15(3):565–580. https://doi.org/10.1007/s11440-019-00900-z

Garofalo PS, Maffei J, Papeschi S, Dellisanti F, Neff C, Schwarz G, Schmidt PK, Günther D (2023) Fluid-rock interaction, skarn genesis, and hydrothermal alteration within an upper crustal fault zone (Island of Elba, Italy). Ore Geol Rev 154:105348. https://doi.org/10.1016/j.oregeorev.2023.105348

Geller RJ (1976) Scaling relations for earthquake source parameters and magnitudes. Bull Seismol Soc Am 66(5):1501–1523. https://doi.org/10.1785/BSSA0660051501

Geuzaine C, Remacle J (2009) Gmsh: A 3-D finite element mesh generator with built-in pre- and post-processing facilities. Int J Numer Methods Eng 79(11):1309–1331. https://doi.org/10.1002/nme.2579

Gibowicz SJ (2009) Seismicity induced by mining: Recent research. In: Dmowska R (ed) Advances in Geophysics, vol 51. Elsevier, pp 1–53. https://doi.org/10.1016/S0065-2687(09)05106-1

Gong F, Yan J, Li X, Luo S (2019) A peak-strength strain energy storage index for rock burst proneness of rock materials. Int J Rock Mech Min Sci 117:76–89. https://doi.org/10.1016/j.ijrmms.2019.03.020

Haimson B, Chang C (2000) A new true triaxial cell for testing mechanical properties of rock, and its use to determine rock strength and deformability of Westerly granite. Int J Rock Mech Min Sci 37(1–2):285–296. https://doi.org/10.1016/S1365-1609(99)00106-9

Haimson B, Chang C (2002) True triaxial strength of the KTB amphibolite under borehole wall conditions and its use to estimate the maximum horizontal in situ stress. J Geophys Res 107(B10):15-1–ETG 15-14. https://doi.org/10.1029/2001JB000647

Haimson B, Lin W, Oku H, Hung J, Song SR (2010) Integrating borehole-breakout dimensions, strength criteria, and leak-off test results, to constrain the state of stress across the Chelungpu fault, Taiwan. Tectonophysics 482(1–4):65–72. https://doi.org/10.1016/j.tecto.2009.05.016

Haines SH, van der Pluijm BA (2012) Patterns of mineral transformations in clay gouge, with examples from low-angle normal fault rocks in the western USA. J Struct Geol 43:2–32. https://doi.org/10.1016/j.jsg.2012.05.004

Han P, Hattori K, Huang Q, Hirooka S, Yoshino C (2016) Spatiotemporal characteristics of the geomagnetic diurnal variation anomalies prior to the 2011 Tohoku earthquake (Mw 9.0) and the possible coupling of multiple pre-earthquake phenomena. J Asian Earth Sci 129:13–21. https://doi.org/10.1016/j.jseaes.2016.07.011

Hanks TC, Kanamori H (1979) A moment magnitude scale. J Geophys Res 84:2348–2350. https://doi.org/10.1029/JB084iB05p02348

Harris RA, Day SM (1993) Dynamics of fault interaction: parallel strike-slip faults. J Geophys Res 98(B3):4461–4472. https://doi.org/10.1029/92JB02272

Hatherly P (2013) Overview on the application of geophysics in coal mining. Int J Coal Geol 114:74–84. https://doi.org/10.1016/j.coal.2013.02.006

Havskov J, Ottemoller L (2010) Routine data processing in earthquake seismology: With sample data, exercises and software. Springer Science + Business Media. https://doi.org/10.1007/978-90-481-8697-6

He B, Zelig R, Hatzor YH, Feng X (2016) Rockburst generation in discontinuous rock masses. Rock Mech Rock Eng 49(10):4103–4124. https://doi.org/10.1007/s00603-015-0906-8

He J, Dou L, Gong S, Li J, Ma Z (2017) Rock burst assessment and prediction by dynamic and static stress analysis based on micro-seismic monitoring. Int J Rock Mech Min Sci 93:46–53. https://doi.org/10.1016/j.ijrmms.2017.01.005

He M, Cheng T, Qiao Y, Li H (2023) A review of rockburst: experiments, theories, and simulations. J Rock Mech Geotech Eng 15(5):1312–1353. https://doi.org/10.1016/j.jrmge.2022.07.014

He MC, Nie W, Zhao ZY, Guo W (2012) Experimental investigation of bedding plane orientation on the rockburst behavior of sandstone. Rock Mech Rock Eng 45(3):311–326. https://doi.org/10.1007/s00603-011-0213-y

He MC, Ren FQ, Liu DQ (2018) Rockburst mechanism research and its control. Int J Min Sci Technol 28(5):829–837. https://doi.org/10.1016/j.ijmst.2018.09.002

Heaton TH (1990) Evidence for and implications of self-healing pulses of slip in earthquake rupture. Phys Earth Planet Inter 64(1):1–20. https://doi.org/10.1016/0031-9201(90)90002-F

Hedley DGF (1992) Rockburst Handbook for Ontario Hardrock Mines. Energy, Mine and Resources, Ottawa, Canada.

Hildyard MW, Young RP (2002) Modelling seismic waves around underground openings in fractured rock. Pure Appl Geophys 159(1–3):247–276. https://doi.org/10.1007/PL00001253

Hok S, Fukuyama E, Hashimoto C (2011) Dynamic rupture scenarios of anticipated Nankai-Tonankai earthquakes, southwest Japan. J Geophys Res 116. https://doi.org/10.1029/2011JB008492

Hu L, Yu L, Ju M, Li X, Tang C (2023) Effects of intermediate stress on deep rock strain bursts under true triaxial stresses. J Rock Mech Geotech Eng 15(3):659–682. https://doi.org/10.1016/j.jrmge.2022.06.008

Ida Y (1972) Cohesive force across the tip of a longitudinal-shear crack and Griffith's specific surface energy. J Geophys Res 77(20):3796–3805. https://doi.org/10.1029/JB077i020p03796

Indraratna B, Welideniya H, Brown E (2005) A shear strength model for idealised infilled joints under constant normal stiffness. Géotechnique 55(3):215–226. https://doi.org/10.1680/geot.55.3.215.61524

Ishikawa T, Hirono T, Matsuta N, Kawamoto K, Fujimoto K, Kameda J, Nishio Y, Maekawa Y, Honda G (2014) Geochemical and mineralogical characteristics of fault gouge in the median tectonic line, Japan; evidence for earthquake slip. Earth Planets Space 66(1):36. https://doi.org/10.1186/1880-5981-66-36

Islam MR, Shinjo R (2009) Mining-induced fault reactivation associated with the main conveyor belt roadway and safety of the Barapukuria coal mine in Bangladesh; constraints from BEM simulations. Int J Coal Geol 79(4):115–130. https://doi.org/10.1016/j.coal.2009.06.007

Itasca Consulting Group, Inc. (2021a) FLAC3D - Fast Lagrangian Analysis of Continua in 3 Dimensions, Version 7.0. Minneapolis: Itasca Consulting Group, Inc.

Itasca Consulting Group, Inc. (2021b) 3DEC – 3 Dimensional Distinct Element Code, Version 7.0. Minneapolis: Itasca Consulting Group, Inc.

Jaeger JC, Cook NGW, Zimmerman RW (2007) Fundamentals of Rock Mechanics (4th Ed.). Blackwell Pub, 475pp.

Jaeger JC, Cook NGW, Zimmerman RW (2009) Fundamentals of Rock Mechanics (4th Ed.). Blackwell Pub.

Jarufe Troncoso JA, Perez S, Hurtado JP, Cifuentes C (2022) Seismic hazard calculation using the equivalent magnitude obtained from numerical modelling. Int J Rock Mech Min Sci 153:105081. https://doi.org/10.1016/j.ijrmms.2022.105081

Jian Z, Li X, Mitri HS (2018) Evaluation method of rockburst; state-of-the-art literature review. Tunn Undergr Space Technol 81:632–659. https://doi.org/10.1016/j.tust.2018.08.029

Jiang B, Wu K, Wang Q, Kang H, Zhang B, Zhang Z, Chen C (2024) Development of physical model test system for fault–slip induced rockburst in underground coal mining. J Rock Mech Geotech Eng. https://doi.org/10.1016/j.jrmge.2024.04.003

Jiang L, Kong P, Zhang P, Shu J, Wang Q, Chen L, Wu Q (2020) Dynamic analysis of the rock burst potential of a longwall panel intersecting with a fault. Rock Mech Rock Eng 53(4):1737–1754. https://doi.org/10.1007/s00603-019-02004-2

Jiao Z, Wang L, Zhang M, Wang J (2021a) Numerical simulation of mining-induced stress evolution and fault slip behavior in deep mining. Adv Mater Sci Eng 2021:1–14. https://doi.org/10.1155/2021/8276408

Jiao Z, Yuan Q, Zou P, Shi B (2021b) Case study of the characteristics and mechanism of rock burst near fault in Yima coalfield, China. Shock Vib 2021:1–12. https://doi.org/10.1155/2021/9950273

Kaiser PK, Cai M (2012) Design of rock support system under rockburst condition. J Rock Mech Geotech Eng 4(3):215–227. https://doi.org/10.3724/SP.J.1235.2012.00215

Kaiser PK, Tannant DD, McCreath DR (1996) Overview of the Canadian Rockburst Support Handbook.

Kame N, Yamashita T (1999) Simulation of the spontaneous growth of a dynamic crack without constraints on the crack tip path. Geophys J Int 139(2):345–358. https://doi.org/10.1046/j.1365-246x.1999.00940.x

Kanamori H, Anderson DL (1975) Amplitude of the earth's free oscillations and long-period characteristics of the earthquake source. J Geophys Res 80(8):1075–1078. https://doi.org/10.1029/JB080i008p01075

Kang H, Gao F, Xu G, Ren H (2023) Mechanical behaviors of coal measures and ground control technologies for China's deep coal mines – A review. J Rock Mech Geotech Eng 15(1):37–65. https://doi.org/10.1016/j.jrmge.2022.11.004

Kang H, Yang J, Gao F, Li J (2020) Experimental study on the mechanical behavior of rock bolts subjected to complex static and dynamic loads. Rock Mech Rock Eng 53(11):4993–5004. https://doi.org/10.1007/s00603-020-02205-0

Karacan CO, Ulery JP, Goodman GVR (2008) A numerical evaluation on the effects of impermeable faults on degasification efficiency and methane emissions during underground coal mining. Int J Coal Geol 75(4):195–203. https://doi.org/10.1016/j.coal.2008.06.006

Kato A, Obara K, Igarashi T, Tsuruoka H, Nakagawa S, Hirata N (2012) Propagation of slow slip leading up to the 2011 Mw 9.0 Tohoku-Oki earthquake. Science 335(6069):705–708. https://doi.org/10.1126/science.1215141

Kidybinski A (1981) Bursting liability indices of coal. Int J Rock Mech Min Sci Geomech Abstr 18(4):295–304. https://doi.org/10.1016/0148-9062(81)90630-6

Kong P, Jiang LS, Shu JM, Sainoki A, Wang QB (2019) Effect of fracture heterogeneity on rock mass stability in a highly heterogeneous underground roadway. Rock Mech Rock Eng 52(11):4547–4564. https://doi.org/10.1007/s00603-019-01887-5

Kong P, Wang C, Xing L, Liang M, He J (2023) Study on the fault slip rule and the rockburst mechanism induced by mining the panel through fault. Geomech Geophys Geo-Energy Geo-Resour 9(1):1–16. https://doi.org/10.1007/s40948-023-00697-y

Konicek P, Ptacek J, Waclawik P, Kajzar V (2019) Long-term Czech experiences with rockbursts with applicability to today's underground coal mines. Rock Mech Rock Eng 52(5):1447–1458. https://doi.org/10.1007/s00603-018-1489-y

Kostrov BV, Das S (1988) Principles of Earthquake Source Mechanics. Cambridge University Press, 286pp.

Kozlowska M, Jamroz M, Olszewska D (2021) On the aftershock productivity in mining-induced seismicity; insight into seismicity of Rudna copper ore mine, Poland. Geophys J Int 225(2):1258–1270. https://doi.org/10.1093/gji/ggaa613

Kozłowska M, Orlecka-Sikora B, Kwiatek G, Boettcher MS, Dresen G (2015) Nanoseismicity and picoseismicity rate changes from static stress triggering caused by a Mw 2.2 earthquake in Mponeng gold mine, South Africa. J Geophys Res Solid Earth 120(1):290–307. https://doi.org/10.1002/2014JB011410

Lei W, Linqi H, Taheri A, Xibing L (2017) Rockburst characteristics and numerical simulation based on a strain energy density index: a case study of a roadway in Linglong gold mine, China. Tunn Undergr Space Technol 69:223–232. https://doi.org/10.1016/j.tust.2017.05.011

Li CC, Mikula P, Simser B, Hebblewhite B, Joughin W, Feng XW, Xu NW (2019) Discussions on rockburst and dynamic ground support in deep mines. J Rock Mech Geotech Eng 11(5):1110–1118. https://doi.org/10.1016/j.jrmge.2019.06.001

Li P, Ren F, Wang H, Qian J (2018) An overview of fault rockburst in coal mines. IOP Conf Ser Earth Environ Sci 199(5):52039. https://doi.org/10.1088/1755-1315/199/5/052039

Li T, Cai MF, Cai M (2007) A review of mining-induced seismicity in China. Int J Rock Mech Min Sci 44(8):1149–1171. https://doi.org/10.1016/j.ijrmms.2007.06.002

Li X, Gong F, Tao M, Dong L, Du K, Ma C, Zhou Z, Yin T (2017) Failure mechanism and coupled static-dynamic loading theory in deep hard rock mining: A review. J Rock Mech Geotech Eng 9(4):767–782. https://doi.org/10.1016/j.jrmge.2017.04.004

Li X, Wang E, Li Z, Liu Z, Song D, Qiu L (2016) Rock burst monitoring by integrated microseismic and electromagnetic radiation methods. Rock Mech Rock Eng 49(11):4393–4406. https://doi.org/10.1007/s00603-016-1037-6

Li Y (2024a) Fault quasi-static and dynamic ruptures in deep coal mining: Impacts on working faces. Bull Eng Geol Environ 83(12):515. https://doi.org/10.1007/s10064-024-04017-w

Li Y (2024b) Spatial distribution of strain energy changes due to mining-induced fault coseismic slip: Insights from a rockburst at the Yuejin coal mine, China. Rock Mech Rock Eng. https://doi.org/10.1007/s00603-024-04232-7

Li Y (2025) Heterogeneous layer effects on mining-induced dynamic ruptures. Comput Geosci 195:105776. https://doi.org/10.1016/j.cageo.2024.105776

Li Y, Gao X (2025) Assessment of variations in shear strain energy induced by fault coseismic slip in deep longwall mining. Int J Coal Sci Technol. https://doi.org/10.1007/s40789-024-00742-5

Li Y, Fukuyama E, Yoshimitsu N (2024a) Mining-induced fault failure and coseismic slip based on numerical investigation. Bull Eng Geol Environ 83(10):386. https://doi.org/10.1007/s10064-024-03888-3

Li Y, Fukuyama E, Yoshimitsu N (2024b) Comprehensive 3–D modeling of mining-induced fault slip: impact of panel length, panel orientation and far-field stress orientation. Rock Mech Rock Eng (submitted).

Li Y, Fukuyama E (2024c) 3-D numerical modeling of deep mining-induced fault rupture and seismic wave radiation to the working face of Yuejin coal mine. J Rock Mech Geotech Eng (submitted). https://dx.doi.org/10.2139/ssrn.5015573

Li Y, Yang J, Gao X (2025) Fault slip amplification mechanisms in deep mining due to heterogeneous geological layers. Engineering Failure Analysis, 169, 109155. https://doi.org/10.1016/j.engfailanal.2024.109155

Li Z, Dou L, Cai W, Wang G, He J, Gong S, Ding Y (2014) Investigation and analysis of the rock burst mechanism induced within fault-pillars. Int J Rock Mech Min Sci 70:192–200. https://doi.org/10.1016/j.ijrmms.2014.03.014

Li Z, Dou L, Cai W, Wang G, Ding Y, Kong Y (2016) Mechanical analysis of static stress within fault-pillars based on a voussoir beam structure. Rock Mech Rock Eng 49(3):1097–1105. https://doi.org/10.1007/s00603-015-0754-6

Li Z, Wang C, Shan R, Yuan H, Zhao Y, Wei Y (2021) Study on the influence of the fault dip angle on the stress evolution and slip risk of normal faults in mining. Bull Eng Geol Environ 80(5):3537–3551. https://doi.org/10.1007/s10064-021-02149-x

Linkov AM (1994) Dynamic phenomena in mines and the problem of stability: Notes from courses of lectures. University of Minnesota, Minneapolis/Lisboa.

Liu B, Geng Z, Kang Y, Liu X, Zhou Y, Liu Q, Huang Y, Zhou X (2024) Fault slip behaviors and frictional stability controlled by particle size of fault gouge under fluid injection. Int J Rock Mech Min Sci 183:105919. https://doi.org/10.1016/j.ijrmms.2024.105919

Liu F, Tang C, Ma T, Tang L (2019) Characterizing rockbursts along a structural plane in a tunnel of the Hanjiang-to-Weihe-River diversion project by microseismic monitoring. Rock Mech Rock Eng 52(6):1835–1856. https://doi.org/10.1007/s00603-018-1649-0

Liu H, Yu B, Liu J, Wang T (2019) Investigation of impact rock burst induced by energy released from hard rock fractures. Arab J Geosci 12(12):1–12. https://doi.org/10.1007/s12517-019-4536-4

Lizurek G, Rudzinski L, Plesiewicz B (2015) Mining-induced seismic event on an inactive fault. Acta Geophys 63(1):176–200. https://doi.org/10.2478/s11600-014-0249-y

Lu A, Song D, Li Z, He X, Dou L, Xue Y, Yang H (2024) Numerical simulation study on pressure-relief effect of protective layer mining in coal seams prone to rockburst hazard. Rock Mech Rock Eng 57(8):6421–6440. https://doi.org/10.1007/s00603-024-03826-5

Lu CP, Liu B, Liu B, Liu Y, Wang HY, Heng Z (2019) Anatomy of mining-induced fault–slip and a triggered rockburst. Bull Eng Geol Environ 78(7):5147–5160. https://doi.org/10.1007/s10064-019-01464-8

Lu C, Liu G, Liu Y, Zhang N, Xue J, Zhang L (2015) Microseismic multi-parameter characteristics of rockburst hazard induced by hard roof fall and high stress concentration. Int J Rock Mech Min Sci 76:18–32. https://doi.org/10.1016/j.ijrmms.2015.02.005

Luo Y, Ampuero J (2018) Stability of faults with heterogeneous friction properties and effective normal stress. Tectonophysics 733:257–272. https://doi.org/10.1016/j.tecto.2017.11.006

Lyu P, Lu J, Wang E, Chen X (2021) The mechanical criterion of activation and instability of normal fault induced by the movement of key stratum and its disaster-causing mechanism of rockburst in the hanging wall mining. Adv Civil Eng 2021:1–11. https://doi.org/10.1155/2021/6618957

Ma T, Tang C, Tang S, Kuang L, Yu Q, Kong D, Zhu X (2018) Rockburst mechanism and prediction based on microseismic monitoring. Int J Rock Mech Min Sci 110:177–188. https://doi.org/10.1016/j.ijrmms.2018.07.016

Morris A, Ferrill DA, Henderson DB (1996) Slip-tendency analysis and fault reactivation. Geology (Boulder) 24(3):275–278. https://doi.org/10.1130/0091-7613(1996)024<0275:STAAFR>2.3.CO;2

Ma C, Li T, Zhang H (2020) Microseismic and precursor analysis of high-stress hazards in tunnels; a case comparison of rockburst and fall of ground. Eng Geol 265:105435. https://doi.org/10.1016/j.enggeo.2019.105435

Ma X, Zhang P (2023) Unstable shear slip failure and seismic potential investigation using DEM in underground mining. Min Eng 40(1):405–420. https://doi.org/10.1007/s42461-023-00730-4

Manouchehrian A, Cai M (2017) Analysis of rockburst in tunnels subjected to static and dynamic loads. J Rock Mech Geotech Eng 9(6):1031–1040. https://doi.org/10.1016/j.jrmge.2017.07.001

Mark C (2016) Coal bursts in the deep longwall mines of the United States. Int J Coal Sci Technol 3(1):1–9. https://doi.org/10.1007/s40789-016-0102-9

Masethe RTT, Manzi MSD, Durrheim RJ (2023) Using legacy 3D seismic data and source parameters of mining-induced earthquakes to mitigate the risk of rockbursting in Kloof gold mine, South Africa. Geophys Prospect 71(7):1281–1311. https://doi.org/10.1111/1365-2478.13319

Mayeda K, Walter WR (1996) Moment, energy, stress drop, and source spectra of western United States earthquakes from regional coda envelopes. J Geophys Res Solid Earth 101(B5):11195–11208. https://doi.org/10.1029/96JB00112

McKinnon SD (2006) Triggering of seismicity remote from active mining excavations. Rock Mech Rock Eng 39(3):255–279. https://doi.org/10.1007/s00603-005-0072-5

Meng F, Zhou H, Wang Z, Zhang L, Kong L, Li S, Zhang C, Hu S (2017) Experimental study of factors affecting fault slip rockbursts in deeply buried hard rock tunnels. Bull

Eng Geol Environ 76(3):1167–1182. https://doi.org/10.1007/s10064-016-0926-y

Mngadi SB, Durrheim RJ, Manzi MSD, Ogasawara H, Yabe Y, et al. (2019) Integration of underground mapping, petrology, and high-resolution microseismicity analysis to characterise weak geotechnical zones in deep South African gold mines. Int J Rock Mech Min Sci 114:79–91. https://doi.org/10.1016/j.ijrmms.2018.10.003

Mo PQ, Yong F, Yu H (2020) Benchmark solutions of large-strain cavity contraction for deep tunnel convergence in geomaterials. J Rock Mech Geotech Eng 12(3):596–607. https://doi.org/10.1016/j.jrmge.2019.07.015

Mogi K (1967) Effect of the intermediate principal stress on rock failure. J Geophys Res 72(20):5117–5131. https://doi.org/10.1029/JA072i020p05117

Mogi K (1971) Fracture and flow of rocks under high triaxial compression. J Geophys Res 76(5):1255–1269. https://doi.org/10.1029/JB076i005p01255

Mogi K (2007) Experimental Rock Mechanics. Taylor & Francis, London, UK.

Morad D, Sagy A, Tal Y, Hatzor YH (2022) Fault roughness controls sliding instability. Earth Planet Sci Lett 579:117365. https://doi.org/10.1016/j.epsl.2022.117365

National Coal Mine Safety Administration (2000) State coal industry bureau building, water, railway and main shaft coal pillar of coal mining and coal mining regulations. Coal Industry Publishing House, Beijing, pp 236–238.

Nguyen GD, Nguyen CT, Bui HH, Nguyen VP (2016) Constitutive modeling of compaction localization in porous sandstones. Int J Rock Mech Min Sci 83:57–72. https://doi.org/10.1016/j.ijrmms.2015.12.018

Niwa M, Shimada K, Aoki K, Ishimaru T (2016) Microscopic features of quartz and clay particles from fault gouges and infilled fractures in granite; discriminating between active and inactive faulting. Eng Geol 210:180–196. https://doi.org/10.1016/j.enggeo.2016.06.013

Naji AM, Rehman H, Emad MZ, Yoo H (2018) Impact of shear zone on rockburst in the deep Neelum-Jehlum hydropower tunnel: A numerical modeling approach. Energies

11(8):1935. https://doi.org/10.3390/en11081935

Ohnaka M (1996) Nonuniformity of the constitutive law parameters for shear rupture and quasistatic nucleation to dynamic rupture: A physical model of earthquake generation processes. Proc Natl Acad Sci USA 93(9):3795–3802. https://doi.org/10.1073/pnas.93.9.3795

Ohnaka M, Shen L (1999) Scaling of the shear rupture process from nucleation to dynamic propagation: Implications of geometric irregularity of the rupturing surfaces. J Geophys Res 104(B1):817–844. https://doi.org/10.1029/1998JB900007

Okada Y (1985) Surface deformation due to shear and tensile faults in a half-space. Bull Seismol Soc Am 75(4):1135–1154. https://doi.org/10.1785/BSSA0750041135

Okada Y (1992) Internal deformation due to shear and tensile faults in a half-space. Bull Seismol Soc Am 82(2):1018–1040. https://doi.org/10.1785/BSSA0820021018

Ortlepp WD (1992) Note on fault–slip motion inferred from a study of micro-cataclastic particles from an underground shear rupture. Pure Appl Geophys 139(3–4):677–695. https://doi.org/10.1007/bf00879958

Ortlepp WD (1997) Rock fracture and rockbursts — an illustrative study. Johannesburg: The South African Institute of Mining and Metallurgy.

Ortlepp WD (2000) Observation of mining-induced faults in an intact rock mass at depth. Int J Rock Mech Min Sci 37(1):423–436. https://doi.org/10.1016/S1365-1609(99)00117-3

Ortlepp WD, Stacey TR (1994) Rockburst mechanisms in tunnels and shafts. Tunn Undergr Space Technol 9(1):59–65. Int J Rock Mech Min Sci Geomech Abstr 31(4):220. https://doi.org/10.1016/0148-9062(94)91313-7

Ødegaard H, Nilsen B (2021) Rock stress measurements for unlined pressure tunnels: A true triaxial laboratory experiment to investigate the ability of a simplified hydraulic jacking test to assess fracture normal stress. Rock Mech Rock Eng 54(6):2995–3015. https://doi.org/10.1007/s00603-021-02452-9

Palmer A, Rice JR (1973) The growth of slip surfaces in the progressive failure of over-consolidated clay. Proc R Soc Lond A Math Phys Sci 332(1591):527–548. https://doi.org/10.1098/rspa.1973.0040

Patton FD (1966) Multiple modes of shear failure in rocks. In: Proceedings of the 1st International Congress on Rock Mechanics, Lisbon, pp 509–513.

Perrin G, Rice JR, Zheng G (1995) Self-healing slip pulse on a frictional surface. J Mech Phys Solids 43(9):1461–1495. https://doi.org/10.1016/0022-5096(95)00036-I

Piane CD, Giwelli A, Clennell MB, Esteban L, Nogueira Kiewiet MC, Kiewiet L, Kager S, Raimon J (2016) Frictional and hydraulic behaviour of carbonate fault gouge during fault reactivation — an experimental study. Tectonophysics 690:21–34. https://doi.org/10.1016/j.tecto.2016.07.011

Rahimi B, Sharifzadeh M, Feng X (2020) Ground behaviour analysis, support system design and construction strategies in deep hard rock mining – justified in Western Australian's mines. J Rock Mech Geotech Eng 12(1):1–20. https://doi.org/10.1016/j.jrmge.2019.01.006

Ranjith PG, Zhao J, Ju M, De Silva RVS, Rathnaweera TD, Bandara AKMS (2017) Opportunities and challenges in deep mining: A brief review. Engineering 3(4):546–551. https://doi.org/10.1016/J.ENG.2017.04.024

Ristau J, Rogers GC, Cassidy JF (2005) Moment magnitude-local magnitude calibration for earthquakes in western Canada. Bull Seismol Soc Am 95(5):1994–2000. https://doi.org/10.1785/0120050028

Romanet P, Sato DSK, Ando R (2020) Curvature, a mechanical link between the geometrical complexities of a fault; application to bends, kinks and rough faults. Geophys J Int 223(1):211–232. https://doi.org/10.1093/gji/ggaa308

Romanet P, Saito T, Fukuyama E (2024) The mechanics of static non-planar faults in infinitesimal strain theory. Geophys J Int 239(3):1664–1693. https://doi.org/10.1093/gji/ggae337

Ruina A (1983) Slip instability and state variable friction laws. J Geophys Res 88(B12):10359–10370. https://doi.org/10.1029/JB088iB12p10359

Russenes BF (1974) Analysis of rock spalling for tunnels in steep valley sides. Norwegian Institute of Technology.

Ryder JA (1988) Excess shear stress in the assessment of geologically hazardous situations. J South Afr Inst Min Metall 88(1):27–39.

Sainoki A, Mitri HS (2014a) Dynamic modelling of fault–slip with Barton's shear strength model. Int J Rock Mech Min Sci 67:155–163. https://doi.org/10.1016/j.ijrmms.2013.12.023

Sainoki A, Mitri HS (2014b) Dynamic behaviour of mining-induced fault slip. Int J Rock Mech Min Sci 66:19–29. https://doi.org/10.1016/j.ijrmms.2013.12.003

Sainoki A, Mitri HS (2014c) Simulating intense shock pulses due to asperities during fault–slip. J Appl Geophys 103:71–81. https://doi.org/10.1016/j.jappgeo.2014.01.009

Sainoki A, Mitri HS (2015a) Effect of slip-weakening distance on selected seismic source parameters of mining-induced fault–slip. Int J Rock Mech Min Sci 73:115–122. https://doi.org/10.1016/j.ijrmms.2014.09.019

Sainoki A, Mitri HS (2015b) Evaluation of fault–slip potential due to shearing of fault asperities. Can Geotech J 52(10):1417–1425. https://doi.org/10.1139/cgj-2014-0375

Sainoki A, Hirohama C, Schwartzkopff AK (2020) Dynamic modelling of induced seismicity by using seismic efficiency constraints and a new scaling law for slip-weakening distance. Pure Appl Geophys 177(2):637–659. https://doi.org/10.1007/s00024-019-02342-w

Sainoki A, Schwartzkopff AK, Jiang L, Mitri H (2023) Numerical modelling of spatially and temporally distributed on-fault induced seismicity: Implication for seismic hazards. Int J Coal Sci Technol 10(1):4–16. https://doi.org/10.1007/s40789-022-00560-7

Sandoval E, Bobet A (2017) Effect of frequency and flexibility ratio on the seismic response of deep tunnels. Undergr Space 2(2):125–133. https://doi.org/10.1016/j.undsp.2017.04.003

Sandoval E, Bobet A (2020) Effect of input frequency on the seismic response of deep circular tunnels. Soil Dyn Earthq Eng 139:106421. https://doi.org/10.1016/j.soildyn.2020.106421

Sato R (1972) Stress drop for a finite fault. J Phys Earth 20(4):397–407. https://doi.org/10.4294/jpe1952.20.397

Scholz CH (2019) The Mechanics of Earthquakes and Faulting (3rd Ed.). Cambridge University Press, 493pp.

Shan R, Liu D, Wang H, Tong X, Li Z, Zhao Y (2023) Study of the fracture instability and fault slip risk of overlying strata during mining near faults. Bull Eng Geol Environ 82(3). https://doi.org/10.1007/s10064-023-03112-8

Sharifzadeh M, Lou J, Crompton B (2020a) Dynamic performance of energy-absorbing rockbolts based on laboratory test results. Part I: Evolution, deformation mechanisms, dynamic performance and classification. Tunn Undergr Space Technol 105:103510. https://doi.org/10.1016/j.tust.2020.103510

Sharifzadeh M, Lou J, Crompton B (2020b) Dynamic performance of energy-absorbing rockbolts based on laboratory test results. Part II: Role of inherent features on dynamic performance of rockbolts. Tunn Undergr Space Technol 105:103555. https://doi.org/10.1016/j.tust.2020.103555

Shi Z, Day SM (2013) Rupture dynamics and ground motion from 3-D rough-fault simulations. J Geophys Res 118(3):1122–1141. https://doi.org/10.1002/jgrb.50094

Shibazaki B, Matsu'ura M (1992) Spontaneous processes for nucleation, dynamic propagation, and stop of earthquake rupture. Geophys Res Lett 19(12):1189–1192. https://doi.org/10.1029/92GL01072

Shibazaki B, Matsu'ura M (1998) Transition process from nucleation to high-speed rupture propagation: Scaling from stick-slip experiments to natural earthquakes. Geophys J Int 132(1):14–30. https://doi.org/10.1046/j.1365-246x.1998.00409.x

Sibson, R. H. (1990). Rupture nucleation on unfavorably oriented faults. Bulletin of the Seismological Society of America, 80(6), 1580–1604. https://doi.org/10.1785/BSSA0800061580

Soliva R, Maerten F, Petit J, Auzias V (2010) Field evidences for the role of static friction on fracture orientation in extensional relays along strike-slip faults; comparison with photoelasticity and 3-D numerical modeling. J Struct Geol 32(11):1721–1731. https://doi.org/10.1016/j.jsg.2010.01.008

Song C, Lu C, Zhang X, Wang C, Xie H, Yan X, Yang H (2022) Moment tensor inversion and stress evolution of coal pillar failure mechanism. Rock Mech Rock Eng 55(4):2371–2383. https://doi.org/10.1007/s00603-022-02783-1

Song W, Liang Z (2021) Theoretical and numerical investigations on mining-induced fault activation and groundwater outburst of coal seam floor. Bull Eng Geol Environ 80(7):5757–5768. https://doi.org/10.1007/s10064-021-02245-y

Stacey TR (2012) A philosophical view on the testing of rock support for rockburst conditions. J South Afr Inst Min Metall 112(8):703–710.

Stephens TL, Walker RJ, Healy D, Bubeck A, England RW, McCaffrey KJW (2017) Igneous sills record far-field and near-field stress interactions during volcano construction; Isle of Mull, Scotland. Earth Planet Sci Lett 478:159–174. https://doi.org/10.1016/j.epsl.2017.09.003

Stewart RA, Reimold WU, Charlesworth EG, Ortlepp WD (2001) The nature of a deformation zone and fault rock related to a recent rockburst at Western Deep Levels Gold Mine, Witwatersrand Basin, South Africa. Tectonophysics 337(3–4):173–190. https://doi.org/10.1016/S0040-1951(01)00028-2

Su, Z., Zhou, S., Zang, A., Sun, J., Zhang, T., Niu, Y., Zhang, J., Liang, J. (2024). Analysis of near-field stresses in an analogue strike-slip fault model. Rock Mechanics and Rock Engineering, 57(4), 2739-2754. https://doi.org/10.1007/s00603-023-03714-4

Sun Y, Zuo J, Mi C, Li Y, Wu G, Yu M, Yang J (2023) Investigation on fault activation–induced floor water inrush and its pressure relief control in a 1000-m depth coal mine. Bull Eng Geol Environ 82(6). https://doi.org/10.1007/s10064-023-03239-8

Tada T, Fukuyama E, Madariaga R (2000) Non-hypersingular boundary integral equations for 3-D non-planar crack dynamics. Comput Mech 25(6):613–626. https://doi.org/10.1007/s004660050508

Tal Y, Goebel T, Avouac J (2020) Experimental and modeling study of the effect of fault roughness on dynamic frictional sliding. Earth Planet Sci Lett 536:116133. https://doi.org/10.1016/j.epsl.2020.116133

Tal Y, Hager BH, Ampuero JP (2018) The effects of fault roughness on the earthquake nucleation process. J Geophys Res Solid Earth 123(1):437–456. https://doi.org/10.1002/2017JB014746

Talwani P, Acree S (1984) Pore pressure diffusion and the mechanism of reservoir-induced seismicity. Pure Appl Geophys 122(6):947–965. https://doi.org/10.1007/BF00876395

Tan X, Chen W, Liu H, Chan AHC, Tian H, Meng X, Wang F, Deng X (2017) A combined supporting system based on foamed concrete and U-shaped steel for underground coal mine roadways undergoing large deformations. Tunn Undergr Space Technol 68:196–210. https://doi.org/10.1016/j.tust.2017.05.023

Tan Y (1992) Rockbursting characteristics and structural effects of rock mass. Sci China Ser B Chem Life Sci Earth Sci 35(8):981–990.

Tenthorey E, Cox SF (2006) Cohesive strengthening of fault zones during the interseismic period; an experimental study. J Geophys Res 111(B9). https://doi.org/10.1029/2005JB004122

Tenthorey E, Cox SF, Todd HF (2003) Evolution of strength recovery and permeability during fluid-rock reaction in experimental fault zones. Earth Planet Sci Lett 206(1–2):161–172. https://doi.org/10.1016/S0012-821X(02)01082-8

Uenishi K (2009) On the mechanical destabilization of a three-dimensional displacement-softening plane of weakness. Proceedings of the 38th Symposium on Rock Mechanics, Tokyo, Japan, pp 332–337.

Uenishi K, Rice JR (2003) Universal nucleation length for slip-weakening rupture instability under nonuniform fault loading. J Geophys Res 108(B1):2042. https://doi.org/10.1029/2001JB001681

Vardar O, Wei C, Zhang C, Canbulat I (2022) Numerical investigation of impacts of geological faults on coal burst proneness during roadway excavation. Bull Eng Geol Environ 81(1). https://doi.org/10.1007/s10064-021-02508-8

Vardar O, Zhang C, Canbulat I, Hebblewhite B (2018) A semi-quantitative coal burst risk classification system. Int J Rock Mech Min Sci 28(5):721–727. https://doi.org/10.1016/j.ijmst.2018.08.001

Verdon JP, Kendall JM, Butcher A, Luckett R, Baptie BJ (2018) Seismicity-induced by longwall coal mining at the Thoresby colliery, Nottinghamshire, UK. Geophys J Int 212(2):942–954. https://doi.org/10.1093/gji/ggx465

Wallace RE (1951) Geometry of shearing stress and relation to faulting. J Geol 59(2):118–130. https://doi.org/10.1086/625831

Wallace RE, Morris HT (1986) Characteristics of faults and shear zones in deep mines. Pure Appl Geophys 124(1–2):107–125. https://doi.org/10.1007/bf00875721

Wang CB, Si G, Zhang C, Cao A, Canbulat I (2023) Variation of seismicity using reinforced seismic data for coal burst risk assessment in underground mines. Int J Rock Mech Min Sci 165:105363. https://doi.org/10.1016/j.ijrmms.2023.105363

Wang C, Cao A, Zhu G, Jing G, Li J, Chen T (2017) Mechanism of rock burst induced by fault slip in an island coal panel and hazard assessment using seismic tomography; a case study from Xuzhuang Colliery, Xuzhou, China. Geosci J 21(3):469–481. https://doi.org/10.1007/s12303-016-0065-2

Wang F, Chen T, Chen Z, Chen S, Ding X, Liu Z (2023) Failure analysis of overlying strata in fault fracture zone during coal mining. J Geophys Eng 20(6):1127–1139. https://doi.org/10.1093/jge/gxad072

Wang G, Gong S, Li Z, Dou L, Cai W, Mao Y (2016) Evolution of stress concentration and energy release before rock bursts; two case studies from Xingan Coal Mine, Hegang, China. Rock Mech Rock Eng 49(8):3393–3401. https://doi.org/10.1007/s00603-015-0892-x

Wang G, Jin F, Gong S, Dou L, Fan C, Cai W, Yuan X (2019) Generating behaviors of strong tremors and experimental study of rock burst-triggering criterion. Shock Vib 2019:1–12. https://doi.org/10.1155/2019/6319612

Wang G, Li G, Dou L, Mu Z, Gong S, Cai W (2020) Applicability of energy-absorbing support system for rockburst prevention in underground roadways. Int J Rock Mech Min Sci 132:104396. https://doi.org/10.1016/j.ijrmms.2020.104396

Wang HW, Shi R, Deng D, Jiang Y, Wang G, Gong W (2020b) Characteristic of stress evolution on fault surface and coal bursts mechanism during the extraction of longwall face in Yima mining area, China. J Struct Geol 136:104071. https://doi.org/10.1016/j.jsg.2020.104071

Wang HW, Shi R, Song J, Tian Z, Deng D, Jiang Y (2021) Mechanical model for the calculation of stress distribution on fault surface during the underground coal seam mining. Int J Rock Mech Min Sci 144:104765. https://doi.org/10.1016/j.ijrmms.2021.104765

Wang HW, Xue S, Shi RM, Jiang YS, Gong WL, Mao LT (2020a) Investigation of fault displacement evolution during extraction in longwall panel in an underground coal mine. Rock Mech Rock Eng 53(10):1809–1826. https://doi.org/10.1007/s00603-019-02015-z

Wang J, Zeng X, Zhou J (2012) Practices on rockburst prevention and control in headrace tunnels of Jinping II hydropower station. J Rock Mech Geotech Eng 4(3):258–268. https://doi.org/10.3724/SP.J.1235.2012.00258

Wang K, Ma K, Tang C, Liu H, Wang X, Li Q (2023) Study on deep mining-induced strata behavior based on the evolutional laws of multiple indices from microseismic monitoring. Rock Mech Rock Eng 56(9):6481–6501. https://doi.org/10.1007/s00603-023-03411-2

Wang Q, Jiang B, Xu S, He M, Jiang Z, Li S, Wei H, Xiao Y (2022) Roof-cutting and energy-absorbing method for dynamic disaster control in deep coal mine. Int J Rock Mech Min Sci 158:105186. https://doi.org/10.1016/j.ijrmms.2022.105186

Wang YH, Nguyen NHT, Lianheng Z (2021b) Micromechanical study on hard rock strainburst using the discrete element method. Tunn Undergr Space Technol 109:103793. https://doi.org/10.1016/j.tust.2020.103793

Wei C, Zhang C, Canbulat I (2020) Numerical analysis of fault–slip behavior in longwall mining using linear slip weakening law. Tunn Undergr Space Technol 104:103541. https://doi.org/10.1016/j.tust.2020.103541

Wei C, Zhang C, Canbulat I, Anye C, Linming D (2018) Evaluation of current coal burst control techniques and development of a coal burst management framework. Tunn Undergr Space Technol 81:129–143. https://doi.org/10.1016/j.tust.2018.07.008

Wei C, Zhang C, Canbulat I, Wanpeng H (2021) Numerical investigation into impacts of major fault on coal burst in longwall mining; a case study. Int J Rock Mech Min Sci 147:104907. https://doi.org/10.1016/j.ijrmms.2021.104907

Wells DL (2013) Updated empirical relationships among magnitude, rupture area, rupture length, and surface displacement. Seismol Res Lett 84(2):309.

Wells DL, Coppersmith KJ (1994) New empirical relationships among magnitude, rupture length, rupture width, rupture area, and surface displacement. Bull Seismol Soc Am 84(4):974–1002. https://doi.org/10.1785/bssa0840040974

Wiebols GA, Cook NGW (1968) An energy criterion for the strength of rock in polyaxial compression. Int J Rock Mech Min Sci Geomech Abstr 5(6):529–549. https://doi.org/10.1016/0148-9062(68)90040-5

Wu H, Zhao G, Dai B, Liang W (2020) A scientometric review on rockburst in hard rock: two decades of review from 2000 to 2019. Geofluids 2020:1–17. https://doi.org/10.1155/2020/8763283

Wu Q, Wu Q, Yuan A, Wu Y (2021) Analysis of mining effect and fault stability under the influence of normal faults. Geotech Geol Eng 39(1):49–63. https://doi.org/10.1007/s10706-020-01400-8

Xiang C, Yang H (2020) Effects of seismogenic width and low-velocity zones on estimating slip-weakening distance from near-fault ground deformation. Geophys J Int 223(3):1497–1510. https://doi.org/10.1093/gji/ggaa385

Xiao P, Li D, Zhao G, Zhu Q (2023) Characteristics and mechanism of rockburst at five deep gold mines in Jiaodong Peninsula of China. Int J Rock Mech Min Sci 171:105574. https://doi.org/10.1016/j.ijrmms.2023.105574

Xiao Z, Gu S, Zhang Y, Wang H (2022) A coal seam-roof-floor coupling destressing control method of fault coal bursts induced by deep coal seam mining. Energy Sci Eng 10(7):2170–2190. https://doi.org/10.1002/ese3.1124

Xu S, Fukuyama E, Ben-Zion Y, Ampuero J (2015) Dynamic rupture activation of backthrust fault branching. Tectonophysics 644–645:161–183. https://doi.org/10.1016/j.tecto.2015.01.011

Xu S, Fukuyama E, Yamashita F, Kawakata H, Mizoguchi K, Takizawa S (2022) Fault strength and rupture process controlled by fault surface topography. Zenodo. https://doi.org/10.5281/zenodo.6860899

Xue YR, Song DZ, Chen JQ, Li ZL, He XQ, Wang HL, Chao Z, Sobolev A (2023) Integrated rockburst hazard estimation methodology based on spatially smoothed seismicity model and Mann-Kendall trend test. Int J Rock Mech Min Sci 163:105329. https://doi.org/10.1016/j.ijrmms.2023.105329

Yabe Y, Nakatani M, Naoi M, Philipp J, Janssen C, Watanabe T, Katsura T, Kawakata H, Georg D, Ogasawara H (2015) Nucleation process of an M2 earthquake in a deep gold mine in South Africa inferred from on-fault foreshock activity. J Geophys Res Solid Earth 120(8):5574–5594. https://doi.org/10.1002/2014JB011680

Yamashita F, Fukuyama E, Xu S, Mizoguchi K, Kawakata H, Takizawa S (2018) Rupture preparation process controlled by surface roughness on meter scale laboratory fault. Tectonophysics 733:193–208. https://doi.org/10.1016/j.tecto.2018.01.034

Yan H, He F (2012) A new cable truss support system for coal roadways affected by dynamic pressure. Int J Min Sci Technol 22(5):613–617. https://doi.org/10.1016/j.ijmst.2012.08.003

Yang Y, Wei S, Li K (2021) Inverse analysis of dynamic failure characteristics of roadway surrounding rock under rock burst. Energy Sci Eng 9(12):2298–2310. https://doi.org/10.1002/ese3.977

Yang Z, Liu C, Zhu H, Xie F, Dou L, Chen J (2019) Mechanism of rock burst caused by fracture of key strata during irregular working face mining and its prevention methods. Int J Min Sci Technol 29(6):889–897. https://doi.org/10.1016/j.ijmst.2018.07.005

Yao Z, Fang Y, Zhang R, Pu S, Zhao G, Yu T, Ma C (2023) The mechanism of stick-slip as a rockburst source in jointed rock mass: An experimental study. Rock Mech Rock Eng 56(5):3573–3593. https://doi.org/10.1007/s00603-023-03220-7

Younger PL (2016) How can we be sure fracking will not pollute aquifers? Lessons from a major longwall coal mining analogue (Selby, Yorkshire, UK). Earth Environ Sci Trans R Soc Edinb 106(2):89–113. https://doi.org/10.1017/S1755691016000013

Zhang J, Zhang Y, Han Y, Fan W, Song Z, Yu H, Zhang J, Zhang H, Liu J (2024) Study on stress distribution law of surrounding rock of roadway under the goaf and mechanism of pressure relief and impact reduction. Eng Fail Anal 160:108210. https://doi.org/10.1016/j.engfailanal.2024.108210

Zhang N, Zhang Z, Shan R, Qi Q, Zhao S, Sun Z, Guo Y (2023) An experimental study of fault slips under unloading condition in coal mines. Bull Eng Geol Environ 82(4). https://doi.org/10.1007/s10064-023-03125-3

Zhang Q, Zhang X, Liu Q, Chi J, Qiu J (2023) Microseismic characteristic and development mechanism of fault–slip rockburst in a deep-buried TBM excavated tunnel: A case study. Tunn Undergr Space Technol 142:105451. https://doi.org/10.1016/j.tust.2023.105451

Zhang W, Feng X, Xiao Y, Feng G, Yao Z, Hu L, Niu W (2020) A rockburst intensity criterion based on the geological strength index, experiences learned from a deep tunnel. Bull Eng Geol Environ 79(7):3585–3603. https://doi.org/10.1007/s10064-020-01774-2

Zhang W, Feng X, Yao Z, Hu L, Xiao Y, Feng G, Niu W, Zhang Y (2022) Development and occurrence mechanisms of fault–slip rockburst in a deep tunnel excavated by drilling and blasting: A case study. Rock Mech Rock Eng 55(9):5599–5618. https://doi.org/10.1007/s00603-022-02927-3

Zhang W, Lei Y, Shao J, Wu X, Li S, Ma C (2022) Simulation of the activation of mining faults and grouting reinforcement under thick loose layer and thin bedrock. Sci Rep 12(1):17049. https://doi.org/10.1038/s41598-022-21654-x

Zhao T, Guo W, Tan Y, Yin Y, Cai L, Pan J (2018) Case studies of rock bursts under complicated geological conditions during multi-seam mining at a depth of 800 m. Rock Mech Rock Eng 51(5):1539–1564. https://doi.org/10.1007/s00603-018-1411-7

Zheng Y, Deng S (2015) Failure probability model considering the effect of intermediate principal stress on rock strength. Math Probl Eng 2015:1–7. https://doi.org/10.1155/2015/960973

Zhou K, Dou L, Li X, Song S, Cao J, Bai J, Ma X (2022) Coal burst and mining-induced stress evolution in a deep isolated main entry area - A case study. Eng Fail Anal 137:106289. https://doi.org/10.1016/j.engfailanal.2022.106289

Zhu Q, Zhao X, Westman E (2021) Review of the evolution of mining-induced stress and the failure characteristics of surrounding rock based on microseismic tomography. Shock Vib 2021:1–19. https://doi.org/10.1155/2021/2154857

Zhou X, He Y, Shou Y (2021) Experimental investigation of the effects of loading rate, contact roughness, and normal stress on the stick-slip behavior of faults. Tectonophysics 816:229027. https://doi.org/10.1016/j.tecto.2021.229027